Ad maiorem Dei gloriam

Resonance production and decays in nucleon-nucleon collisions with HADES

Witold Przygoda

Jagiellonian University

Kraków, 2018

Printed by:
Drukarnia Eikon Plus
ul. Wybickiego 46
31-302 Kraków
tel. (12) 636 27 13
www.eikon.net.pl

ISBN 978-83-60391-99-0

First edition. Kraków 2018

Cover design by Witold Przygoda
Photo cover by Jan Michael Hosan
Typeset with the LaTeX Documentation System

Resonance production and decays in nucleon-nucleon collisions with HADES

Abstract

The High Acceptance Di-Electron Spectrometer (HADES), installed at GSI, allows to study both hadron and rare dilepton production in a fixed target experiments in the beam energy range of a few GeV per nucleon, reaching up to 4.5 GeV for a proton beam and 1.5 GeV/nucleon for a heavy-ion beam. The present interpretation of dilepton spectra measured in heavy-ion reactions at various energies is based on hadronic models. They predict in-medium modifications of the ρ–meson spectral function due to its coupling to resonance-hole states. In the energy range of the HADES experiments, the ρ–meson can be produced in primary NN or secondary πN collisions. The measurement of a dielectron emission in elementary reactions opens the possibility to constrain the interpretation of medium effects and better understand the relation between the couplings of the baryonic resonances to the ρ–meson. The Dalitz decay of baryonic resonances ($R \to Ne^+e^-$) gives access to the electromagnetic structure of baryonic transitions in a timelike region at small positive values of the squared four-momentum transferred, where couplings to light vector ρ/ω mesons are expected.

In this monograph the systematic studies of resonance excitation and decays, measured in NN collisions with the increasing energy, are presented. First, the pp collisions at 1.25 GeV allowed to measure exclusive channels with one-pion in the final state. They were put to extended studies based on various observables in one-pion exchange models and with solutions obtained within the framework of a partial wave analysis (PWA) of the Bonn-Gatchina group. The obtained $\Delta(1232)$ production cross section was further used for the first experimental extraction of the Δ Dalitz decay and compared to the models of the electromagnetic transition form factors. The branching ratio of this decay, achieved in the exclusive $pp \to ppe^+e^-$ channel, has been included in the 2018 Review of Particle Physics.

In quasi-free np collisions at 1.25 GeV, two-pion production was studied to conclude on double–Δ, $N(1440)$, and $\Delta(1600)$ excitation with the aim of studying the production of the ρ–meson in the isospin $I = 1$ channel. In addition, this analysis provided an independent verification of the existence of the $d^*(2370)$ resonance observed by the WASA Collaboration. Furthermore, a strong excess of the dielectron yield, in comparison to the pp reaction at 1.25 GeV, was observed in the e^+e^- inclusive channel. This reaction is well suited for studies of the np bremsstrahlung with strong isospin effects effects predicted by one-boson-exchange models. The excess was confirmed also in the e^+e^- exclusive channel and the data were compared with the models explaining the enhancement at large invariant masses due to the off-shell ρ–meson production.

The exclusive hadronic channels with one-pion and η–meson were identified in pp collisions at 2.2 GeV. The π^0 and η exclusive production cross sections were extracted and compared to the predictions of a resonance model. Further, the analysis of the ppe^+e^- exclusive channel allowed for the reconstruction of π^0 and η Dalitz decays. The angular distributions of e^+ or e^- in the γ^* rest frame were determined to be in agreement with the QED prediction for pseudoscalar mesons.

In the pp collisions measured at energy T = 3.5 GeV, a peak corresponding to direct ω decays, with 2% mass resolution, was reconstructed. The inclusive production cross sections for ω and ρ mesons were determined from dielectron experimental data for the first time at this energy. In addition, the upper bound for the direct $\eta \to e^+e^-$ decay was defined. The exclusive one pion production ($pp \to pp\pi^0$ and $pp \to np\pi^+$) and dielectron ($pp \to ppe^+e^-$) channels were used to extract the N^* and Δ resonance production cross sections. The e^+e^- emission from baryonic decays was identified with the dielectron invariant mass distribution strongly modified by the intermediate ρ–meson. This observation has been interpreted within the Vector Dominance Model of the resonance electromagnetic transition form factor. Comparison with various transport models (PYTHIA, GiBUU/SMASH, HSD, UrQMD) unraveled the ambiguities of the model descriptions and the important role of the intermediate ρ production.

To tackle this problem a systematic investigation focused on the role of $N(1520)$ production and decay in pion-induced reactions was started. Data at four different pion beam momenta (656, 690, 748 and 800 MeV/c) were collected in π^-p collisions. In the outlook, exclusive channels with one pion (π^-p), two pions ($n\pi^+\pi^-$) and dileptons (ne^+e^-) in the final state were discussed, with a special interest for the ρN channel, since it has a direct impact on the in-medium distortions of the ρ–meson spectral function. Pion beam experiments will be continued in GSI in the next years, then the HADES experimental program will be pursued using the proton and ion beams at FAIR.

This monograph has been extended by Appendices covering details on dielectron production channels as well as the models of the electromagnetic transition form factors for baryon resonance Dalitz decays. The HADES spectrometer and the analysis strategy were described, too. The author hopes that this book will serve not only as a report on the scientific achievements but also as a source of information on resonance production and decays in nucleon-nucleon collisions at energies of a few GeV.

Contents

Chapter 1

Baryon resonances

The path to understanding of nuclear forces usually begins with the studies of elementary reactions. High precision measurements and final state complete reconstruction provide invaluable insight into the nature of nucleon-nucleon interactions. Those studies have to be performed with increasing energy since new processes are involved above the one-pion and two-pion production thresholds. The key issues in this research are the investigation of baryon resonances, i.e. short-lived excited states of nucleons. Resonance is identified as a pole in the complex energy plane located on the unphysical sheet closest to the physical one (called second Riemann sheet). From experimental point of view a resonance manifests as a peak in excitation function, located around a certain energy in differential cross section. Its nature is probed in scattering experiments and is characterized not only by the complex pole position of the scattering amplitude but also by the couplings to the various channels and hence decay branching ratios. Particularly the important region of $1-2$ GeV is occupied by light-flavoured baryons. Such baryons are built out of three quarks (u, d, s) with possible isospin either 1/2 or 3/2. Accounting for orbital motion, a supermultiplet SU(6)×O(3) defines all combinations resulting in 434 possible resonances. It highly exceeds the number of 112 identified resonances (Particle Data Group [PDG16]) many of which do not have well determined parameters. The resonance properties were tackled by many models, including quark models [Cre13], Dyson-Schwinger approach [Rob94] and lattice QCD calculations [Edw11]. Those models are still confronting the fundamental question of "missing resonances". A possible explanation (as suggested in Ref. [Kon80]) lies in the fact that missing states can couple weakly to the $N\pi$ channel, which is the main source of knowledge about baryon properties. Additional difficulty stems from the fact that resonance spectral functions are usually quite broad and various resonances overlap.

The excited states of the nucleon have been studied in many formation and production experiments, and their Breit-Wigner masses and widths, the pole positions, and the elasticities of the N and Δ resonances were first obtained from partial wave analysis of πN total, elastic, and charge-exchange scattering data. The former naming convention (used up to the year 2010 in the Review of Particle Physics [PDG10]) was related to labeling resonances with the incoming pion-nucleon partial wave $L_{2I,2J}$ (where I is isospin, J is spin), i.e. $\Delta(1232)P_{33}$, $N(1440)P_{11}$, $N(1520)D_{13}$ or $N(1535)S_{11}$. In recent years, a large amount of data on photoproduction has been accumulated improving the knowledge on properties of baryon resonances [Kle10, Cre13]. The naming convention (beginning since year 2012 [PDG12]) has been replaced with the spin-parity J^P of the state, i.e. $\Delta(1232)\frac{3}{2}^+$, $N(1440)\frac{1}{2}^+$, $N(1520)\frac{3}{2}^-$ or $N(1535)\frac{1}{2}^-$.

1.1 Resonance properties

The cross section for the production of a resonance R in a $ab \to R$ reaction is usually describer by the Breit-Wigner formula:

$$\sigma_{ab\to R}(s) = \frac{2J_R+1}{(2J_a+1)(2J_b+1)}\,\frac{4\pi}{k^2}\,\frac{s\,\Gamma_{ab}^{in}\,\Gamma_{tot}^{out}}{\left(s-m_0^2\right)^2 + s\,\Gamma_{tot}^{out\,2}}, \tag{1.1}$$

where J_R, J_a, and J_b denote the spins of the resonance, and the particles a and b, respectively. k is the c.m.s. momentum of the incoming particles, s is the squared invariant energy, and the m_0 corresponds to the pole mass of the resonance. The total decay width Γ_{tot}^{out} is given as a sum over the partial decay widths of the resonance. For a specific channel ab, the resonance R partial decay width can be denoted by

$$\Gamma_{R\to ab}(m) = \Gamma_{R\to ab}^0 \frac{\rho_{ab}(m)}{\rho_{ab}(m_0)}, \tag{1.2}$$

where m and m_0 is the off-shell mass and the pole mass of the resonance R, respectively, $\Gamma_{R\to ab}^0 = \Gamma_{R\to ab}(m_0)$ is the partial width at the pole mass and $\rho_{ab}(m)$ is defined as

$$\rho_{ab}(m) = \int \mathcal{A}_a(m_a^2)\mathcal{A}_b(m_b^2)\tfrac{p_f}{m}B_L^2(p_f r)\mathcal{F}_{ab}^2(m)dm_a^2 dm_b^2. \tag{1.3}$$

$\mathcal{A}_a$ and $\mathcal{A}_b$ are spectral functions of the particles a and b with the masses m_a and m_b, respectively. The spectral function $\mathcal{A}$ of an unstable particle i reads:

$$\mathcal{A}_i(\mu) = \frac{2}{\pi}\frac{\mu\Gamma_{tot}(\mu)}{\left(\mu^2-m_{i0}^2\right)^2 + \mu^2\,\Gamma_{tot}^2(\mu)}, \tag{1.4}$$

where m_{i0} is the pole mass, and $\Gamma_{tot}(\mu)$ is the total width of a particle i. Any spin degrees of freedom as well as a momentum dependence of the real part of the self-energy are here neglected. For a stable particle with respect to the strong interaction the spectral function can be replaced by $\mathcal{A}(\mu) = \delta(\mu - m_{i0})$. p_f is the final state momentum of a and b in the mother particle (resonance) reference frame:

$$p_f(m, m_a, m_b) = \frac{1}{2m}\sqrt{m^2-(m_a+m_b)^2)(m^2-(m_a-m_b)^2}\,, \tag{1.5}$$

and L is the orbital angular momentum of a or b in the final state. B_L denotes the Blatt-Weisskopf angular momentum barrier functions and r presents the interaction radius (usually ~1 fm). The expressions of the first few B_L are:

$$\begin{aligned} B_0(x) &= 1, \\ B_1(x) &= \frac{x}{\sqrt{1+x^2}}, \\ B_2(x) &= \frac{x^2}{\sqrt{9+3x^2+x^4}}, \\ B_3(x) &= \frac{x^3}{\sqrt{225+45x^2+6x^4+x^6}}. \end{aligned} \tag{1.6}$$

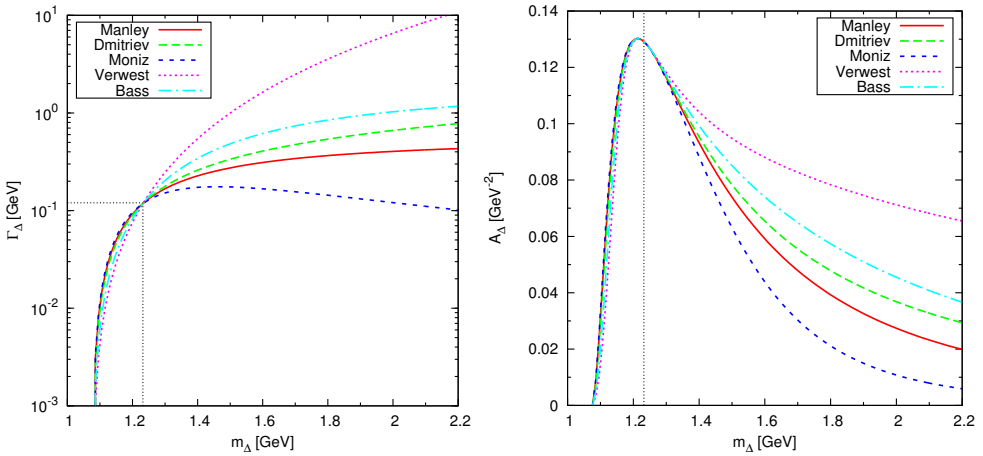

Figure 1.1: Δ resonance various parametrizations: the mass-dependent vacuum width $\Gamma\Delta \to \pi N(m)$ (left panel) and the spectral function (right panel) according to Manley (red curve), Dmitriev (dashed green), Moniz (dashed blue), Verwest (dotted magenta) and Bass (dashed dotted cyan). Figure taken from Ref. [Wei13].

It is worth discussing the case of $P-$wave decays such as $\Delta \to \pi N$ due to significance of the Δ resonance contribution to dilepton spectra. In such a case the width parametrization is

$$\Gamma(m) = \Gamma_0 \, \frac{m_0}{m} \left(\frac{q}{q_0}\right)^3 \frac{q_0^2 + \kappa^2}{q^2 + \kappa^2}, \tag{1.7}$$

where m and m_0 are, as above, the off-shell and pole mass of the resonance, Γ_0 is the resonance width at $m = m_0$, q and q_0 are the final state (i.e. pion) momenta in the center-of-mass reference frame for the resonance mass m and m_0, respectively. The cutoff parameter amounts to $\kappa = 1/r = 1$ fm^{-1}, (1 fm^{-1} = 197.3 MeV). The Eq. 1.7 is cited in the literature as Blatt-Weisskopf or Manley Δ resonance parametrization. However, there are other parametrizations (Fig. 1.1) which differ significantly in the modeling of the Δ resonance in the high mass tail:

$$\begin{aligned}
\Gamma(m)_{Dmitriev} &= \Gamma_0 \left(\frac{q}{q_0}\right)^3 \frac{q_0^2 + \kappa^2}{q^2 + \kappa^2}, \quad \kappa = 0.2 \text{ GeV}, \\
\Gamma(m)_{Moniz} &= \Gamma_0 \, \frac{m_0}{m} \left(\frac{q}{q_0}\right)^3 \left(\frac{q_0^2 + \kappa^2}{q^2 + \kappa^2}\right)^2, \quad \kappa = 0.3 \text{ GeV}, \\
\Gamma(m)_{Verwest} &= \Gamma_0 \left(\frac{q}{q_0}\right)^3 \frac{\sqrt{q^2 + m_\pi^2} + m_N}{\sqrt{q_0^2 + m_\pi^2} + m_N}, \\
\Gamma(m)_{Bass} &= \Gamma_0 \left(\frac{q}{q_0}\right)^3 \frac{1.2}{1 + 0.2\,(\frac{q}{q_0})^2}.
\end{aligned} \tag{1.8}$$

Among all formulas, VerWest parametrization [Ver79] was obtained by fitting to old experimental data at the beam kinetic energy 800 MeV and overshoots all other descriptions. The Dmitriev [Dmi86] and Bass [Bas98] parametrizations are equivalent to Manley description [Man92] but with a different interaction radius. In many cases the

radius can be treated as a free parameter adjusted within the model (as discussed in Sec. 2.1.2). The Koch and Moniz parametrization [Koc84] provides a strong suppression of the resonance tail. The ambiguous descriptions are populated further in various calculations. The Hadron String Dynamics (HSD) transport model [Bra97,Cas99,Bra08,Bra13] and the resonance model by Teis *et al.* [Tei97] use Moniz parametrization, the Giessen BUU (GiBUU) transport model [Bus12, Wei12, Wei13] uses Manley parametrization, the UrQMD [Bas98] and the Isospin QMD (IQMD) [Har98, Tho07, Har12] transport models use their own parametrizations. The partial wave analysis of Bonn-Gatchina group in the photo-, pion- [Ani05, Ani06, Ani12] and proton-induced [Erm11, Erm14] reactions uses Blatt-Weisskopf (Manley) form factors, and, consequently, the partial wave analysis of the HADES data for proton-proton collisions at T = 1.25 GeV [HC15a] does (Sect. 2.1). Similarly, Ramalho and Peña [Ram12, Ram16] calculations, describing the eTFF of Δ resonance (Sec. B.4), follow the GiBUU description, that is, Manley parametrization. The experimental data of the proton-proton reaction at T = 3.5 GeV [HC14a] seem to favor Moniz parametrization (Sect. 2.4). It has to be mentioned, however, that not only the decay width matters in the description of the Δ resonance excitation, but also the vertex cut-off (Sect. 1.2.1) entering the production amplitude.

$\mathcal{F}_{ab}$ cut-off function in Eq. 1.3 is introduced to describe the form factor of the unstable decay products (i.e. ρN, ηN, σN, $\pi\Delta$, πN^*, $\rho\Delta$ and $\sigma\Delta$) [Pen02] and in the case of stable particles it amounts to $\mathcal{F}_{ab}(m) = 1$. It has been also shown in Ref. [Bus08] that the cut-off itself has only a minor influence on the resonance spectral shapes.

1.2 Resonances in semi-classical models

Nucleon-nucleon interactions provide a fundamental knowledge about the nature of nuclear forces with a strong impact on the construction of many dynamic models. Although the elastic NN scattering is a dominant process at the low energies, the understanding of inelastic collisions is mandatory above the one-pion and two-pion production thresholds (for a review see Ref. [Mos02]). One of the first semi-phenomenological models by Mandelstam [Man58] was describing the pion production by the formation of the intermediate $N\Delta$ state and a decay of the Δ into a nucleon and a pion. However, the absence of dependence of the production amplitude on energy was in contradiction to experimental data at energies above 0.7 GeV. A more advanced approach was realized by one-pion (OPE, see Refs. [Fer61, Fer63, Sel65]) or by a one-boson exchange (OBE) models, developed by several groups (see Refs. [Ger71, Bry72, Bry73, Sch72, Erk74, Hol75, Hol76, Mac87, Eng96]).

An improved version of the OPE model was proposed by Suslenko and Gaisak [Sus86], describing the experimental data in the $pp \to np\pi^+$ reaction in the energy range 0.6 – 1.0 GeV with an accuracy of 10 – 15%. The model was tested also in the $pp \to pp\pi^0$ reaction at seven energies of the incident proton in the range 0.6 – 0.9 GeV with the data collected at the PNPI [And94]. Although various differential distributions are described by the model qualitatively well, the predicted total cross sections are lower than the reconstructed from the experimental data. Similar conclusions were reported in the study of the neutral pion production at proton beam momentum 1.581 GeV/c and 1.628 GeV/c [Sar04], supplemented by the recent studies of $np\pi^+$ channel (Refs. [Erm14, Erm11]) for the same beam momenta. The good data description in the $np\pi^+$ channel leads to the underestimation of the total cross section by the OPE model [Sus86] in the $pp\pi^0$ channel.

1.2.1 Δ resonance production in OPE model

Another OPE model, successfully describing the data at slightly higher energies of 0.97 GeV [Bug64], 1.48 GeV [Eis65] and 4 GeV [Col67] in the $pp \to np\pi^+$ channel, was introduced by Dmitriev, Sushkov and Gaarde [Dmi86]. The matrix element in the model is calculated based on the direct and exchange graphs (Fig. 1.2) for Δ−production in pp collisions, with the form factors taking into account the off-shellness of the pion, in the πNN and $\pi N\Delta$ vertices

$$F(t) = \frac{\Lambda_\pi^2 - m_\pi^2}{\Lambda_\pi^2 - t}, \tag{1.9}$$

where Λ_π is the coupling constant adjusted to the data (i.e. Λ_π = 0.63 GeV for the [Bug64]) and t denotes the Mandelstam variable for the momentum transfer. The pion-exchange amplitude is derived from the density matrix for spin−$\frac{3}{2}$ particle (Ref. [Ose82]) and the interference between both graphs is taken into account. The finite Δ width is parametrized (see Eq. 1.8) with the cutoff parameter κ reproducing the $\pi^+p \to \pi^+p$ cross section [Fla83]. The Γ parametrization takes into account the Δ off-shell correction.

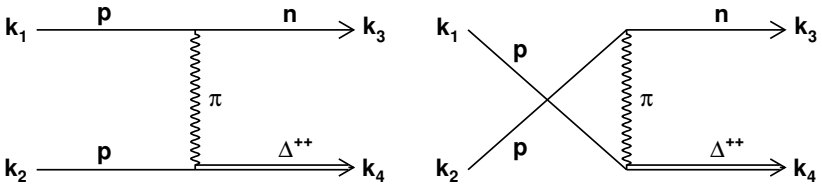

Figure 1.2: Direct (left panel) and exchange (right panel) graphs in pp collisions contributing to the Δ−production in OPE model by Dmitriev *et al.* [Dmi86].

The model fit describes the slightly asymmetric $p\pi^+$ invariant mass distribution with the Δ^{++} resonance (Fig. 1.3, left panel). The neutron (or Δ^{++}) angular distribution in the center-of-mass system shows a strong anisotropy (Fig. 1.3, right panel), in agreement with the OPE description [Dmi86]. It is also stated in this model, that due to the isospin factors, Δ production is less dominant in the $pp\pi^0$ case, and hence the background is larger. For this reason the $np\pi^+$ channel was usually used to fix the cutoff parameters.

1.2.2 Resonance model

A more versatile dynamical model by Teis *et al.* [Tei97] describes the production of light mesons in proton-proton (or neutron-proton) collisions and extends it to heavy-ion collisions in the energy range of 1−2 GeV/nucleon. The major assumptions of this model are: (i) the entire meson production proceeds via intermediate resonance excitation (ii) the total cross section amounts to the incoherent sum of all resonances contributing to a specific channel. The resonance list includes $\Delta(1232)$, $\Delta(1600)$, $\Delta(1620)$, $\Delta(1675)$, $\Delta(1700)$, $\Delta(1905)$, $\Delta(1910)$, $\Delta(1950)$, and $N(1440)$, $N(1520)$, $N(1535)$, $N(1650)$, $N(1680)$, $N(1720)$. Their properties (the width and branching ratios) were taken from Ref. [PDG94], apart from $N(1535)$ resonance (see Ref. [Kru95]). The matrix elements for the resonance production were obtained from a fit to the data of 1π, η, ρ and 2π production cross sections in nucleon-nucleon reactions. They were assumed to be constant, except for the Δ where dependency on t was adopted from Ref. [Dmi86].

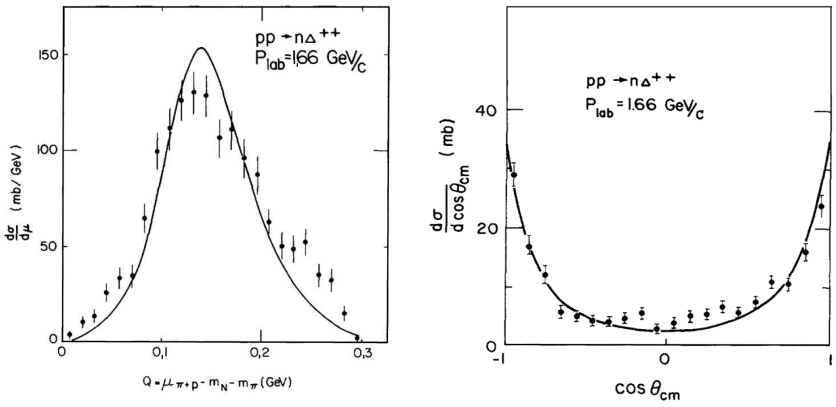

Figure 1.3: Reaction $pp \to np\pi^+$ at a proton kinetic energy of 0.97 GeV [Bug64]: excitation energy of the (p, π^+) pairs (left panel) and neutron angular distribution in the c.m.s. (right panel). Solid curves present the OPE model [Dmi86].

An example of one-pion production cross sections in proton-proton collisions is shown in Fig. 1.4. The cross sections used to the fit are taken from the collective works of Baldini *et al.* [Bal88]. The experimental data represent e.g. measurements with bubble chambers from the 1960s [Fic62, Bug64, Eis65], quite often with large statistical uncertainties. Nevertheless, a similar approach is widely used with only small modifications in other resonance models, e.g. GiBUU [Bus12, Wei12] and UrQMD [Bas98].

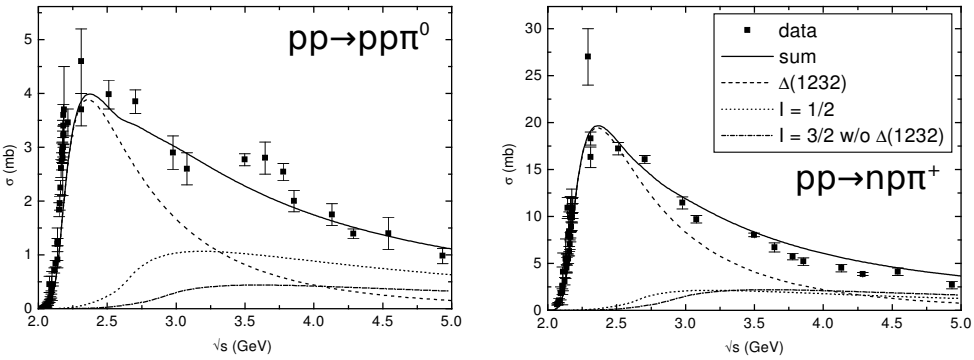

Figure 1.4: One-pion production in $pp \to pp\pi^0$ (left panel) and $pp \to np\pi^+$ (right panel) channels according to Teis fit [Tei97].

1.2.3 Δ resonance decay - angular distributions

In high-energy collision processes with multiparticle final states, resonances are quite often produced in quasi-two-body reactions where one (or both) of the final systems is dynamically unstable. The modeling of the angular distributions of the produced resonances allows for a more detailed comparison with experimental data and is essential when measurements within a limited acceptance coverage are considered. For example, the angular distribution of the Δ decay depends on the population of different spin states excited in the $NN \to N\Delta$ process. For a spin–$\frac{3}{2}$ particle like Δ the spin-density matrix can be described in terms of a 4×4 Hermitian matrix ρ_{ij} [Got64]:

$$\rho^{\Delta} = \begin{pmatrix} \rho_{3\,3} & \rho_{3\,1} & \rho_{3\,-1} & \rho_{3\,-3} \\ \rho^{*}_{3\,1} & \rho_{1\,1} & \rho_{1\,-1} & \rho_{1\,-3} \\ \rho^{*}_{3\,-1} & \rho^{*}_{1\,-1} & \rho_{-1\,-1} & \rho_{-1\,-3} \\ \rho^{*}_{3\,-3} & \rho^{*}_{1\,-3} & \rho^{*}_{-1\,-3} & \rho_{-3\,-3} \end{pmatrix}, \tag{1.10}$$

where the diagonal elements are real and satisfy the trace condition,

$$\rho_{33} + \rho_{11} + \rho_{-1\,-1} + \rho_{-3\,-3} = 1, \tag{1.11}$$

and the off-diagonal elements satisfy the relationship $\rho_{ij} = \rho^{*}_{ji}$. The number of elements is constrained by the invariance of the production mechanism and of the decay interaction under reflection. Choosing the judicious axes, e.g. in the $\Delta \to N\pi$ decay process, the pion angle θ with respect to the momentum transfer in the reference frame, where the selected nucleon is at rest, leads to the fact that the pion angular distribution can be expressed as a function of spin density matrix elements:

$$\begin{aligned} \frac{d\sigma}{d\Omega} \;\sim\; & \rho_{33}\sin^2\theta + \Big(\frac{1}{2} - \rho_{33}\Big)\Big(\frac{1}{3} + \cos^2\theta\Big) \\ & - \frac{2}{\sqrt{3}}\,\mathrm{Re}\,\rho_{3-1}\sin^2\theta\cos 2\phi \;-\; \frac{2}{\sqrt{3}}\,\mathrm{Re}\,\rho_{31}\sin 2\theta cos\phi. \end{aligned} \tag{1.12}$$

Integrating over the full azimuthal range leads to

$$\begin{aligned} \frac{d\sigma}{d\cos\theta} \;&\sim\; \frac{2\pi^2}{3}\,(1 + 4\rho_{33})\Big[1 + \frac{3\,(1 - 4\,\rho_{33})}{1 + 4\,\rho_{33}}\,\cos^2\theta\Big] \\ &\sim\; 1 + A\cos^2\theta, \end{aligned} \tag{1.13}$$

where $A = 3\,(1 - 4\,\rho_{33})/(1 + 4\,\rho_{33})$ and the differential cross section depends only on ρ_{33}. Assuming solely a one-pion exchange and the excitation of the Δ on the nucleon target, $\rho_{33} = 0$, and the decay angular distribution $\Delta \to N\pi$ follows a $\sim (1 + 3\cos^2\theta)$ distribution, where θ is the angle of the pion (or the nucleon) in the Δ rest frame with respect to the beam axis.

If the exchange mechanism includes also ρ meson, the ρ_{33} matrix element is expected to be different from 0. The spin density matrix coefficients have been extracted from the π^+ angular distribution in $pp \to np\pi^+$ reaction in the beam momentum range $1.18 - 1.98$ GeV/c in Ref. [Wic87] (also at $3 - 12$ GeV/c in Ref. [Wic86]), with polarized beams. For the forward emission of Δ^{++} resonance, $\rho_{33} = 0.16 \pm 0.03$, which results in an anisotropy coefficient $A = 0.66^{+0.29}_{-0.25}$, smaller than the value 3 derived within the one-pion exchange model. The other experiments essentially confirm this result at higher beam momenta, i.e. $A = 0.55$ at 2.5 GeV/c [Eis65], or $A = 0.85^{+0.32}_{-0.28}$ at 2.8 GeV/c [Bac67]. Such a parameterization is also corroborated by the experimental data $pp \to pp\pi^0$ in the energy range $600 - 900$ MeV [And94]. Yet another analysis of Shimizu *et al.* [Shi82] reports a lower value $A = 0.34$.

All these experiments could derive only effective matrix elements considering that only one graph contributes, with excitation either of the projectile or of the target. The assumption is valid only for the forward or backward angles, and if the Δ^{++} excitation is the dominant contribution. The analysis of the π angular distribution confirmed the anisotropic Δ decay, but with an anisotropy smaller than expected from a pure OPE model. However, in transport models, the pionic decay of the Δ resonance is treated isotropically. There is also not much information on higher mass resonances, and usually isotropic distributions are used.

Chapter 2

Resonances in hadronic channels

Baryon resonance production in NN collisions can be determined by the investigation of one-pion, two-pion or η production as a function of the excitation energy. This goal has been addressed by the HADES Collaboration in experiments with a proton kinetic beam energy of 1.25 GeV, 2.2 GeV, and 3.5 GeV, as well as deuteron beam energy of 1.25 GeV/nucleon. The multi-differential data were measured with the High Acceptance DiElecton Spectrometer (HADES) which is a unique spectrometer to study both dielectron (e^+e^-) and hadron production in heavy-ion collisions, as well as in proton- and pion-induced reactions in the energy range of 1 – 4 GeV. The detailed description of the spectrometer and the analysis strategy is presented in Appendix C.

Exclusive channels with one pion ($np\pi^+$ and $pp\pi^0$) and η ($pp\eta$) in the final state were put to extended studies based on various observables in the framework of a resonance model (see Sect. 1.2), assuming saturation of the meson production by an incoherent sum of baryonic resonances with masses < 2 GeV/c^2. In addition, solutions obtained within the framework of a partial wave analysis of the Bonn-Gatchina group (Sect. 2.1.2) were obtained for the 1.25 GeV energy. In proton-proton collisions at a kinetic energy of 3.5 GeV a very good description of the one-pion production was achieved by the adjustment of resonance angular production. It allowed for an estimate of individual baryon resonance (Δ, N^*) production cross sections.

The two-pion production ($\pi^+\pi^-$) in quasi-free np collisions was confronted with various models (Sect. 2.2.2) and the total cross section was extracted, based on the model-driven acceptance correction. This measurement established also constraints for the existence of the dibaryon resonance at mass $M \approx 2.38$ GeV/c^2 and with $\Gamma \sim 70$ MeV.

The collected pp and np data allow to test meson production mechanisms and the contribution of baryonic resonances with a high statistical precision, in complement to previous low-statistics but high-acceptance experiments. The obtained results, presented in the following sections, serve also as an input to calculate dielectron Dalitz yields. They are further compared to the direct exclusive ppe^+e^- and npe^+e^- channel reconstruction (see Chapter 4).

2.1 Proton-proton collisions at T = 1.25 GeV

In proton-proton collisions, a kinetic beam energy of 1.25 GeV and intensity of 10^7 particles/s was incident on a 5 cm long liquid-hydrogen target of 1% interaction probability. The energy $\sqrt{s}$ = 2.42 GeV was selected below the η meson production threshold in order to favor $\Delta(1232)$ production. To study one-pion production mechanisms in the hadronic channels, only events with one proton and one pion ($p\pi^+$) and two protons (pp) were identified with the help of the missing mass technique (Fig. 2.1, right panel). The background estimation was done on the base of a double-differential missing mass spectrum obtained for 20 different bins in the variable $cos\ \theta_{\pi N}^{c.m.s.}$ and 25 bins in $M_{\pi N}^{inv}$. Prior to the background evaluation, the two-pion contribution to the missing mass spectrum, not very sensitive to details of the two-pion production model, was simulated and subtracted. The background contribution obtained from the fit procedure applied to the $np\pi^+$ final state amounts to a few percents. In the case of the $pp\pi^0$ sample the background contribution yields to about ten percents (see Fig. 2.1, right panel).

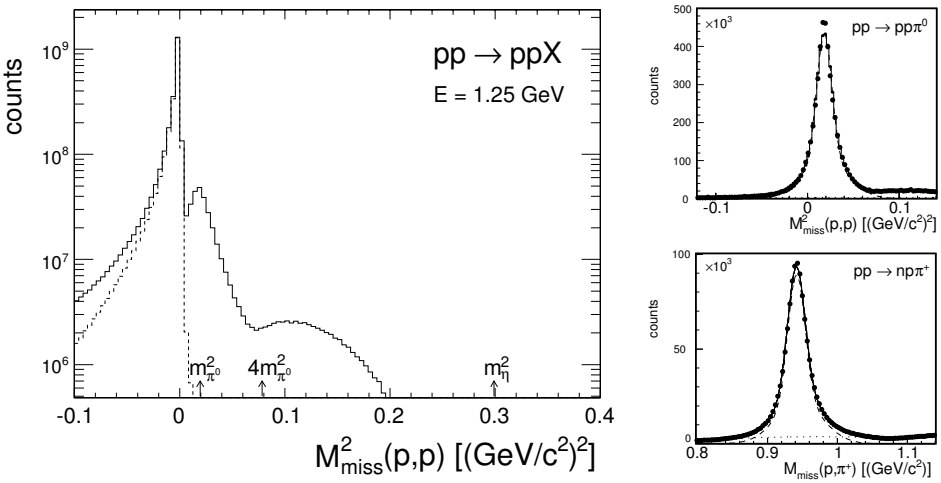

Figure 2.1: Left panel: Experimental spectrum of pp missing mass squared for the reaction $pp \to ppX$ at 1.25 GeV. The most prominent peak stems from pp elastic channel (also denoted with a dashed curve), followed by the one-pion and two-pion contributions. Right panel: Inelastic one-pion exclusive channels, pp missing mass squared (upper) and $p\pi^+$ missing mass (lower). Solid curves represent the fit of a sum of one polynomial (dotted curves) and two Gauss functions (dashed curves). The two-pion contribution deduced from the simulation is subtracted before the fit.

The collected statistics amounts to 2.73×10^6 events with an identified π^+ and $0.53{\times}10^6$ events with an identified π^0, respectively. All spectra were normalized to the pp elastic scattering yield measured in the same experimental run (see App. C.3.6.1). The normalization error is estimated to be 8%, where 5.8% is derived from the error of the reference differential cross section and 6% is the systematic error of the reconstruction of events with elastic scattering.

2.1.1 One-pion production in resonance model

To describe the production of the one-pion channels from the pp reaction, the resonance model by Teis *et al.* [Tei97] was implemented in the framework of the PLUTO event generator [Frö07]. Then, the full GEANT simulation and the Monte Carlo simulations of the detector response, followed by the same analysis steps employed for the experimental data, were performed. The following hadronic channels, with the cross sections summarized in Table 2.1, were included:

- $pp \to n + \Delta^{++}(1232)$ followed by:
  - $\Delta^{++} \to p + \pi^+$ (BR = 1)
- $pp \to p + \Delta^{+}(1232)$ followed by:
  - $\Delta^{+} \to n + \pi^+$ (BR = 1/3)
  - $\Delta^{+} \to p + \pi^0$ (BR = 2/3)
- $pp \to p + N(1440)$ with decays via $\Delta(1232)$ to:
  - $N(1440) \to n + \pi^+$ (BR = 0.65*2/3)
  - $N(1440) \to p + \pi^0$ (BR = 0.65*1/3)

The simulation employs the OPE model of Dmitriev *et al.* (Ref. [Dmi86], introduced in Sect. 1.2.1) but replaces, as in the resonance model (Ref. [Tei97], see Sect. 1.2.2), the original parametrization of the Δ resonance total width by the one given in the Moniz model (Ref. [Koc84], see Eq. 1.8 in Sect. 1.1). Such a parametrization which suppresses the high-mass tail of the resonance, is compatible with the description of the HADES data at a higher energy (Ref. [HC14a], see Sect. 2.4.4). The parametrization of the one-pion decay width for the Roper resonance is defined in a similar manner (see Ref. [Tei97] for details).

final state	**intermediate process**	σ_{RES} **(mb)**	σ_{PWA} **(mb)**
$np\pi^+$	$pp \to n\Delta^{++}(1232)$	16.90	11.1 ± 0.4
	$pp \to p\Delta^{+}(1232)$	1.89	1.2 ± 0.2
	$pp \to pN(1440)$	0.54	1.7 ± 0.2
	$Total:$	19.35	16.34 ± 0.8
$pp\pi^0$	$pp \to p\Delta^{+}(1232)$	3.76	2.96 ± 0.07
	$pp \to pN(1440)$	0.27	0.86 ± 0.06
	$Total:$	4.03	4.2 ± 0.15

Table 2.1: Cross sections for the $p(1.25\ \mathrm{GeV}) + p$ reaction and one-pion final states with the intermediate baryon resonance excitation: σ_{RES} for the resonance model [Tei97], σ_{PWA} for the partial wave fit.

The resonance behavior can be observed on Dalitz plots in Fig. 2.2. For the $pp\pi^0$ channel (left panel), an accumulation of yield for the invariant mass squared $M^2_{inv}(p,\pi^0)$ = 1.5 $(\mathrm{GeV/c^2})^2$, corresponding to the excitation of the Δ^+ resonance, is clearly seen. Similarly, for the $np\pi^+$ channel (right panel) a strong Δ^{++} signal at $M^2_{inv}(p,\pi^+)$ = 1.5 $(\mathrm{GeV/c^2})^2$, and less pronounced Δ^+ signal at $M^2_{inv}(n,\pi^+)$ = 1.5 $(\mathrm{GeV/c^2})^2$, can be observed. The missing coverage in the plots are due to the acceptance of the spectrometer, with the dominant effect being due to the minimum proton

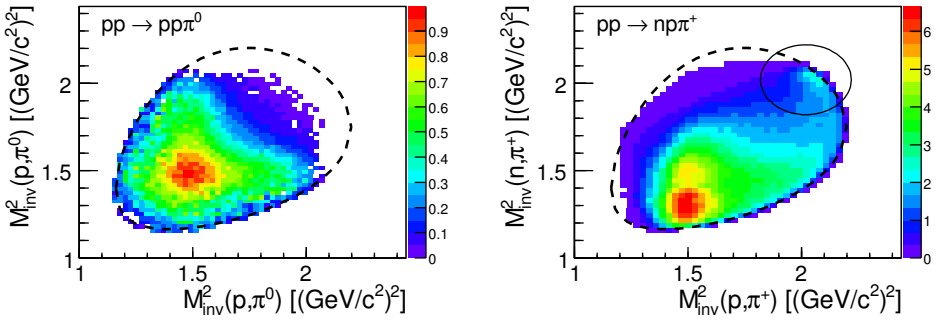

Figure 2.2: Dalitz plots of the $pp \to pp\pi^0$ (left panel) and $pp \to np\pi^+$ (right panel) at 1.25 GeV, with the dashed curves indicating their kinematical limits. In the right panel, the region affected by the final-state interaction is marked by a circle. Data are corrected for the reconstruction efficiency.

polar detection angle of 18°. For the $pp \to np\pi^+$ reaction, the enhanced population for both $M^2_{inv}(p,\pi^+)$ and $M^2_{inv}(n,\pi^+)$ around 2 $(\mathrm{GeV/c^2})^2$ is seen (Fig. 2.2, right panel), due to the np final-state interaction (FSI), which enhances events with small relative momentum between the proton and the neutron. The FSI between the outcoming nucleons was modeled according to the Jost parametrization [Tit00], as a weight applied directly on the cross section, following the probability function:

$$W_{FSI} = \left| \frac{k + i\frac{1}{r_0}(\sqrt{1 - 2r_0 a_0^{-1}} + 1)}{k + i\frac{1}{r_0}(\sqrt{1 - 2r_0 a_0^{-1}} - 1)} \right|^2 , \tag{2.1}$$

where k is proton or neutron momentum in the (n,p) reference frame, and the effective range r_0 and scattering length a_0 for np singlet spin state are taken from Ref. [Dum83], $r_0 = 2.75 \pm 0.05$, $a_0 = -23.748 \pm 0.010$.

The production cross sections for the intermediate resonances were taken from the resonance model [Tei97], except for the Roper resonance, where a slightly larger cross section was used, based on a lagrangian model [Cao10], describing two-pion production. Decay branching ratios to one and two pions at resonance pole masses are taken from the PDG review [PDG16]. Isospin relations lead to the following ratios between cross sections:

$$\sigma_{pp\to np\pi^+} = 5\sigma_{pp\to pp\pi^0} \tag{2.2}$$

for the Δ resonance with the isospin $I = \frac{3}{2}$, and

$$\sigma_{pp\to pp\pi^0} = 2\sigma_{pp\to np\pi^+} \tag{2.3}$$

for the $N(1440)$ (Roper) resonance with the isospin $I = \frac{1}{2}$. The cross sections are listed in Table 2.1 (column σ_{RES}); the subsequent contributions to the total cross section were added incoherently.

2.1.1.1 $np\pi^+$ channel

The description of the intermediate Δ^{++} resonance in the $pp \to np\pi^+$ channel within the OPE model [Dmi86] required the adjustment of the cross section as well as the cut-off parameter Λ_π in Eq. (1.9) (Sect. 1.2.1) for the vertex form factor.

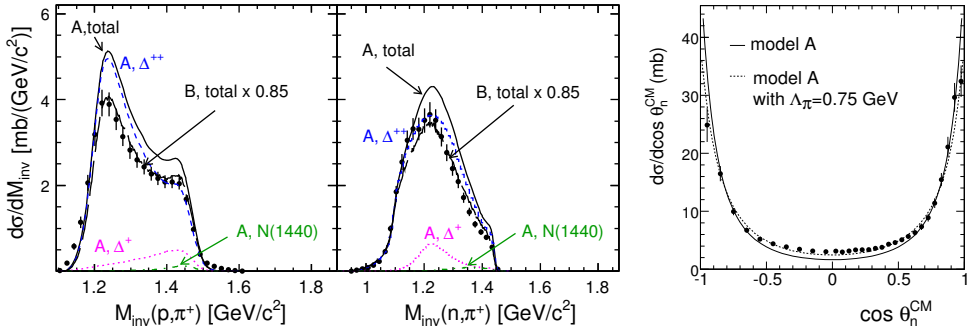

Figure 2.3: Left panel: The $p\pi^+$ and $n\pi^+$ invariant mass distributions within the HADES acceptance. The data points (efficiency corrected) are compared to the resonance model (model A), with contribution of $\Delta^{++}(1232)$ (dashed blue curve), $\Delta^+(1232)$ (dotted magenta) and $N(1440)$ (dash-dotted green). The long-dashed black curve, denoted as model B, results from the yield and neutron angular distribution adjustment. Right panel: The angular distribution of neutron in c.m.s., the data points are acceptance corrected and compared to resonance model with the cut-off parameter $\Lambda_\pi = 0.63$ (solid curve, model A), and $\Lambda_\pi = 0.75$ (dashed curve).

Figure 2.3, left panel, presents the $p\pi^+$ and $n\pi^+$ invariant mass. The data are corrected for reconstruction efficiencies and normalized using the total pp elastic cross section. Error bars include statistical and systematic errors (see discussion below). The distributions, peaked around 1.23 GeV/c^2, confirm that most of the pions are produced via Δ decay. The simulated contribution (black solid curves, model A), within the HADES acceptance, is the sum of dominant Δ isobar and small $N(1440)$ admixture. The trend of the data is rather well reproduced, although some discrepancies concerning both the yields and the shapes can be observed. The model A overestimates the experimental yield by about 20%. The acceptance corrected neutron angular distribution is shown in Fig. 2.3, right panel. The HADES data favour $\Lambda_\pi = 0.75$ GeV (dashed curve). Further improvement could be achieved with the empirical parametrization of the angular distribution $cos\theta^{c.m.s.}_{p\pi^+}$ as a function of $M^{inv}_{p\pi^+}$. It allows to describe the anisotropic production of the resonance, in agreement with the observations of the former proton-proton experiments at higher energies [Col71]. The modifications affect mainly the $\Delta \to \pi N$ decay at large c.m.s. angles. Both adjustments (cross section scaled down by a factor 0.85 and a neutron angular distribution) are plotted as a model B.

The comparison of the modified resonance model with data has been extended to more differential observables, as shown in Fig. 2.4. The various projections of the uncorrected data and the Monte Carlo simulation (black dotted histogram), within the HADES acceptance, are presented: single particle angular distributions in the center of mass ($a-c$), two-particle invariant mass spectra ($d-f$), helicity ($g-i$) and Gottfried-Jackson ($j-l$) frames (see Appendix C.3.5.3). In addition, the results obtained with a partial wave analysis (explained in Sect. 2.1.2) and phase space distributions (grey-shaded area) are presented, with the normalization to the yield of the data.

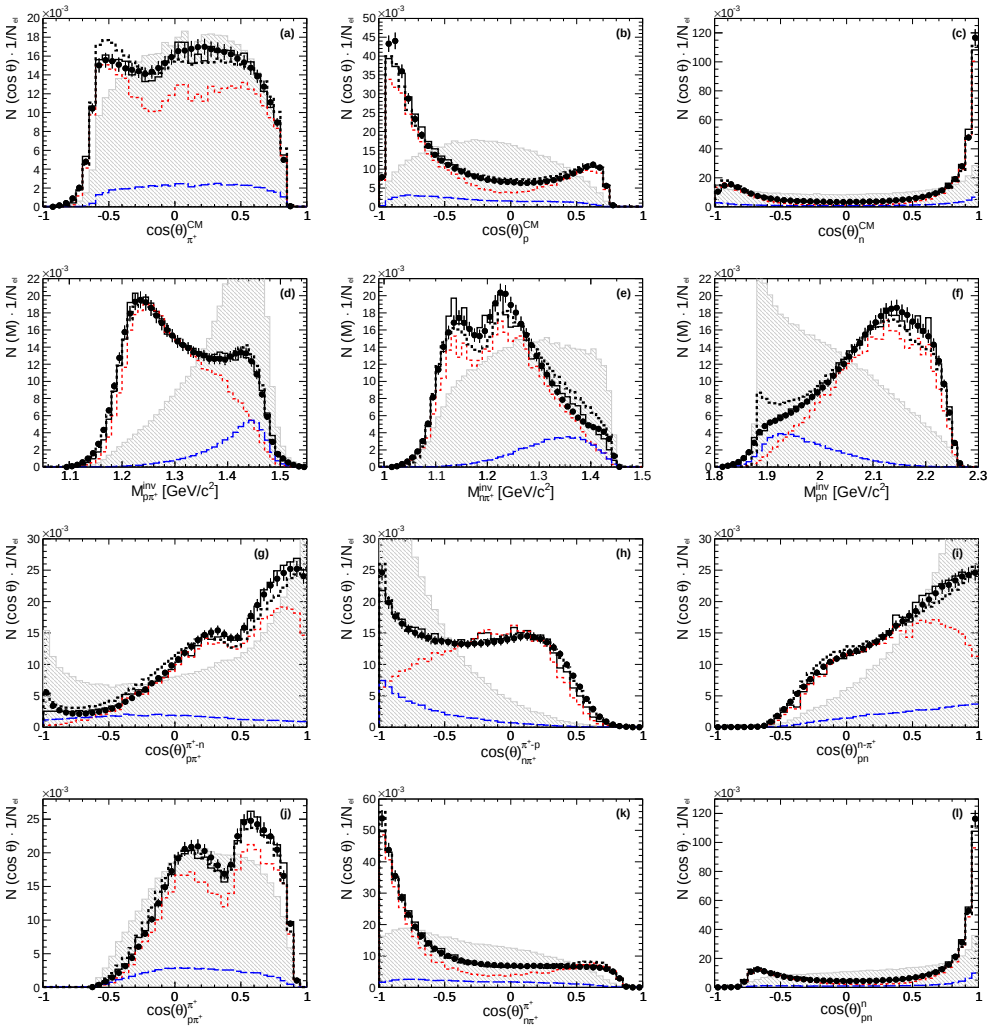

Figure 2.4: $np\pi^+$ channel projections: Angular distribution of (a) π^+, (b) p and (c) n in c.m.s.; Invariant mass of (d) $p\pi^+$, (e) $n\pi^+$ and (f) pn; Helicity distribution of (g) π^+ in $p\pi^+$ reference frame, (h) π^+ in $n\pi^+$ reference frame and (i) n in pn reference frame; Angular distribution of (j) π^+ in $p\pi^+$ GJ reference frame, (k) π^+ in $n\pi^+$ GJ reference frame and (l) n in pn GJ reference frame. Uncorrected data points (black) are within the HADES acceptance with systematic and statistical vertical error bars, normalized to the number of pp elastic scattering (N_{el}). Histograms: total PWA solution folded within the HADES acceptance and efficiency (solid black) and normalized to the respective yields of experimental data, contributions: the $\Delta(1232)$, short-dashed red, and the $N(1440)$, long-dashed blue. Dotted histogram (black): modified resonance model. The grey hatched area shows the distribution in the case of isotropically simulated particles.

Thanks to a good solid angle coverage and a good model description, the data could be corrected for the reconstruction inefficiencies and the detector acceptance, each distribution with the respective one-dimensional correction function. The correction function is constructed, for a given distribution, as ratio of the modified resonance model yield in 4π and the yield within the HADES acceptance, including all detection

and reconstruction inefficiencies obtained using the full analysis chain. The integrated correction factor in the $np\pi^+$ channel varies in the range 20 – 40, depending on the distribution. The extracted cross section for the $np\pi^+$ channel amounts to 17.0 ± 2.2 (systematic error) mb, with a negligible statistical error. The systematic error includes: 5% error due to the particle identification (selection cuts and the missing mass cut) and the background subtraction, 10% error due to the correction and model uncertainty and 8% is the normalization error (errors are added quadratically). The background subtraction error was deduced by varying of a polynomial function used together with a Gauss function to fit the missing mass spectrum. The model error was estimated from the differences in the integrated yields of the various distributions obtained after acceptance corrections.

2.1.1.2 $pp\pi^0$ channel

The identification of two protons in the HADES spectrometer results in a reduced acceptance for the $pp\pi^0$ reaction channel. The resonance model [Tei97] does not reproduce satisfactorily the measured observables in this channel, as shown in Fig. 2.5. The $p\pi^0$ invariant mass (left panel) is underestimated by about 20% (model A), the proton angular distribution (right panel) is much flatter in the data than in the model. To improve the description, the aforementioned parametrization of the resonance angular distribution, deduced from the $np\pi^+$ channel analysis, was applied for the Δ^+ production, resulting in a better agreement (model B, shown by the dashed curve). This confirms that the two isospin channels can be described consistently with the same Δ production angular distribution.

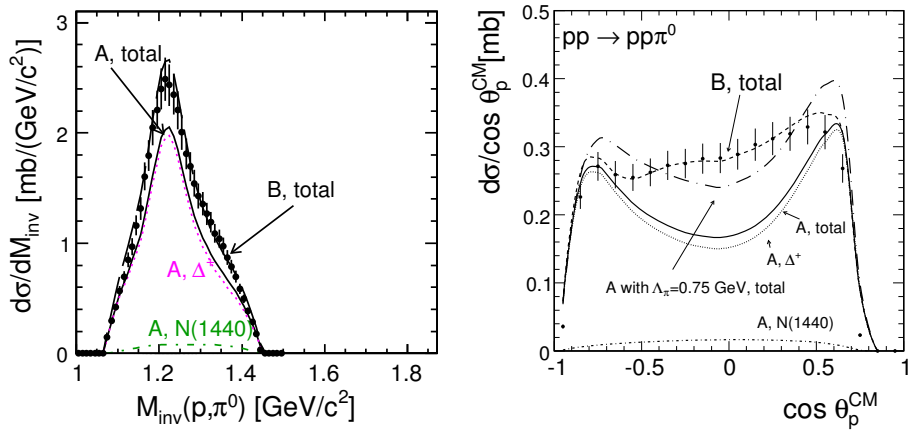

Figure 2.5: The $p\pi^0$ invariant mass distribution (left panel) and the angular distribution of protons in c.m.s. (right panel), within the HADES acceptance. The resonance model contribution description as in Fig. 2.3.

Similarly to $np\pi^+$ channel, the comparison of the modified resonance model with data has been studied with various observables in the $pp\pi^0$ channel, as shown in Fig. 2.6. Although some angular projections still unravel slight discrepancies between the data and the model, the overall description is quite good. It allows for the correction of the data for the reconstruction inefficiencies and detector acceptance, with the model-driven extrapolation, in an analogous way as it was done for the $np\pi^+$ channel. The integrated correction factor in the $pp\pi^0$ channel varies in the range 15 – 25, depending

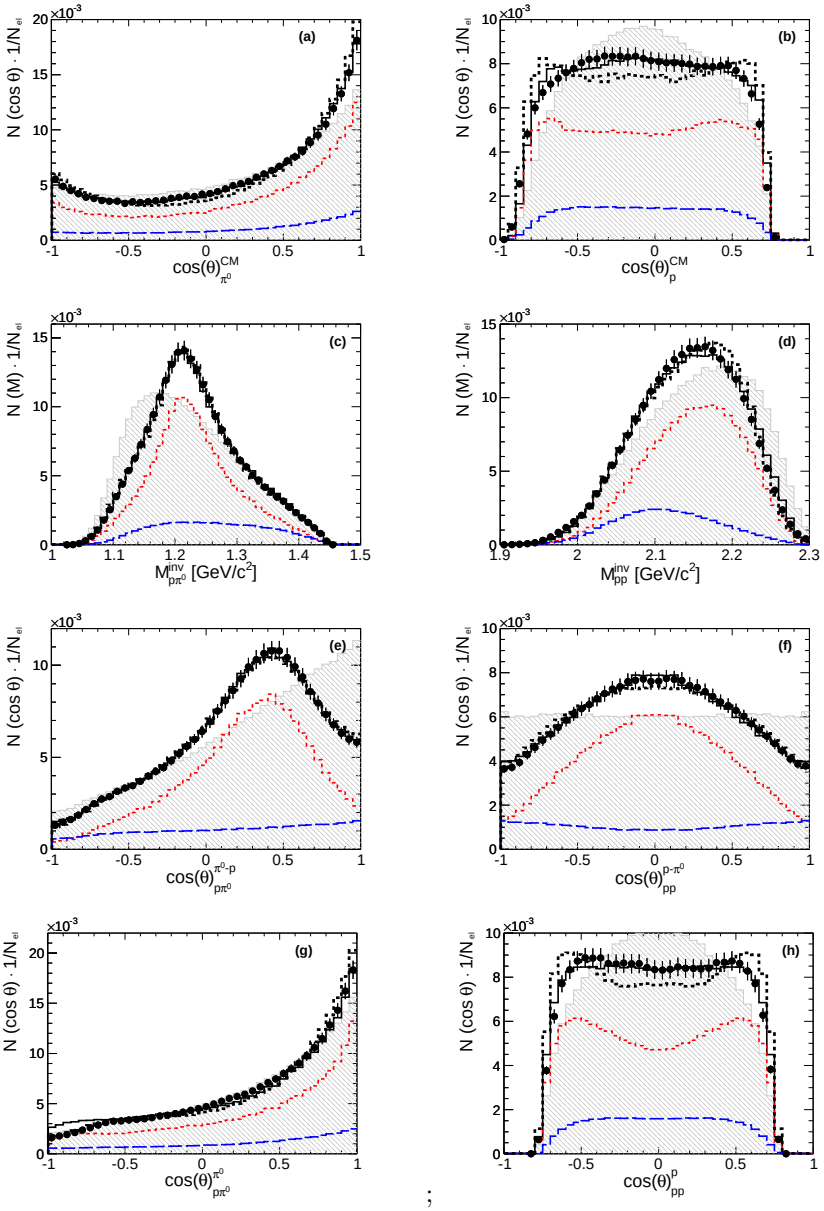

;

Figure 2.6: $pp\pi^0$ channel projections: Angular distribution of (a) π^0 and (b) p in c.m.s. reference frame; Invariant mass of (c) $p\pi^0$ and (d) pp; Helicity distribution of (e) π^0 in $p\pi^0$ reference frame and (f) p in pp reference frame; Angular distribution of (g) π^0 in $p\pi^0$ GJ reference frame and (h) p in pp GJ reference frame. Uncorrected data points (black) within the HADES acceptance with systematic and statistical error bars, normalized to the number of pp elastic scattering (N_{el}). Histograms: total PWA solution (solid black), the $\Delta(1232)$ contribution (short-dashed red) and the $N(1440)$ contribution (long-dashed blue). Dotted histogram (black): modified resonance model. The grey hatched area in each panel shows the distribution in the case of isotropically simulated particles.

on the distribution. The deduced total cross section amounts to 3.87 ± 0.60 mb. Due to the smaller, as compared to the $np\pi^+$ channel, acceptance coverage, the systematic error related to the acceptance corrections is 12% (estimated as in the previous case), the background subtraction error is similar and amounts to 6%.

Taking into account the isotopic relations between the final state channels, one gets the total cross section for the Δ^+ production equal to either 4.98 ± 0.72 mb (deduced from the $np\pi^+$ channel, where the Δ^{++} contribution is 14.86 ± 2.19 mb) or 5.42 ± 0.69 mb (deduced from the $pp\pi^0$ channel). The expected ratio $\sigma_{\Delta^{++}}/\sigma_{\Delta^+}$ is 3, which is satisfied within the errors in both cases: 2.98 ± 0.61 or 2.74 ± 0.53, respectively. One should notice that the $N(1440)$ contribution is negligible in the resonance model approach. Despite the discrepancies, the calculations with the OPE model [Dmi86] are utilized in various modern resonance models (e.g. GiBUU [Bus12]).

2.1.2 Partial wave analysis

The above modified resonance model describes fairly well the angular and mass distributions and can be used for the acceptance correction of the data and determination of the total cross sections. However, the introduced modification of the angular distributions of the Δ resonance does not provide insight into the production mechanism. Moreover, the non-resonant contribution is completely neglected and $N(1440)$ contribution is treated in a very simplified manner.

In view of the limitations of the resonance model, the partial wave analysis provides a significant advantage - it includes the coherent sum of both resonant and non-resonant contributions within the solution based on the simultaneous fit to many experimental data samples. The extraction of contributions from different partial waves is performed event by event and based on the maximum-likelihood method. The angular distributions for a given partial wave in the final state, characterized by the spin and parity, are naturally accounted for. Therefore, resonant and non-resonant contributions, including interferences, can be extracted.

The successful partial wave analysis was demonstrated in the case of one-pion production in pp reactions measured at PNPI at lower energies (see Refs. [Erm11, Erm14, Erm17]) by the Bonn-Gatchina group. In this approach, the total reaction amplitude A is described as a sum of partial wave amplitudes with the corresponding angular dependencies:

$$A = \sum_{\alpha} A^{\alpha}_{tr}(s) Q^{in}_{\mu_1 \ldots \mu_J}(SLJ) A_{2b}(j, S_2 L_2 J_2)(s_j) \times \\ Q^{fin}_{\mu_1 \ldots \mu_J}(j, S_2 L_2 J_2 S' L' J) \ . \tag{2.4}$$

Here S, L and J are the spin, the orbital momentum and the total angular momentum of the initial NN system, S_2, L_2 and J_2 denote spin, orbital momentum and total angular momentum of the two-particle system in the final state, and S' and L' are spin and orbital momentum between this two-particle system and the spectator particle with index j, e.g. $\pi(1)$, $p(2)$, $n(3)$. The invariant mass of the two-body system is determined by $s_j = (P - q_j)^2$, where q_j is the four-momentum of the spectator and P is the total momentum of the reaction. The operators Q^{in} and Q^{fin} are tensors of the rank J constructed for each event from the momenta of the initial and final state particles. Their convolution provides the angular dependence of the amplitude (see Ref. [Ani06] for the explicit formulas). For the transition amplitude A^{α}_{tr} from the initial NN to the $NN\pi$ system, the multi-index α that summarizes all quantum numbers described

above is introduced. The differential cross section calculated from this amplitude is maximized for the data events with the event-by-event maximum likelihood method, thus taking into account all correlations in the multidimensional phase space.

The likelihood function is normalized by the Monte Carlo integral calculated with events generated according to the phase space distribution passed through the simulated detector response and signal reconstruction. It means that the distribution of these events weighted by the cross section from the found solution should closely reproduce, within the HADES acceptance, the distribution of the experimental data. The solution provides also a possibility to extrapolate the cross section to the regions of low detection capabilities and therefore to perform the acceptance correction of the data.

The resonance production in the πN channel is parametrized by relativistic Breit-Wigner amplitudes. For the Δ and Roper states the following parametrization is used (j=2, 3):

$$A_{2b}(j,\beta)(s_{\pi N}) = \frac{g^R_{\pi N}}{M_R^2 - s_{\pi N} - iM_R\Gamma_R} \quad , \tag{2.5}$$

where the multi-index β stands for $S_{\pi N}, L_{\pi N}, J_{\pi N}$. The resonance total width is equal to the sum of partial widths, and the $g^R_{\pi N}$ coupling is connected with the πN partial width by:

$$M_R\Gamma_{\pi N} = (g^R_{\pi N})^2 \frac{2k_{\pi N}}{\sqrt{s}_{\pi N}} \frac{1}{16\pi} \frac{k^{2L}_{\pi N}}{F(k^2_{\pi N}, L_{\pi N}, r)} \, . \tag{2.6}$$

Here, the quantity $k_{\pi N}$ is the relative momentum of the pion and nucleon in the πN rest frame, and $F(k^2_{\pi N}, L_{\pi N}, r)$ denotes the Blatt-Weiskopf form factor with interaction radius r (see Ref. [Ani06]).

Equation 2.6 defines the energy dependence of the resonance partial width. The initial values of masses and of total widths of the resonances were taken from the review of the Particle Data Group [PDG16] and adjusted in the course of the fit procedure. The interaction radius r was fixed at 0.8 fm. The total width of the Δ state is completely defined by the decay into the πN system with $L_{\pi N}$=1 ($S_{\pi N}$=$\frac{1}{2}$, $J_{\pi N}$=$\frac{3}{2}$). This form of Blatt-Weiskopf parametrization is also used in the Manley and Saleski partial wave analysis fit [Man92]. The difference of the cut-off function, as compared to the Moniz parametrization Eq. (1.8), is not so pronounced at the energy of 1.25 GeV, but becomes important at higher energies (see Sect. 2.4.4). In the case of the Roper resonance, the πN partial width contributes about 65% to the total width of the state. In general, the partial widths defined by the two pion-nucleon channel should have a complicated energy dependence. However, possible parametrizations of the Roper resonance do not change the solutions very much, as discussed below.

The non-resonant contributions in the NN scattering channel are parametrized by a modified scattering length approximation expression (j=1):

$$A_{2b}(j,\beta)(s_{NN}) = \frac{r_\beta a_\beta \sqrt{s_{NN}}}{1 - \frac{1}{2} r_\beta k^2_{NN} a_\beta + \frac{i a_\beta k^{2L_\beta+1}_{NN}}{F(k^2_{NN}, r_\beta, L_{NN})}}, \tag{2.7}$$

where k_{NN} is the nucleon-nucleon relative momentum calculated in the NN rest system, L_{NN} is the orbital momentum of the NN system, r_β is the effective range and a_β is the scattering length of the system ($\beta = S_{NN}, L_{NN}, J_{NN}$). For the S−waves, Eq. 2.7 corresponds to the scattering-length approximation formula suggested in Refs. [Wat52, Mig55]. The np scattering length and effective range are fixed for the S−waves: $a(^{2S+1}L_J) = a(^1S_0) = -23.7$ fm, $r(^1S_0) = 2.8$ fm, $a(^3S_1) = 5.3$ fm, and $r(^3S_1) = 1.8$ fm.

The final solution for the HADES data was obtained in an iterative procedure, starting from the solution found in Ref. [Erm14], describing low-energy data very well. The first fit produced a satisfactory description of the data, except of very forward neutron and very backward proton angles in c.m.s. of the $pp \to np\pi^+$ reaction. Moreover, large interferences between partial waves with Roper production and partial wave with non-resonant production of the NN system were found. To stabilize the solution, the lower energy data fitted in Ref. [Erm14], were included in the fit. The fitted data base is given in Table 2.2. Number of events N_{data} used in the PWA is lower than the full available statistics in the case of Ref. [ES06] (154972 events) and in the case of the HADES data (for the full statistics, see Sect. 2.1).

Reaction	$\sqrt{s}$ (MeV)	N_{data}	σ_{tot} (mb)	Reference
$pp \to \pi^0 pp$	2066	50000	0.10±0.03	[ES06]
$pp \to \pi^0 pp$	2157	542	2.07±0.09	[And94]
$pp \to \pi^0 pp$	2178	615	2.85±0.13	[And94]
$pp \to \pi^0 pp$	2200	882	3.31±0.19	[And94]
$pp \to \pi^0 pp$	2217	993	3.70±0.14	[And94]
$pp \to \pi^0 pp$	2234	914	3.73±0.15	[And94]
$pp \to \pi^0 pp$	2251	996	3.96±0.15	[And94]
$pp \to \pi^0 pp$	2269	1315	4.20±0.15	[And94]
$pp \to \pi^0 pp$	2284	903	4.19±0.17	[Sar04]
$pp \to \pi^0 pp$	2300	688	4.48±0.20	[Erm11]
$pp \to \pi^0 pp$	2319	1086	4.50±0.17	[Sar04]
$pp \to \pi^0 pp$	2422	60000	3.87±0.55	[HC15a]
$pp \to \pi^+ pn$	2285	4153	17.8±0.4	[Erm14]
$pp \to \pi^+ pn$	2300	2912	17.6±0.6	[Erm11]
$pp \to \pi^+ pn$	2319	2564	19.0±0.6	[Erm17]
$pp \to \pi^+ pn$	2422	60000	17.0±2.2	[HC15a]

Table 2.2: The data sets (number of events N_{data}) used for the fit, except the data from Ref. [Erm17] which were published recently.

To describe simultaneously the data in the energy range between $\sqrt{s} = 2.06$ GeV and $\sqrt{s} = 2.42$ GeV, a dependence on the total energy of the initial NN system of transition amplitudes was introduced in the same form as in Refs. [Erm14, Erm11]. Thus, the production of resonant and non-resonant two-body states was fitted by:

$$A^{\alpha}_{tr}(s) = \frac{a^{\alpha}_1 + \sqrt{s}\, a^{\alpha}_3}{s - s^{\alpha}_0}\, e^{i a^{\alpha}_2}, \tag{2.8}$$

where $a^{\alpha}_1, a^{\alpha}_2, a^{\alpha}_3$ and s^{α}_0 are real numbers, and the poles at $s = s^{\alpha}_0$ are located in the region of left-hand side singularities of the partial wave amplitudes. Indeed, in most of the fits, the only fitted function was the transition amplitude $A^{\alpha}_{tr}(s)$. In the case of transition from an initial NN state to a two-body state with stable particles, this function is a complex number at a fixed initial energy. In the case of the transition to a two-body subsystem (a resonance or non-resonant rescattering and a spectator) the transition amplitude has contributions from logarithmic singularities defined by the

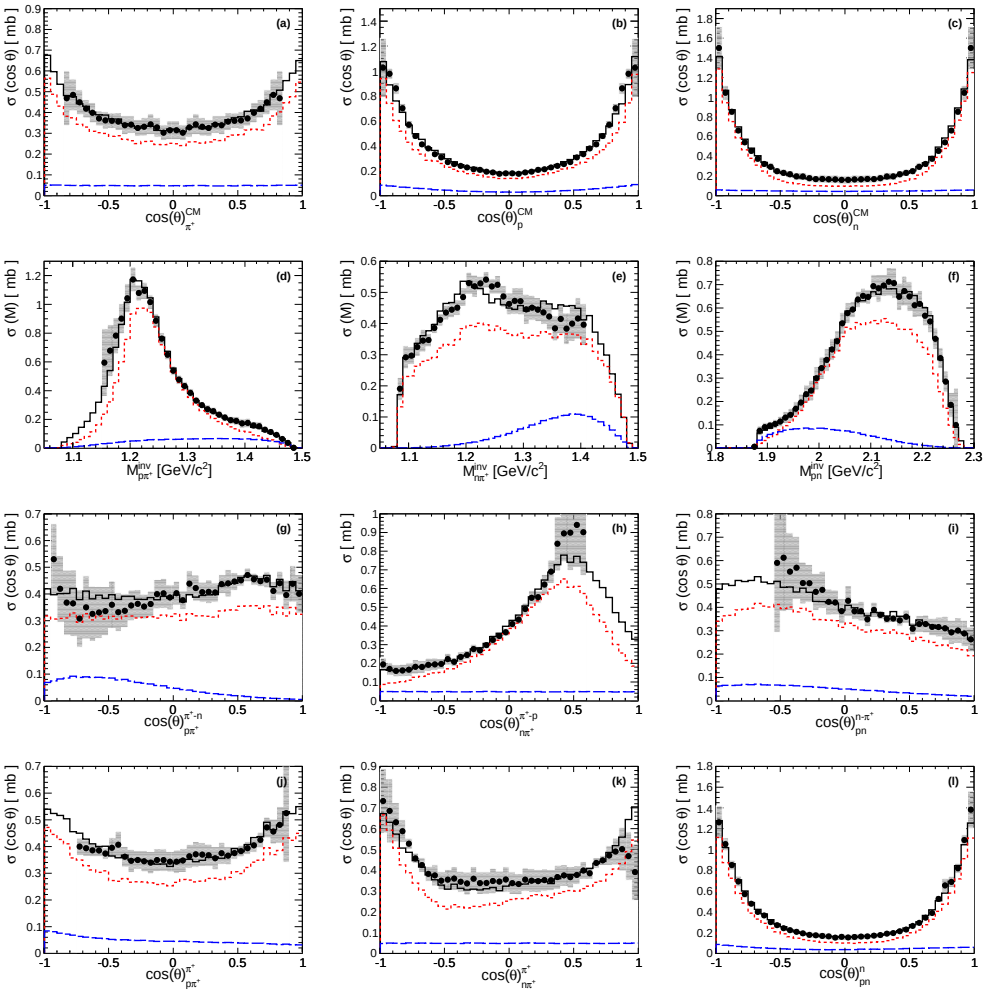

Figure 2.7: $np\pi^+$ channel, acceptance and efficiency corrected distributions: Angular distribution of (a) π^+, (b) p and (c) n in c.m.s. reference frame; Invariant mass of (d) $p\pi^+$, (e) $n\pi^+$ and (f) pn; Helicity distribution of (g) π^+ in $p\pi^+$ reference frame, (h) π^+ in $n\pi^+$ reference frame and (i) n in pn reference frame; Angular distribution of (j) π^+ in $p\pi^+$ GJ reference frame, (k) π^+ in $n\pi^+$ GJ reference frame and (l) n in pn GJ reference frame. Data points after acceptance corrections (black dots) based on the partial wave analysis solution. Data points in the areas of very low acceptance are omitted. Uncertainties originating from the various PWA solutions (as explained in the text) and statistical errors are visualized as grey band. Normalization error is not indicated. Histograms: total PWA solution (solid black), the $\Delta(1232)$ contribution (short-dashed red) and the $N(1440)$ contribution (long-dashed blue).

three-particle rescattering. Therefore, it should have a logarithmic dependence on the energy of the intermediate systems. However, this dependence is not important for the production of such a relatively narrow state, as the $\Delta(1232)$ resonance. In the case of the Roper resonance, there was no difference between fits, where (i) the Roper total width was parametrized with the same energy dependence as the πN channel only or (ii) fits with a more complicated parametrization of the width with the following decay

branching ratios: πN (60%), $\Delta\pi$ (20%) and N$(\pi\pi)_{S-wave}$ (20%) (see Ref. [Sar08]). The fits with free masses and widths of the Δ and Roper states were made, too. For $\Delta(1232)$ the parameters hardly changed from the PDG values [PDG16], and for the Roper resonance only problems with convergence of the fit were observed, but no notable improvement of the description of the data. Extensive tests did not show any need for a more complicated energy dependence for the non-resonant amplitudes, either. All these solutions were included for the estimate of systematic errors.

Various solutions with a maximum total angular momentum $J = 3$ or $J = 4$ were considered. At first, the data base fit was performed (see Table 2.2) with partial waves with total angular momentum up to $J = 3$, since only these partial waves were found to be important for the description of the lower (than HADES) energy data (Ref. [Erm14]). As in the case of the analysis of the HADES data alone, such a fit describes rather well the $pp \to pp\pi^0$ single state but shows some problems in the description of the $pp \to np\pi^+$ reaction. In particular, the forward region of the neutron angular distribution calculated in c.m.s. of the reaction, completely covered by the HADES geometrical acceptance, was underestimated by the fit. As a consequence of such a description an underestimated total cross section for the $pp \to np\pi^+$ reaction was obtained.

The very sharp behavior of the cross section at forward neutron angles (see Fig. 2.4c) is reproduced well by the resonance model. This model includes an infinite number of partial waves based on one-pion exchange and, indeed, one should expect the largest contribution from high angular momentum waves at extreme angles. To check this idea, the partial waves with total angular momentum $J = 4$ decaying into the ΔN intermediate state were added. A similar investigation was performed in Ref. [Erm14]. It was found that partial waves with the total angular momentum equal to four can contribute up to 6% to the total cross section at highest energy (data set $\sqrt{s} = 2.3$ GeV) but cannot be unambiguously identified. The present analysis produces a rather stable solution which defines the contribution from $J = 4$ partial waves. It is found to be on the level of 5% at $\sqrt{s} = 2.3$ GeV in agreement with Ref. [Erm14] and it reaches 15% at the HADES energies. Indeed, the fit with high spin partial waves reproduces rather well the forward angular distribution of the neutron in c.m.s. of the reaction (see Figs. 2.4c and 2.7c). If partial waves with even higher $J = 5$ are added to the fitting program, no improvement of the solution was seen but loss of the convergence only.

The comparison of the measured data and Monte Carlo events passed through the detector is shown in Figs. 2.4 and 2.6. The PWA solution describes the data better than the one obtained with the modified resonance model and can be used for the acceptance correction of the HADES data. The acceptance corrected distributions are shown in Figs. 2.7 and 2.8. The statistical errors are taken from the data, and model uncertainty errors are calculated from the set of solution described above (see the discussion below). Both statistical and model errors were added quadratically and are shown as a grey band.

Figure 2.9 shows the energy dependence of the pion production cross section ($np\pi^+$ upper panel, $pp\pi^0$ lower panel) and its decomposition into contributions of $\Delta(1232)$, $N(1440)$ (left panel) and incoming pp partial waves (right panel). As expected, the cross section is dominated by the contributions from the partial waves with the $\Delta(1232)$ resonance produced in the intermediate state. In the combined analysis of the data the partial waves with Roper production contributes about 20% to the $pp \to pp\pi^0$ cross section and on the level of 12% to the $pp \to np\pi^+$ cross section. The calculated contribution of the non-resonant terms amounts to 22 – 25% in the $np\pi^+$ channel and 8 – 10% in the $pp\pi^0$ channel.

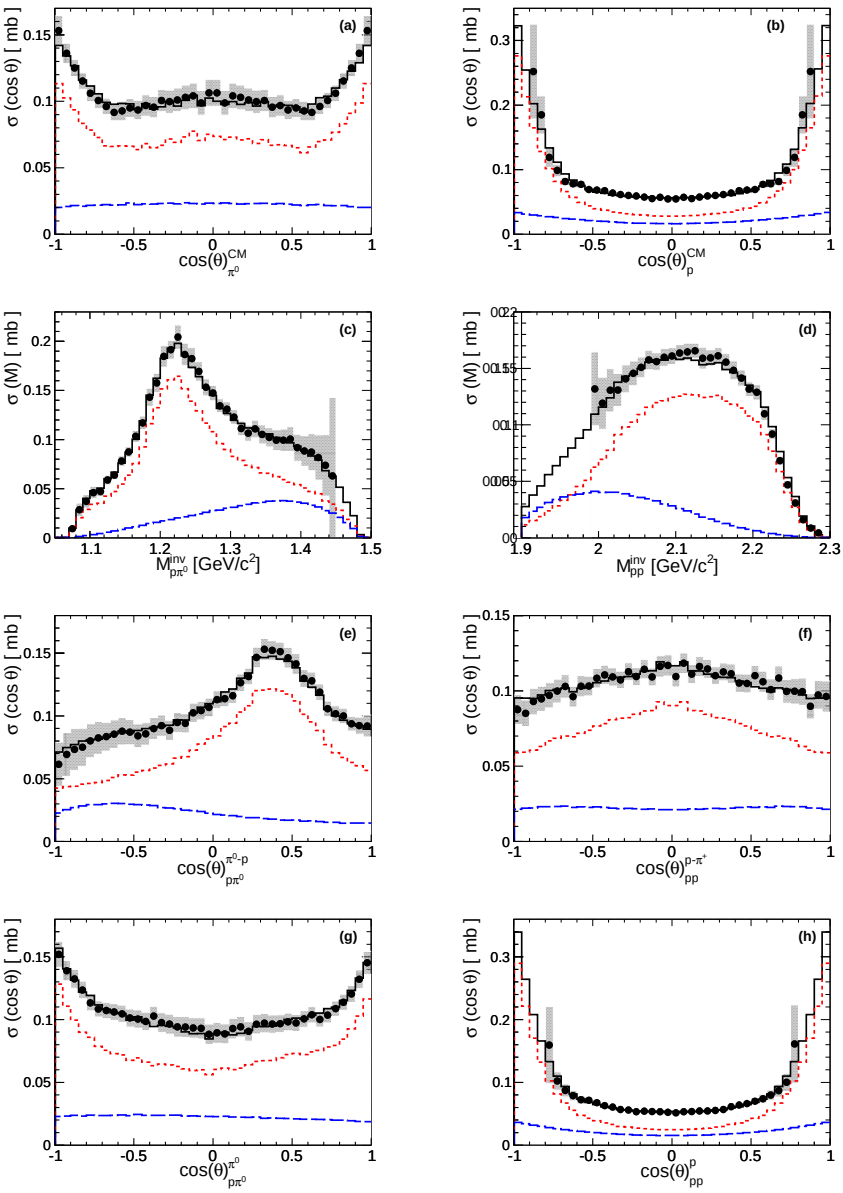

Figure 2.8: Various acceptance and efficiency corrected projections for the $pp\pi^0$ channel: Angular distribution of (a) π^0 and (b) p in c.m.s. reference frame; Invariant mass of (c) $p\pi^0$ and (d) pp; Helicity distribution of (e) π^0 in $p\pi^0$ reference frame and (f) p in pp reference frame; Angular distribution of (g) π^0 in $p\pi^0$ GJ reference frame and (h) p in pp GJ reference frame. Data points (black dots) in the areas of very low acceptance are omitted. Uncertainties originating from the various PWA solutions (as explained in the text) and statistical errors are visualized as grey band. Normalization error is not indicated. Histograms: total PWA solution (solid black), the $\Delta(1232)$ contribution (short-dashed red) and the $N(1440)$ contribution (long-dashed blue).

The fit to the HADES data alone is optimized with a smaller Roper contributions: it was found to be around 10% for $pp \to pp\pi^0$ and 6% for the $pp \to pn\pi^+$ cross sections, in agreement with the modified resonance model results. Contrary to that model, which includes an infinite number of the partial waves, the Bonn-Gatchina approach describes the data with a restricted number of partial waves. It is based on an observation for the dominance of partial waves with low orbital momenta near production threshold. Thus, at the HADES energies, the amplitudes with production of a Roper state are included only with orbital momenta $L' = 0, 1$ between Roper and the spectator nucleon. The stability of the obtained solutions was tested by including in the fit partial waves with higher orbital momentum and checking that these contributions are small.

	Total [%]	$\Delta(1232)N$ [%]	$N(1440)p$ [%]
$pp \to pp\pi^0$			
$^1S_0$	1.8 ± 0.7	<1	1.8 ± 0.7
$^3P_0$	6.8 ± 1.0	1.5 ± 0.5	5.5 ± 1.0
$^3P_1$	21.0 ± 4.4	2.0 ± 1.0	12 ± 2.0
$^3P_2$	29.5 ± 3.5	30.5 ± 4.0	2.3 ± 1.0
$^1D_2$	4.9 ± 1.0	4.2 ± 1.0	<1
$^3F_2$	11.8 ± 2.0	6.5 ± 1.0	<1
$^3F_3$	2.0 ± 2.0	2.0 ± 2.0	<1
$^3F_4$	12.0 ± 3.5	12.0 ± 3.0	<1
$^1G_4$	4.0 ± 1.0	4.0 ± 1.0	<1
$^3H_4$	5.5 ± 1.0	5.5 ± 1.0	<1
$pp \to pn\pi^+$			
$^1S_0$	3.5 ± 0.8	<1	2.2 ± 0.7
$^3P_0$	4.0 ± 1.5	1.0 ± 0.5	1.7 ± 0.4
$^3P_1$	14.0 ± 6.0	2.0 ± 1.0	6.7 ± 1.0
$^3P_2$	33.5 ± 3.0	29.5 ± 3.0	1.0 ± 0.5
$^1D_2$	11.8 ± 1.5	8.8 ± 1.3	<1
$^3F_2$	8.0 ± 1.0	6.5 ± 0.8	<1
$^3F_3$	2.0 ± 2.0	2.0 ± 2.0	<1
$^3F_4$	11.5 ± 2.5	11.5 ± 2.5	<1
$^1G_4$	5.0 ± 1.0	5.0 ± 1.0	<1
$^3H_4$	5.5 ± 1.0	5.5 ± 1.0	<1

Table 2.3: Contributions of the initial partial waves to the single pion production reaction $pp \to pp\pi^0$ and $pp \to np\pi^+$ at $\sqrt{s} = 2.42$ GeV.

The contributions of the initial partial waves to the HADES data as well as contributions of the partial waves with Δ and Roper resonances are listed in Table 2.3. The errors are defined from the set of solutions which include the combined fit of the whole database, the fit of the HADES data alone, and fits with contributions from higher spin states ($J = 4$). In some of the fits the notable interferences between non-resonant contributions in the NN channel and Roper production were found. In the case of a large correlation, the non-resonant contributions were suppressed and re-fitting redone.

If the deterioration of the likelihood value was less than 1000 (11%) for the $pp\pi^0$ channel, and less than 1500 (4%) for the $pn\pi^+$ channel, and the fit did not show large systematic deviations in a particular distribution, it was also included in the systematic error. The uncertainties of initial partial waves and final state differential projections, span from minimum to maximum values obtained from the accepted set of the PWA solutions.

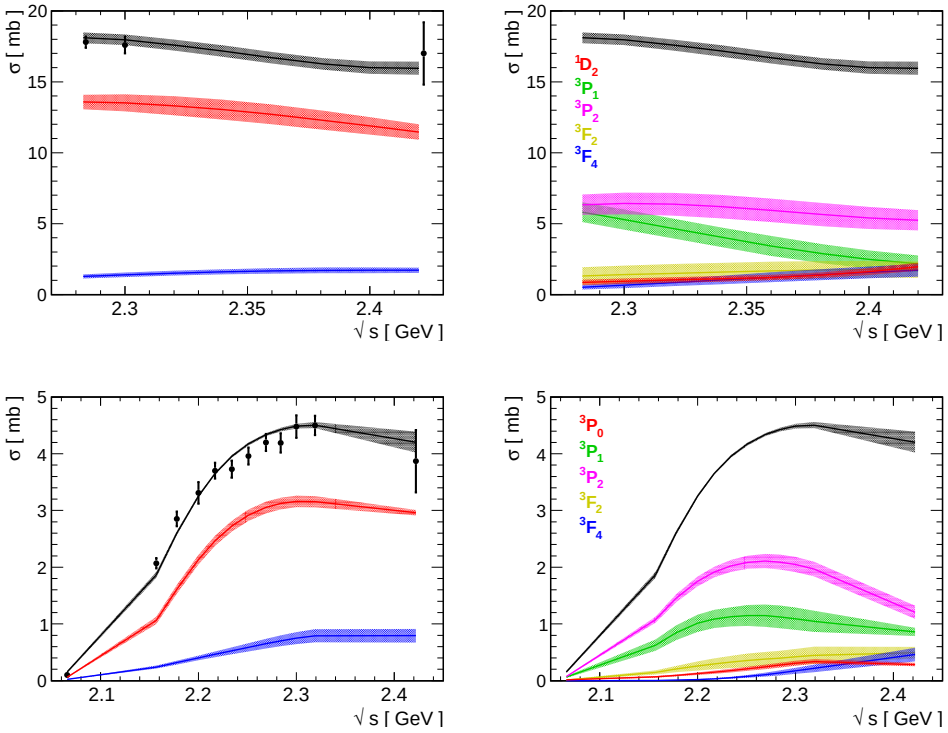

Figure 2.9: The description of the total cross section (data points with systematic error bars) in the combined analysis: $np\pi^+$ channel (upper panel), and $pp\pi^0$ channel (lower panel). Total partial wave solution (black curve) and contribution of $\Delta(1232)$ (red) and $N(1440)$ (blue) resonance in the PWA description (left panel), contributions of initial partial waves (right panel). Shaded bands reflect systematic uncertainties.

The same systematic approach was used for the calculation of errors for the total cross section obtained from the integration of the PWA solutions in the full solid angle. It was found to be 4.2 ± 0.15 mb for the $pp \to pp\pi^0$ reaction and 16.34 ± 0.8 mb for the $pp \to pn\pi^+$ reaction. The quoted errors are treated as the model uncertainty (see Table 2.1, column σ_{PWA}). The correction of experimental data with the obtained PWA solution provides very similar to the PWA prediction, cross section values: 4.1 ± 0.46 mb and 16.26 ± 1.96 mb, respectively. The errors, added quadratically, include: 5 – 6% due to background subtraction and particle identification, 3 – 5% the PWA model correction uncertainty and 8% due to normalization. Both cross sections agree well within errors with the cross sections obtained with the modified resonance model approach. However the contribution of the partial waves with Δ production is smaller and there is a notable contribution from the non-resonant terms. These terms provide a rather stable common contribution but show a rather large variation between initial partial waves. The total cross section obtained in the partial wave analysis of all fitted data together with main

contributions are shown in Fig. 2.9 (right panel). The contributions from leading partial waves have a peak in the region slightly below 2.3 GeV. This peak is created due to a compromise between decreasing partial wave amplitudes and three-body phase volume which grows rapidly near the pion production threshold. A similar behavior was observed in the isospin $I = 0$ sector [Sar10].

2.1.3 Summary and conclusion

The HADES data of the pion production in proton-proton collision were analyzed with a modified OPE model and with the Bonn-Gatchina partial wave analysis method. A detailed study of various observables indicates that the partial wave solution provides not only a better control of the underlying physics but also a better description of experimental data (Figs. 2.4 and 2.6). In the $pp\pi^0$ channel the discrepancies between PWA and the modified OPE model are visible in all spectra. Hence, the obtained PWA solution suits better to perform a full phase space acceptance correction of the measured data (Figs. 2.7 and 2.8).

The contribution of initial waves to the reactions cross section is defined as well as the contributions of partial waves with $\Delta(1232)$ and Roper production in the intermediate state. The analysis shows that at given energy of $\sqrt{s} = 2.42$ GeV the dominant contribution is defined by the production of $\Delta(1232)$ in the intermediate state. This is visible not only in the proton-pion invariant mass distributions but also in the related helicity distributions. Furthermore, the pion angular distributions in the GJ frame shows a strong anisotropy, as expected from the Δ decay. The PWA solution attributes 75% of the total cross section to the Δ in the $pp \to np\pi^+$ channel and 70% to the Δ in the $pp \to pp\pi^0$ channel. Since no notable influence of the non-resonant partial waves was observed for the $\Delta(1232)$ contribution, one can repartition the cross section for the $pp \to pp\pi^0$ reaction, obtaining the value 2.96 ± 0.22 (syst.) $\pm$ 0.24 (norm.) mb for the Δ resonance. The partial waves including the Roper production can contribute up to 20% for $pp \to pp\pi^0$ and up to 12% for $pp \to np\pi^+$.

2.2 Neutron-proton quasi-free collisions at T = 1.25 GeV

The excitation of a resonance decaying into two pions is usually studied in the $\pi N \to \pi\pi N$ [CBC04] and $\gamma N \to \pi\pi N$ [CEC08] reactions, however the simultaneous excitation of two baryons can be investigated in the NN reactions. A significant amount of data for proton-proton collisions has been accumulated for various two-pion final channels in bubble chamber experiments (see Refs. [Pic62a, Har62, Eis65, Bru69, Coc72, Cve81, Shi82, Dak82, Dak83, Bys87, Tsu00, Dor03, Sar07]), for energies from the threshold up to 2.85 GeV. Precise differential cross sections have been obtained at CELSIUS and COSY up to 1.4 GeV [Bro02, Joh02, Pät03, CTC08, CTC09, Dym09, Sko08, Sko09, Sko11a, Sko11b, CC12b], with an emphasis on the $\pi^0\pi^0$ production. The database for the np reaction from the bubble chamber experiments is scarce [Bru69, Dak82, Dak83, Tsu00, Bes86]. Recently, precise measurements of total and differential cross sections for the $np \to pp\pi^-\pi^0$ and $np \to np\pi^0\pi^0$ became available from WASA at COSY at neutron energies from 1.075 to 1.36 GeV [CC13b, CC15]. In the $np \to np\pi^+\pi^-$ channel, differential cross sections are also known from Dubna measurements [Jer11, Jer15], covering the beam incident energy range from 0.624 to 4.346 GeV. The tagged quasi-free $np \to np\pi^+\pi^-$ reaction was measured by HADES at a deuteron incident beam energy of 1.25 GeV/nucleon ($\sqrt{s} \sim 2.42$ GeV for the quasi-free collision). In this channel, the excitation of baryonic resonances coupled to the ρ meson can be studied in the isospin $I = 1$ channel, what is of relevance for understanding of the dilepton production (see Sections 4.5, 4.8, 4.9), and the expected modifications of the ρ−meson spectral functions in the nuclear matter [Leu10]. In particular, the ρ production mechanism via $\Delta\Delta$ final state interaction, which does not contribute in the pp channel, was proposed as an explanation for the different dilepton yield measured in pp and np channels [Bas14]. The two-pion production in NN collisions is also interesting for the check of a dibaryon resonance, observed in a double-pionic fusion reaction (see Refs. [CC09a, CC11, CC15, Cle15, CC16, Pla16, Bas17, Cle17]).

2.2.1 np$\pi^+\pi^-$ channel

In the experiment, the deuteron beam with intensity up to 10^7 particles/s and 1.25 GeV/nucleon of kinetic energy was directed onto a 5 cm long liquid-hydrogen target of 1% interaction probability. In order to select the quasi-free np reactions, the HADES spectrometer was equipped a Forward Wall (FW) scintillator hodoscope for registering the spectator protons, covering polar angles from 0.33° up to 7.17°. A Monte Carlo simulation for deuteron-proton breakup verified that approximately 90% of all spectator protons are within the FW acceptance [HC10]. Quasi-free np interactions were selected by the detection of the proton spectators with scattering angles $\leq 2°$ and momenta between 1.7 GeV/c and 2.3 GeV/c, reconstructed from the time-of-flight measurement in the FW.

Besides the proton spectator in the FW, the $np \to np\pi^+\pi^-$ channel was reconstructed based on the identification of three charged hadrons (p, π^+, π^-) in the HADES spectrometer. Any of the selected particles was used as the reference track in order to calculate the time-of-flight, using the reconstructed momentum and trajectory length. The velocities of the other two particles were then deduced, using only the time-of-flight difference with the reference particle (see App. C.3.4). In conjunction with the reconstructed momentum (with resolution of 2 – 3%) it was possible to build all possible particle combinations (hypotheses) out of the pool of hadronic tracks.

The purity of the $np \to np\pi^+\pi^-$ channel selection is demonstrated by the missing mass squared distribution of $p\pi^+\pi^-$ shown as black dots in Fig. 2.10, which peaks close to the neutron mass. The grey area displays the result of a simulation of the quasi-free $np \to np\pi^+\pi^-$ reaction, where the neutron momentum distribution in the deuteron was taken into account using the Paris potential [Lac81] and the $\pi^+\pi^-$ production in the np reaction was treated using phase-distributions and considering a rise of the cross section with the np center-of-mass energy according to Ref. [Bys87]. The total number of selected events in the $np \to np\pi^+\pi^-$ channel was 8×10^5.

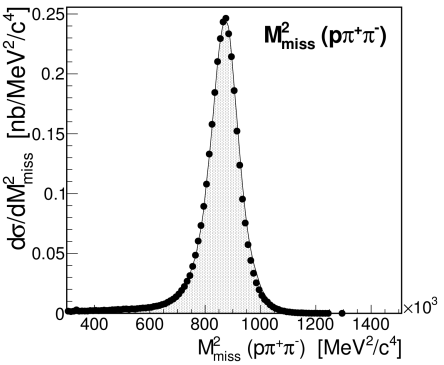

Figure 2.10: $np \to np\pi^+\pi^-$ reaction at 1.25 GeV: Squared missing mass distributions of the $p\pi^+\pi^-$. The experimental data are denoted by black dots, the shaded area displays the phase space distributions at 1.25 GeV, corrected for the energy dependence of total cross section taken from Ref. [Bys87].

The comparison of experimental distributions with theoretical models is done within the HADES acceptance. Based on the Monte Carlo simulation and full analysis reconstruction, three-dimensional acceptance and efficiency matrices (functions of the momentum, polar and azimuthal angles) for each particle species were produced. The acceptance of the $np \to np\pi^+\pi^-$ reaction within the HADES spectrometer amounts to about 6%. The resulting detection and reconstruction efficiency is typically about 90% for protons and pions.

2.2.2 Production of two pions

The description of double pion production in NN collisions in the GeV energy range is possible only within the framework of phenomenological models, since the chiral perturbation theory is available only near one-pion threshold [Liu13]. The first attempts were based on the one-pion exchange (OPE) model (see Sect. 1.2). The improved version is the reggeized π exchange model (OPER) [Jer12a,Jer12b], which uses the partial wave analysis results for πN elastic scattering from the SAID group [Arn03]. Another approach present the Lagrangian models. The Valencia model by Alvarez-Ruso *et al.* [AR98] describes NN collisions at energies lower than 1.4 GeV, including only $\Delta(1232)$ and $N(1440)$ excitations. The Cao *et al.* model [Cao10] includes resonances with masses up to 1.72 GeV/c^2. Both models reproduce the fast increase of the cross section above threshold in the different two-pion production channels and predict, both the double–Δ excitation, and production of the $N(1440)$ resonance followed by the decay into $\Delta\pi$ or $N\sigma$. Yet, both models fail to reproduce the $\pi^0\pi^0$ spectra for the $pp \to pp\pi^0\pi^0$ reaction at beam energies above 1.0 GeV [Sko11b, CC12b]. The enhancement observed in the low mass of the two-pion invariant mass spectra, in pn or pd fusion reaction (the so-called ABC effect), triggered the development of double–Δ excitation models [Ris73]. Later, the WASA Collaboration observed the resonant behavior of the cross section in the $pn \to d\pi^0\pi^0$ channel [CC09a, CC11], associated with a structure at low $\pi^0\pi^0$ invariant mass. They used the modified Valencia model (Ref. [Sko11b]) supplemented with the deuteron formation, however not being able to describe the double pionic data. The hypothesis of a dibaryon resonance in the $I = 0$ NN channel, with a mass of 2.37 GeV/c^2 and a width of 70 MeV, was suggested and supported by

the isospin decomposition of the $pn \to d\pi\pi$ reaction [CC13a]. The modified Valencia model, supplemented with the new d^* resonance, provided a consistent description of both $I = 0$ and $I = 1$ channels, also for the $pn \to pp\pi^0\pi^-$ [CC13b] reaction. Moreover, the SAID partial wave analysis, based on new polarized $\vec{n}p$ scattering data, confirmed the resonance pole in the ${}^3D_3 - {}^3G_3$ coupled partial waves at (2380±10-i40±5) MeV (see Refs. [CC14b, CC14a]).

The collected data with HADES spectrometer, in quasi-free $np \to np\pi^+\pi^-$ reaction, using a deuteron beam of 1.25 GeV/nucleon, allow for precise investigation of the total and differential cross sections. The sensitivity to the double−$\Delta(1232)$ and $N(1440)$ excitation, as well as higher lying resonances, can be studied. The data are complementary to comparison to the already measured $np \to d\pi^+\pi^-$ (see Refs. [Fäl11, Alb13]). In the analysis, the results were averaged over the available range of np center-of-mass energies. For the interpretation of the HADES results, three models: the modified Valencia [Sko11a], the Cao [Cao10], and OPER model [Jer12b] are used.

In the modified Valencia model [Sko11a], a number of adjustments have been done as compared to the original model [AR98]. The two-pion contribution from the $N(1440)$ decay via $\Delta\pi$ or $N\sigma$, calculated as a ratio $\Gamma(N(1440) \to \Delta\pi)$ to $\Gamma(N(1440) \to N\sigma)$, has been reduced from 4 to 1. This is supported by the analysis of the $\pi^0\pi^0$ opening angle and invariant mass distributions obtained in the $pp \to pp\pi^0\pi^0$ reaction at beam energies below 900 MeV [Sko08], and a recent Partial Wave Analysis [Sar08, Ani12]. Furthermore, the $N(1440)$ cross section was adjusted according to the isospin decomposition of the two-pion production channels in the pp reaction at different energies between 0.775 GeV and 1.36 GeV [Sko09], resulting in the smaller Roper contribution as compared to the double−Δ excitation. The shape of the $\pi^0\pi^0$ invariant mass distribution measured in $pp \to pp\pi^0\pi^0$ at an incident energy larger than 1 GeV, where the double−Δ mechanism dominates [Sko11b], suggested the change of the sign of the ρ exchange contribution in the Δ excitation mechanism and its reduction. Finally, the $\Delta(1600) \to \Delta(1232)\pi$ was introduced in order to improve the $pp \to nn\pi^+\pi^+$ description, especially the $\pi^+\pi^+$ opening angle and invariant mass distributions measured for this channel at 1.1 GeV [Sko11a]. However, one should note that such a large contribution of the $\Delta(1600)$ resonance at this low energy is controversial.

The Cao model [Cao10] neglects the interferences between the different contributions, included in the Valencia model. It has higher contributions for both Δ and N^* than the Valencia model, e.g., the $N(1440)$ contribution corresponds to about 40 % of the total $np \to np\pi^+\pi^-$ cross section at an incident energy of 1.25 GeV. The Cao model favors $N(1440) \to \Delta\pi$ by a factor 2 with respect to $N(1440) \to N\sigma$ decay. The $\Delta(1600)$ starts to contribute to the $pp \to nn\pi^+\pi^+$ reaction for energies larger than 1.6 GeV. The larger double−Δ contribution leads to a good description of this channel but, on the other hand, it overestimates the $pp \to pp\pi^0\pi^0$ cross section.

The OPER model [Jer12b] is based on a reggeized π−exchange model, in which the form factors and propagators take into account the off-shellness of the exchanged pion. The model uses on-shell amplitudes of the elastic πN scattering from the SAID group. The inelastic $\pi N \to \pi\pi N$ reaction amplitudes are deduced from a parametrization obtained in the analysis of Manley [Man92], which provided a good description of the $np \to np\pi^+\pi^-$ reaction at 5.2 GeV/c, measured at Dubna [Jer11], and in $\bar{p}p \to \bar{p}p\pi^+\pi^-$ at 7.23 GeV/c, measured at CERN [Ape76, Ape79]. The two-pion production from the exchange pion line uses amplitudes for $\pi\pi$ scattering, improving the description of the two-pion invariant mass spectra in the low mass region [Jer12b]. Such graphs are taken into account in the Valencia model, but are neglected in the Cao model.

	Cao	mod. Valencia	OPER
$\Delta(1232)\Delta(1232)$	47.0 %	60 %	38.0 %
$N(1440) \rightarrow \Delta(1232)\pi$	23.0 %	2.1 %	4.5 %
$N(1440) \rightarrow N\sigma$	20.0 %	8.2 %	0.2 %
$\Delta(1600) \rightarrow \Delta(1232)\pi$	3.0 %	21.0 %	4.5 %

Table 2.4: Main contributions in the Cao [Cao10], modified Valencia [Sko11b] and OPER [Jer12b] models in the $np \rightarrow np\pi^+\pi^-$ reaction, for a neutron incident energy of 1.25 GeV. The contribution of interference terms is neglected.

Table 2.4 presents the main contributions of the models discussed above, at an incident neutron energy of 1.25 GeV. Although the numbers do not take into account interference effects, they show major differences between the models which will be compared to HADES data. The momentum distribution of the neutron inside the deuteron was takien into account via the Paris [Lac81] deuteron wave functions for the phase space calculation, the Hulthen [Hul57] wave function for the modified Valencia [Sko11a] and CD-Bonn [Mac01] for OPER [Jer12b] and Cao [Cao10] models. No significant difference is expected from these different inputs.

2.2.3 Experimental results compared with models

The distributions for the $np \rightarrow np\pi^+\pi^-$ reaction at 1.25 GeV are presented in Figs. 2.11-2.14 within the HADES acceptance. The data, corrected for the reconstruction efficiency, are plotted as solid dots with statistical errors only. The model predictions from the modified Valencia [Sko11a], Cao [Cao10] and OPER [Jer12b] models, as well as the phase space distributions, have been normalized to the total experimental yield. Additionally, contributions from the double–Δ, $N(1440)$, and $\Delta(1600)$ excitation in the OPER and modified Valencia model description, are compared with experimental data in Figs. 2.12 and 2.14.

2.2.3.1 Invariant masses

The sensitivity of the experimental data distributions, measured within the limited acceptance of HADES, can be tested by comparison with the phase space Monte Carlo simulation. In the invariant mass projections (Fig. 2.11), the resonant behavior is pronounced in the $p\pi^+$ distribution, where a position of the maximum in the data roughly corresponds to the Δ^{++} mass. This distribution is also well described by the different models and deviates significantly from the phase space distribution. It clearly points to the double–Δ excitation, where the $\Delta^{++}\Delta^-$ production is favored in comparison to $\Delta^+\Delta^0$ by a factor 8/5 due to the isospin relation. The $N(1440)^+ \rightarrow \Delta^{++}\pi^-$ decay is also expected in $p\pi^+$ channel, however with the lower intensity. In addition, the $N(1440)^0$ excitation, followed by decay to $\Delta^-\pi^+$, has the same probability, but is enhanced by the HADES spectrometer acceptance. Similarly, a small contribution of the $\Delta(1600)$ as a source of Δ^{++} is supported by the modified Valencia model (see Figs. 2.11 d and 2.12 f) and also favored by the acceptance. The double–Δ contribution is larger in the modified Valencia model than in the Cao model. The model differences are reflected in the invariant mass width, however, this observable is not sensitive enough. The deviations from phase space distributions, hence the resonance behavior, are less pronounced for

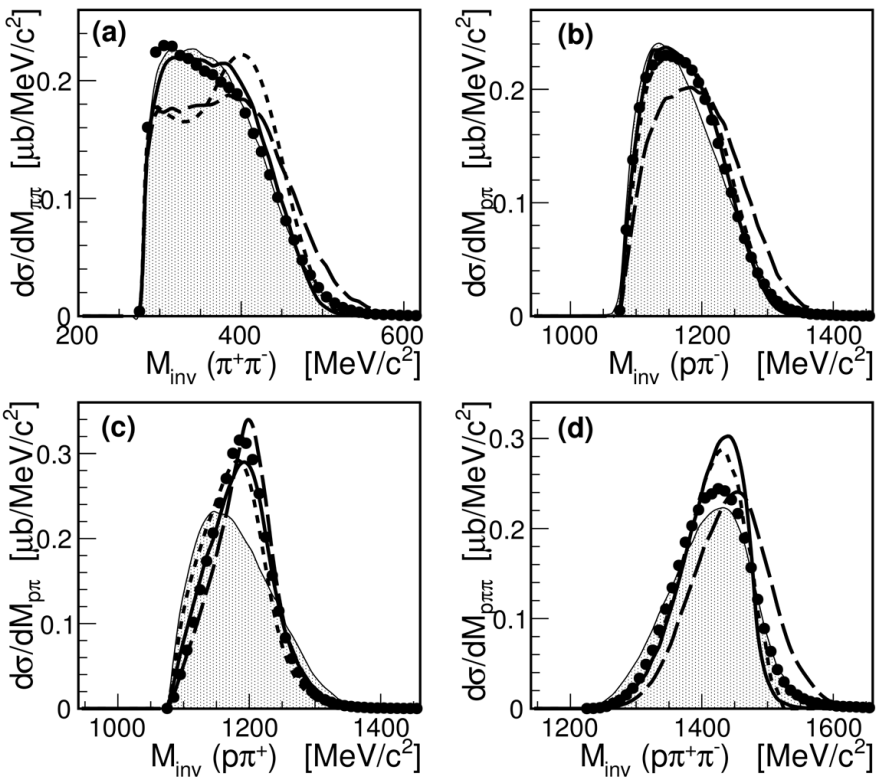

Figure 2.11: $np \to np\pi^+\pi^-$ reaction at 1.25 GeV: Invariant mass of (a) $\pi^+\pi^-$, (b) $p\pi^-$, (c) $p\pi^+$, and (d) $p\pi^+\pi^-$. The experimental data are shown by solid symbols. The theoretical predictions within the HADES acceptance are from OPER [Jer12b] (solid curve), Cao [Cao10] (dashed curve), and modified Valencia model [Sko11b] (long-dashed curve). The grey area shows the phase space distributions.

the $p\pi^-$ and $p\pi^+\pi^-$ invariant mass distributions (Fig. 2.11 b and d). The Δ^0 production is attenuated as compared to the Δ^{++} due to isospin relations in all channels (double–Δ, $N \to \Delta(1232)\pi$, and the $\Delta(1600) \to \Delta(1232)\pi$). The OPER and Cao models give similar predictions for the $p\pi^-$ invariant mass distribution, very close to experimental data, but their $p\pi^+\pi^-$ invariant mass is too narrow. The Valencia model overestimates both $p\pi^-$ and $p\pi^+\pi^-$ distributions. The largest deviations between experiment and models are observed for the $\pi^+\pi^-$ invariant mass distribution. The Cao model presents double maximum, not present in the data, probably due to overestimation of the $N^* \to \Delta\pi$ process. The Valencia model is slightly peaked towards the $\pi^+\pi^-$ mass above 350 MeV/c^2. It is due to the $\Delta(1600)$ and the $N(1440)$ contributions, and their interference with the double–$\Delta(1232)$ contribution. The contribution at lower mass is insufficient (see Fig. 2.12, right column). The OPER model gives the best description of the low mass part of $\pi^+\pi^-$ distribution, however, the double–Δ contribution is much broader than in the case of the modified Valencia model (Fig. 2.12, left column).

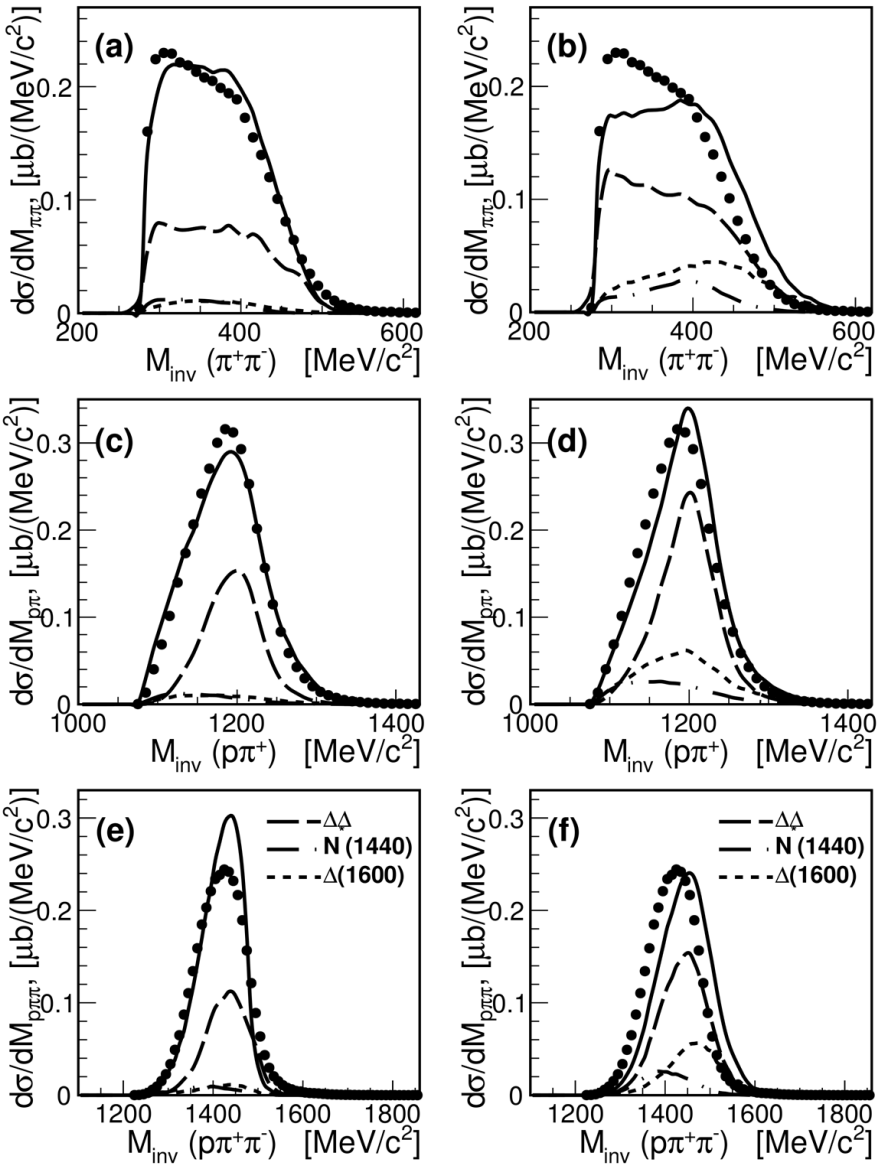

Figure 2.12: $np \to np\pi^+\pi^-$ reaction at 1.25 GeV: Invariant mass of (a, b) $\pi^+\pi^-$, (c, d) $p\pi^+$, and (e, f) $p\pi^+\pi^-$. Experimental data (full dots) are compared to the total yield (solid curves) for the OPER model [Jer12b] (left column) and modified Valencia model [Sko11a, Sko11b] (right column). The contributions denoted by curves: $\Delta\Delta$ (long-dashed), $N(1440)$ (long dash-dotted) and $\Delta(1600)$ (short-dashed).

2.2.3.2 Angular distributions

The angular distributions are more sensitive observables to the production mechanism, but also challenging due to the limited acceptance. Figure 2.13 presents the angular distributions for the $np \to np\pi^+\pi^-$ reaction at 1.25 GeV, where in most cases the phase space distribution is very different from the experimental data and various

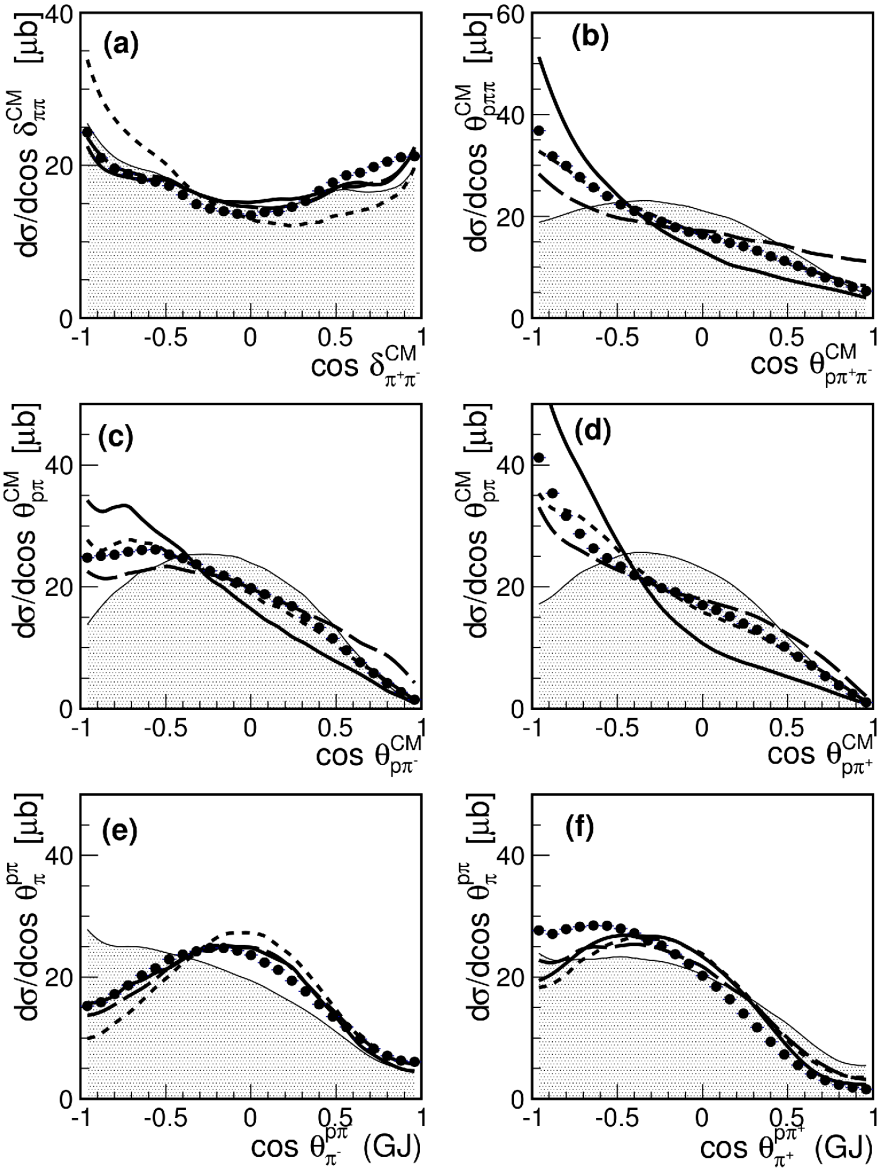

Figure 2.13: $np \to np\pi^+\pi^-$ reaction at 1.25 GeV, angular distributions: (a) $\pi^+\pi^-$ opening angle in c.m.s., (b) $p\pi^+\pi^-$ polar angle in c.m.s.,(c) $p\pi^-$ polar angle in c.m.s., (d) $p\pi^+$ polar angle in c.m.s., (e) π^- polar angle in the $p\pi^-$ Gottfried-Jackson frame, (f) π^+ polar angle in the $p\pi^+$ Gottfried-Jackson frame. Curve description and grey area as in Fig. 2.11.

models. The panels *a-d* present the projections in the center-of-mass system: the $\delta_{\pi^+\pi^-}$ opening angle, and polar (θ) angles of the $p\pi^+\pi^-$, $p\pi^-$, and $p\pi^+$ systems. The center-of-mass frame was defined assuming the neutron at rest in the deuteron. The panels *e-f* present π^- and π^+ polar angles with respect to the beam axis, boosted first to the $p\pi^-$ and $p\pi^+$ Gottfried-Jackson frames, respectively.

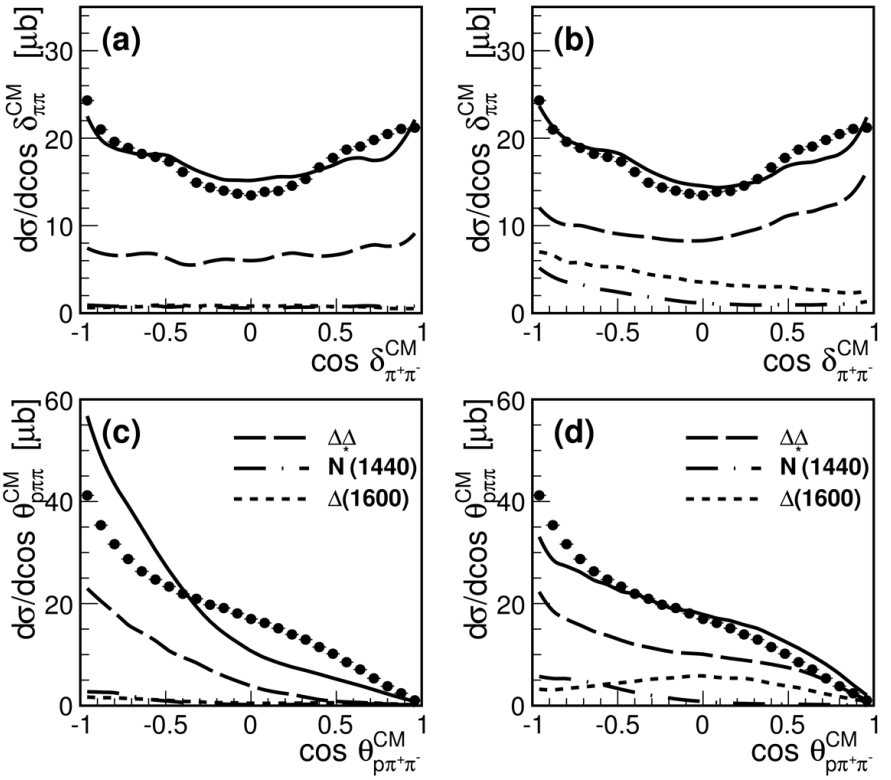

Figure 2.14: $np \to np\pi^+\pi^-$ reaction at 1.25 GeV, angular distributions in the center-of-mass (np) rest frame: (a, b) $\pi^+\pi^-$ opening angle, (c, d) $p\pi^+$ polar angle. Experimental data are compared to the the OPER model (left column) and modified Valencia model (right column). Curve description as in Fig. 2.12.

There is a correlation between the $\pi^+\pi^-$ invariant mass (Fig. 2.11a) and $\pi^+\pi^-$ opening angle (Fig. 2.13a). It is seen as an excess of the measured yields at small opening angle and invariant mass. The large asymmetry of the distribution in the case of the Cao model and its steep peaking for back to back $\pi^+\pi^-$ emission ($\cos\delta^{CM}_{\pi^+\pi^-}$ = -1) are related to the high-mass structure (Fig. 2.11a, dashed curve), which is due to the $N(1440) \to \Delta(1232)\pi$ decay. The other models, OPER and modified Valencia model (Figs. 2.14a, b), are smooth for all contributions and close to experimental data. The difference of the shapes of the $\cos\delta^{CM}_{\pi^+\pi^-}$ distributions obtained for the double–Δ contributions in these models is consistent with the different behavior of the $\pi^+\pi^-$ invariant masses.

The polar angles (Figs. 2.13b, c, d), $\theta^{CM}_{p\pi^+\pi^-}$, $\theta^{CM}_{p\pi^-}$ and $\theta^{CM}_{p\pi^+}$, show a strong forward/backward asymmetry, enhanced by the spectrometer acceptance, covering angles larger than 18°. This asymmetry is mainly due to the strong $\Delta^{++}\Delta^-$ production, which occurs at small four-momentum transfers between the proton from target and the Δ^{++}, and the neutron from the beam and the Δ^-, respectively. The protons are emitted preferentially backward in the center-of-mass. The description provided by the Cao model is closest to experimental data. The Valencia model presents the asymmetry smaller than in experimental data. In the OPER description (Fig. 2.11 solid curve, Fig. 2.14 left column), much steeper slope is due to strongly backward peaked the double–Δ con-

tribution. The difference with this contribution in the modified Valencia model is due to the much lower cut-off parameters in the vertex form factors which induce a much steeper four-momentum transfer dependence. Similarly to the $\pi^+\pi^-$ invariant mass distributions, the description of the $\theta^{CM}_{p\pi^+}$ distribution could be improved by a reduction of the $\Delta(1600)$ contribution. The distributions of the pion angles $\theta^{p\pi^-}_{\pi^-}(GJ)$ and $\theta^{p\pi^+}_{\pi^+}(GJ)$ are shown in Figs. 2.14 e and f, respectively. The $\theta^{p\pi^-}_{\pi^-}(GJ)$ distribution is very well reproduced, especially by the OPER and modified Valencia model, while none of the models predict the observed enhancement for backward $\theta^{p\pi^+}_{\pi^+}(GJ)$.

Is summary, the Valencia model provides a better description than the Cao model, and the changes introduced by the WASA Collaboration in the original Valencia model, except perhaps for the $\Delta(1600)$ contribution, seem to be justified by the HADES analysis. The OPER model, which is based on a very different approach, gives also a good description of the data. In particular, it fits better the $\pi^+\pi^-$ invariant masses than the modified Valencia model, but the predictions are worse for the center-of-mass angular distributions.

2.2.3.3 Total cross sections

The models can be compared with data also in terms of the integrated cross section. The measured differential cross section integrated within the HADES acceptance amounts to σ^{acc}_{HADES} = 34.9 ± 1.5 μb. The closes but lower value, 26.4 μb, is predicted by the modified Valencia model [Sko11b]. The other models predict much larger cross sections, the Cao model [Cao10] integral amounts to 72.4 μb, and the OPER model [Jer12b] amounts to 86 μb.
In order to minimize the model dependence of the total production cross section and estimate the model-driven systematic error, the acceptance corrections are constructed based on several projections, corresponding to the differential distributions: $M_{\pi^+\pi^-}$, $M_{p\pi^+}$, $M_{p\pi^-}$, $M_{p\pi^+\pi^-}$ (see Fig. 2.11), and $\cos^{CM}_{\delta_{\pi^+\pi^-}}$,$\cos^{CM}_{p\pi^+\pi^-}$, $\cos\theta^{CM}_{p\pi^+}$, $\cos\theta^{CM}_{p\pi^-}$ (see Fig. 2.14 a-d). The OPER and the modified Valencia are the models selected for the one-dimensional correction, since they give a reasonable shape description. The obtained total cross section amounts to $\sigma^{Valencia}_{HADES}$ = 0.65 ± 0.03 mb, using the modified Valencia model, and σ^{OPER}_{HADES} = 0.795 ± 0.040 mb, using the OPER model. The cross section is averaged over neutron energies accessible in the quasi-free $np \to np\pi^+\pi^-$ reaction at a deuteron beam energy of 1.25 GeV/nucleon. The average neutron energy for the HADES measurement (see Fig. 2.15) is 1.273 ± 0.063 GeV. The final cross section estimate amounts to σ_{HADES} = 0.722 ± 0.108 mb. It is denoted in Fig. 2.15 with a full solid dot and compared with the world data. In addition, the spread of the neutron momentum in the different measurements is marked with the horizontal error bars.

There are two data points close to the HADES measurement. The NIMROD *pd* measurement [Bru69] was obtained at an incident energy 120 MeV higher than the HADES experiment, and the reported the cross section was 1.75 ± 0.20 mb. The KEK *dp* measurement [Tsu00] was obtained for an incident energy only 70 MeV lower than the HADES energy and reported the cross section was 1.25 ± 0.05 mb. Such a difference with the HADES cross section, lower by a factor 2 in such a small energy range, is difficult to explain. Figure 2.15 presents also the selected model predictions. The Cao model was omitted since it does not reproduce satisfactorily the $np \to np\pi^+\pi^-$ reaction in the HADES energy range, with the predicted cross section 1.73 mb, higher by a factor 2.4 than the HADES point. The OPER model does not provide cross sections and was normalized to the Bystricky parametrization [Bys87] (solid curve), which is an

interpolation between measurements over a wide energy range up to 2.2 GeV. This parametrization predicts the cross section of 1.88 mb at 1.25 GeV, largely overestimating the HADES value. The modified Valencia (short dahs-dotted curve) gives a prediction of 0.59 mb, close to the HADES value. The advantage of this model is the good reproduction of the differential distributions for the $np \to np\pi^+\pi^-$ channel, as well as the data measured by the WASA Collaboration below 1.4 GeV for the $nn\pi^+\pi^+$ [Sko11a] and $pp \to pp\pi^0\pi^0$ [Sko11b] channels. Unfortunately, the model underestimates the $np \to np\pi^+\pi^-$ reaction both at lower and at higher energies. The latter might be due to the lack of the $N(1520)$ and $N(1535)$ resonances in the model.

Another contribution to $np \to np\pi^+\pi^-$ channel was calculated by the WASA Collaboration, assuming formation of the dibaryon resonance with a mass around 2.38 GeV/c^2. The contribution estimated in Ref. [Alb13], i.e. $pn \to d^\star \to pn\pi^+\pi^-$, is denoted in Fig. 2.15 as a long dash-dotted curve with a maximum around 1.13 GeV neutron energy. This contribution should be added to the non-resonant contribution. The combined description, obtained by adding the dibaryon contribution from Ref. [Alb13] to the modified Valencia model prediction, is presented as a dashed curve. The result perfectly matches the HADES data point and, except for the KEK point [Tsu00], is in agreement with the cross sections obtained for incident energies between 1 and 1.3 GeV within 20%. This energy range was used to adjust the Valencia model for the $pp \to pp\pi^0\pi^0$ and $pp \to nn\pi^+\pi^+$ data. The worse description outside this energy range could probably be reduced by further adjustments of the Valencia model. The final conclusion cannot be made until the full model, including in a consistent way the $t-$channel processes, based on the modified Valencia model, and the resonant $s-$channel, is developed, due to the unknown interference effects. The resonance contribution investigated is various differential distributions remains also an open question.

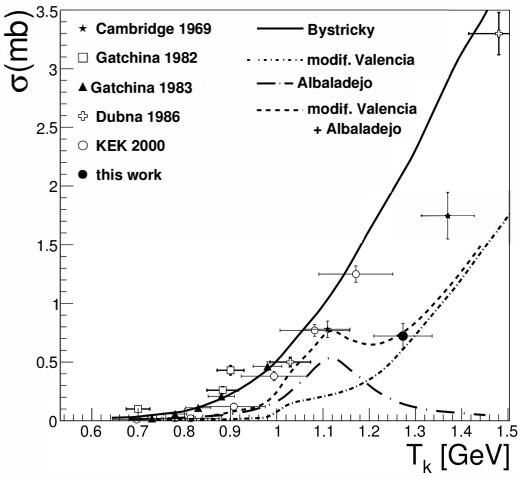

Figure 2.15: HADES measurement for the quasi-free $np \to np\pi^+\pi^-$ reaction at 1.25 GeV (full dot at σ = 0.72 ± 0.11 mb) compared to the world data. The solid curve represents the Bystricky parametrization [Bys87] used for the OPER model normalization, the short dash-dotted curve shows the estimation of the modified Valencia model [Sko11a]. The long dash-dotted curve estimates the contribution of the dibaryon resonance from Ref. [Alb13]. The dashed curve is the sum of the modified Valencia model and dibaryon resonance contributions.

2.3 Proton-proton collisions at T = 2.2 GeV

In proton-proton collisions at a kinetic beam energy of 2.2 GeV (the energy $\sqrt{s}$ = 2.765 GeV), the larger phase space available for inelastic processes is reflected in a significant contribution of the two-pion production, visible in Fig. 2.16, left panel, presenting two-proton missing mass squared. In addition, the η–meson production shows up for $M^2_{miss}(p,p)$ around 0.3 $(\mathrm{GeV/c^2})^2$. Due to that fact, studying one-pion production mechanisms in the hadronic channels requires the modeling of multipion background. At 2.2 GeV, they were simulated as resulting from a double–Δ production, with normalization adjusted such as to fit the data at the highest missing masses. Figure 2.16, right panel, shows events with two protons (pp), and one proton and one pion ($p\pi^+$). The missing particles are clearly visible, albeit with a significant two-pion contribution. Likewise in the other pp experiment, at lower energy, all spectra were normalized to the pp elastic scattering yield measured in the same experimental run. The resulting normalization factor has a precision of about 11%, reflecting mainly the uncertainty on the global efficiency of the reconstruction and analysis.

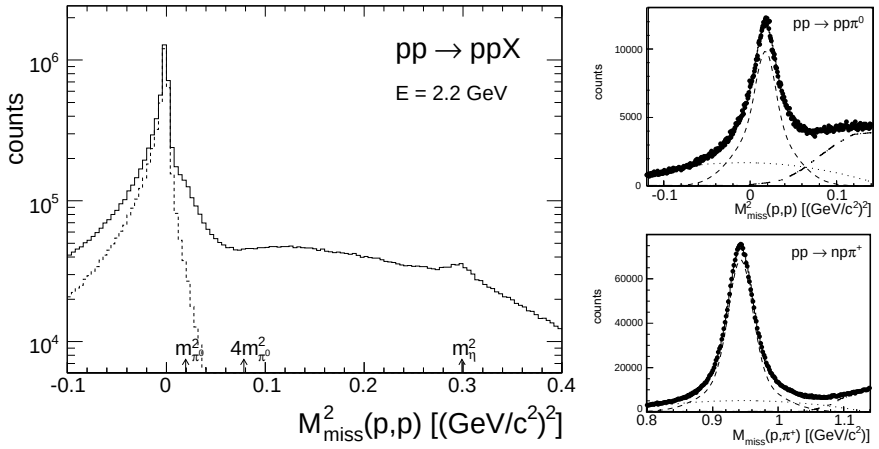

Figure 2.16: Left panel: Experimental spectrum of pp missing mass squared for the reaction $pp \to ppX$ at 2.2 GeV. The most prominent peak stems from pp elastic channel (also denoted with a dashed curve), followed by the one-pion and two-pion continuum and η production. Right panel: Inelastic one-pion exclusive channels, pp missing mass squared (upper) and $p\pi^+$ missing mass (lower). The two-pion contribution (dot-dashed curve), deduced from the double–Δ simulation followed by the decays to $N\pi$ final states, is subtracted before the fit.

2.3.1 One-pion production and resonance model

The production of one-pion channels from the pp reaction at 2.2 GeV energy is described within the resonance model by Teis *et al.* [Tei97]. Like in pp collisions at 1.25 GeV, the contributing resonances are Δ–isobar and Roper resonance, but also higher lying resonances, mainly $N(1520)$ and $N(1535)$, play a role. The isospin relations between channels are preserved (see Sect. 2.1.1, Eqs. 2.2 and 2.3). The resonance model cross sections are listed in Table 2.5 (column σ_{RES}), in addition the cross sections adjusted to experimental data are given in a column σ_{ADJ}. Resonances heavier than

$N(1535)$ were neglected in this approach. They contribute 7% and 11% to the $np\pi^+$ and $pp\pi^0$ final states, respectively. Besides the $\Delta(1232)$, modeled according to the OPE calculation [Dmi86] adopted in Teis fit, the angular distributions for the production of the other resonances are assumed to be isotropic in the pp center-of-mass frame, except for the $N(1440)$ resonance, where a steep distribution following the one-boson exchange (OBE) model of Ref. [Hub94] was implemented.

final state	**intermediate process**	σ_{RES} **(mb)**	σ_{ADJ} **(mb)**
$np\pi^+$	$pp \to n\Delta^{++}(1232)$	10.80	10.80
	$pp \to p\Delta^{+}(1232)$	1.20	1.20
	$pp \to pN(1440)$	0.82	1.60
	$pp \to pN(1520)$	0.18	0.36
	$pp \to pN(1535)$	0.19	0.64
	non-resonant	0.0	0.3
	$Total:$	13.09	14.90
$pp\pi^0$	$pp \to p\Delta^{+}(1232)$	2.40	2.40
	$pp \to pN(1440)$	0.41	0.80
	$pp \to pN(1520)$	0.09	0.18
	$pp \to pN(1535)$	0.10	0.32
	non-resonant	0.0	0.15
	$Total:$	2.99	3.85
$pp\eta$	$pp \to pN(1535)$	0.0725	0.082
	non-resonant	0.0525	0.06
	$Total:$	0.125	0.142

Table 2.5: Cross sections for the $p(2.2\text{ GeV}) + p$ reaction and one-pion final states with the intermediate baryon resonance excitation: σ_{RES} for the resonance model [Tei97], σ_{ADJ} adjusted to the data.

The resonance excitation is reflected in the Dalitz plots in Fig. 2.17. Besides the dominating Δ–isobar contributions, the invariant mass squared around $M^2_{inv}(p,\pi^0)$ = 2.3 $(\text{GeV/c}^2)^2$ is populated, corresponding to the higher N^* resonance excitation. The final state interaction, clearly seen in the $pp \to np\pi^+$ at 1.25 GeV is less apparent at 2.2 GeV, since it affects events with proton angles below the acceptance limit. For the $pp\pi^0$ channel, the pp FSI is suppressed by the trigger configuration (see App. C.2).

2.3.2 One-pion channels

Figure 2.18 presents the $p\pi^0$ (left panel) and both $p\pi^+$, and $n\pi^+$ (right panel) invariant masses, respectively. The subsequent contributions of the resonance model were added incoherently. Unlike in the analysis of pp at 1.25 GeV (Sect. 2.1.1.1 and 2.1.1.2), the Δ resonance contributions were not adjusted and the cut-off parameter (see Eq. 1.9) was left at $\Lambda_\pi = 0.63\ \text{GeV}^2$. On the other hand, $N(1440)$ was modeled anisotropically. The sum of Δ and $N(1440)$ resonances, as well as the higher-lying resonances, $N(1520)$ and $N(1535)$, is denoted by a black solid curve (model A). Contrary to the results in pp at 1.25 GeV (Sect. 2.1), the total cross section in this model description is clearly underestimated in all distributions.

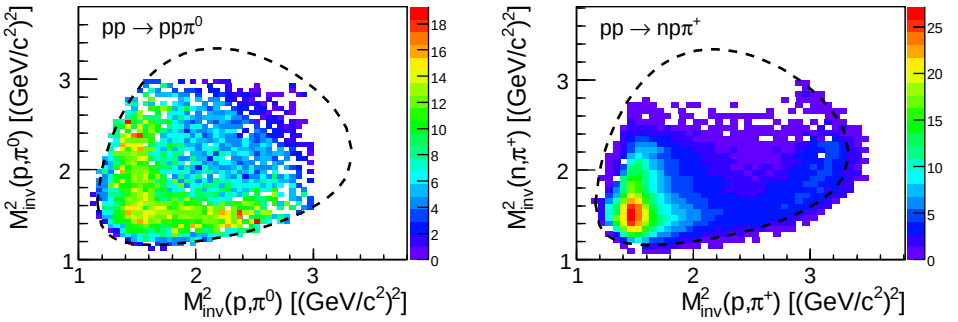

Figure 2.17: Dalitz plots of the $pp \to pp\pi^0$ (left panel) and $pp \to np\pi^+$ (right panel) at 2.2 GeV, with the dashed curves indicating their kinematical limits.

The cross sections of N^* resonances, $N(1440)$, $N(1520)$ and $N(1535)$, were increased and a non-resonant contribution, generated with a phase space distribution, was added (Table 2.5, column σ_{ADJ}). A better description of the two-particle invariant mass distributions, $p\pi^0$, $p\pi^+$, and $n\pi^+$ (Fig. 2.18), as well as the neutron angular distribution in Fig. 2.19 in the $np\pi^+$ channel, were obtained.

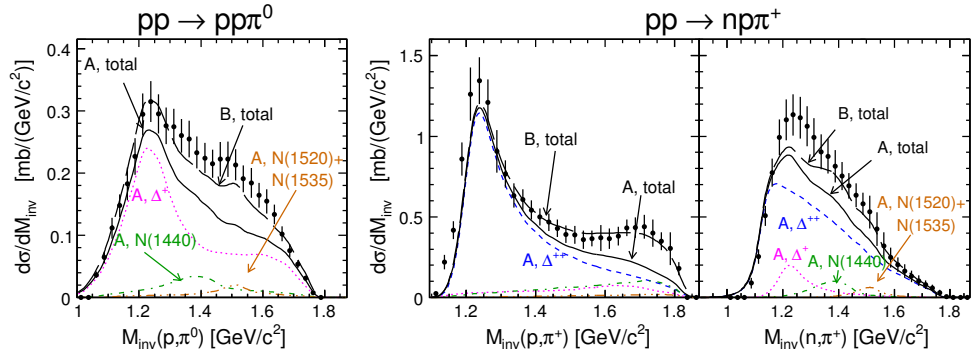

Figure 2.18: Two-particle invariant mass distributions: $p\pi^0$ (left panel) and $p\pi^+$, and $n\pi^+$ (right panel), within the HADES acceptance. The data points (efficiency corrected) are compared to the resonance model contribution (model A), with contributions of $\Delta^{++}(1232)$ (blue dashed curve), $\Delta^{+}(1232)$ (magenta dotted curve), $N(1440)$ (green dash-dotted curve), and the sum $N(1520)$ plus $N(1535)$ (brown solid curve). The long-dashed black curve, denoted as model B, results from the yield of N^* resonance adjustment and a small non-resonant admixture (not in the figure).

The modified resonance model was used to extrapolate the measured yield to the full solid angle. This was achieved by the calculation of the acceptance correction factors as a ratio of the number of events generated in the simulation (according to model B) to the number of events after filtering by the HADES geometrical acceptance and analysis cuts. The obtained cross sections are: $\sigma(pp \to np\pi^+) = 14.45 \pm 3.2$ mb, and $\sigma(pp \to pp\pi^0) = 4.15 \pm 0.85$ mb. The quoted systematic error is composed of the model dependence of the acceptance corrections, the normalization error, the efficiency corrections and event selection (mainly, geometrical cuts). The detailed discussion and numbers can be found in Ref. [HC12b]. The statistical errors are negligible. The comparison with the other experimental data from the resonance model fit is presented in Fig. 2.31 in Sect. 2.4.4, together with the results from pp collisions at 1.25 GeV and 3.5 GeV.

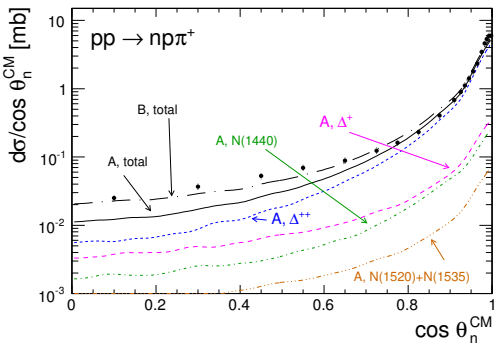

Figure 2.19: The angular distribution of neutron in c.m.s.. The data (black points) are acceptance corrected and compared to model A (solid curve) including Δ^{++} (blue dashed), Δ^{+} (magenta dotted), $N(1440)$ (green dash-dotted), $N(1520)$ and $N(1535)$ (brown dot-dot-dashed). The black dot-dashed curve shows the result of model B (see text for details).

2.3.3 ppη channel

The kinetic beam energy E = 2.2 GeV allows for the production of η–meson. The dominant decay mode is $\eta \to \pi^+\pi^-\pi^0$ with branching ratio 0.2292 ± 0.0028 [CC07], then dielectron Dalitz decay (see App. A.3.1), $\eta \to e^+e^-\gamma$ with BR = (6.9 ± 0.4) × 10^{-3} (see Sect. 4.5). The investigation of hadronic channel in HADES requires selection of events with two protons (pp), and one positive and one negative pion ($pp\pi^+\pi^-$). The correlation of observables, the missing mass $M_{miss}(p,p)$ and $M_{miss}(p,p,\pi^+,\pi^-)$ is displayed in Fig. 2.20, left panel. The concentration of events with a $pp\pi^+\pi^-$ missing mass slightly above zero is due to the $pp \to pp\pi^+\pi^-$ reaction. Another clear signal, selected with a rectangular cut, is due to $pp \to pp\eta$ signal.

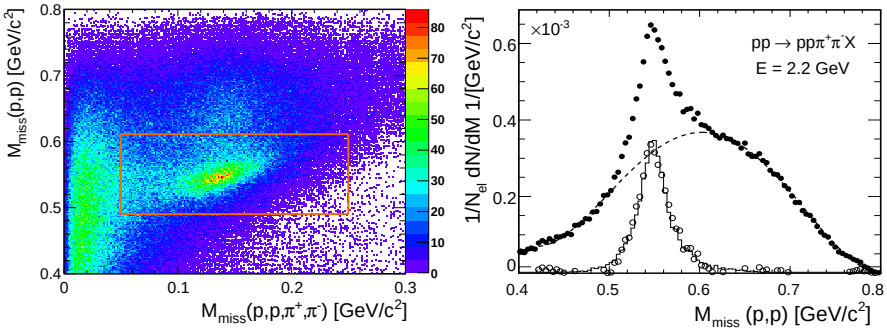

Figure 2.20: $pp \to pp\pi^+\pi^-$ reaction at 2.2 GeV. Left panel: The correlation between the two-proton missing mass ($M_{miss}(p,p)$) and the four-particle missing mass ($M_{miss}(p,p,\pi^+,\pi^-)$) is shown. The orange rectangle selects the region of the η peak, clearly visible for $M_{miss}(p,p)$ around the η mass and $M_{miss}(p,p,\pi^+,\pi^-)$ close to the π^0 mass. Right panel: Distribution of the two-proton missing mass ($M_{miss}(p,p)$) for the selected $pp\pi^+\pi^-$ events (left panel). The dashed curve shows the fit of the non resonant three-pion background. The empty circles result from the subtraction of this background and define the η signal. The full histogram (black solid) is the result of the simulation of the $pp \to pp\eta$ reaction.

The resulting $M_{miss}(p,p)$ spectrum, normalized to the pp elastic yield, is shown in Fig. 2.20, right panel. It shows a peak at the mass of the η–meson on top of a broad continuum, which is mainly due to the non-resonant $\pi^+\pi^-\pi^0$ production. Its contribution in the peak region was obtained from a polynomial fit of the data outside the peak region. The η signal was defined as the yield above this background, corresponding to about 24800 counts. The sensitivity to the background suppression was studied by varying the limits for the fit, resulting in a systematic error of ±4%.

The simulation of the η production is composed of a non-resonant and $N(1535)$ contribution (see Table 2.5), with the same proportion as in the analysis of the DISTO Collaboration [DC04], measured at similar beam energies. For both non-resonant and resonant contributions, the angular distribution was deduced from the DISTO data. The η production cross section, which was not measured in the DISTO experiment, is taken from the resonance model fit [Tei97]. The $N(1535) \to N\eta$ decay branching ratio is 0.42 ± 0.10 [PDG16]. The missing mass distribution obtained from the simulation of the $pp \to pp\eta$ channel is shown in Fig. 2.20 (right panel) as a full histogram. Its width depends only slightly on the ingredients of the model for the η production. The agreement of simulation and experimental signal confirms the consistency of the extracted η signal and the good description of the detector resolution in the simulation.

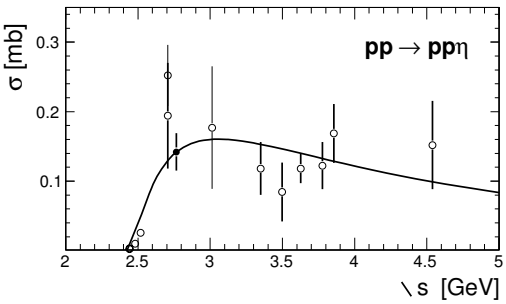

Figure 2.21: η cross section measured by HADES (full dot) for the $pp \to pp\eta$ reaction, followed by the $\eta \to \pi^+\pi^-\pi^0$ decay, compared to existing data (empty symbols) and Teis fit [Tei97] (solid curve).

The extraction of the η production cross section was performed in a similar way as described in Sect. 2.3.2. The model dependence was tested with the variation of the proportion of non-resonant and resonant contribution. The value $\sigma(pp \to pp\eta)$ = 0.142 ± 0.022 mb is compared with other data in Fig. 2.21. In this energy range only the two measurements from Ref. [Pic62b] existed. The value obtained in neutral channels σ = 0.197 ± 0.077 mb is, within the error, in agreement with the HADES value. The cross section obtained in the three-pion channel, 0.242 ± 0.042 mb, is above the HADES point. However, the error of the latter result might be underestimated, as discussed in Ref. [DC04]. The HADES measurement is in agreement with the resonance model [Tei97], where the η–meson production proceeds only via $N(1535)$ resonance decay. This assumption is in contradiction with the DISTO analysis [DC04]. The HADES measurement provides a constraint for various models of the η production.

2.3.4 Summary and conclusion

The HADES has provided a measurement of the reactions $pp \to pp\pi^0$, $pp \to np\pi^+$, and $pp \to pp\eta$ at 2.2 GeV. The exclusive hadronic channels were identified with high statistics and studied in various differential distributions. The comparisons to model predictions based on a resonance model [Tei97] were presented. The studies of the various contributions of the model, compared to the present data allow to determine resonance cross sections on one-pion and η production. Such constraints are important for modeling of dielectron sources (see Sect. 4.5). This approach, however, suffers from some uncertainties due to free parameters in the models, e.g. vertex functions, couplings strengths, and incoherent summation of the subsequent contributions. Despite it all, thanks to a good acceptance coverage, one-pion cross sections were extracted. Furthermore, determination of the exclusive η production cross section is important, as it provides the first precise measurement of the exclusive production cross section in this energy region.

2.4 Proton-proton collisions at T = 3.5 GeV

In the studies of one-pion production in pp reactions at 1.25 and 2.2 GeV it has been shown that the resonance model by Teis *et al.* [Tei96] describes the data well if the angular distributions of the dominant $\Delta(1232)$ are slightly modified with respect to the original OPE results [HC12b]. Even better description has been achieved in the description of pp data at 1.25 GeV, with the partial wave analysis [HC15a]. There are, however, also other prescriptions to parameterize resonance production amplitudes, e.g. the one used in the UrQMD transport model [Bas98]. In the course of the systematic baryon resonance production, the HADES Collaboration measured the pp collisions at the kinetic beam energy of 3.5 GeV ($\sqrt{s}$ = 3.18 GeV). In the experiment a proton beam with intensities of up to 10^7 particles/s was impinging on a 5 cm long liquid-hydrogen target (1% interaction probability). Similarly to measurements at lower energies, the analysis of the exclusive one-pion production channels, $pp \to pn\pi^+$, and $pp \to pp\pi^0$, was focused on baryon resonance excitation. The channels with pions were selected using events containing at least two tracks from positively charged particles. The subsequent final states were identified via cuts in one-dimensional missing mass distributions of $p\pi^+$ and pp systems, around the value of the not detected particle, neutron or π^0, respectively. The reaction cross sections were determined using the yield N_{el} of elastic proton-proton scattering measured simultaneously to the other reaction channels, the overall normalization error was estimated to be 8%.

Figure 2.22, left panel, displays the distribution of missing mass squared of the $p\pi^+$ pair with respect to the beam-target system, where the prominent peak centered around the nominal neutron mass (squared) is clearly visible. In order to extract the yield related to the $np\pi^+$ final state, the background under the peak had to be subtracted. For this purpose a fit function consisting of a polynomial (second and third order were considered) and two Gauss functions accounting for the background and the peak, respectively, were used to fit the experimental distributions. It has been checked that such a fit describes the missing mass distributions obtained from simulations (see below) and that the widths of both distributions agree very well. The signal yield was determined as the difference between the measured yield and the fitted background around the missing mass peak. Various background parametrizations and fit ranges were considered to evaluate the systematic error related to the extracted reaction yield. An example of such a fit for the $p\pi^+$ events is presented in Fig. 2.22, right panel, in the missing mass range used for the signal yield extraction. Typical systematic errors amount to 5 – 11%, depending on the particle momenta and background distributions. The same procedure was applied to determine the signal yield in each bin of various distributions presented below.

Figure 2.23, left panel, displays the square of the two-proton missing mass distribution for $2p$ events after rejection of the proton-proton elastic scattering events. The background on the right hand side of the π^0 mass is much higher (black dots) and not well separated from the dominant π^0 peak. The other two peaks visible on top of the continuum stemming from two-pion production, correspond to the mass squared of η and ω mesons, respectively. The shape of the two-pion contribution (dashed blue curve) was obtained from dedicated Monte Carlo simulations (see below), assuming uniform phase space population and with normalization to the measured yield. It was verified that details of the modeling of the two-pion production did not modify the shape of the background and led only to slight changes of its magnitude. In order to extract the signal yield related to the $pp\pi^0$ channel, first the two-pion contribution was subtracted

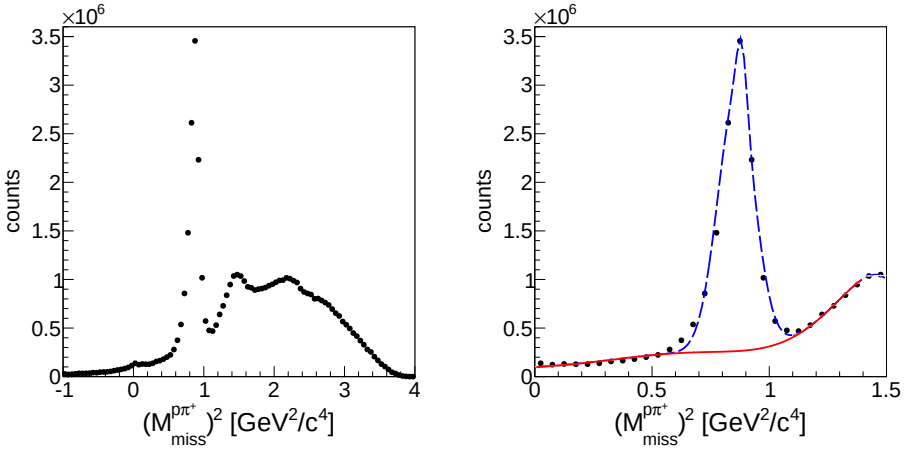

Figure 2.22: Left panel: missing mass squared of the $p\pi^+$ system with respect to the beam-target pp system. Right panel: an example of a fit within the squared missing mass window around the neutron peak at $(M^{p\pi^+}_{miss})^2$=0.88 GeV$^2/c^4$.

followed by a signal and background fit done in a similar way as in the $p\pi^+$ case. Finally, the yield of the $pp\pi^0$ final state was calculated in the window depicted in Fig. 2.23, right panel, as the difference between the measured yield and the fitted background. To correct for a small contribution from the η, the signal was calculated based on the left half of the π^0 peak position multiplied by factor 2. The same procedure was applied to extract the pion production yields as a function of other kinematical variables.

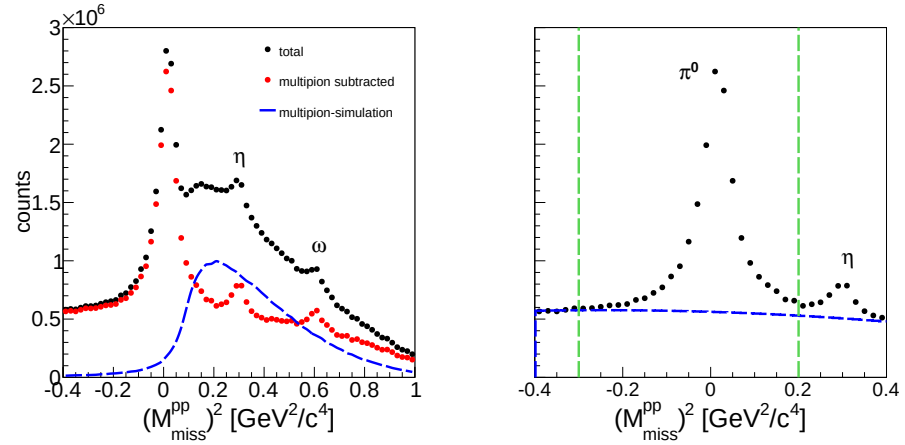

Figure 2.23: Left panel: missing mass squared of the pp system (black dots), simulated two-pion (blue curve) and the difference distributions (red points) after rejection of the elastic proton-proton scattering events. Right panel: an example of a fit to the subtracted spectrum in the squared missing mass window (limited by the vertical dashed lines) around the missing mass π^0 peak.

2.4.1 Baryon resonance cocktail in simulation

Simulations of pion and dielectron production in proton-proton collisions at kinetic energy of 3.5 GeV were performed by means of the PLUTO event generator [Frö07]. A resonance model, assuming that the pion production cross section is given by the incoherent sum of various baryon resonance contributions, was implemented. All four-star resonances, used by Teis *et al.* [Tei96] to fit the total one-pion and the η–meson production cross sections in the range $2.0 < \sqrt{s} < 5.0$ GeV, were included. The production amplitudes of the resonances extracted in Ref. [Tei96] are constant and depend neither on the beam energy nor on the resonance production angle, except for the $\Delta(1232)$ resonance for which a strong dependence on the four-momentum transfer from the incoming proton is included in accordance with the OPE results (see Ref. [Dmi86], Sect. 1.2.1). The model was, however, confronted only with data at lower energies [HC12b], where the $\Delta(1232)$ resonance is dominating. The most important extension in this analysis was the implementation of the dependence of resonance production on the production angle to all resonances, as described below. Furthermore, the resonance production cross sections were treated in simulations as free parameters but with fixed isospin relations between production cross sections for the $pn\pi^+$ and the $pp\pi^0$ final states in the respective $I = 3/2$ (Δ) and $I = 1/2$ (N^*) channels.

Table 2.6 summarizes the relevant resonance properties implemented in the simulations: the total decay widths (Γ), the branching ratios (BR) for $N\pi$ and, in addition, the pe^+e^- decays (the dielectron decays will be discussed in Sect. 4.9). For the resonances, the relativistic Breit-Wigner formula with mass dependent widths was used as in Ref. [Tei97]. The resonance widths and the $N\pi$ decay branches are adopted from resonance model, except for $N(1535)$, $\Delta(1910)$ and $\Delta(1950)$ the properties of which were taken from Ref. [PDG16], due to large differences with respect to more recent evaluations. Resonances of similar masses and the same isospin, $I = 3/2$ (Δ) or $I = 1/2$ (N^*), are grouped together in the table, since various resonances in the analysis are identified by means of the $N\pi$ invariant mass distributions only, hence the Δ^{++} and N^{*+} resonances can be observed as peaks in the $p\pi^+$ and the $n\pi^+$ invariant mass distributions. The resonances grouped together in Table 2.6 cannot be isolated by means of the respective $N\pi$ invariant mass distributions because they overlap. In such cases the resonances (printed in bold style) with the largest decay branches to the nucleon-pion and to the proton-dielectron final states were selected.

2.4.2 Baryon resonance angular distributions

Modeling of the angular resonance production is of utmost importance in the case of the spectrometer with the limited acceptance. The anisotropic emission in the proton-proton center-of-mass frame, depending on the four-momentum transfer $t = (p_1 - p_R)^2$, was calculated between the four-momentum vectors of the outgoing resonance (p_R) and the incoming nucleon (p_1):

$$d\sigma_R/dt \sim A/t^{\alpha} \tag{2.9}$$

where A and $\alpha(M)$ are constants to be derived from the comparison to the data, and M is the respective Breit-Wigner resonance mass. In the calculation of the momentum transfer, the following convention was used for the definition of the incoming proton p_1: if the resonance is emitted forward in the c.m.s., p_1 denotes the projectile, otherwise the target proton. The choice of such a parametrization was motivated by the experimental results on the resonance angular distributions from earlier proton-proton experiments [Col71], where a strong forward-backward peaking of the resonance production was

observed. Moreover, it was found that the anisotropy of the distribution decreases with increasing resonance mass. Such a behavior is expected for peripheral reactions, where the production of heavier resonances requires a larger four-momentum transfer and, consequently, a flattening of the angular distributions. The respective α dependency on M has to be, however, found from a comparison to the data.

J^P	Resonances	Γ_R $[MeV]$	$BR(N\pi)$	$BR(pe^+e^-)$
$3/2^+$	**Δ(1232)**	120	1	4.2e-5
$1/2^+$	**N(1440)**	350	0.65	3.06e-6
$3/2^-$	**N(1520)**	120	0.55	3.72e-5
$1/2^-$	**N(1535)**	150	0.46	1.45e-5
$3/2^+$	$\Delta(1600)$	350	0.15	0.73e-6
$1/2^-$	**Δ(1620)**	150	0.25	1.73e-6
$1/2^-$	$N(1650)$	150	0.8	8.03e-6
$5/2^-$	$N(1675)$	150	0.45	1.02e-6
$5/2^+$	**N(1680)**	130	0.65	1.97e-5
$3/2^+$	$N(1720)$	150	0.2	3.65e-6
$3/2^-$	**Δ**(1700)	300	0.15	1.38e-5
$5/2^+$	$\Delta(1905)$	350	0.15	1.46e-6
$1/2^+$	**Δ(1910)**	280	0.25	0.73e-5
$7/2^+$	$\Delta(1950)$	285	0.4	3.06e-6

Table 2.6: List of resonances and their properties included in the simulations. Some groups of resonances cannot be separated in data. In such a case the resonance with the largest coupling to pion and dielectron channels (printed in bold) is used in simulations. See the text for details.

The decay angular distributions $R \to N\pi$ of all resonances, except $\Delta(1232)$, have been assumed isotropic, since little is known on the alignment of resonances after production. The $\Delta(1232)$ decay has been modeled proportional to $1 + 3cos^2(\theta)$, where θ is the angle of the pion (or nucleon) in the Δ rest frame with respect to the beam axis. Such a parametrization is predicted by the OPE model (see Sect. 1.2.3) and also corroborated by the experimental data [And94].

2.4.3 npπ^+ and ppπ^0 final states

In order to evaluate the resonance cocktail, various differential distributions for the $np\pi^+$ and the $pp\pi^0$ final states need to be compared with Monte Carlo simulations within the HADES acceptance. Since the HADES acceptance is not complete, all acceptance corrections can be performed only by means of a model, and a detailed comparison of such a model with the data is a mandatory.

To begin with, the $pp \to pn\pi^+$ reaction channel allows for a separation of the double (Δ^{++}) and the single charged resonances (Δ^+, N^{*+}) by an analysis of the $p\pi^+$ and the $n\pi^+$ invariant mass distributions, respectively. Figure 2.24 shows the data overlayed with the result of the simulation assuming contributions from the resonances listed in Table 2.6. The data points are normalized to the elastic scattering yields (N_{el}) and are displayed together with the errors stemming from the background subtraction procedure (statistic errors are negligible). The normalization error is not included.

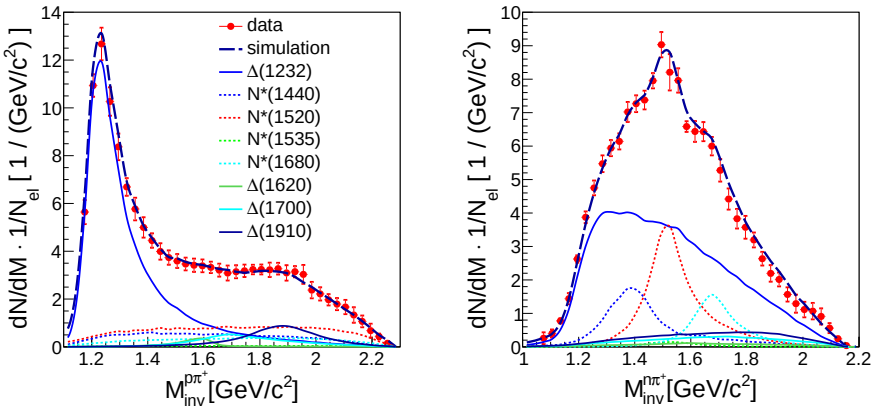

Figure 2.24: $np\pi^+$ final state: $p\pi^+$ (left panel) and $n\pi^+$ (right panel) invariant mass distributions compared to the result of simulations (dashed curves) assuming an incoherent sum of the resonance contributions shown by separate curves, as indicated in the legend. The data are normalized to the proton-proton scattering yield N_{el} measured within the HADES acceptance. Indicated error bars are dominated by the systematic errors related to the signal extraction, the constant normalization error (8%) is not included. Normalization to the bin width is applied.

Since the resonance line shapes are fixed in the simulations, the only free parameters, to be found by a comparison to the data, are the resonance production yields and the angular distributions, given by Eq. 2.9. The yields were obtained from simultaneous fits to the invariant mass and the four-momentum transfer distributions using an iterative procedure. In the first step the $\Delta(1232)^{++}$ resonance, dominating the $p\pi^+$ invariant mass distribution, was considered. In order to extract the slope parameter $\alpha(M)$ for the $\Delta(1232)$, the acceptance and efficiency corrected distribution of the $p\pi^+$ yield as a function of t for the events with an invariant mass window centered around the resonance pole were plotted, as shown in Fig. 2.25, left panel. The experimental distribution was fitted with a function given by Eq. 2.9, and the constants $A(M)$, $\alpha(M)$ were determined. In the next step, the obtained $\Delta(1232)^{++}$ and $\Delta(1232)^{+}$ contributions were subtracted and the same procedure was performed for the $n\pi^+$ events in the region of the $N(1440)$ resonance, selected by the respective cut on the invariant mass. The yield of the Δ^+ was calculated using the isospin relation, $\sigma_{\Delta^{++}\to p\pi^+} = 9\sigma_{\Delta^{+}\to n\pi^+}$. The sum of both Δ contributions produces a broad smooth distribution in the $n\pi^+$ invariant mass spectrum, as it can be seen in Fig. 2.24, right panel. On the other hand, the N^* contributions in the $p\pi^+$ invariant mass under the $\Delta(1232)$ peak are very small and influence the fit of the Δ^{++} angular distribution only marginally.

The contributions of higher mass resonances $N(1520)^+$, $N(1680)^+$ and $\Delta(1910)^+$ were extracted in the similar steps. Figure 2.25, left panel, shows the acceptance and efficiency corrected t distributions for the three proton (neutron)-pion mass regions together with the fits and the dependence of the α parameter (middle panel) on the resonance mass extracted from the data. The points with the errors (red) correspond to all investigated resonances, while the points without errors (blue) indicate the values of α deduced from the fit which are used for the other resonances. The observed decrease of α with the resonance mass is equivalent to the flattening of the angular distributions. The angular distribution of the $\Delta(1232)$ production, obtained from the fit, agrees quite well with the one obtained from the OPE model of Dmitriev *et al.* [Dmi86].

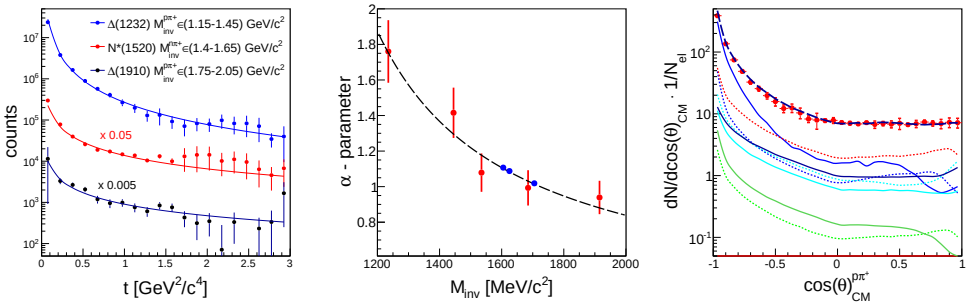

Figure 2.25: $np\pi^+$ final state: Left panel: Acceptance and efficiency corrected distributions of $p\pi^+$ and $n\pi^+$ yield as a function of the four-momentum transfer t compared to fits (solid curves) for the three indicated mass regions. Data from the high mass region are scaled, as indicated, for better visualization. Middle panel: Dependency of the constant α from Eq. 2.9 on the resonance mass, obtained from fits to the data (points with errors). The points without errors are the α values deduced from the fit shown by the dashed curve and used in simulations. Right panel: Center-of-mass (CM) distribution of the $p\pi^+$ system within the HADES acceptance, decomposed into various resonance contributions (same legend as in Fig. 2.24), using the t dependence of the resonance production presented in the middle panel.

The consistency of the procedure was verified by a simulation with all components included, according to the derived cross sections and the resonance angular distributions. The acceptance correction of the t distributions has been repeated with the improved model and new α parameters were determined. The second iteration changed only marginally the fit parameters. The final decomposition of the simulated $p\pi^+$ yield as a function of $cos(\theta_{CM}^{p\pi^+})$ into individual contributions from the resonances is displayed, within the HADES acceptance, in Fig. 2.25, right panel. The asymmetric shape of the angular distribution is due to the acceptance favoring the detection of $p\pi^+$ pairs emitted in the c.m.s. in backward direction (or, equivalently, $n\pi^+$ pairs in forward direction). The HADES acceptance and reconstruction efficiency increase as a function of the resonance mass from 6% to 15%.

Finally, the extracted resonance yields and the angular distributions were included in the simulation of the $pp \to pp\pi^0$ reaction channel. The cross sections for the $pn\pi^+$ and $pp\pi^0$ final states are fixed by their isospin relations. A very good agreement between simulation and the data was also achieved for this reaction channel. Figure 2.26 presents a comparison of the $p\pi^0$ invariant mass and the c.m.s. angle distributions of the $p\pi^0$ system, obtained in the experiment and in the simulation. Since the two final-state protons are indistinguishable, both combinations of protons with a neutral pion were included in the presented distributions (each with a weight 0.5). Contrary to the $np\pi^+$ final state, the intensity of the $\Delta(1232)$ resonance is reduced and the contributions of higher mass resonances are more pronounced. The distributions are strongly affected by the HADES acceptance which is smaller by a factor 2–3, depending on the $p\pi^0$ mass, as compared to the acceptance for the $np\pi^+$ final state. In the angular distributions for the two reaction channels (right panels of Figs. 2.25 and 2.26), a clear cut-off is visible in the $p\pi^0$ case. While the acceptance for the $np\pi^+$ channel is large for the backward emitted $p\pi^+$ pairs, the acceptance for the $pp\pi^0$ is strongly reduced in this region. Consequently, $p\pi^0$ events from reactions characterized by small momentum transfer are suppressed with respect to the $p\pi^+$ case.

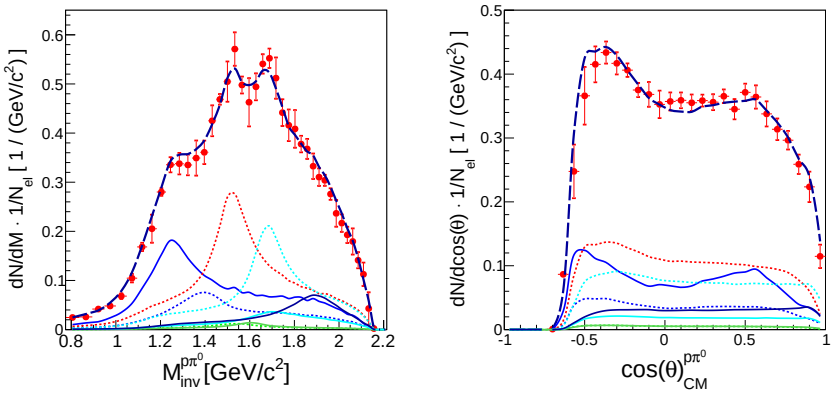

Figure 2.26: $pp\pi^0$ final state: $p\pi^0$ invariant mass distribution (left panel) and the CM angular distributions (right panel) compared to the result of the simulation (line style as in Fig. 2.24, normalization to the bin width is applied).

To perform more detailed comparisons between the data and the adjusted resonance model, the angular distributions defined in the Gottfried-Jackson (GJ) and the helicity (H) reference frames were studied (see App. C.3.5.3 for definition). Figure 2.27 displays the angular distributions for the $np\pi^+$ final state in the GJ reference frame and in the H reference frame. Although they are strongly affected by the HADES acceptance, they still reveal interesting features related to resonance production. The helicity distributions are connected to the invariant mass distributions and exhibit structures related to the contributions of individual resonances. As expected, the $n\pi^+$ helicity frame allows to reveal the $p\pi^+$ states. In the case of $p\pi^+$ helicity frame, the resonant states deriving from the single charge states, are covered by the decay pattern of the Δ^{++} resonances.

The angular distributions of nucleons calculated in the GJ frame display a strong forward-backward peaking. The angle $\theta^{\pi^+}_{p\pi^+}$ in the GJ frame describes the decay angle of the double-charged Δ^{++} and should be sensitive to the expected anisotropy of the $\Delta(1232)$ decay. Indeed, the data seem to follow the trend expected for the $\Delta(1232)$ but are not perfectly described by the simulation. This might be a consequence of the isotropically modeled decays of the other resonances. However, only a small sensitivity to modeling of these distributions within the HADES acceptance was determined.

Figure 2.28 displays the angular distributions in the GJ and H reference frames for the $pp\pi^0$ final state. Since the final state includes two indistinguishable protons, only four distributions are presented. The two distributions, including two protons, were averaged, as explained above. For the $pp\pi^0$ reaction, even a better description of the data by the adjusted model has been achieved. It is interesting to note that the GJ distribution for the $p\pi^0$ system, which is dominated by the N^* contributions (particularly $N(1520)$), is well described by simulation, hence corroborating the assumption of an isotropic resonance decay.

2.4.4 Baryon resonance cross sections

Based on the studies presented in the previous section, the modified resonance model within the HADES acceptance reproduces the data satisfactorily. Therefore the simulation can be used to correct the data for losses due to limited acceptance and inefficiencies of the detection and the reconstruction processes. Acceptance corrected distributions can then be compared to other reaction models than those used

in the simulation. The correction factors were calculated from the simulations as the ratio between the generated and the accepted and reconstructed distributions as one-dimensional functions for all studied kinematical variables separately (i.e the invariant masses and the various angular projections).

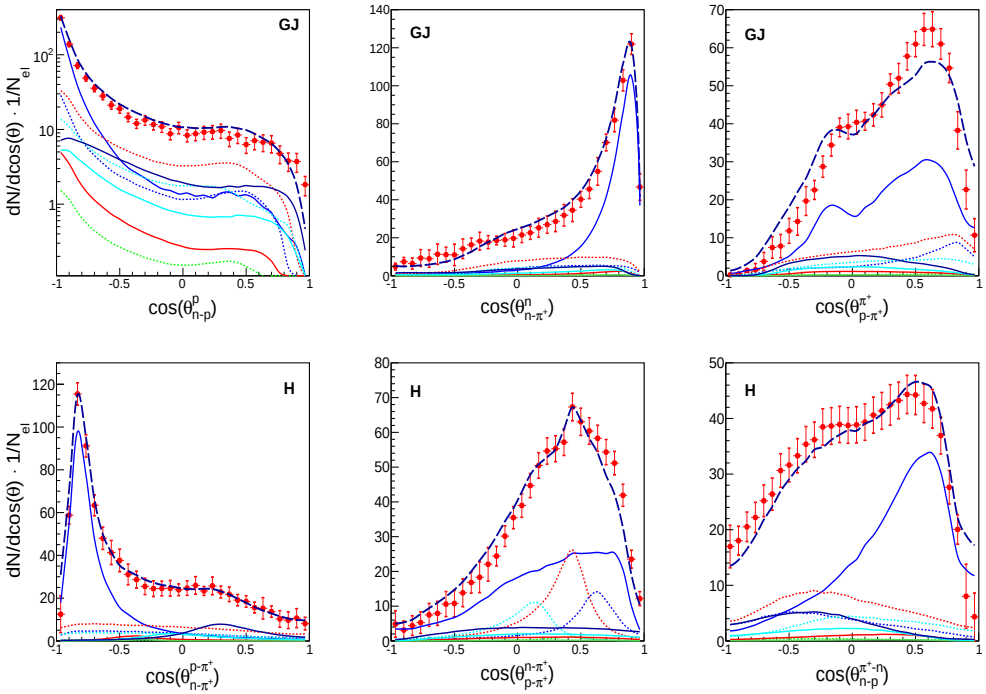

Figure 2.27: Angular distributions in the Gottfried-Jackson reference frame (top row) for the $np\pi^+$ final state compared to the results of simulations (dashed curve) decomposed into contributions of various resonances and in the helicity (bottom row) reference frame. For the legend, see Fig. 2.24.

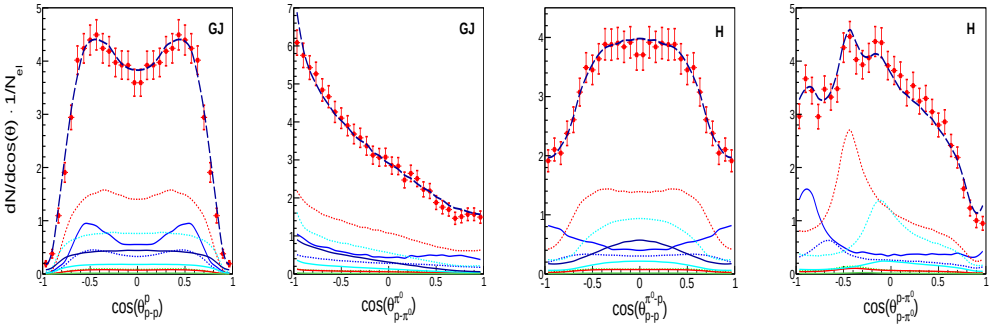

Figure 2.28: Angular distributions in the Gottfried-Jackson (GJ) and the helicity (H) reference frames for the $pp\pi^0$ final state compared to the results of simulations (dashed curves) decomposed into contributions of various resonances. Line style as in Fig. 2.24.

Figure 2.29 displays the acceptance and efficiency corrected charged pion differential cross sections as a function of the $p\pi^+$ and the $n\pi^+$ invariant masses for the $np\pi^+$ final state. The distributions are overlayed with the simulation decomposed into contributions of the Δ and the N^* resonances (see legend as in Fig. 2.24). One can notice, by comparing to the respective uncorrected distributions shown in Fig. 2.24, that the corrections enhance the low-mass $\Delta(1232)$ region for the $p\pi^+$ and $n\pi^+$ systems and the high-mass region ($M_{n\pi^+} > 1.9\ GeV/c^2$) for the $n\pi^+$ system. The marked feature of the $p\pi^+$ system is, as already observed in the uncorrected spectra, a dominant $\Delta(1232)^{++}$ contribution and a slight enhancement around $M_{p\pi^+} = 1.9$ GeV/c^2, which may indicate contributions from the higher mass Δ states. The line shape of the $\Delta(1232)^{++}$, which dominates the $p\pi^+$ invariant mass distribution up to 1.6 GeV/c^2, is perfectly described by the simulation. This observation is important in view of the various parameterizations of the resonance spectral function used in transport models which substantially differ at high Δ masses, as discussed in Ref. [Bra13]. The HADES fit supports a parametrization of the total width based on the Moniz model (Ref. [Koc84], and Eq. 1.8 in Sect. 1.1) which strongly suppresses the high-mass tail of the resonance.

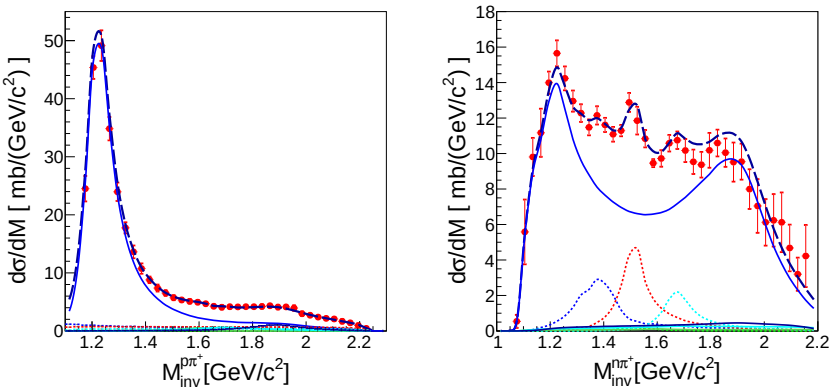

Figure 2.29: $np\pi^+$ final state: Acceptance corrected $p\pi^+$ (left panel) and $n\pi^+$ (right panel) invariant mass distributions compared to the simulation result (dashed curves). Resonance contributions are shown separately (legend as in Fig. 2.24).

The $n\pi^+$ invariant mass distribution reveals also contributions of the single-charged resonances: $\Delta(1232)^+$, $N(1440)$, $N(1520)$ and $N(1680)$. This region is, however, dominated by $n\pi^+$ pairs from the $\Delta(1232)^{++}n \to p\pi^+n$ final state and is characterized by a continuous invariant mass distribution with an enhancement around 1.9 GeV/c^2. It is interesting to note that the enhancement is due to the assumed anisotropy of the $\Delta(1232)^{++}$ decay $1 + 3cos^2(\theta)$ which is also corroborated by the angular distributions obtained in the GJ frame (see Fig. 2.27). The $\Delta(1232)$ contribution shown in Fig. 2.29 presents the sum of $\Delta(1232)^{++}$ and $\Delta(1232)^+$, where the latter resonance peaks approximately at the pole position. It is particularly important to note the strong contributions of the $N(1520)$ and $N(1680)$ resonances which are relevant for dielectron production because of their relatively large Dalitz decay branching ratios (see Table 2.6).

The acceptance corrected invariant mass distributions for $pp\pi^0$ final states are shown in Fig. 2.30 together with the simulation results. In contrast to the $np\pi^+$ reaction channel, the $pp\pi^0$ final state is sensitive only to the contributions of single-charged resonances, hence the very strong signal from the double-charged $\Delta(1232)^{++}$ is absent and other resonances are more prominent. On the other hand, a disadvantage of this

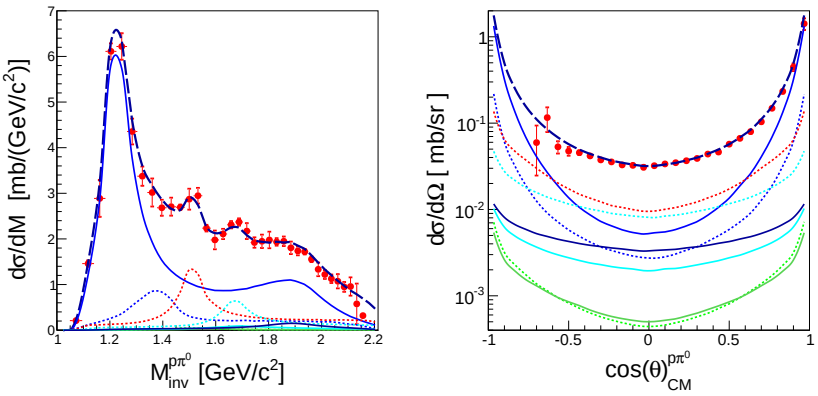

Figure 2.30: $pp\pi^0$ final state: Acceptance corrected $p\pi^0$ invariant mass (left panel) and the CM angular distributions (right panel) compared to the simulation result (dashed curves). Resonance contributions are shown separately (legend as in Fig. 2.24).

channel is that the final state of two protons does not allow for a unique reconstruction of the resonance mass and leads to a slight spectral distortion due to averaging between two possible pion-proton combinations. Nevertheless, the enhancements around $N(1520)$ and $N(1680)$ are also clearly visible, as it is the case in the $pp \to np\pi^+$ reaction channel. Figure 2.30, right panel, shows the differential cross section as a function of the CM angle of the proton-pion system in comparison to the model calculations. The expected strong anisotropy, decreasing with increasing resonance mass of the $p\pi^0$ production, is clearly visible (see the components). The lack of data points below $cos(\theta_{CM}^{p\pi^0}) < -0.6$ reflects the acceptance losses in the HADES spectrometer.

The total cross sections for the $pp\pi^0$ and the $np\pi^+$ final states can be calculated from the acceptance corrected spectra. They have been obtained as an average of the integrated differential cross sections expressed as a function of the pion-nucleon invariant mass and various angles presented above. The respective cross sections amount to $\sigma_{pp\pi^0} = 2.50 \pm 0.23\ (syst.) \pm 0.2\ (norm.)$ mb and $\sigma_{np\pi^+} = 10.69 \pm 1.2\ (syst.) \pm 0.85\ (norm.)$ mb, the statistical errors are negligible. The systematic errors were estimated from the differences between the integrated differential cross sections obtained after the respective acceptance corrections on the above mentioned distributions.

The $pp\pi^0$ distributions are particularly interesting since they provide a direct input to calculations of the resonance conversion $R \to pe^+e^-$. However, as discussed above, in the simulation a subset of resonances was used because the overlapping states in the pion-nucleon invariant mass distributions could not be separated. Nevertheless, using the resonance model ansatz it is possible to extract the upper limits on contributions from other possible resonances within the given groups in Table 2.6 and calculate the respective uncertainty of the dielectron yield. For this purpose, the simulations substituting the selected resonance with other resonances belonging to the same group (see Table 2.6) were done, keeping the other components in the simulations unchanged. The obtained cross sections are listed in the second column of Table 2.7. The errors in the determination of the cross section for production of resonances were estimated for each resonance separately from the pion-nucleon invariant mass distributions by altering the respective yield within the experimental error bars but with all other components fixed. The relative errors for some resonances are quite large due to their small contribution to the pion production, leading to a limited sensitivity.

Resonances	σ_R	$\sigma_R^{Teis}(\sigma_R^{GiBUU})$	σ_R^{UrQMD}
$\Delta(1232)$	2.53 ± 0.31	2.0 (2.2)	1.7
N(1440)	1.50 ± 0.37	0.83 (3.63)	1.15
N(1520)	1.8 ± 0.3	0.22 (0.27)	1.7
N(1535)	0.152 ± 0.015	0.53 (0.53)	0.8
$\Delta(1600)$	$< 0.24 \pm 0.10$	0.70 (0.14)	0.4
$\Delta(1620)$	$< 0.10 \pm 0.03$	0.60 (0.10)	0.2
$N(1650)$	$< 0.81 \pm 0.13$	0.23 (0.24)	0.4
$N(1675)$	$< 1.65 \pm 0.27$	2.26 (0.94)	1.2
N(1680)	$< 0.90 \pm 0.15$	0.21 (0.22)	1.2
$N(1720)$	$< 4.41 \pm 0.72$	0.15 (0.14)	0.68
$\Delta(1700)$	0.45 ± 0.16	0.10 (0.06)	0.35
$\Delta(1905)$	$< 0.85 \pm 0.53$	0.10 (0.06)	0.25
$\Delta(1910)$	$< 0.38 \pm 0.11$	0.71 (0.14)	0.08
$\Delta(1950)$	$< 0.10 \pm 0.06$	0.08 (0.10)	0.25

Table 2.7: Cross sections in units of *mb* for the single positively charged resonances extracted from the HADES data (second column), the Teis *et al.* model [Tei96] (third column) and used in the GiBUU [Bus12,Wei12] (number in brackets in the third column) or the UrQMD [Bas98] (fourth column).

The last two columns in Table 2.7 present the resonance cross sections from the model of [Tei97], and the modified values used in the GiBUU code [Bus12,Wei12] (values in brackets), as well as the values used in the UrQMD [Bas98] code. Figure 2.31 shows the total one-pion exclusive cross sections as a function of $\sqrt{s}$, separated into contributions of the $\Delta(1232)$, the higher mass Δ (I = 3/2) and the N^* (I = 1/2) resonances in comparison to the parametrization of Ref. [Tei97]. The HADES results are marked as red symbols with error bars. The total pion production cross sections are equal to the sum of the resonance contributions listed in Table 2.7. For the isospin decomposition the cross sections of the selected resonances indicated in bold were selected. Although the identification of resonances is ambiguous in the nucleon-pion invariant mass region of overlapping states, the decomposition is still feasible. It is performed by a comparison of the corresponding yields in the $n\pi^+$ and $p\pi^+$ invariant mass distributions for the N^* and Δ resonances and is given as the product of the resonance cross section and the respective branching ratio. The comparison (see extracted values in the second column of Table 2.7) shows a qualitative agreement with the decomposition in Ref. [Tei97] (third column). The differences are discussed below.

The $\Delta(1232)^+$ cross section obtained in the present analysis is slightly higher than that of Ref. [Tei97] and is closer to the cross section value used in GiBUU [Bus12]. The total contribution of higher mass Δ, with masses around $M_\Delta \sim 1620$ MeV/c^2 and $M_\Delta \sim 1910$ MeV/c^2, is clearly larger in the fit [Tei97] as compared to the HADES results. One can hence conclude that the reduction of the respective cross sections applied in the GiBUU version [Bus12] are in line with the result of this analysis. One can also notice that the cross sections for the higher mass Δ resonances are by a factor 2 – 3 larger in the UrQMD code [Bas98] as compared to the GiBUU [Bus12], but lower for the $\Delta(1232)$.

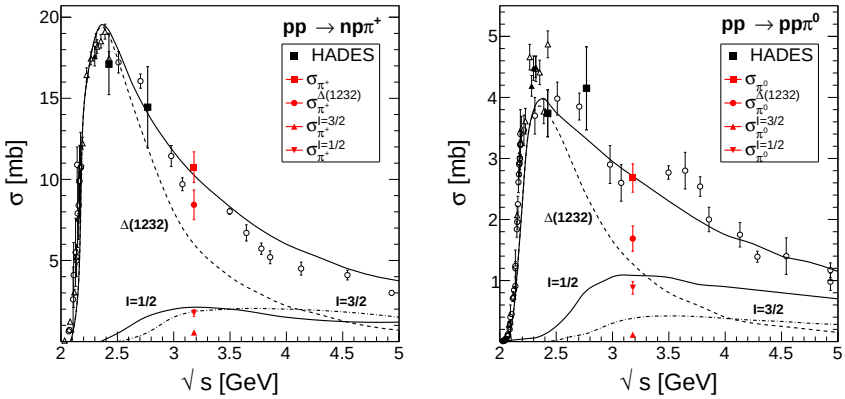

Figure 2.31: One-pion (left: charged, right: neutral) exclusive cross sections as a function of the total c.m.s. energy $\sqrt{s}$ separated into contributions of the $\Delta(1232)$, the higher mass $I = 3/2$ (Δ) and the $I = 1/2$ (N^*) resonances in comparison to the parametrization from Ref. [Tei97] and experimental data. The data compilation is taken from Ref. [Tei97]. The HADES results at $\sqrt{s} = 3.18$ GeV are depicted as full symbols (including black squares from the measuremets at lower energies [HC12b, HC15a]).

For the N^* resonances, a direct comparison of the $N(1520)$, $N(1535)$, and $N(1440)$ cross sections can be done. The HADES cross sections are closer to the values used in UrQMD [Bas98], except for $N(1535)$ which appears to be much larger in all models. As explained above, the HADES cross section for $N(1535)$ was fixed by the data on η production. Although in Ref. [Bus12] the sum of the cross sections for all N^* resonances is similar to the model [Tei97], the relative partition is different, giving the largest weight to the $N(1440)$ and a smaller one to the $N(1675)$. One should also notice that the cross sections for $N(1720)$ and $N(1680)$ used in Ref. [Bas98] are also much higher by a factor of about 5 – 6 than the ones used in Ref. [Bus12]. These cross sections, together with the cross section for the $N(1520)$, $\Delta(1620)$ and $\Delta(1905)$ resonances play a major role for dielectron production because of their large $p\rho$ branching ratios.

The aforementioned features are visible in a comparison to the $np\pi^+$ differential cross sections plotted as a function of the nucleon-pion invariant mass (Fig. 2.32). The $p\pi^+$ invariant mass distribution is better described by simulations based on the cross sections used in Ref. [Bus12] (dashed histogram, denoted as *model*1). The parametrization used in Ref. [Bas98] (dotted histogram, denoted as *model*2) underestimates the $\Delta(1232)$ production, but overestimates the production of higher mass Δ states. On the other hand, the $n\pi^+$ invariant mass distribution, reflecting enhancements mainly due to the N^* resonances, clearly shows that the strong $N(1440)$ production implemented in *model*1 is not supported by the HADES data. There is also missing intensity around $N(1520)$ which could be explained by a larger resonance cross section, as deduced from the present fit. Indeed, by taking the cross sections for both resonances and $N(1535)$ from the HADES fit and leaving all the others without any change, one can reproduce the result shown in Fig. 2.29.

The comparison of the $n\pi^+$ invariant mass distribution to the calculations using the parametrization of resonance cross sections applied in *model*2 shows a clear overshoot in the mass region around $N(1680)$ / $N(1675)$, indicating too strong contributions from these resonances. On the other hand, the undershoot at low invariant masses is related to a too small $\Delta(1232)^{++}$ cross section.

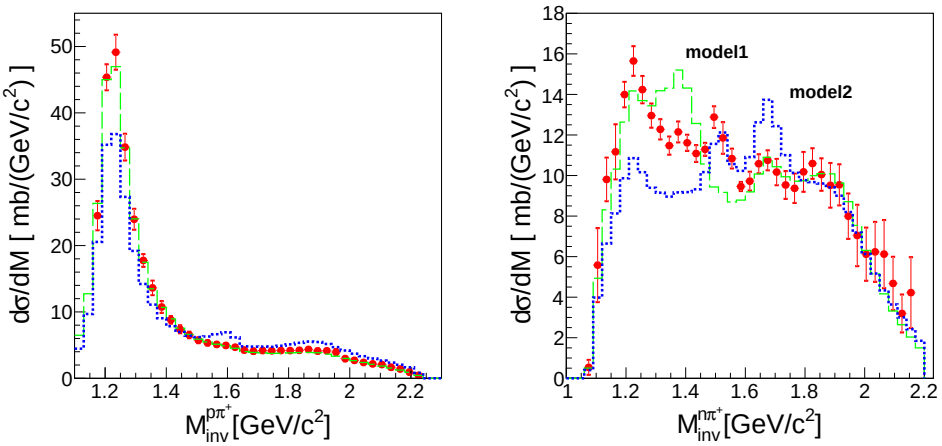

Figure 2.32: $np\pi^+$ final state: Acceptance corrected $p\pi^+$ (left panel) and $n\pi^+$ (right panel) invariant mass distributions (symbols with error bars) compared to the simulation results using the resonance cross sections according to parametrizations taken from Ref. [Bus12] (dashed green line histogram - *model*1) or from Ref. [Bas98] (dotted blue line histogram - *model*2).

2.4.5 Summary and conclusions

A combined analysis of one-pion exclusive channels $pp\pi^0$, $pn\pi^+$ in pp collisions, using a beam with a kinetic energy of 3.5 GeV ($\sqrt{s}$ = 3.18 GeV), was performed. It allowed for the estimation of Δ and N^* resonance production cross sections by means of a resonance model. Empirical angular distributions derivation for the production of resonances showed a strong forward-backward peaking which is characteristic for peripheral reactions. A good description of the experimental data in the detector acceptance was achieved allowing for an extrapolation to the full solid angle and an extraction of the pion and, to some extent, resonance production cross sections. Although the applied model assumes a simplified reaction mechanism, ignoring interferences between various intermediate states, it describes the data in various observables surprisingly well. Further studies, by means of the partial wave analysis, are on the way, in order to estimate the interference effect and to study resonance production in more detail. Nevertheless, the obtained results are very useful for a comparison of various parametrizations of the production of resonances used in the modern transport codes, as shown for the GiBUU and UrQMD codes.

Chapter 3

Dilepton probes

The dilepton (lepton pairs: $l^+l^- = e^+e^-, \mu^+\mu^-$) production takes place during the whole space-time evolution of the colliding particles and processes involved depend both on the system and the energy. Dileptons are coupled to the electromagnetic current of hadrons through intermediate virtual photons. Once the lepton pair is produced, it decouples from the strongly interacting medium and carries information about the production process undisturbed to the detectors. The virtual photon, reconstructed from the momenta of the two identified, correlated leptons, is characterized by four independent coordinates of its four-momentum. The final experimental observables are typically the invariant mass (Fig. 3.1), the transverse momentum, the rapidity, and angular projections. Generally, dilepton production in heavy-ion collisions can be divided into a few chronological stages. Before the interaction between nuclei happens, their movement is decelerated first in their Coulomb field and dileptons are produced by a coherent bremsstrahlung, however this contribution is usually small. In the first stage of the overlapping nuclei, within the time span of $1-2$ fm/c, the system is far from equilibrium and dileptons are produced in hard processes, i.e. Drell-Yan annihilation or quark-gluon Compton scattering. They contribute at large invariant mass, $M_{ll} \geq 3$ GeV/c^2. The next stage may reach the quark-gluon plasma (QGP) phase where quark-antiquark annihilation contributes to the dilepton production. The expanding system cools down and the nuclear matter undergoes the hadronization process. The main dilepton sources are then the pion and kaon annihilations and hadronic collisions. Light vector mesons, ρ, ω and ϕ, are produced and decay directly into a dilepton channel. The l^+l^- invariant mass can carry out the information about vector mesons inside hot and dense nuclear matter. The heavy quarkonium states, e.g. J/ψ or Υ, can also decay to dilepton pairs but after the freezout phase, due to their long lifetime. The intermediate mass $1 \leq M_{ll} \leq 3$ GeV/c^2 is populated mostly by charmed meson pairs $D\bar{D}$ and partly by Drell-Yan process. The main source of the l^+l^- pairs in the low invariant mass region, below $\phi(1020)$ meson, are the decays of objects built out of light quarks u, d, s, e.g. baryon and meson resonances.

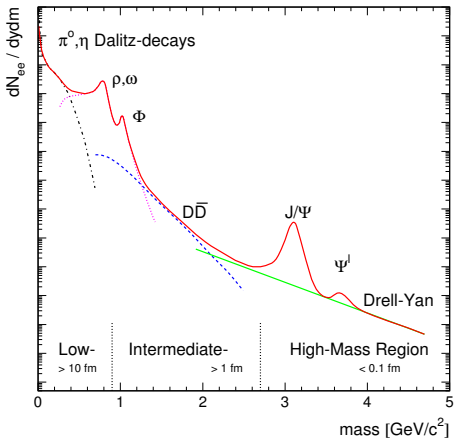

Figure 3.1: Dilepton pair sources as a function of l^+l^- invariant mass in ultra-relativistic nuclear collisions [Rap00].

3.1 Decays to dilepton channels

In the 1 – 2 GeV/nucleon energy range, accessible by the HADES experiment at SIS accelerator (see Ref. [HC09]), the dielectron sources (e^+e^-) can be characterized by the following decay processes:

- direct two-body decays (App. A.2)
  - $V \to e^+e^-$, where $V = \rho^0, \omega, \phi$
  - $P \to e^+e^-$, where $P = \pi^0, \eta$ (rare processes)
- meson Dalitz decays (App. A.3)
  - $V \to \pi^0 / \eta\, e^+e^-$, where $V = \omega\ /\ \phi$
  - $P \to \gamma e^+e^-$, where $P = \pi^0, \eta, \eta'$
- baryon resonance Dalitz decays (Sect. 3.4)
  - $\Delta(N^*) \to N e^+e^-$
- NN bremsstrahlung (Sect. 3.5)
  - $NN \to NN e^+e^-$

3.2 Electromagnetic structure of baryon resonances

The electromagnetic structure of baryon transitions is encoded by a set of electromagnetic transition form factors (eTFF), depending on the resonance isospin, spin, parity and the four-momentum transfer squared (q^2) of the virtual photon. It can be probed in the two kinematical regimes defined by the sign of $q^2 = M^2_{\gamma^*}$ (Fig. 3.2). They are either $q^2 < 0$ (spacelike), probed in electro-production experiments or $q^2 = M^2_{inv}(e^+e^-) > 0$ (timelike), probed in annihilation experiments. The timelike electromagnetic structure of baryonic transitions can be also directly studied in low-energy NN and πN collisions at 1 – 2 GeV energies via resonance ($R = N^*, \Delta$) Dalitz decays, $R \to N\gamma^* \to N e^+e^-$. They give a unique insight into the timelike region at small positive four-momentum transfer squared ($0 < q^2 < (M_R - M_N)^2$, where M_R and M_N are resonance and nucleon masses, respectively), which is best suited to study the coupling to vector mesons. The real photon experiments (with unpolarized, circularly or linearly polarized beam) settle the boundary point at $q^2 = 0$.

The $\Delta(1232)$ resonance is the first excited state of the nucleon which dominates pion production in NN reactions for $\sqrt{s} < 2.6$ GeV/c^2. Despite its relatively large width (117 MeV) it is quite well isolated from higher lying resonances. The total width Γ can be decomposed into the sum of contributions from the independent decay channels:

$$\Gamma(m) = \Gamma_{\pi N} + \Gamma_{\gamma N} + \Gamma_{e^+e^-N} + \dots . \tag{3.1}$$

The dominating decay channel $\Delta \to N\pi$ is 99.4% and the only measured electromagnetic decay $\Delta \to N\gamma$ is 0.55 – 0.65% [PDG16]. For the unmeasured $\Delta \to N\gamma^*$ transition, a theoretical estimate on the level of 4×10^{-5} has been given, e.g. in Refs. [Kri02, Zét03a]. The electromagnetic transition $N \to \Delta$ is predominantly magnetic dipole (M1) involving the spin and isospin flip of a single quark in the $S-$wave state (Fig. 3.3). A small $D-$wave admixture of quadrupole (electric E2 and Coulomb C2) amplitudes describes small deformations of the resonance from a spherical shape [Pas07, CC09b].

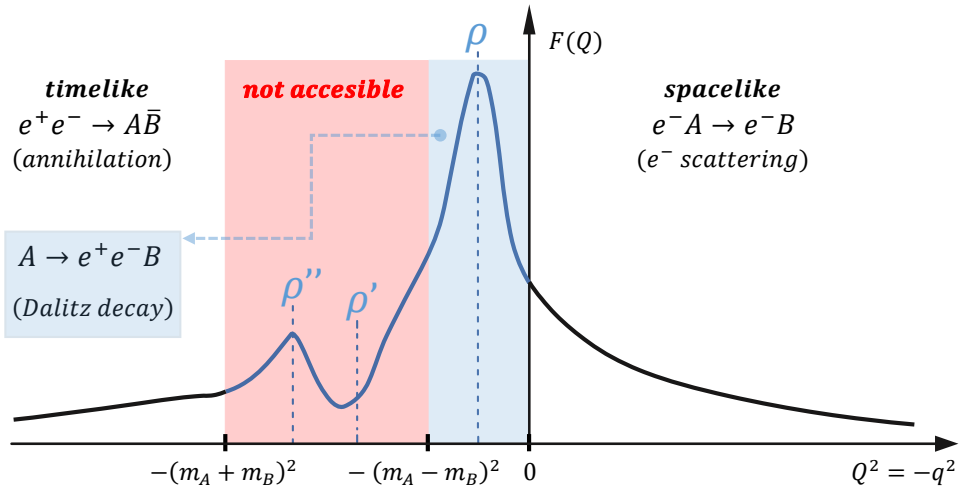

Figure 3.2: A form factor $F(Q)$ in the spacelike and timelike region with characteristic ρ–meson peaks in the timelike region. Dalitz decays allow to probe the timelike region at low q^2 and resonance couplings to vector mesons. Here, $Q^2 = -q^2$.

Electromagnetic decays are described with the help of three helicity amplitudes $A_{1/2}(q^2)$, $A_{3/2}(q^2)$ and $S_{1/2}(q^2)$, defined in the Δ rest frame (Fig. 3.4). First two of them are related to the transverse photon polarization, the last one is related to a virtual (massive) longitudinal photon polarization. In the limit of a real photon ($q^2 = 0$) the $S_{1/2}$ amplitude vanishes. The best estimations of helicity amplitudes $A_{1/2}$, $A_{3/2}$ for the real photon coupling were measured in the pion photoproduction experiments by the CLAS [Wor12], MAMI/A2 [Bec97, Bec00] and LEGS [Bla97, Bla01] Collaborations.

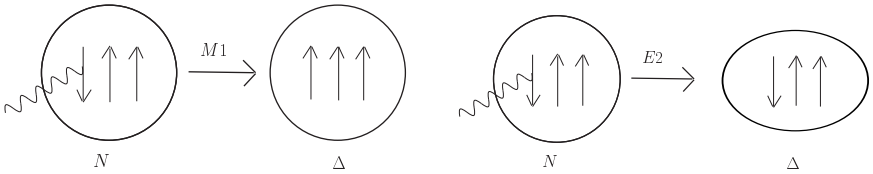

Figure 3.3: Schematic picture of the $N \to \Delta$ transition induced by the interaction of a photon with a single quark in the nucleon: M1 transition involves a S–wave spatial wave function (left panel) and E2 transition requires N and/or Δ wave functions to have a D–wave component (right panel). Figure taken from [Pas07].

These helicity amplitudes are completely unknown for $q^2 > 0$. This region can be accessed via the Dalitz decay $\Delta \to Ne^+e^-$. The differential decay width $d\Gamma/dm_{\gamma^*}$ as a function of the virtual photon mass can be expressed in terms of the resonance decay width $\Gamma^{\Delta \to N\gamma^*}$

$$\frac{d\Gamma^{\Delta \to Ne^+e^-}_{m_\Delta}}{dm_{\gamma^*}} = \frac{2\alpha}{3\pi m_{\gamma^*}} \Gamma^{\Delta \to N\gamma^*}_{M_\Delta}(m_{\gamma^*}), \tag{3.2}$$

hence it is also related to the radiative width $\Gamma^{\Delta \to N\gamma}_{m_\Delta}$. In fact, the real photon decay width is the limit of the dilepton decay width, when $m_{\gamma^*} \to 0$. The calculation of the partial decay width $\Gamma_{e^+e^-N}$ requires the knowledge of the evolution of the electromagnetic transition form factors (eTFF) as a function of q^2, which are real in the spacelike

region, but get an imaginary part in the timelike region. They can be equivalently expressed in terms of γ^*NΔ form factors: magnetic dipole (G_M^*), electric quadrupole (G_E^*) and Coulomb quadrupole (G_C^*), or in terms of helicity amplitudes, which are related by, as introduced in the paper of Jones and Scadron [Jon73]:

$$\begin{aligned} A_{3/2} &= -N\,\frac{\sqrt{3}}{2}\,(G_M^* + G_E^*), \\ A_{1/2} &= -N\,\frac{1}{2}\,(G_M^* - 3G_E^*), \\ S_{1/2} &= N\,\frac{q_\Delta}{\sqrt{2}M_\Delta} G_C^*. \end{aligned} \tag{3.3}$$

$q_\Delta = \frac{Q_+Q_-}{2m_\Delta}$ is the magnitude of the virtual photon three-momentum in the Δ rest frame, and $Q_\pm = \sqrt{(m_\Delta \pm m_N)^2 + Q^2}$, m_Δ and m_N are Δ and nucleon masses, respectively, q^2 is the photon four-momentum transfer squared and $Q^2 = -q^2$. Further, N is defined as

$$N = \frac{e}{2}\left(\frac{Q_+Q_-}{2m_N^3}\right)^{1/2} \frac{(m_N + m_\Delta)}{Q_+}, \tag{3.4}$$

where e is the elementary electric charge. The helicity amplitudes (and form factors) are expressed in units GeV$^{-1/2}$ (and without units, respectively), and reduce to the photo-couplings at $Q^2 = 0$.

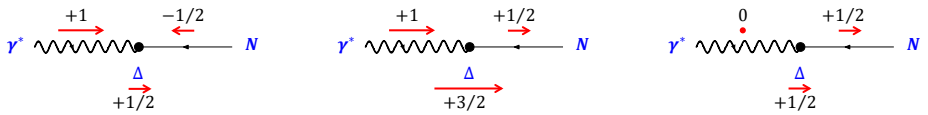

(a) $A_{1/2}$ (b) $A_{3/2}$ (c) $S_{1/2}$

Figure 3.4: $\gamma^* N \to \Delta$ helicity amplitudes in the Δ rest frame. The γ, N, and Δ spin projections are along the z–axis (chosen along the virtual photon direction).

The other electromagnetic N–N^* transition form factors for the abnormal- and normal-parity transitions related to helicity amplitudes can be found in Refs. [Dev76, Kri02].

3.3 Baryon resonances and vector mesons

A rich data sample of the transition amplitudes for $\Delta(1232)P_{33}$, $N(1440)P_{11}$, $N(1520)D_{13}$, $N(1535)S_{11}$, $\Delta(1620)S_{31}$ and $N(1650)S_{11}$, $N(1680)F_{15}$, $N(1700)D_{33}$, and $N(1720)P_{13}$ has been obtained in the spacelike region in a wide q^2 range (for a review, see Ref. [Azn12]). On the other hand, no experimental data on the Dalitz decays of resonances exist, though many theoretical calculations predict a sensitivity of the dilepton invariant mass distribution to the $RN\gamma^*$ vertex structure. According to the Vector Meson Dominance (VMD) model of Sakurai [Sak60, Sak69] the virtual photon coupling to a hadron is mediated entirely by intermediate vector mesons $\rho/\omega/\phi$. Hence, it is expected that the contribution of mesons to the interaction vertex modifies the q^2 dependence of the respective eTFF and produces an enhancement near the vector meson poles. However, it has also been realized that a strict VMD used together with

the $NN\rho$ Lagrangian (Refs. [Sak60, Sak69]) leads to an overestimation of the radiative $R \to N\gamma$ decay widths when the known $R \to N\rho$ branching ratios are used in calculations (see e.g. [Kro67, Fae03]). Various solutions of this problem were proposed, as for example the use of the alternative $NN\rho$ Lagrangian given in Ref. [Kro67], where two independent coupling constants are applied for the vector mesons and photon couplings, or destructive interferences between contributions from higher ρ/ω states [Kri02]. Two-component quark models with direct and VMD couplings [Wan05, Ram17] also avoid this problem. The striking feature of all these models is a significant modification of the eTFF due to the vector meson-resonance couplings.

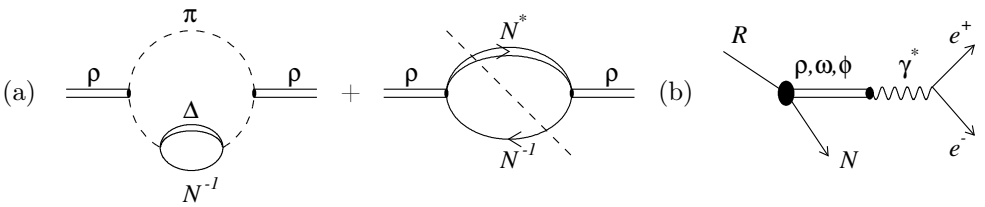

Figure 3.5: (a) Modifications of ρ meson in the nuclear matter via resonance-hole excitations. The cut on the right diagram defines the imaginary part of the self-energy. (b) Within the Vector Meson Dominance (VMD) theorem [Sak60] the spectral distribution of the virtual photons γ^* reflects the strength of the vector meson coupling.

Understanding the couplings of vector-meson resonances is important also due to a strong modification of the ρ meson spectral function observed in dilepton invariant mass distributions measured in ultra-relativistic heavy ion collisions at SPS [CC08, NC10, NC06] and also at RHIC [Col13,PC10]. They lead to the conclusion, that the in-medium propagator of the ρ meson can be modified by a strong coupling of the pion loop to $\pi\Delta N^{-1}$ or direct ρ meson- $N^{-1}N^*$ excitation, where N^* is a baryonic resonance [Hee08, Leu10] (see Fig. 3.5a). In particular, calculations of Rapp and Wambach [Rap97,Rap99] support the in-medium broadening scenario, yet the modification itself depends both on the temperature of the colliding system and the ρ momentum.

Although the dominant production mechanism for the ρ is different in the high energy experiments ($\pi^+\pi^-$ annihilation) and at lower energies where baryons play a dominant role, the in-medium spectral function depends in any case on the ρNN^* coupling with the close connection to the electromagnetic structure of the resonance-nucleon transition (Fig. 3.5b). The calculations for cold nuclear matter predict also strong off-shell ρ couplings to the low-mass baryon resonances like $N(1440)$, $N(1520)$, $N(1720)$ and $\Delta(1620)$ shifting part of the strength of the ρ meson spectral function down below the meson pole [Pet98] (for a review see also Ref. [Leu10]). The respective coupling strengths are usually constrained in models by the data from meson photoproduction and/or known resonance$-\rho N$ branchings and the e^+e^- yield is deduced using VMD (see for example Ref. [Rap00]).

The road to resonance properties is linked also with the question about the fundamental symmetries in the nature. In the beginning of the 1990s a vivid discussion about the chiral symmetry restoration in the hot and dense nuclear matter was triggered by the work of Brown and Rho [Bro91]. It is expected that chiral symmetry restoration should manifest itself in the decrease of the quark condensate value [Kli90]. Brown and Rho gave a phenomenological link between quark condensate and experi-

mental observables: vector mesons. Similar results were postulated from the QCD sum rules, using a very simple ρ spectral function [Hat92]. The ρ–meson, with its short life time (τ = 1.3 fm/c), smaller than the average life time of a fireball created in heavy-ion collisions, should decay in medium and one of the promising channels is the decay into dilepton pairs. Dileptons do not interact strongly and hold unbiased information about the meson still decaying in medium, hence they could be the optimum carrier to investigate its properties. The observable related to the spectral function is invariant mass, it could tell about the possible ρ medium modifications (e.g. meson pole mass shift or broadening). Unfortunately, the branching ratio $\rho \to e^+e^-$ is very small and amounts to 4.72×10^{-5} [PDG16] what is very challenging from the experimental point of view. The role of vector mesons, their origin, and the dielectron production in two- and three-body decays of vector and pseudoscalar mesons is presented in Appendix A.

3.4 Dalitz decays of baryon resonances

The decay width of a resonance R (of a mass m_R), decaying into a nucleon N (of a mass m_N) and a photon γ^* (of a mass m_{γ^*}), can be written in terms of the helicity amplitudes (see Sect. 3.2). They describe the transition from a resonance of a given spin J and helicity λ_R to a nucleon with the helicity $\lambda_N = \pm 1/2$ and a (virtual) photon with the helicity $\lambda_\gamma = \pm 1$ or 0, where $\lambda_R = -\lambda_N + \lambda_\gamma > 0$. The independent helicity amplitudes (three for spin $J \geq \frac{3}{2}$ resonances, two for spin $J = \frac{1}{2}$ resonances), can be related to the transition form factors (see Eq. 3.3), resulting in the following decay width formulas, as in Ref. [Kri02]. For spin $J \geq \frac{3}{2}$ resonances,

$$\begin{aligned}\Gamma(R_\pm \to N\gamma^*) = \frac{9\alpha}{16}\,\frac{(l!)^2}{2^l\,(2l+1)!}\,\frac{(m_R \pm m_N)^2}{m_R^3 m_N^2}\left[(m_R \pm m_N)^2 - m_{\gamma^*}^2\right]^{1/2} \\ \times \left[(m_R \mp m_N)^2 - m_{\gamma^*}^2\right]^{3/2} \times \left|F_R^\pm(m_{\gamma^*})\right|^2,\end{aligned} \tag{3.5}$$

where l is related to the incoming partial wave of a resonance, and the resonance electromagnetic transition form factor is

$$\left|F_R^\pm(m_{\gamma^*})\right|^2 = \frac{l+1}{l}|G_{M/E}^\pm|^2 + (l+1)(l+2)|G_{E/M}^\pm|^2 + \frac{m_{\gamma^*}^2}{m_R^2}|G_C^\pm|^2. \tag{3.6}$$

The $\Gamma(R_\pm \to N\gamma^*)$ depends on the normality of a resonance, defined as $P(-1)^{J-1/2}$ where P is intrinsic parity, that is, resonances with normal parity ($J^P = 1/2^-$, $3/2^+$, $5/2^-$, ...) are denoted with a " + ", and with abnormal parity ($J^P = 1/2^+$, $3/2^-$, $5/2^+$, ...) are denoted with a " − ".

The resonance decay width for spin $J = \frac{1}{2}$ resonances reads:

$$\begin{aligned}\Gamma(R_\pm \to N\gamma^*) = \frac{\alpha}{8\,m_R}\left[(m_R \mp m_N)^2 - m_{\gamma^*}^2\right]^{1/2} \\ \times \left[(m_R \pm m_N)^2 - m_{\gamma^*}^2\right]^{3/2} \times \left|F_R^\pm(m_{\gamma^*})\right|^2,\end{aligned} \tag{3.7}$$

with the form factor

$$\left|F_R^\pm(m_{\gamma^*})\right|^2 = 2\,|G_{E/M}^\pm|^2 + \frac{m_{\gamma^*}^2}{m_R^2}|G_C^\pm|^2. \tag{3.8}$$

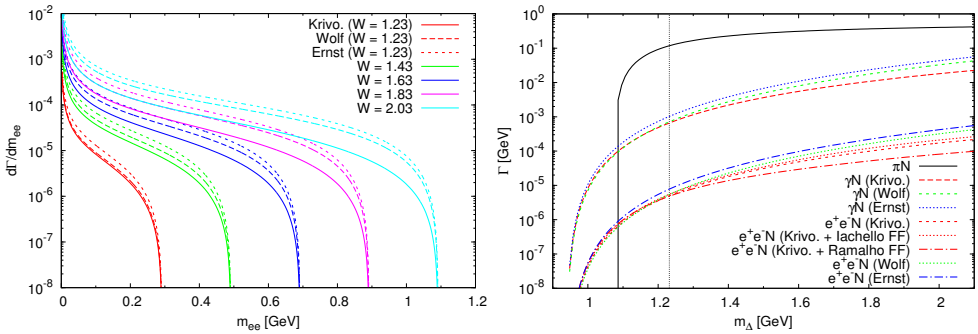

Figure 3.6: Left panel: Δ Dalitz decay differential width for a few off-shell Δ masses (W = 1.23, 1.43, 1.63, 1.83 and 2.03 GeV/c^2) in the description of [Kri02, Wol90, Ern98]. Right panel: The $\Gamma^{\Delta\to\pi N}$ (black solid curve) and $\Gamma^{\Delta\to\gamma N}$ compared to the integrated Δ Dalitz decay yield in the description of various models (see the legend), Ref. [Wei13].

For example, for the Δ(1232) resonance (l = 1), Eq. 3.5 reduces to the form derived by Krivoruchenko and Fässler in Ref. [Kri01]:

$$\Gamma^{\Delta\to N\gamma^*}_{m_\Delta}(m_{\gamma^*}) = \frac{\alpha}{16}\,\frac{(m_\Delta+m_N)^2}{m_\Delta^3 m_N^2}\left[(m_\Delta+m_N)^2-m_{\gamma^*}^2\right]^{1/2} \times\left[(m_\Delta-m_N)^2-m_{\gamma^*}^2\right]^{3/2}\times\,|F_\Delta(m_{\gamma^*})|^2\,. \tag{3.9}$$

$m_{\gamma^*} = m_{e^+e^-}$ is the invariant mass of the dilepton pair, m_N and m_Δ are the nucleon and Δ masses and α = 1/137 is the fine-structure constant. This formula is related to the Δ Dalitz decay as in Eq. 3.2. Further, the Δ form factor (Eq. 3.6) can be decomposed into a magnetic, electric and Coulomb component:

$$|F_\Delta(m_{\gamma^*})|^2 = |G_M^2(m_{\gamma^*})| + 3\,|G_E^2(m_{\gamma^*})| + \frac{m_{\gamma^*}^2}{2m_\Delta^2}\,|G_C^2(m_{\gamma^*})|, \tag{3.10}$$

but most models neglect the G_E and G_C and treat only the dominant magnetic dipole form factor G_M. In the literature, other parametrizations of the Δ Dalitz decay exist [Wol90, Ern98]. However, as pointed out by Krivoruchenko in Ref. [Kri01], many former expressions of the Dalitz decays of baryonic resonances were inconsistent even in the real photon decay limit, e.g. Δ → Nγ. Figure 3.6, left panel, shows that the off-shell contributions in $d\Gamma/dm_{\gamma^*}$ strongly dominate over the on-shell contribution and the Dalitz width grows strongly with $W = m_\Delta$. The dilepton yield from Δ Dalitz decays is very sensitive to uncertainties in the off-shell behavior. Figure 3.6, right panel, shows also the comparison of the hadronic width $\Gamma^{\Delta\to\pi N}$, the real-photon width $\Gamma^{\Delta\to\gamma N}$ and the integrated dilepton width $\Gamma^{\Delta\to Ne^+e^-}$, defined as:

$$\Gamma^{\Delta\to Ne^+e^-}_{m_\Delta} = \int_{2m_e}^{m_\Delta-n_N}\frac{d\Gamma^{\Delta\to Ne^+e^-}}{dm_{\gamma^*}}\,dm_{\gamma^*}. \tag{3.11}$$

The total Γ^Δ width is dominated by the hadronic part, but for the dilepton width large differences appear, related to various width parametrizations and form factors. The electromagnetic transition form factor $F_\Delta(m_{\gamma^*})$ (Eq. 3.10) is only constrained in the spacelike region, but remains unknown in the timelike region. The latter regime can be probed by the Dalitz decays. At the real-photon point it is fixed by the decay width $\Gamma^{\Delta\to N\gamma}$ = 117 MeV × 0.0055 = 0.66 MeV [PDG16] resulting in the value $|F_\Delta(0)|$ = 3.03.

Equation 3.9 was accomodated in various model calculations [Kri02,Wan05,Ram12]. In the calculations of Zétényi and Wolf [Zét03a] an equivalent set of form factors has been used but giving the same result. The detailed overview of the models is given in Appendix B.

3.5 NN bremsstrahlung

The charged objects under acceleration radiate real or virtual photons, the latter ones decay into dilepton pairs. In case of the interaction of two nucleons such a process is called nucleon-nucleon bremsstrahlung. Among the reactions $pp \to pp$, $np \to np$ and $nn \to nn$, the last one has no charged particles in the initial and the final states, and $pp \to pp$ bremsstrahlung is highly suppressed due to destructive interferences between graphs involved and is often neglected. Therefore significant contribution is expected only in the $np \to np$ case.

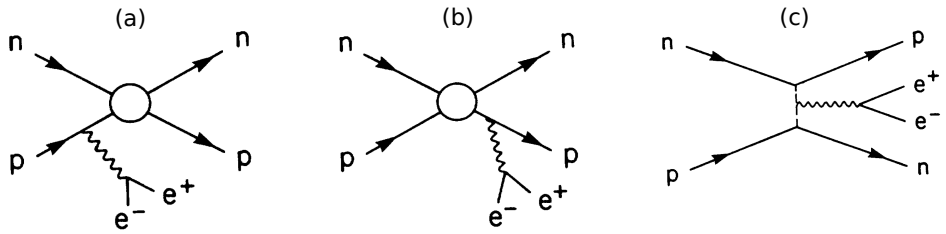

Figure 3.7: The (virtual) photon radiation from the external proton lines (a, b) in the Soft Photon Approximation [Gal87] and the radiation from an internal charged pion line (c) in np scattering.

In the Soft Photon Approximation (SPA) [Gal87,Gal89,Wol90,Lic95,Zha97] photons are radiated only from the initial or from the final charged lines (Fig. 3.7a, b). The vertex $NN\gamma^*$ is treated on-shell and this approximation is valid only for low photon energies $E_\gamma = 100-200$ MeV. The hard photons can be emitted from the strong interaction lines, e.g. radiation from the exchange line of the charged pion (Fig. 3.7c). In the limit of the soft photons this radiation is a sub-leading contribution. Most of the calculations of dielectron production take as a starting point a formula introduced by Rückl [Rüc76] linking the dilepton production cross section via virtual photon bremsstrahlung to the cross section of real photons bremsstrahlung. The differential cross section reproduces the kinematics associated with the on-shell elastic differential nucleon-nucleon cross section:

$$\frac{d\sigma_{np\to npe^+e^-}}{dm_{e^+e^-}dEd\Omega} = \frac{\alpha^2}{6\pi^3}\,\frac{q}{m_{e^+e^-}E^2}\,\frac{s-(m_1+m_2)^2}{2m_1^2}\,\sigma_{el}(s)\,\frac{R_2(s_2)}{R_2(s)}, \tag{3.12}$$

where m_1 is the mass of a charged particle (proton), m_2 is the nucleon mass, σ_{el} is the elastic NN cross section, q, E and Ω are dilepton momentum, energy and solid angle in the neutron-proton center-of-mass frame, s is the total available energy. Since the four-momentum q of the virtual photon in the phase space δ function is neglected, the ratio of two-body phase space is evaluated by $R_2(s_2)/R_2(s)$ [Byc73], where

$$R_2(s) = \sqrt{1-(m_1+m_2)^2/s}, \quad s_2 = s + m_{e^+e^-} - 2E\sqrt{s}. \tag{3.13}$$

3.6 One-Boson Exchange models

The final state of ppe^+e^- or npe^+e^- at the energy of a few GeV may result from both baryon resonance Dalitz decay and NN bremsstrahlung, and both processes can interfere. The coherent sum of the contributing amplitudes has been evaluated within one-boson exchange (OBE) models, e.g. by Kaptari and Kämpfer [Kap09] and Shyam and Mosel [Shy09]. These models provide the total e^+e^- contribution based on a coherent treatment of many amplitudes including contributions of the Δ resonance and the nucleon-nucleon bremsstrahlung. Despite the similar approaches the models give different predictions for the energy dependence of differential cross sections. One should note that according to both OBE models, interference effects between the Δ and NN bremsstrahlung are small and play a role only at higher e^+e^- invariant mass ($M_{e^+e^-} > 0.4$ GeV/c^2). This seems to justify the statement that in proton-proton collisions the NN bremsstrahlung contribution can be treated separately and added incoherently to the Δ contribution.

3.6.1 Kaptari and Kämpfer model

The fully covariant and gauge-invariant calculation by Kaptai and Kämpfer [Kap06, Kap09] provides the exclusive e^+e^- production in NN collisions:

$$N_1(P_1) + N_2(P_2) \rightarrow N_1'(P_1') + N_2'(P_2') + e^+(k_1) + e^-(k_2) \tag{3.14}$$

The differential cross section $d\sigma/dM$ includes the sum over all spin states of hadronic currents J_μ. They are defined by effective interaction Lagrangians consisting of two parts describing strong and electromagnetic interaction. The strong interaction among nucleons is mediated by the exchange mesons: σ (scalar), π (pseudoscalar-isovector), ω (neutral vector), ρ (vector-isovector). The currents have to obey gauge invariance, hence the condition $q_\mu J^\mu = 0$. In such approximation (one-boson exchange, OBE) the current J_μ is determined by two types of diagrams. One set describes the creation of a virtual photon ($q^2 = M^2_{\gamma^*} > 0$) as a pure bremsstrahlung (Fig. 3.8).

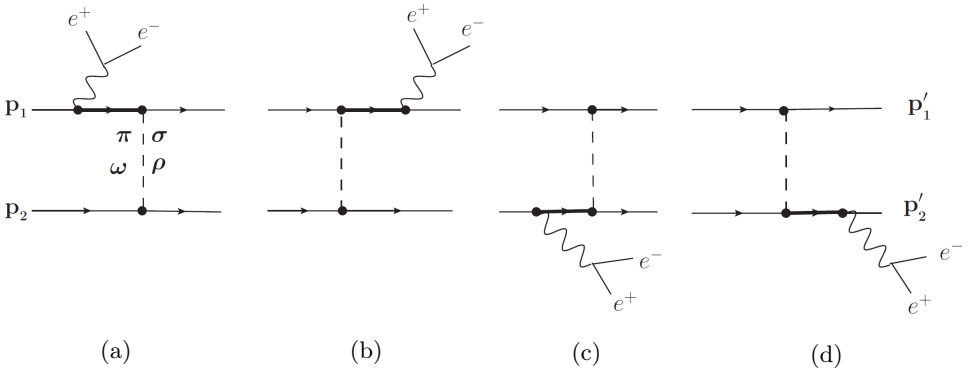

Figure 3.8: Bremsstrahlung diagrams describing exclusive production in $N_1 + N_2 \rightarrow N_1' + N_2' + e^+ + e^-$ reaction [Kap09] with pre-emission (a, c) and post-emission (b, d). Thick lines represent resonance excitation. The same set of diagrams for $1' \leftrightarrow 2'$.

The gauge invariance is easily obtained in the case of neutral meson exchange, since the pair of diagrams with pre-emission (Fig. 3.8a) and post-emission (Fig. 3.8b) of γ^* ensures gauge invariance, also in the case of dressing the vertices with phenomenological form

factors. This is not the case for charged meson exchange and another set of diagrams describing the emission of a virtual photon γ^* from internal meson line (Fig. 3.9a) is necessary. However, application of additional form factors again leads to violation of current conservation. The solution of this problem requires the presence of another pair of seagull-like diagrams (Fig. 3.9b and 3.9c). The numerical calculations show that the contribution of $\rho-$meson exchange for seagull-type diagrams varies from 10% (low dielectron invariant masses) to 35% (at kinematical limit). The proposed solution for the gauge invariance restoration is not unique.

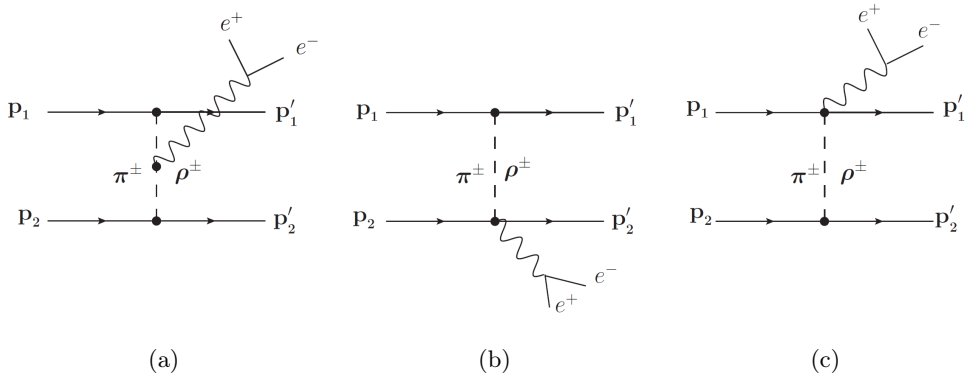

Figure 3.9: Contribution of meson exchange currents (a) and seagull terms (b, c) to the process $p + n \to n + p + e^+ + e^-$ [Kap09].

The e^+e^- invariant mass distribution calculated in pp and np collisions (at kinetic beam energy $T = 1.25$ GeV) but only for nucleon lines is presented in Fig. 3.10a. The np cross section is 5–6 times larger than the pp cross section due to destructive interferences in the latter case. In addition, there is a notable contribution from the emission of charged exchange mesons (graphs in Fig. 3.9) in the np case. Further investigation includes contribution from graphs with the low-lying baryon resonances $P_{33}(1232)$, $P_{11}(1440)$, $D_{13}(1520)$ and $S_{11}(1535)$. The main contribution to the cross section stems from the Δ resonance. Due to the isospin $I = 3/2$ of the Δ resonance, only the isovector mesons π and ρ can be associated to a $N - \Delta$ transition. Figure 3.10b shows the contribution calculated for the Δ only, which dominates over the nucleon contribution (Fig. 3.9) in the whole kinematic range except the end of the kinematic limit. The coupling constants related to the Δ eTFF are fixed at the photon point ($q^2 = 0$) [Feu97] but authors notice the importance of the proper off-shell resonance treatment, especially at large resonance masses. The contributions of the isospin$-\frac{1}{2}$ resonances, $P_{11}(1440)$ and $S_{11}(1535)$, which couple both to isospin-1 and isoscalar mesons, are small. The last considered resonance, $D_{13}(1520)$, has a comparable contribution to NN bremsstrahlung at the dielectron invariant mass $M_{e^+e^-} > 0.45$ GeV/c^2.

The quantum mechanic interference effects seem to play an important role in Kaptari and Kämpfer calculation (Fig. 3.10c). The comparison of the coherent sum of all amplitudes (solid curves) with the incoherent sum of separate contributions of bremsstrahlung and the low-lying resonances (dashed curves) shows that the interference effects become significant at higher values of e^+e^- invariant mass, reducing the cross section by a factor of $2 - 2.5$.

The cross section for $pn \to pne^+e^-$ is estimated to be larger by a factor of $1.5 - 3$ than the cross section for $pp \to ppe^+e^-$ and it does not scale up simply with the isospin relation (factor 2). This is due to resonance contribution and interferences, different

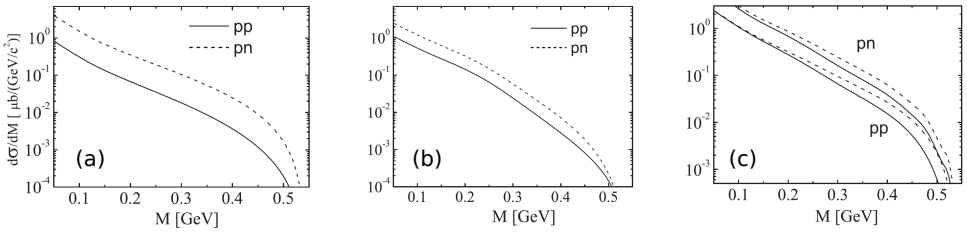

Figure 3.10: Contribution of bremsstrahlung diagrams (Figs. 3.8 and 3.9) to the e^+e^- invariant mass distribution at the $T = 1.25$ GeV for pp and pn reactions: (a) with only nucleon lines, (b) with only Δ decays, (c) as a coherent sum (solid curves) and an incoherent sum (dashaed curves) of the contributions from bremsstrahlung, $P_{33}(1232)$, $P_{11}(1440)$, $D_{13}(1520)$ and $S_{11}(1535)$ [Kap09].

couplings in γp and γn system, and the exchange of the isoscalar σ and ω mesons. Kaptari and Kämpfer conclude that bremsstrahlung process has a smooth behavior as a function of dielectron invariant mass and can be treated as a background process.

3.6.2 Shyam and Mosel model

The role of baryonic resonances in the dielectron invariant mass spectrum produced in pp and pn collisions at various beam energies in the 1−5 GeV range is also investigated by Shyam and Mosel [Shy03, Shy09]. The general production mechanism is presented in Fig. 3.11b. A virtual photon decaying into e^+e^- pair can be emitted from a nucleon or resonance line, before (Fig. 3.11a) and after (Fig. 3.11b) collision, plus the analogous diagrams with an emission from the lower line. The important source, depicted in Fig. 3.11c, presents the dilepton emission from the internal meson line.

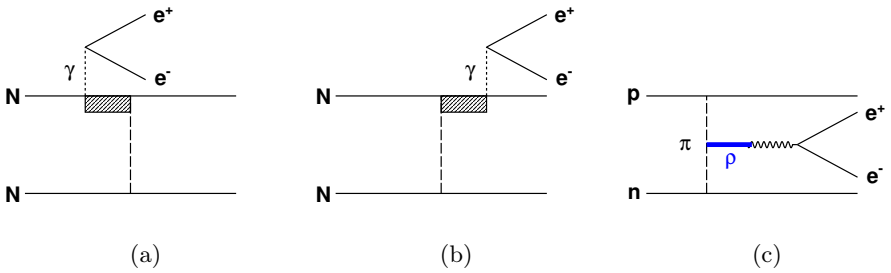

Figure 3.11: A representation of Feynman diagrams describing e^+e^- production in $NN \to NNe^+e^-$ reaction [Shy09]: emission (a) before NN collision, (b) after collision and (c) during collision from an internal charged meson line. The hatched box represents an off-shell nucleon or Δ.

Similar to Kaptari and Kämpfer calculations (Sec. 3.6.1), the interaction between two nucleons is modeled by an effective Lagrangian which is based on the exchange of the π, ρ, ω, and σ mesons. In addition to nucleon lines (NN bremsstrahlung), the two intermediate resonances, $P_{33}(1232)$ and $D_{13}(1520)$, are taken into account. At each interaction vertex a form factor with an energy independent cutoff parameter is introduced, suppressing the contribution at high momentum transfer. The meson-

nucleon and meson-nucleon-Δ ($g_{\Delta N\pi}$, $g_{\Delta N\rho}$) coupling constants are energy dependent, as determined in Refs. [Sch94, Eng96]. The coupling constants $g_{N^*N\pi}$ and $g_{N^*N\rho}$ have been determined from the branching ratios for the decay of the $N(1520)$ resonance to $N\pi$ and $N\rho$ channels, respectively [Shy99, Shy01]. The coupling constants $g_{N^*N\omega}$ and $g_{N^*N\sigma}$ have been determined by vector meson dominance [Pos01b] with a large uncertainty, but their contributions to the dilepton production amplitude are negligible.

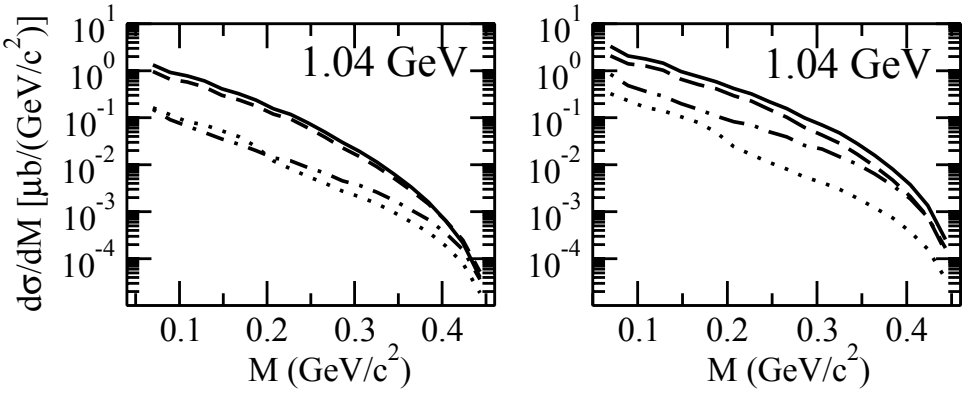

Figure 3.12: The dielectron invariant mass distributions produced in proton-proton (left panel) and proton-neutron (right panel) collisions. The NN non-resonant bremsstrahlung (dashed-dotted), $\Delta(1232)$ (dashed) and $N(1520)$ (dotted) and the solid curves present the coherent sum, the total cross sections.

The subsequent contributions are presented in Fig. 3.12 at the beam energy of 1.04 GeV. The pn cross sections (right panel) are about 2 – 3 times larger than the ones in the pp reactions (left panel). In both cases, the dominant contribution stems from the $\Delta(1232)$ resonance. In the pp case, the NN bremsstrahlung (graphs involving only intermediate nucleon lines) and $N(1520)$ resonance are similar, however in the pn case, the NN bremsstrahlung is significantly larger. In addition, it has been shown in Ref. [Shy09] that the dominant $\Delta(1232)$ contribution stems from the post-emission graphs (see Fig. 3.11b) at the low energy 1.04 GeV.

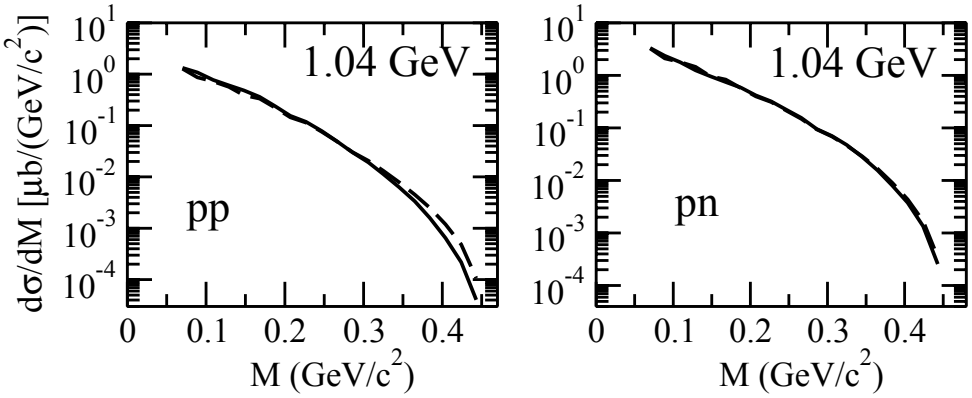

Figure 3.13: The dielectron invariant mass distributions produced in proton-proton (left panel) and proton-neutron (right panel) collisions at the beam energy of 1.04 GeV (see Ref. [Shy03]). The solid and dashed curves present the cross sections obtained by the coherent and incoherent summations of various terms, respectively.

The role of the interference effects in pp and pn collisions is investigated in Fig. 3.13. The cross sections obtained by coherent (solid curve) and incoherent (dashed curve) sums of the amplitudes corresponding to the NN non-resonant bremsstrahlung, $\Delta(1232)$ and $N(1520)$ are presented, respectively. The interference effects become more important at the larger masses ($M_{e^+e^-} > 0.3$ GeV/c^2) for the pp collisions, while they are rather small everywhere for the pn collisions. This is at variance with Kaptari and Kämpfer model, where interferences are larger. Both results on the dominant Δ contribution from the post-emission graphs and the negligible interference effects at the low dielectron invariant mass, make an assumption of the resonance model to be acceptable, but only at the low energies and low dielectron invariant masses.

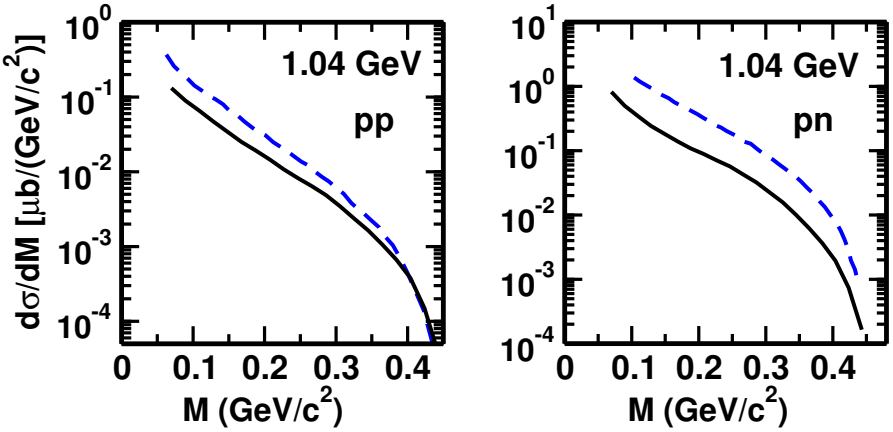

Figure 3.14: Model comparison: the invariant mass distribution of the NN bremsstrahlung contributions to the dilepton spectra in pp (left panel) and pn (right panel) collisions at the beam energy of 1.04 GeV. Solid curves present Shyam-Mosel calculations [Shy09] while dashed curves present Kaptari-Kämpfer caluclations [Kap09].

The main difference between Refs. [Shy09] and [Kap09] is the implementation of the gauge invariance of the NN bremsstrahlung amplitudes (Fig. 3.14). In Shyam and Mosel approach (black solid curves) the $NN\pi$ coupling is calculated as a pseudoscalar and does not require additional contact terms (seagull diagrams) in order to preserve the gauge invariance for bare pointlike nucleons. The resulting cross sections are lower than obtained in Ref. [Kap09] (blue dashed curves) by factors of $2-4$ for dilepton invariant mass values below 0.6 GeV/c^2 for both pp and pn collisions at 1.04 GeV (but also higher) incident energies. The difference is not a constant factor and changes over the mass value.

The total dilepton production cross sections in the elementary NN collisions are implemented in most transport calculations with semi-classical models which, in general, differ noticeably from the predictions of full quantum mechanical models. However, the differences in the $NN\pi$ couplings among various OBE models lead to huge discrepancies. The ambiguities can be solved by the precise experimental results, preferably measured in the exclusive channels.

Chapter 4

Resonances in dilepton channels

The goal of this chapter is to present the results obtained in the inclusive and exclusive channels with e^+e^- pairs, measured in the NN experiments by the HADES Collaboration. The unique feature of the HADES spectrometer (App. C) is that the contributions of baryonic sources can be also studied by identification of dielectron (e^+e^-) pairs. They origin mainly from the meson (App. A.3.1) and baryon (Sect. 3.4) resonance Dalitz decays, and from NN bremsstrahlung (Sect. 3.5). In the case of pp collisions at the beam energy T = 1.25 GeV, below the η meson production threshold, the baryonic sources completely determine the e^+e^- invariant mass distribution above the π^0 mass. The exclusive ppe^+e^- channel is dominated by Δ Dalitz decay. In the dp collisions at 1.25 GeV/nucleon, the dielectron production offers an additional possibility to study np bremsstrahlung radiation with timelike virtual photons. The relevant final state is $NN\gamma^*(e^+e^-)$ resulting from the interaction between the nucleons or/and their excited states (such as Δ) formed in the collisions. In pp at 2.2 GeV, the data obtained on both inclusive e^+e^- and exclusive ppe^+e^- channels allows for determination of π^0 and η mesons production. In addition, various angular distributions represent sensitive observables in dielectron channels. Data for pp collisions at 3.5 GeV on dielectron production provided results on Δ and N^* excitation. In the ppe^+e^- final state, the Dalitz decays of $\pi^0/\eta \to \gamma e^+e^-$ and $\omega \to \pi^0 e^+e^-$ could be effectively suppressed via kinematical constraints, with the focus on the studies of the two-body vector meson decays and the resonance Dalitz decays, $R \to pe^+e^-$. The Dalitz decays are compared to calculations assuming a pointlike $RN\gamma^*$ coupling, raising the subject of the electromagnetic transition form factors and the role of the ρ–meson production, and the ρN coupling.

4.1 Inclusive e^+e^- production at T = 1.25 GeV

The proton-proton (Sect. 2.1) and deuteron-proton (Sect. 2.2) experiments were performed at the energy of 1.25 GeV/nucleon. Figure 4.1 presents the efficiency corrected invariant mass distribution of e^+e^- signal pairs within the HADES acceptance, for pp (left panel) and quasi-free np (right panel) collisions. The dielectron pairs from deuteron-induced reactions are measured in coincidence with the spectator proton in the Forward Wall hodoscope (App. C.1.7), which is selected with the condition on its momentum, $1.6 < p_{sp} < 2.6$ GeV/c. The moderate experimental momentum resolution obtained from a time-of-flight measurement in FW enforces the given range of p_{sp}. The total number of signal pairs amounts to 39×10^3 (pp collisions), and 36×10^3 (np collisions), respectively. The number of pairs in the region above the π^0 mass, $M_{ee} > 0.15$ GeV/c^2, amounts to 350 and 1450, for pp and np collisions, respectively,

with a signal-to-CB ratio ≥ 1 [Col09]. The measured pair yield was normalized to the *pp* elastic scattering yield (App. C.3.6). The normalization error of this procedure is estimated to be 9% and does not show any pair-mass dependence. It results from the error on the published elastic cross section (5%) and from systematic errors related to the reconstruction of elastic-scattering events (7%). An additional uncorrelated systematic uncertainty of 20% comes from the pair reconstruction efficiency, including a smooth invariant mass dependence.

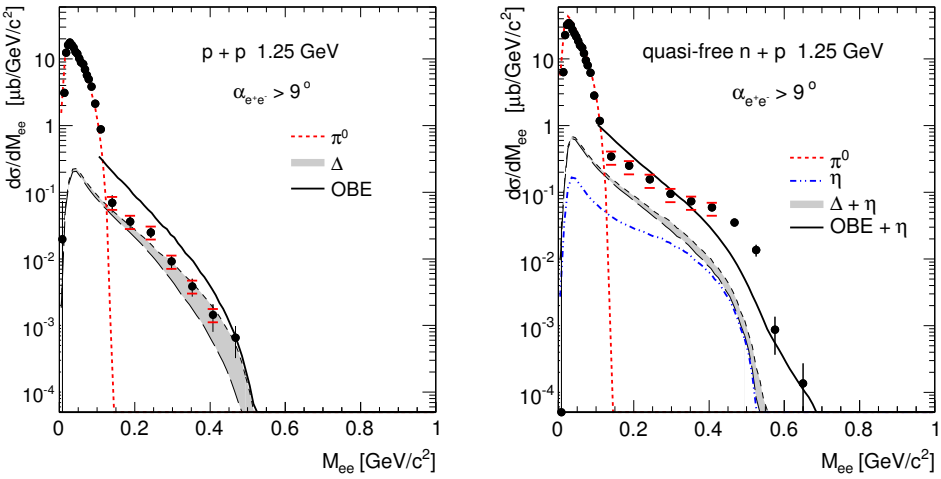

Figure 4.1: e^+e^- final state: invariant mass (full circles) measured in *pp* reactions (left panel) and in quasi-free *np* reactions (right panel) at 1.25 GeV. Systematic errors are indicated by red horizontal bars, statistical errors by vertical bars. In the analysis, e^+e^- pairs with an opening angle of $\alpha \leq 9°$ are removed from the sample. The curves show results of model calculations (see text for explanations).

4.1.1 e^+e^- production channels

In proton-proton collisions at 1.25 GeV, the resonance model [Tei97] (Sect. 1.2.2) predicts that mesons are produced mostly through intermediate Δ resonances. In particular, the Δ^+ decays into $p\pi^0$ followed by the π^0 Dalitz decay with a branching ratio $1.174 \pm 0.035 \times 10^{-2}$ (see App. A.3.1). The measured yield in the π^0 Dalitz decay region is reproduced (red short-dashed curve in Fig. 4.1, left panel) taking into account the inclusive π^0 production cross section $\sigma^{pp}_{\pi^0} = 4.5 \pm 0.9$ mb from the resonance model, which describes the existing data [Bys87]. The respective cross section for Δ^+ production is fixed by the isospin conservation to $\sigma_{\Delta^+} = 3/2\ \sigma_{\pi^0}$. The dielectron emission in the mass region above the π^0 Dalitz region is dominated by the Δ Dalitz decay. The prescription for the differential partial decay width $d\Gamma_{\Delta \to N e^+e^-}(M_{e^+e^-})/dM_{e^+e^-}$ used in the PLUTO simulation [Doh10] follows Krivoruchenko formula from Eq. 3.9 (Sect. 3.4). The Δ form factor is decomposed in Eq. 3.10 into a magnetic, electric and Coulomb component, with the dominant magnetic transition form factor (G_M). Its magnitude, extracted from pion photoproduction experiments [Pas07] at the photon point, amounts to $G_M(0) = 3.02 \pm 0.03$ and is kept constant within the simulation. The G_E and G_C are

neglected, similar to Zétényi and Wolf model (App. B.1). The result is shown in the left panel of Fig. 4.1 with a long dashed curve. The Δ Dalitz contribution to the e^+e^- spectrum can be regarded as a lower bound in this approach. A possible modification of the magnetic transition form factor due to intermediate vector mesons is illustrated with a short dashed curve. Here a calculation using the two-component quark model of Iachello and Wan (App. B.3) was used. In the four-momentum q^2 range of the $\Delta(1232)$ Dalitz decay, the G_M form factor is described mostly by the Vector Dominance Model in terms of the dressed ρ–meson propagator. The enhanced yield is observed (gray hatched area), in particular for high pair masses, providing a better description of the pp data. A microscopic one-boson exchange model by Kaptari and Kämpfer [Kap09] is another approach (see Sect. 3.6.1) compared with the data. The total e^+e^- contribution is calculated there as a coherent sum of amplitudes including contributions of the Δ resonance and the nucleon-nucleon bremsstrahlung. The virtual photon emission was modeled isotropically and corrections due to NN final state interactions were included in the parametrization implemented in the PLUTO event generator [Doh10]. The result of the simulation is shown in Fig. 4.1 (left panel) as a solid black curve. The yield calculated in this approach significantly overestimates the measured spectrum.

In quasi-free neutron-proton collisions induced with a deuteron beam at kinetic beam energy of 1.25 GeV/nucleon, the cross section in the π^0 mass region amounts to $\sigma_{\pi^0}^{np} = 8.56 \pm 1.7$ mb. It is a factor of 2 larger as compared to the pp reaction, in line with the resonance model prediction [Tei97]. The good agreement between the measured and the simulated yield in the π^0 mass region is shown in Fig. 4.1 (right panel). However, a dramatic change in the mass spectrum at higher masses is observed, in comparison to pp spectrum. In the intermediate mass region ($0.15 < M_{ee} < 0.35$ GeV/c^2) the dielectron np yield is enhanced by a factor of ten over the pp yield, clearly indicating that the Δ is not the only dielectron source. At the high invariant mass ($M_{ee} > 0.35$ GeV/c^2) the yield excess is even larger, reaching almost a value of 100 for the ratio np/pp at $M_{ee} = 0.5$ GeV/c^2. Dependence on the shape of e^+e^- invariant mass was investigated by restricting the spectator emission angle to a very forward cone ($0.3^\circ \leq \theta_{sp} \leq 2^\circ$). No significant change of the shape of the resulting pair spectrum was observed [Lap09]. To model the np data, the available energy in the center-of-mass was smeared to include the neutron momentum distribution in the deuteron using the Paris potential [CTC06]. Additionally, the η Dalitz decay was accounted for (blue dash-double dotted curve) with the cross sections for $np \to np\eta$ and $np \to d\eta$ reactions known down to the production threshold (see Ref. [Mos09]). The contribution of Δ Dalitz decay, modeled with a pointlike form factor, added with η Dalitz decay (Fig. 4.1, right panel, short dashed curve) is far from the data description. Similar to pp reactions, the OBE calculations [Kap09], which include effects enhancing bremsstrahlung in np collisions, were simulated. The OBE contribution summed with the η Dalitz decay contribution (black solid curve) overshoots the data at a mass just above the π^0 mass but underestimates the observed yield in the high mass region, where the data show an enhanced dielectron emission.

4.1.2 Comparison to models

The dilepton spectra measured in NN collisions by the DLS [DC97] and HADES (as discussed above) Collaborations at low energies unravel significant enhancement observed in the intermediate dilepton mass region over the contributions predicted by various models from the electromagnetic decays of hadrons and long-lived mesons, mainly η. The results triggered a progress in description which is summarized below.

4.1.2.1 Shyam and Mosel model

In Shyam and Mosel report [Shy10b], the effective Lagrangian model of Refs. [Sch94, Shy03, Shy09] (Sect. 3.6.2) was used to investigate the dilepton production in pp and quasi-free np reactions. The neutron momentum distribution in the deuteron was modeled using deuteron wave function from Ref. [Wir95] (Argonne v_{18}), resulting in a smeared np (quasi-free) reaction and center-of-mass energy above the threshold for the η–meson production. The total cross section parametrization for the η–meson was taken from Ref. [Shy07], corresponding to the good description of experimental data from Refs. [Cal98, Cal99]. The η–meson production was factorized as a two-step process, with a reaction either $p+n \to p+n+\eta$ or $p+n \to d+\eta$, followed by the η–meson Dalitz decay (see App. A.3.1). In addition, the contributions from the production and dileptonic decay of the subthreshold ρ_0–meson via the baryonic resonance $N(1520)$ were included for both pp and quasi-free np reactions. The ρ–meson exchange terms contribute less than 5% total bremsstrahlung cross sections [Shy10a]. The important modification in the NN bremsstrahlung is the inclusion of the pion electromagnetic form factor $F_\pi(M^2)$ at the charged internal meson line (graphs in Fig. 3.11c).

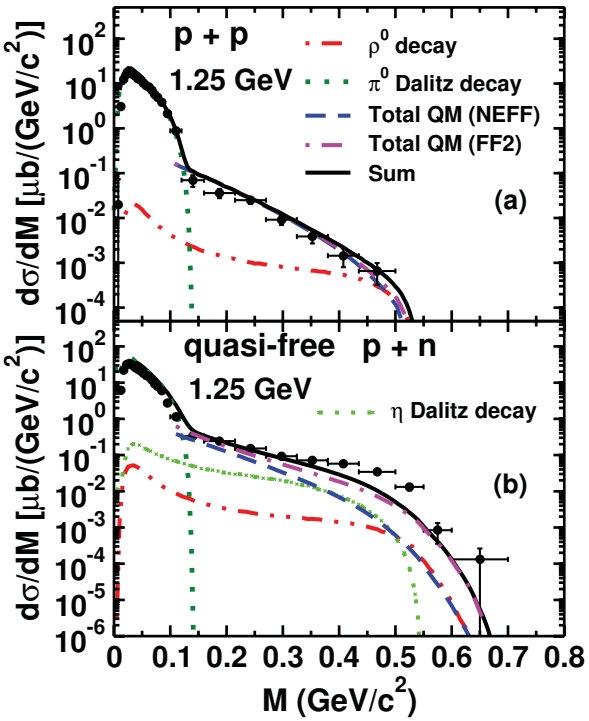

Figure 4.2: Dilepton invariant mass distributions in (a) $pp \to ppe^+e^-X$ and quasi-free (b) $np \to npe^+e^-X$ reactions at a beam energy of 1.25 GeV within the HADES acceptance. Total cross section is marked with a black solid curve. The contributions obtained with (FF2) and without (NEFF) pion electromagnetic form factor are shown by purple dot-dashed and blue dashed curve, respectively. Figure adopted from Ref. [Shy10b].

The same form factors at both the pion and the nucleon vertices are used in order to preserve gauge invariance. Two parametrizations for $F_\pi(M^2)$ were used. The first one assumes that the photon couples to the pion only via the ρ_0 meson

$$F_\pi(M^2) = \frac{m_\rho^2}{m_\rho^2 - M^2 - im_\rho\Gamma_\rho(M^2)}, \tag{4.1}$$

where m_ρ is the ρ–meson mass and Γ_ρ is the width for $\rho \to \pi\pi$ decay (see Ref. [Eri88]).

The second parametrization is derived from the assumption that the photon couples about 50% directly to the intrinsic quark core of the pion and the remaining 50% indirectly through the pion cloud:

$$F_\pi(M^2) = \frac{0.4}{1 - M^2/\lambda^2} + \frac{0.6}{1 - M^2/2m_\rho^2} \frac{m_\rho^2}{m_\rho^2 - M^2 - im_\rho\Gamma_\rho(M^2)}, \tag{4.2}$$

where $\lambda^2 = 1.9$ GeV^2. This parametrization provides a better description of the pion form factor in the timelike region [Bro86].

Figure 4.2 shows the results of the model calculation inside the HADES acceptance. The total cross section (solid curve) is obtained by the coherent sum of the dominant Δ resonance amplitudes and NN bremsstrahlung (graphs in Fig. 3.11 a and b), and added incoherently η and ρ contributions. The addition of the pion form factor does not make any difference in the proton-proton case (Fig. 4.2a), because the $\Delta(1232)$ dominates over NN bremsstrahlung, and the model describes the data very well. It is very different in the neutron-proton collisions (Fig. 4.2b) where the pion form factor parametrization from Eq. 4.2 significantly enhances the dielectron yield for $M_{ee} > 0.3$ GeV/c^2 (purple dot-dashed curve) as compared to the no form factor case (blue long-dashed curve), making it larger than η Dalitz decay (green dotted) and ρ_0 decay (red double dot-dashed curve) contributions. Yet, it is not sufficient to describe the measured enhancement in the high mass region. Moreover, the explicit inclusion of the ρ–meson production can lead to double counting due to the pion form factor, which also implicitly includes the ρ. Shyam and Mosel [Shy10b] conclude that the dilepton production data in elementary neutron-proton reactions are very sensitive to the pion electromagnetic form factors.

4.1.2.2 Martemyanov and Krivoruchenko model

Another approach of Martemyanov *et al.* [Mar11] is based on the resonance model of Ref. [Fae03], developed to describe the production of dileptons in nucleon-nucleon collisions at $T_{lab} = 1 - 6$ GeV. The major dilepton production via baryon resonances, as in Ref. [Tei97], is supplemented by the bremsstrahlung contribution [Shy10b], scaled by a monopole form factor, $1/(1 - M^2/m_\rho^2)$, originating from the vector meson dominance (VMD) model. In addition, $np \to de^+e^-$ channel is included and gives large dilepton contribution in the region of masses $M_{ee} > 0.4$ GeV/c^2. The cross section of this process was deduced from the experimental data of the inverse process, deuteron photodisintegration $\gamma d \to np$ [Dou76]. The isotopic relations for two-nucleon final states are preserved (see Ref. [Tei97]), that is, $pp : np = 1 : 1$ for all N^*, except $N(1535)$, where $pp : np = 1 : 5$. Since $N(1535)$ is the only significant source of η–meson, the isotopic ratio for the η is the same as for $N(1535)$. The relations of Δ resonance cross sections are $pp : np = 1 : 2$. The radiative decays of resonances R^0 and R^+ in reactions $np \to pR^0$ and $np \to pR^+$ are incoherently summed up. However, the subsequent decays of the resonances preserve the coherent sum of ρ and ω (see App. B.2). The nucleon momentum distribution in the deuteron was determined from the experimental data on the electron scattering cross section on deuteron [Ber81].

The results of the model are presented within the HADES acceptance in Fig. 4.3. In the case of $pp \to e^+e^-X$ inclusive channel (left panel), the whole spectrum is described by the Δ resonance, followed by a decay to $p\pi^0$ and π^0 Dalitz decay, or by a Δ Dalitz decay. The pp bremmstrahlung contribution is noticeable only at high invariant mass and the other resonances, denoted by R, are negligible. In the case of $np \to e^+e^-X$

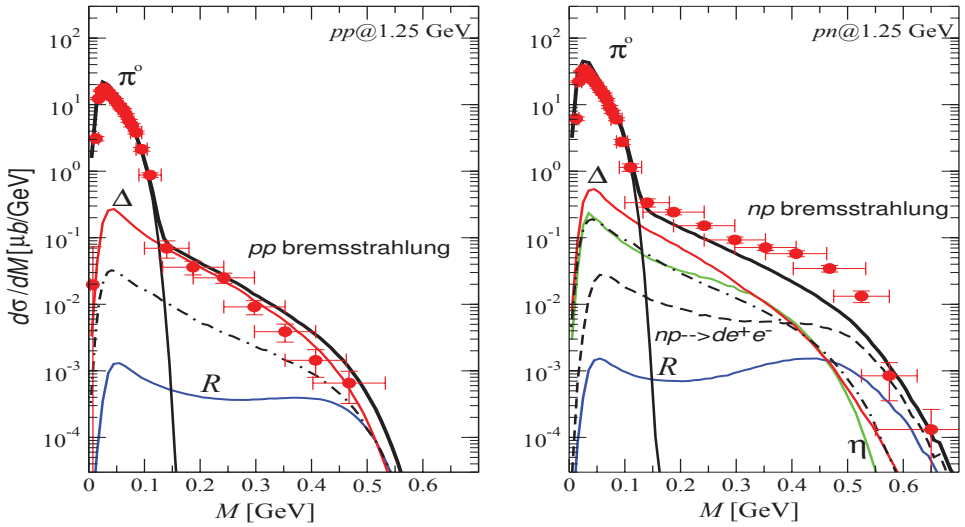

Figure 4.3: Left panel: e^+e^- invariant mass for the $pp \to e^+e^-X$ reaction. The subsequent contributions of π^0–mesons, $\Delta(1232)$, and other baryon resonances R are marked in the figure, pp bremsstrahlung contribution is shown by the dash-dotted curve. Right panel: e^+e^- invariant mass for the $np \to e^+e^-X$ reaction. Additional contributions are η Dalitz decay (green curve) and the radiative capture $np \to de^+e^-$ (dashed curve). All contributions are summed up incoherently (black solid curves in both panels). Figure taken from Ref. [Mar11].

channel (right panel), there are two additional contributions, the η–meson Dalitz decay and the $np \to de^+e^-$ radiative capture. These additional sources, however, are not sufficient to explain of the yield of dileptons in the np collisions.

4.1.2.3 GiBUU model

The GiBUU hadronic transport model is the unified framework for various types of elementary reactions on nuclei as well as heavy-ion collisions [Bus12]. The low-energy part of the nucleon-nucleon collisions are assumed to be dominated by the excitation of baryon resonances, as in the resonance model [Tei97]. The properties (masses, widths and branching ratios) of all resonances are taken from the partial-wave analysis of Manley and Saleski [Man92], based on data from pion-induced reactions. The resonance width parametrization is also used according to Manley prescription (see Eq. 1.7 in Sect. 1.1). The dilepton production in proton-induced reactions at SIS energies with the GiBUU model was presented in Refs. [Wei12, Wei13]. In particular, Fig. 4.4 shows the dielectron invariant mass in the GiBUU approach within the HADES acceptance.

In pp collisions (left panel), the spectrum is dominated by the π^0 and Δ Dalitz decays. The latter decay involves, however, the uncertainty related to the electromagnetic transition form factor which is unknown in the timelike region. The GiBUU incorporates for the Δ Dalitz decay the formula from Ref. [Kri02] (see Eq. 3.5 in Sect. 3.4). At the energy of 1.25 GeV the vector meson pole mass is not reached and the sensitivity to the Δ eTFF is limited. In the figure, the form factor of Iachello-Wan [Iac04, Wan05] (App. B.3) is presented as a red hatched area. Application of of a standard VMD form factor results in the same yield for this energy. The contribution of the subthreshold ρ production (green dashed curve) is negligible. In the π^0 region the GiBUU model

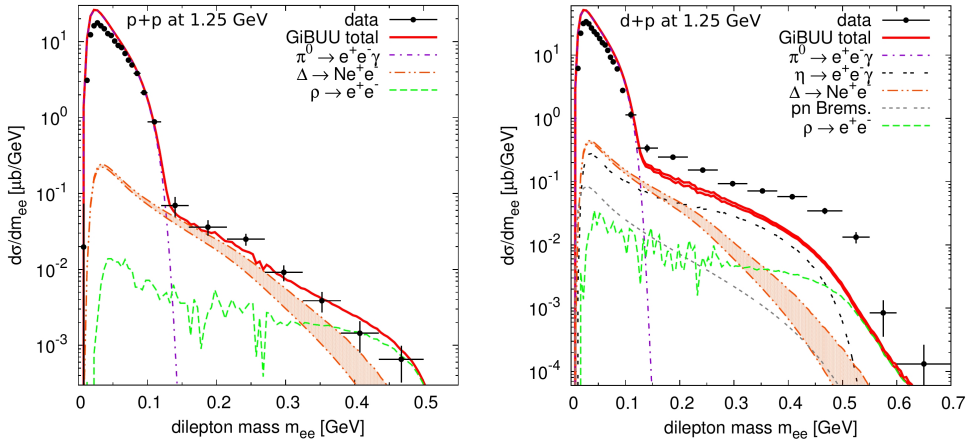

Figure 4.4: Dielectron mass spectrum for pp (left panel) and np (right panel) at 1.25 GeV within the HADES acceptance, compared to the GiBUU contribution (red solid curve) [Wei12]. The red hatched area indicates the effect of the Δ electromagnetic transition form factor in the Iachello-Wan approach [Wan05]. The other contributions are indicated in the figure (see text for details).

overshoots the data what is attributed to the higher resonances, which are produced only in phase space approximation. In quasi-free np collisions (right panel), the available energy is determined by the deuteron potential, which in the GiBUU is given, similarily to Shyam and Mosel OBE calculation (see above), by the Argonne v_{18} potential [Wir95]. In the invariant mass above the π^0, a strong enhancement of the data over the model contribution is observed. The largest contribution in the model stems from η Dalitz decays (short dash-dashed curve), where both channels, $np \to np\eta$ and $np \to d\eta$, are taken into account. The latter one dominates the η production in np collisions at threshold [Cal98]. The Δ resonance form factor (hatched area) does not improve the description since its yield is 1 – 2 orders of magnitude lower than data. The contribution from $np \to np\rho_0$ channel is experimentally not well known. In the GiBUU model, the ρ_0 production in dp at 1.25 GeV/nucleon is dominated by the $D_{13}(1520)$ and $S_{11}(1535)$ resonances. The contribution of NN bremsstrahlung originating from the internal pion lines (as in Shyam and Mosel calculation) is not implemented. Instead, the np bremmstrahlung (short dashed curve) is treated in the soft-photon approximation (see Sect. 3.5) resulting in the much lower yield. The conclusions from Ref. [Wei12] point to the missing ρ–like contributions and emphasize that the comparison of data and model within the spectrometer acceptance is sensitive to the angular distributions of the dilepton sources, which are unknown in many cases.

4.1.2.4 HSD and IQMD model

Yet another analysis was presented in Ref. [Bra13], where the microscopic off-shell Hadron-String-Dynamics (HSD) transport approach [Ehe96, Bra97, Cas99, Bra08] and the Isospin Quantum Molecular Dynamics (IQMD) approach were employed. The HSD model assumes that at higher energies, that is $\sqrt{s_{th}} \geq 2.6$ GeV for inelastic baryon-baryon collisions, and $\sqrt{s_{th}} \geq 2.3$ GeV for inelastic meson-baryon collisions, respectively, hadrons are created by nonresonant mechanisms or string decay [And93]. The low-energy hadron-hadron collisions are modeled using experimental cross sections.

The conventional dilepton sources, π^0, η, ω, Δ Dalitz decays and direct ρ, ω and ϕ vector mesons decays, are described in Ref. [Bra01]. Δ eTFF used in the HSD is derived from Wolf *et al.* calculation [Wol90] (see Fig. 3.6). Only "quasi-elastic" part of the NN bremsstrahlung contribution from Ref. [Kap06] (Sect. 3.6.1) without resonance excitation is taken into account, and the quantum mechanical interference between individual contributions are neglected, as they cannot be treated consistently in transport approaches. The bremsstrahlung calculation does not involve the VMD form factor and the dilepton radiation via the decay of the virtual photon, $pp \to pp\gamma^*$ followed by $\gamma^* \to e^+e^-$, and the direct $\rho \to e^+e^-$ decay are treated separately in the HSD calculations. A proton and a neutron momenta in the deuteron are modeled according to the wave function of the Paris potential [Lac81]. In the IQMD model [Har98, Tho07] all pions are produced by the decay of Δ resonance only. Since no higher mass resonances are included, the model prediction is feasible for beam energies up to 2 GeV/nucleon. As presented on examples of heavy-ion data in Ref. [Bra13], both the IQMD and the HSD models describe the available pion data quite well, which is the good starting point for the dilepton spectra description.

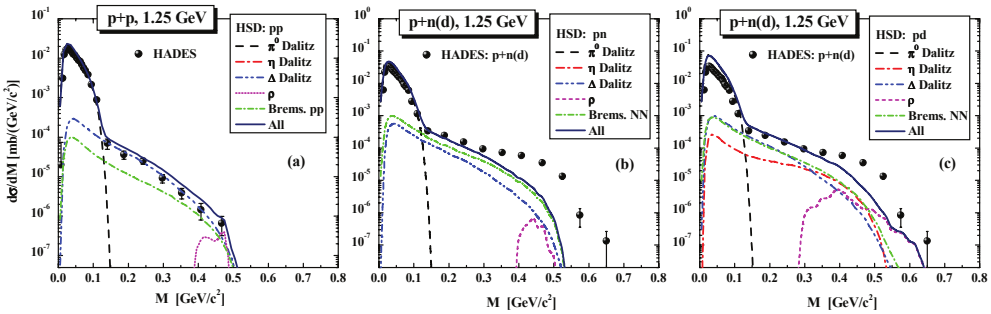

Figure 4.5: The dilepton differential cross section $d\sigma/dM$ of the HSD model for pp (a), np (b), and dp (c) reactions at 1.25 GeV in comparison to the experimental data for pp (a) and quasi-free np (b, c) reactions within the HADES acceptance. The contributions are described in the legends.

Figure 4.5 shows the differential cross section $d\sigma/dM$ for dileptons as a function of the invariant mass M for (a) pp, (b) np, and (c) dp reactions at 1.25 GeV. The pp dilepton yield (left panel) is dominated by the Δ Dalitz decay, but the presented bremsstrahlung contribution is quite significant, too. This reflects, however, only non-resonant part of Kaptari and Kämpfer model [Kap06, Kap09], which, in the case of the full OBE calculation strongly overshoots the data (as presented above in Fig. 4.1). The non-resonant bremsstrahlung is dominating in np collisions (middle panel) but added with the Δ Dalitz decay contribution is not enough to desribe the data. In the right panel (c) the same quasi-free np experimental data are compared to the HSD prediction but for the dp collisions. The idea of this comparison is the statement that the proton does not scatter on a quasi-free neutron but on a deuteron. Although the total dp yield gives a better description just above the π^0 and at the high invariant mass M, it clearly overshoots the π^0 contribution and still does not describe the dielectron excess in the mass range of $0.3 < M < 0.5$ GeV/c^2. Another problem with the quasi-free np scattering is related to the possibility of deuteron formation in the final state, as discussed above in Martemyanov *et al.* model [Mar11]. This is not implemented in the HSD model but the possible impact of the $np \to d\eta$ channel was simulated by the

increased cross section for η production. The missing η contribution turns out to be of the same order of importance as Δ Dalitz decay and np bremsstrahlung around M = 0.4 GeV/c^2. The subthreshold ρ–meson production via excitation and decay of the $N(1520)$ resonance, as shown by the dash-dotted curve in 4.5c, is another possibility to describe the dielectron enhancement. However, the HSD contribution is still well below the data. The IQMD predictions for pp and np collisions are in a very good agreement with the HSD model and therefore fail to describe the much higher dilepton rate in np collisions, in particular regarding the region $M_{e^+e^-} > 0.3$ GeV/c^2.

4.1.2.5 Bashkanov and Clement model

The most recent attempt to explain the enhancement in the np dilepton spectrum was published in Ref. [Bas14], where the observed excess in np data was attributed to $\rho_0 \rightarrow \pi^+\pi^-$ production. At the energy of 1.25 GeV the largest inelastic channel is a single-pion production, dominated by t–channel meson exchange in combination with the excitation of one of the nucleons into the $\Delta(1232)$ resonance or $N(1440)$ resonance, followed by the decay into πN system. The two-pion production process is dominated by t–channel $N(1440)$ at beam energies close to threshold (1 GeV), and $\Delta\Delta$ excitation above 1 GeV. The total inclusive cross section for pp–induced $\pi^+\pi^-$ production at energy 1.25 GeV amounts to about 700 μb. It can be shown from the isospin decomposition (see Ref. [Bas14]) that there is no contribution from $\Delta\Delta$ excitation to ρ_0 channel production and therefore pp dielectron spectrum is not influenced by this production mechanism (Fig. 4.6, left panel).

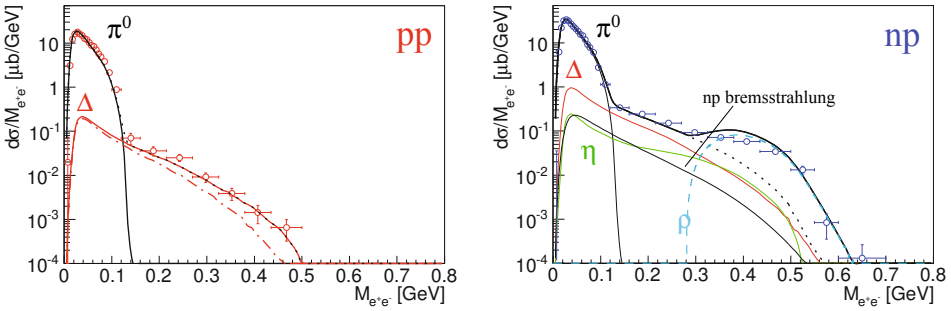

Figure 4.6: Dielectron invariant mass $M_{e^+e^-}$ produced in NN collisions at 1.25 GeV presented within the HADES acceptance. Left panel: pp data (red open circles) with the two leading contributions (π^0 Dalitz and Δ Dalitz decays), with the Δ resonance including form factor (solid curve) and the pointlike form factor (dot-dashed curve). Right panel: np data (blue open circles) with the e^+e^- contribution originating from π^0 and np bremsstrahlung (black curves), signle Δ with VMD form factor (red curve), η (green curve). The sum is denoted by the dotted curve. The cyan dashed curve shows the contribution from the $\rho \rightarrow \pi^+\pi^-$ and the thick solid curve is the sum of all these processes. Figure adopted from Ref. [Bas14].

The situation is very different for two-pion production in np reactions (see Fig. 4.7). This channel us of special importance for the e^+e^- production because of strong dielectron decay branch. Furthremore, the dielectron production is enhanced by the dibaryon resonance structure $d^*(2370)$ with Γ = 70 MeV and I(J^P) = 0(3$^+$), decaying into $d^* \rightarrow \Delta\Delta \rightarrow NN\pi\pi$ [Cle17]. The total inclusive cross section for np–induced $\pi^+\pi^-$ production is about 1300 μb, with the $np\pi^+\pi^-$ and $d\pi^+\pi^-$ channels contributing.

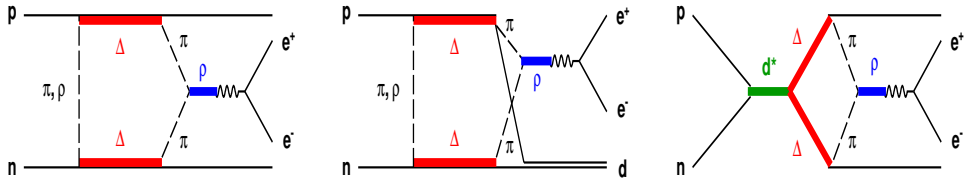

Figure 4.7: e^+e^- production in pn collisions via $\pi^+\pi^- \to \rho^0$ according to Ref. [Bas14], describing sub-process via t–channel $\Delta\Delta$ excitation leading to pn (left graph) and deuteron (middle graph) final states, as well as production via s–channel d^* resonance decaying into $\Delta\Delta$ system (right graph).

The dielectron production from double–Δ excitation proceeds via the intermediate ρ–meson, $\pi^+\pi^- \to \rho_0 \to e^+e^-$, with the isovector $\pi^+\pi^-$ pair being in relative p–wave. The subsequent channels are represented by graphs in Fig. 4.7 and their contributions are:

$$\begin{aligned}
&\sigma(np \to \Delta\Delta \to np[\pi^+\pi^-]_{I=1}) \approx 170\ \mu b,\\
&\sigma(np \to d[\pi^+\pi^-]_{I=1}) = \frac{1}{2}\sigma(pp \to d\pi^+\pi^-) \approx 100\ \mu b,\\
&\sigma(np \to d^* \to np[\pi^+\pi^-]_{I=1}) \approx 40\ \mu b.
\end{aligned} \tag{4.3}$$

The total cross section for the $\rho_0 \to \pi^+\pi^-$ production in np reactions at T_p = 1.25 GeV amounts to 310 μb, with the error estimated to be 20%. The transition from the $[\pi^+\pi^-]_{I=L=1}$ system into the $[e^+e^-]_{L=0}$ system is calculated with the Breit-Wigner formula, as in Refs. [Li95, Koc93] (see also App. A.2.2):

$$|\,\mathcal{M}(\pi^+\pi^- \to \rho_0 \to e^+e^-)\,|^2 \;=\; \frac{m_\rho^2\,\Gamma_{\pi^+\pi^-}\,\Gamma_{e^+e^-}}{(s-m_\rho^2)^2 \;+\; m_\rho^2\,\Gamma_\rho^2}. \tag{4.4}$$

The partial width depends on the invariant masses (see App. A.2.1 and A.2.2), as follows:

$$\begin{aligned}
\Gamma_{\pi^+\pi^-} &= aq^3/M_{\pi^+\pi^-},\\
\Gamma_{e^+e^-} &= bk/M^3_{e^+e^-},
\end{aligned} \tag{4.5}$$

where q and k are the momenta in $\pi^+\pi^-$ and e^+e^- subsystems, respectively. The constants a and b are fixed by adjustment to the branching ratios and widths at the ρ mass pole. Since the models describing $\pi^+\pi^-$ production were adjusted to data, Eq. 4.4 gives the conversion to e^+e^- based on experimental reference. The enhancemet of the e^+e^- yield derives not only from the inverse dependence on the $M_{e^+e^-}$ mass (Eq. 4.5) but also due to the fact, that $\pi^+\pi^-$ pairs in relative p–wave are suppressed near threshold and e^+e^- pairs in relative s–wave are not suppressed. The obtained cross section for the inclusive identification $np \to e^+e^-X$ amounts to 72 nb. As pointed out in Ref. [Wei12], the two-lepton threshold is much lower than the two-pion threshold, therefore modeling of e^+e^- pairs below the two-pion invariant mass requires the virtual ρ_0 treatment. Since it is model dependent, and the $\pi^+\pi^-$ production in Ref. [Bas14] is fitted to experimental results, only on-shell ρ–meson approach is considered.

Figure 4.6 (right panel) presents the e^+e^- invariant mass from np collisions at energy on 1.25 GeV within the HADES acceptance. All standard sources (π^0, η, Δ Dalitz decays as discussed in Sect. 4.1.1 above, and np bremsstrahlung in Shyam and Mosel description [Shy10b]) were added incoherently (dotted curve), giving good description in the π^0 peak, and underestimating the data for $M_{e^+e^-} > 0.3$ GeV/c^2. Additional contribution from $\pi^+\pi^- \to \rho_0 \to e^+e^-$ channel (cyan dashed curve) saturates or even exceeds the whole dielectron excess. The contribution from the direct d^* decay in the $np \to d^* \to de^+e^-$ channel, as suggested in Ref. [Mar11] (see above), was not included in this calculation. In Section 4.3 Bashkanov and Clement calcualtion [Bas14] is compared to exclusive final state npe^+e^- in the quasi-free np reaction, therefore posing more stringent experimental conditions.

4.2 Exclusive ppe⁺e⁻(γ) production (pp at T = 1.25 GeV)

The identification of exclusive dilepton decay channels, ppe^+e^- and $ppe^+e^-\gamma$, allow to access both $\Delta^+ \to p\pi^0(e^+e^-\gamma)$ and $\Delta^+ \to pe^+e^-$ Dalitz decay channels. The reconstruction of the well-known π^0 Dalitz decay can serve as a proof of the consistency of the analysis. The following pp reaction dilepton channels are discussed:

- $\pi^0 \to e^+e^-\gamma$ (BR = 1.194×10^{-2}): The identification of the π^0 in a four-prong channel ($ppe^+e^-\gamma$) allows for the comparison of various differential distributions with the ones extracted from the hadronic channel $pp\pi^0$ [HC15c].
- $\Delta^+ \to pe^+e^-$ (theoretical estimate of BR = 4.2×10^{-5} [Kri02, Zét03a]) for the invariant mass $M_{e^+e^-} > 0.14$ GeV/c^2. The baryonic resonance is identified based on selected characteristic distributions, the Δ angular production, decay, and Δ invariant mass distributions.

All presented spectra (if not stated otherwise) were normalized to the pp elastic scattering yield measured in the same experimental run.

4.2.1 Exclusive ppe⁺e⁻γ channel and π⁰ identification

The production of π^0 has been studied in the analysis of channels with one pion in the final state (Sect. 2.1). Out of the two dominant decay channels ($\pi^0 \to \gamma\gamma$ and $\pi^0 \to \gamma e^+e^-$), the latter one, the π^0 Dalitz decay, can be completely reconstructed with the missing mass technique by the identification of four particles p, p, e^+, e^- in the $ppe^+e^-\gamma$ final state.

Figure 4.8a, shows the e^+e^- invariant mass spectrum as the number of signal pairs (e^+e^- pairs after combinatorial background subtraction) per GeV/c^2, to account for the variable bin size used. The combinatorial background is depicted as a grey hatched area. A strong increase in the CB near the π^0 mass signals the correlated source of dielectrons produced in the conversion of two real photons in the same event, following the $\pi^0 \to \gamma\gamma$ decay. If both e^+ and e^- produced by the same photon are registered, the conversion is effectively suppressed by the e^+e^- opening angle cut of 9°. If only one track from each photon is reconstructed, it contributes to the combinatorial background. The signal-to-background ratio is very high, reaching the value of 400 (see the inset in Fig. 4.8a) and dropping down below 1 near $M_{e^+e^-} \sim 0.14$ GeV/c^2.

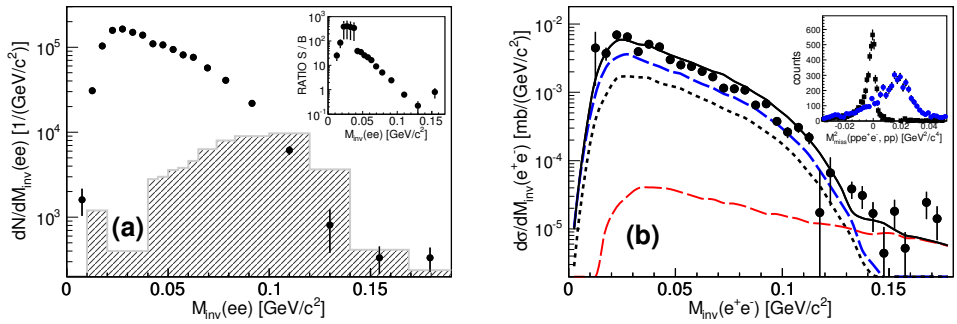

Figure 4.8: $ppe^+e^-\gamma$ final state. (a) e^+e^- uncorrected invariant mass distribution of signal pairs (number of counts is per GeV/c^2 to account for the variable bin width) with the cuts selecting π^0. A grey hatched area represents the combinatorial background (CB). Inset: signal to background ratio. (b) e^+e^- invariant mass within the HADES acceptance. Experimental data (black dots) are corrected for the detection and reconstruction efficiencies. Normalization error is not indicated. The curves display Monte Carlo simulations. Black solid curve represents the total π^0 Dalitz decay as obtained in the partial wave analysis (Sect. 2.1.2). In addition, decomposition to resonances (Δ, blue dashed curve; $N(1440)$, black short dashed curve) decaying to $p\pi^0$; the components are added coherently. Red dashed curve represents Δ Dalitz contribution in a description with a pointlike $\gamma^* NR$ coupling [Zét03a, Doh10]. Inset: missing mass squared of ppe^+e^- (black points) and missing mass squared of two protons (blue points).

To provide a clean signal, a two-dimensional cut on the missing mass of two protons squared (where the missing particle is π^0) and the missing mass of four particles: p, p, e^+, e^- squared (where the missing particle is γ) is applied with a window selecting 95% of all events. Inset in Fig. 4.8b, shows the projected distributions of the missing masses squared. It has been checked both by the experimental data and the Monte Carlo simulation that the variation of the selection window width introduces a systematic error lower than 10%. The number of reconstructed e^+e^- pairs amounts to 7500. Figure 4.8b presents the invariant mass spectrum of e^+e^- within the HADES acceptance. It has been corrected for the detection and reconstruction inefficiencies. The correction is done with the help of a one-dimensional correction histogram, deduced from the Monte Carlo simulations. The correction factor for the masses below π^0 mass amounts to about 20.

4.2.1.1 ppe⁺e⁻γ final state

The partial wave analysis of the final state $pp\pi^0$ (Sect. 2.1.2) provided a very good description of this hadronic channel both in terms of the total cross section 4.2 ± 0.15 mb and the various differential distributions. This analysis provided $pp\pi^0$ events distributed according to the PWA solution. The $\pi^0 \to e^+e^-\gamma$ decay was further implemented in order to generate the full $ppe^+e^-\gamma$ final state and to compare the experimental distributions with the PWA-driven simulated events. Figure 4.8b shows such a comparison for $M_{inv}(e^+e^-)$ within the HADES acceptance. The systematic error of experimental data is 12%. It includes the particle identification, the time reconstruction, the CB rejection, and the missing mass selection. The statistical error is negligible in the π^0 region. The normalization error, given above, is not shown. The Monte Carlo simulation is shown in comparison. The black curve depicts the contribution from all π^0 Dalitz decay events, describing the data very satisfactorily. In addition, the decomposition to the intermediate resonance states is shown: blue dashed curve for $\Delta(1232)$ and

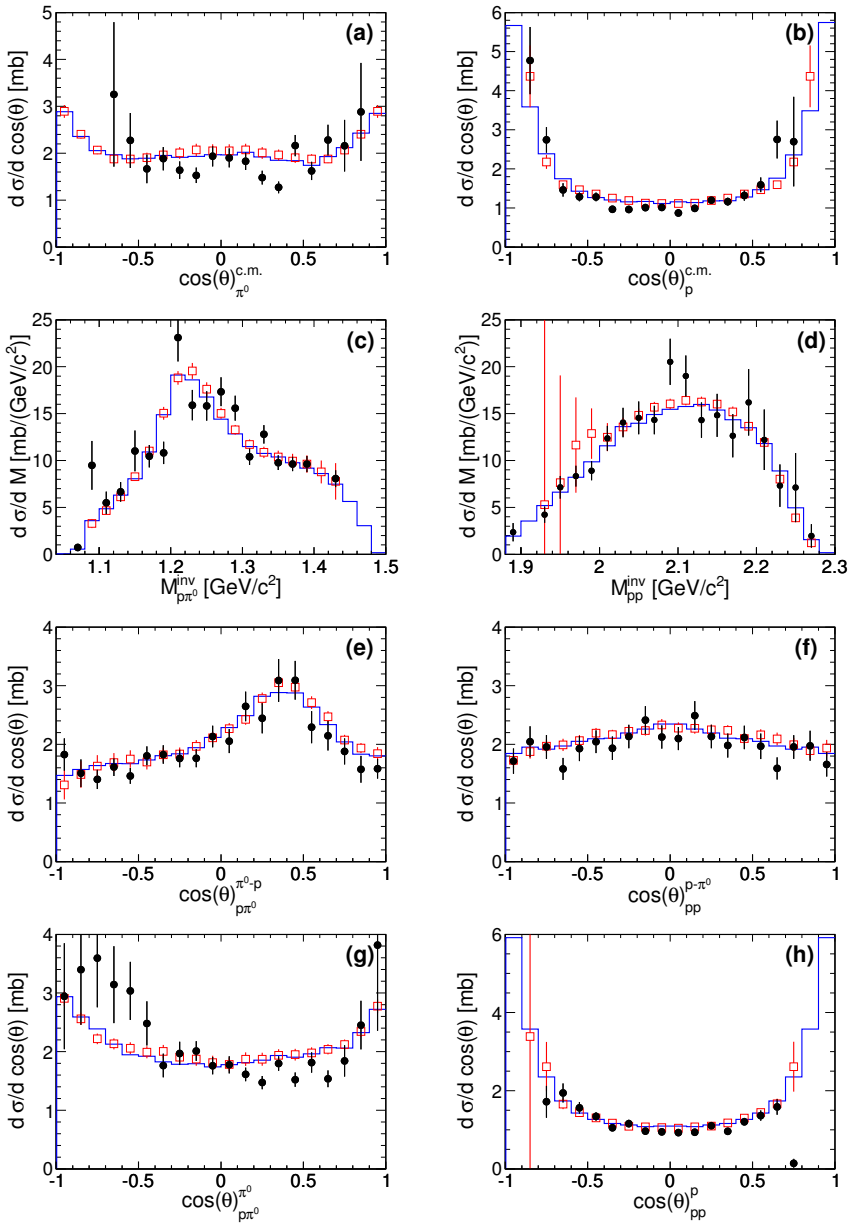

Figure 4.9: Various projections of the $pp\pi^0$ and $pp\pi^0 \to ppe^+e^-\gamma$ channels: angular distributions of (a) π^0 and (b) p in c.m.s. reference frame; invariant mass distributions of (c) $p\pi^0$ and (d) pp; angular distributions in the helicity frame of (e) π^0 in $p\pi^0$ reference frame and (f) p in pp reference frame; and angular distribution of (g) π^0 in $p\pi^0$ GJ reference frame and (h) p in pp GJ reference frame. Dielectron data points after acceptance and BR($\pi^0 \to \gamma e^+e^-$) corrections (black dots) are compared with the data from hadron channel (red open squares). Histograms: total PWA solution (solid blue) obtained for the hadronic channel (see text for details).

black short dashed curve for $N(1440)$, are given by the PWA solutions. There are also non-negligible non-resonant contributions (not shown in the picture). The amplitudes need to be added coherently in order to obtain the total π^0 contribution (black curve). Δ Dalitz decay is shown as a red dashed curve (for details, see Sect. 4.2.2.1).

For a better verification of the dielectron channel in the π^0 Dalitz decay, various distributions of experimental data were compared with the PWA solution and hadron data, as in Sect. 2.1.2. Figure 4.9 shows single particle angular distributions in the center-of-mass (c.m.s.), helicity, and Gottfried-Jackson (GJ) frames and two-particle invariant mass spectra (for definitions, see App. C.3.5.3). The data were corrected for the reconstruction efficiencies and the detector acceptance, each distribution with the respective one-dimensional correction function. The correction factor in the π^0 Dalitz decay channel varies in the range 30 – 50. A direct comparison with the distributions for the hadronic channel requires a correction of dilepton data by the inverse of the BR $= 1.194 \times 10^{-2}$. All projections in Fig. 4.9 demonstrate that the π^0 Dalitz decay reconstruction is well under control and both data in the dielectron and hadronic channels are well described by the PWA solution.

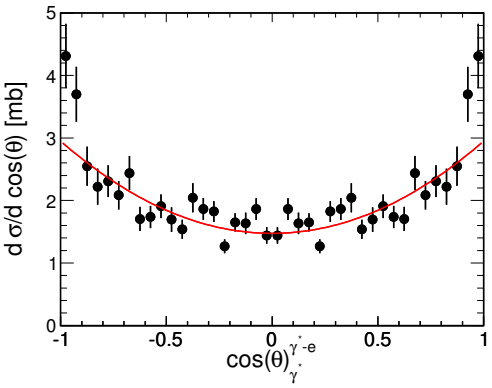

Figure 4.10: $ppe^+e^-\gamma$ final state. The angle between e^+ or e^- and γ^* (upper index) in the γ^* rest frame (lower index) for π^0 Dalitz decay (acceptance corrected). Experiment: black data points with statistical errors only. Fitted formula (red curve) $\propto 1 + B\cos^2\theta$, with $B = 1.00 \pm 0.11$, in agreement with the expected value (see Ref. [Bra95]). The distribution is symmetrized by plotting both e^+ and e^- contributions.

Yet another observable sensitive to the structure of the electromagnetic transition is defined as the angle between a lepton (e^+ or e^-) and the virtual photon γ^* in the rest frame of γ^*, first boosted (leptons and γ^*) to the rest frame of the decaying resonance. This angular distribution has the form $1+B\cos^2\theta$ [Bra95]. In the simplest case of scalar mesons (π^0, η), the anisotropy coefficient is 1, since the helicity conservation in the $\gamma^*\gamma$ decay allows, for the pseudoscalar-vector-vector transitions, only for transverse virtual photons. Figure 4.10 presents the acceptance corrected e^+ or e^- angle in the γ^* reference frame in the reconstructed π^0 Dalitz decay channel. The distribution is symmetrized by plotting both e^+ and e^- contributions. The fit (red curve) returns the parameter B $= 1.00 \pm 0.11$. In addition, the data are also corrected for the BR($\pi^0 \to \gamma e^+e^-$) and the integral over the angular distribution results in the total cross section for the π^0 production, $\sigma(pp \to pp\pi^0) = 4.18$ mb. The statistics error is negligible (less than 2%), and the systematic and normalization errors are 12% and 8%, respectively, as discussed above. Both the anisotropy and the deduced cross section are in agreement with the predictions for the neutral pion Dalitz decay and the description of the π^0 production in the PWA framework ($\sigma_{\pi^0}^{PWA} = 4.2\pm0.15$ mb). These results prove the perfect consistency of the analyses of the leptonic and hadronic channels for the π^0 reconstruction. The high quality of the reconstruction of electromagnetic channels with HADES will be further exploited for the reconstruction of the ppe^+e^- channel. The results confirm the consistency of the PWA analysis, based on hadronic channels, providing the Δ^+ contribution, which is essential for the BR($\Delta \to pe^+e^-$) estimate.

According to the PWA description (Sect. 2.1.2 and Ref. [HC15a]), the contribution of the Δ resonance to the channel with one neutral pion in the final state is 70%. The remaining part results from $N(1440)$ decay and non-resonant $^3P_2$ partial wave, destructively interfering with the Roper resonance. Since no notable influence of interferences with non-resonant partial waves was observed for the $\Delta(1232)$ contribution, the estimate from the PWA can be safely taken as the Δ production cross section input for the simulation of the Δ Dalitz decay. In addition, the contribution of nucleon-nucleon bremsstrahlung is expected to be small, as will be discussed in the next section.

4.2.2 Δ Dalitz decay in the ppe⁺e⁻ channel

The identification of three particles (p, e^+, e^-) in the ppe^+e^- final state allows for the kinematically complete (exclusive) reconstruction of the Δ Dalitz decay channel under two conditions: (a) selection of the missing mass of pe^+e^- ($M_{miss}^{pe^+e^-}$), close to the proton mass as a signature of the exclusive $pp \rightarrow ppe^+e^-$ reaction; (b) invariant mass $M_{e^+e^-} > M_{\pi^0}$ for a rejection of the π^0 Dalitz decay. Although the exit channel is in this case γe^+e^-, it is only partially suppressed by cut a due to the finite missing mass resolution and the cut b is needed for the channel separation.

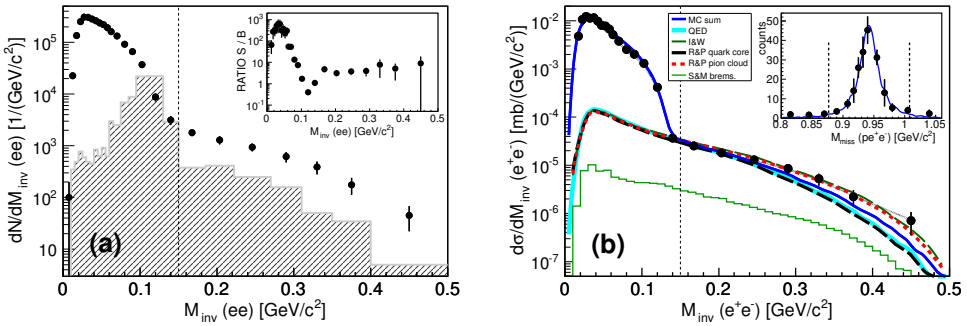

Figure 4.11: ppe^+e^- final state. (a) Invariant mass spectrum of e^+e^- signal pairs (uncorrected data points, number of counts is per GeV/c^2) within the pe^+e^- missing mass selection window. The grey hatched area represents the combinatorial background (CB). Inset: signal-to-background ratio. (b) e^+e^- invariant mass within the HADES acceptance. Experimental data (black dots) are corrected for the detection and reconstruction inefficiencies (the grey thin band indicates the uncertainty of corrections; for more details, see text). Blue curve represents the sum of the following contributions: π^0 Dalitz decay, Δ Dalitz decay according to Ref. [Ram16] (App. B.4) and bremsstrahlung according to Ref. [Shy10b] (Sect. 3.6.2). The cyan curve represents the Δ Dalitz contribution in a description with a pointlike $\gamma^* NR$ coupling (QED model) [Zét03a, Doh10] (App. B.1). The two-component Iachello-Wan model [Iac04, Wan05, Wan06] (App. B.3), depicted with dashed dark green curve, has the largest contribution. The two components of the Ramalho-Peña model [Ram16] are shown after scaling each of them up to the same yield as in the full model: quark core (dashed black curve) and pion cloud (dashed red curve). All model contributions are supplemented with the bremsstrahlung (shown also separately as a green histogram). Normalization error is not indicated. The vertical dashed line at 0.15 GeV/c^2 divides the area of π^0 mass and higher masses. Inset: pe^+e^- missing mass for $M_{inv}^{e^+e^-} > 0.15$ GeV/c^2. The blue curve shows the simulation of the Δ Dalitz scaled to the same yield. Vertical dashed lines limit the window around the mass of the missing proton.

In about 20% of all events, both protons are measured. Since there is no clear identification of the proton produced by the Δ decay, all projections using proton variables in their construction are added with a weight of 0.5 for both protons in the final state, i.e., (a) both protons ($p_1e^+e^-$) and ($p_2e^+e^-$) if p_1 and p_2 are measured and (b) measured proton (pe^+e^-) and missing proton ($p_{miss}e^+e^-$) if only p is measured.

Figure 4.11a shows the e^+e^- invariant mass spectrum as the number of e^+e^- signal pairs per GeV/c^2 to account for the variable bin width used. The CB is depicted as a grey hatched area. The data are plotted for a missing mass selection $0.85 < M_{miss}^{pe^+e^-} < 1.03$ GeV/c^2 around the proton mass (5σ cut, see inset in Fig. 4.11b). Due to the finite reconstruction resolution, a cut to reject π^0 Dalitz decay has been applied at $M_{e^+e^-} > 0.15$ GeV/c^2 (vertical dashed line). The spectrum spans up to the mass $M_{e^+e^-} \sim 0.5$ GeV/c^2, which is close to the excess energy 0.54 GeV available in the pp collisions for the 1.25 GeV kinetic beam energy. The signal-to-background ratio in the area above M_{π^0} reaches 7 – 10 (Fig. 4.11a, inset). The number of reconstructed e^+e^- pairs amounts to ~15500 below 0.15 GeV/c^2 and strongly depends on the missing mass $M_{miss}^{pe^+e^-}$ selection window. The variation of the e^+e^- yield due to the window size shows, however, that it introduces a systematic error of less than 10% as compared to simulation. The number of e^+e^- pairs for $M_{e^+e^-} > 0.15$ GeV/c^2 amounts to 209 pairs. It is not dependent on the missing mass cut unless the selection window is at least 3σ. Figure 4.11b (inset) shows that the Monte Carlo simulation (blue curve) of the Δ Dalitz decay gives a very similar resolution as the experimental data reconstruction.

Figure 4.11b presents the invariant mass spectrum of e^+e^- and Fig. 4.12 displays the invariant mass spectrum of pe^+e^- (equivalent to missing mass of $pp \to pe^+e^-X$) for $M_{inv}^{e^+e^-} > 0.15$ GeV/c^2, within the HADES acceptance, respectively. Both spectra are corrected for the detection and reconstruction inefficiencies. The experimental data corrected with various models span over the grey band, which defines the systematic (root-mean-square) error due to the model dependent inefficiency correction. The correction factor for masses larger than the π^0 mass is essentially almost constant and amounts to about 11. The pe^+e^- invariant mass (Fig. 4.12) does not display the usual Δ resonance shape with the peak at 1.232 GeV/c^2 mass due to the selection of events with $M_{inv}^{e^+e^-} > 0.15$ GeV/c^2, which naturally favors high pe^+e^- masses and results in a distorted Δ spectral function.

4.2.2.1 ppe⁺e⁻ final state

To estimate the contribution of π^0 Dalitz decay in the pe^+e^- channel, corresponding analysis cuts were applied to simulated events generated with the same model as for the $ppe^+e^-\gamma$ analysis (Sect. 4.2.1.1). It can be observed that the e^+e^- invariant mass in π^0 region is described very well by the Monte Carlo simulation within the HADES acceptance (Fig. 4.11b). This proves the consistency of the three- and four-prong analyses and the very detailed description of the pe^+e^- missing mass resolution, since, as observed above, the yield in this region is strongly dependent on the missing mass cuts.

The experimental data are confronted with two descriptions of the Δ eTFF. First, a pointlike γ^*NR model, described in App. B.1, is used (QED model). The second model is a two-component covariant model by Ramalho-Peña [Ram16] (App. B.4). In all cases, the Δ resonance parametrization and production is taken from the PWA solution (as discussed in Sect. 4.2.1.1) as well as the cross section $\sigma_\Delta = 4.45 \pm 0.33$ mb. The Δ Dalitz decay is then implemented using the differential decay width calculated as a function of the running mass of the resonance and of the e^+e^- invariant mass in the description of the Krivoruchenko formula, see Eq. 3.9 and Refs. [Kri01, Doh10].

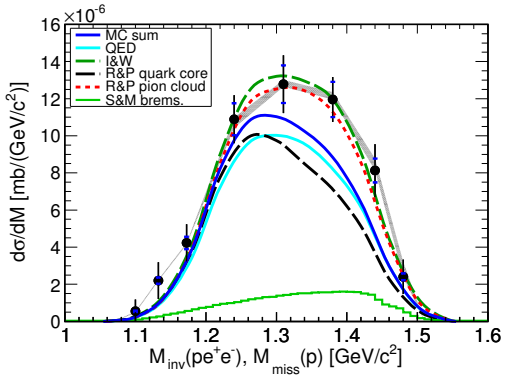

Figure 4.12: ppe^+e^- final state for the $M_{inv}^{e^+e^-} > 0.15$ GeV/c^2. Invariant mass of pe^+e^- and missing mass of a proton within the HADES acceptance (data are corrected for the reconstruction efficiency and plotted with the variable bin width). The grey band indicates the uncertainty of model-dependent one-dimensional efficiency and acceptance corrections (for details, see text). Vertical error bars represent statistical error, and blue horizontal bars indicate normalization error. Monte Carlo simulations: blue curve represents the sum of the Δ Dalitz decay according to Ref. [Ram16] and non-resonant part of NN bremsstrahlung according to Ref. [Shy10b] (solid green line histogram). Color codes of the other curves are as in Fig. 4.11b.

Besides the dominant Δ resonance contribution, a non-resonant virtual photon emission is added to the description, referred to as nucleon-nucleon bremsstrahlung. As discussed in Sect. 3.6, the models provide the total e^+e^- contribution based on a coherent sum of many graphs describing the Δ resonance and the nucleon-nucleon bremsstrahlung contributions. In our simulation we have used the Shyam and Mosel model, which describes better data in pp and np collisions at 1.25 GeV (Sect. 4.1.2.1). It predicts the relative contribution of the nucleon-nucleon bremsstrahlung to Δ production on a level of 9%. It is presented as a green line histogram in Fig. 4.11b and also in Fig. 4.12. The contribution of the $N(1440)$ Dalitz decay can be neglected [Wol90].

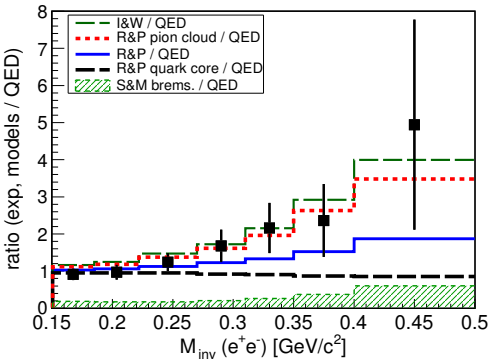

Figure 4.13: ppe^+e^- final state. The ratio of the experimental data (squares with error bars) to the simulated contribution of the Δ resonance with a pointlike form factor (QED model) [Doh10] as a function of the invariant mass of e^+e^-. The experimental data are after subtraction of the simulated non-resonant nucleon-nucleon part of bremsstrahlung according to Ref. [Shy10b]. Vertical error bars represent statistical error only. Various models are also divided by the QED model contribution (see text for details). Distributions are plotted with the same variable bin width as in Fig. 4.11b.

The solid cyan curve in Fig. 4.11b represents the simplest case: the Δ contribution with a pointlike $\gamma^* N\Delta$ form factor [Doh10] (App. B.1) and the NN bremsstrahlung [Shy10b] (Sect. 3.6.2). The QED model can be considered as a lower level estimate of the Δ contribution. The blue solid curve is the sum of the full Ramalho-Peña model contribution [Ram16] (App. B.4) and, as above, the NN bremsstrahlung. The Δ decay in this model is calculated with a mass-dependent eTFF with separate contributions from the quark core and the pion cloud. The presence of the form factor enhances the e^+e^- yield at large invariant masses. The model describes the data just above the

π^0 mass quite well but at higher e^+e^- masses the data points present still an excess above the model. A possible explanation on the origin of the e^+e^- excess might be drawn from the comparison of the components in the Ramalho-Peña model. In order to do a qualitative comparison of the shape of the distribution, both components were scaled up to the same total yield in the full solid angle. The first component, the bare quark core (supplemented by bremsstrahlung), is plotted in Fig. 4.11b by a black dashed curve. Its distribution is similar to the QED model (cyan curve). This is expected, since this part of the form factor stays constant for the four-momentum transfer squared probed in our experiment. The second component, related to the pion cloud (also supplemented by bremsstrahlung), is plotted as the dotted red curve. The distribution practically describes the data points within their error bars, which might indicate that this model component has a correct q^2 dependence and is slightly underestimated in the model. The largest contribution is provided by the Iachello-Wan model [Iac04] (App. B.3), supplemented by the bremsstrahlung yield (dashed dark green curve). It tends to overshoot the experimental contribution at the intermediate-mass $0.14 < M_{inv}(e^+e^-) < 0.28$ GeV/c^2 while giving the good description at the high-mass $M_{inv}(e^+e^-) > 0.28$ GeV/c^2.

The same model contributions are compared with the experimental data within the HADES acceptance in Fig. 4.12, where the invariant mass of pe^+e^- (or missing mass of p) is presented for $M_{inv}(e^+e^-) > 0.15$ GeV/c^2. The grey band reflects again the rms error due to the model-dependent acceptance correction. All curves are the same as in Fig. 4.11b. As observed above for the e^+e^- invariant mass, the pion cloud part of the Ramalho-Peña model (plus bremsstrahlung) delivers the description closest to the data. The Iachello-Wan model (plus bremsstrahlung) has a higher contribution, however, within the experimental error bars.

In order to quantify the effect of the $N-\Delta$ transition form factor, the ratio of the experimental data to the simulations using the pointlike form factor (QED model) [Doh10] is shown in Fig. 4.13 as a function of the e^+e^- invariant mass. It is integrated over the Δ mass distribution as given in Fig. 4.12. First, the simulated contribution of the non-resonant part (bremsstrahlung) [Shy10b] is subtracted from the data (it is shown as a green hatched histogram). The Ramalho-Peña model (solid blue) [Ram16] gives a good description of the data for masses $M_{inv}(e^+e^-) < 0.28$ GeV/c^2 but then it tends to underestimate the excess. The separated pion cloud component of this model (dotted red) is the closest to the data in the whole range. The Iachello-Wan model [Iac04] also describes the data well. However, the vector meson contribution in this model is not consistent with the pion electromagnetic form factor data. The differences in the parametrization of the eTFF of the pion, discussed in Sect. 3.4, are smaller than the experimental uncertainty in the studied mass range. Since they increase with the invariant mass, they have a large impact for dilepton production at higher energies (see Sect. 4.9). The quark core component of the Ramalho-Peña model (dashed black) is very close to the pointlike contribution, as expected.

An important observable describing the resonance is the production angle of the resonance system, which is found to be very anisotropic in the c.m.s., both experimentally and in various model descriptions, i.e., one-pion exchange models [Tei97, Dmi86] (Sect. 1.2) or PWA [Erm11, Erm14, Erm17, HC15a] (Sect. 2.1.2). The strong forward-backward peaking reflects the peripheral character of the Δ resonance excitation. Figure 4.14a presents the angular distribution of pe^+e^- or missing p in the c.m.s. First, the simulated bremsstrahlung contribution with the angular distribution modeled in line with the Δ, depicted as the green shaded histogram at the bottom, was subtracted

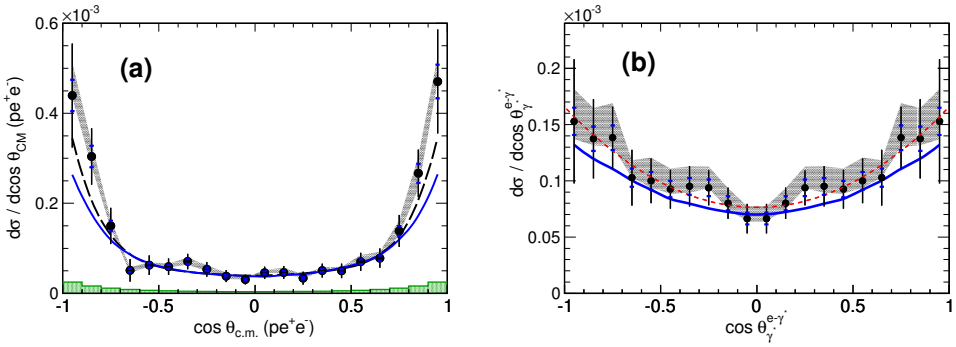

Figure 4.14: ppe^+e^- final state for $M_{inv}^{e^+e^-} > 0.15$ GeV/c^2. Experimental data (see symbols with error bars) are corrected for the acceptance and reconstruction inefficiencies. Both distributions are after subtraction of the simulated bremsstrahlung contribution. (a) Angular distribution of pe^+e^- (or missing p) in the c.m.s. (black dots); green shaded area at the bottom represents bremsstrahlung (see text for details). (b) e^+ and e^- angle along the γ^* direction (upper index) in the γ^* rest frame (lower index). Red dashed curve is a fit $\sim 1 + B\cos^2\theta$, where $B = 1.17 \pm 0.34$. The grey band indicates the uncertainty introduced by the model-dependent correction in both cases. Vertical error bars represent statistical error; blue horizontal bars indicate the normalization error. The blue curve in both cases denotes simulation results, assuming Δ Dalitz decay according to model of Ref. [Ram16]. The black dashed curve [panel (a)] represents the Δ production from hadronic channel in the PWA description (Sect. 2.1.2), renormalized to the same yield as the data points in the angular range -0.8 $< \cos\theta_{c.m.}(pe^+e^-) <$ +0.8.

from the data points. The projection was corrected for the reconstruction inefficiencies and the detector acceptance, with a one-dimensional correction function. The data are compared to the simulation using the Ramalho-Peña model [Ram16] (blue curve). The pe^+e^- distribution is affected by the dependence of the angular distribution on the Δ mass. Indeed, the Ramalho-Peña model enhances the weight of heavier Δs, which are produced with a flatter angular distribution. The predicted yield from this model is not sufficient in the very forward-backward parts of the angular distribution. This is consistent with the observation in the hadronic channel $pp \to p\Delta^+ \to pp\pi^0$ [HC15a], where a similar underestimation of the proton c.m.s. angular distribution was observed at forward-backward angles (dashed black curve).

Another distribution represents angles between e^+ or e^- in the γ^* rest frame and the γ^* itself, where dielectrons and γ^* are boosted to the Δ rest frame (Fig. 4.14b). This angle is measured with respect to the momentum of the γ^* in the Δ reference frame. The data were corrected for the reconstruction inefficiencies and the detector acceptance. The fit to the data in the form of $1 + B\cos^2\theta$ is presented in Fig. 4.14b (red dashed curve) resulting in $B = 1.17 \pm 0.34$ (the fitting error includes statistical error only). This is in agreement with calculations from Ref. [Bra95] where the anisotropy factor $B = 1$ is expected if the contributions of longitudinal photons is negligible. The blue curve represents the Monte Carlo simulation (as in the models discussed). The subtraction of the bremsstrahlung contribution modeled in the Monte Carlo simulation with a homogeneous distribution does not influence the fit result. Both angular distributions confirm the identification of the Δ resonance.

4.2.3 Δ(1232) Dalitz decay branching ratio

The identification of the Δ(1232) resonance in the Dalitz decay channel allows for the experimental determination of the branching ratio. The calculation is based on the yield measured as a function of the pe^+e^- angle (Fig. 4.14a) and is limited to the range -0.8 $< \cos\theta_{c.m.}(pe^+e^-) <$ +0.8, where both the hadronic and dielectron channels agree very well and systematic errors due to acceptance correction are lowest. One should note that the experimental Δ Dalitz decay yield is measured for e^+e^- invariant masses $M_{inv}^{e^+e^-} > 0.15$ GeV/c^2, which favors high Δ masses, as observed in Fig. 4.12. In addition, due to the indiscernibility of two protons, the mass of the resonance cannot be reconstructed in a unique way. Nevertheless, simulations can be used to deduce the branching ratio at the pole from the measured Dalitz decay yield. For this purpose, we have used simulations based on the constituent covariant quark model [Ram16] and QED model [Zét03a, Doh10], which describe the shapes of the experimental distributions very well. In addition, both simulations are based on the Δ production amplitudes deduced from the Δ pionic decay channels via the PWA. Thus, they can be safely used to extrapolate the Dalitz decay yield to the whole phase space. Both models provide a branching ratio value at the pole mass 1.232 GeV/c^2, BR($\Delta \to pe^+e^-$) = 4.2×10^{-5}.

The procedure for deducing the branching ratio is hence enforced in the following steps:

- The experimental yield N_{exp} (after the bremsstrahlung subtraction) in the range of -0.8 $< \cos\theta <$ +0.8 is calculated.
- Similarly, the integrated yield of simulated events N_{model} (QED model as well as Ramalho-Peña model) is extracted.
- The branching ratio at the pole position is calculated by scaling the known BR of the models by the ratio of the integrated experimental and the model yields

$$BR_{exp}(\Delta \to pe^+e^-) = 4.2 \times 10^{-5} \ \frac{N_{exp}}{N_{model}}. \tag{4.6}$$

The obtained Δ Dalitz branching ratio at the pole position is equal to 4.19 × 10^{-5} when extrapolated with the help of the Ramalho-Peña model [Ram16], which is taken as the reference, since it describes the data better. The branching ratio deduced with the QED model differs by 6%. The estimate of the branching ratio also depends on the cross section for the Δ production drawn from the PWA solution which is affected by the error of 7.4% ($\sigma_\Delta = 4.45 \pm 0.33$). Both contributions are included in the systematic error due to model uncertainty which amounts in total to 10%. The systematic error of the PWA solution the error due to the normalization of the data was excluded, since the same error affects the dielectron yield. Systematic errors related to the data reconstruction are similar to those presented in Sect. 4.2.1.1. Contributions to the systematic error, studied carefully by means of a Monte Carlo simulations, are due to the absolute time reconstruction, particle identification, rejection of γ conversion, CB subtraction, missing mass window cut, efficiency, and acceptance correction uncertainty. All errors, added quadratically, result in a total systematic error of 11%. The statistical error amounts to 8%. Finally, the branching ratio is BR($\Delta \to pe^+e^-$) = (4.19 ± 0.42 model ± 0.46 syst. ± 0.34 stat.) × 10^{-5}. This result has been included in the 2018 Review of Particle Physics.

4.3 Exclusive npe⁺e⁻ production (np at T = 1.25 GeV)

In the *dp* collisions at 1.25 GeV/nucleon, the dielectron production in the final state $NN\gamma^*(e^+e^-)$, enables to study bremsstrahlung radiation. In general, the bremsstrahlung yield is given by a coherent sum of two types of amplitudes originating from "pure" nucleon-nucleon interactions and intermediate resonance excitation processes (Sect. 3.5). The nucleon contribution provides information on the elastic timelike electromagnetic form factors in a region of four-momentum transfer squared $0 < q^2 \ll 4m_p^2$, where m_p is the proton mass, which is inaccessible to measurements in e^+e^- or $\bar{p}p$ annihilation. The resonance contribution includes the production of baryon resonance (Δ, N^*) states. One might visualize this contribution as resonance excitation subsequently decaying into Ne^+e^- via the Dalitz process (since momentum-space diagrams have no time ordering, also other resonance - Ne^+e^- vertices are to be accounted for). This process gives access to the timelike electromagnetic form factors of baryonic transitions in a complementary way to meson photo- or electroproduction experiments where negative (i.e. spacelike) values of q^2 are probed.

Full quantum mechanics calculations have been performed for $np \to npe^+e^-$ based on effective model Lagrangians (Sect. 3.6), composing the nucleon-nucleon interaction via the exchange of mesons ($\pi, \rho, \omega, \sigma$,...). The virtual photon production happens at γ^*NN, $\gamma^*NN^\star$ and $\gamma^*N\Delta$ vertices and off meson exchange lines. The production amplitude of the virtual photon γ^* depends on the electromagnetic structure of the nucleons and on the excited baryon resonances. In the kinematic region of small positive (timelike) values of the squared four-momentum transfer $q^2 = M^2_{\gamma^*} = M^2_{e^+e^-}$ ($q^2 > 0$), these electromagnetic amplitudes are related to off-shell light vector meson production [Mos91]. Another approach, often used in microscopic transport model calculations to account for the nucleon-nucleon bremsstrahlung, is the soft photon approximation [Rüc76, Gal87, Gal89] (Sect. 3.5). It assumes photon emission following elastic nucleon-nucleon interactions with an appropriate phase space modification induced by the produced virtual photon, with interference processes to be neglected. Contributions from the Δ isobar and higher resonances are added incoherently and treated as separate source of pairs.

In the energy range relevant to the HADES measurement, the bremsstrahlung production in proton-proton collisions is dominated by the Δ resonance excitation. In neutron-proton collisions, however, the nucleon-nucleon non-resonant contribution also plays a significant role, since it is 5 to 10 times stronger than in proton-proton collisions. The results of various calculations show some sensitivity to the electromagnetic form factors and to details of the implementation of gauge invariance in the calculations, in particular those related to the emission off the charged pion exchange (for details see Sect. 3.6.2). The adjustment of various effects on coupling constants is crucial, too. Consequently, the cross sections can differ between the models substantially (up to a factor 2 – 4) in some phase space regions and need to be constrained further by experimental data.

A very strong isospin dependence in NN reactions was demonstrated by the DLS experiment [DC98] measuring excitation functions of the pair production in *pp* and *dp* collisions in the beam energy range E_{beam} 1 – 4.88 GeV. Despite the limited statistics and large systematic errors related to normalization, a strong increase of the dielectron pairs (in the $M_{e^+e^-} > M_{\pi^0}$ range) in *dp* reactions over the yield measured in *pp* below 2 GeV, was observed.

The main goal of investigating the exclusive reaction $np \to npe^+e^-$ is two-fold: (i) to verify whether the observed enhancement of the inclusive dielectron production over pp data has its origin in the exclusive npe^+e^- final state, and (ii) to provide various multi-particle differential distributions of the exclusive final state to characterize the production mechanism and provide more constraints for the comparison to models.

The procedure of identification of the npe^+e^- final state is initiated by the event selection requesting at least one track with a positive charge, at least one dielectron pair (like-sign or unlike-sign) detected in the HADES, and at least one hit in the FW.

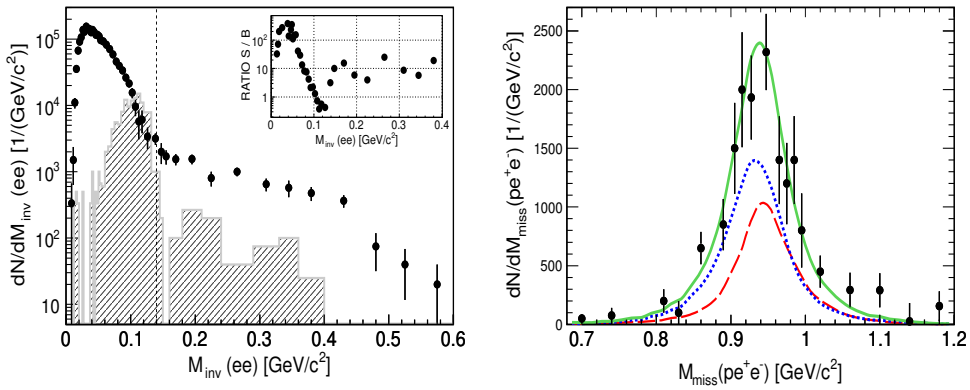

Figure 4.15: Events with npe^+e^- final state. Left: invariant mass distributions of e^+e^- signal pairs (black dots), the combinatorial background (CB) (hatched histogram) and the signal/background ratio (inset). Experimental data (black dots) are within the HADES acceptance and not corrected for reconstruction inefficiency. Right: the pe^+e^- missing mass for $np \to pe^+e^-X$ reaction and dielectron invariant masses $M_{e+e-} > 0.14$ GeV/c^2 (dots) overlayed with a Monte Carlo simulation (green curve) normalized to the same yield as the data. Two major contributions of model A are depicted: dotted blue curve - ρ–meson contribution, dashed red curve - Δ contribution (see text for details). In both cases, the number of counts is given per GeV/c^2 to account for the variable bin width. Only statistical errors are indicated.

Further, for all pe^+e^- candidates in an event, the missing mass for $np \to pe^+e^-X$ was calculated, assuming the incident neutron carrying half of the deuteron momentum. The exclusive npe^+e^- final state was finally selected via a one-dimensional cut centered around the mass of the neutron $0.8 < M^{miss}_{pe^+e^-} < 1.08$ GeV/c^2 (3σ cut). A variation of this selection has no influence on the data at $M_{inv}(e^+e^-) > 0.14$ GeV/c^2 and introduces a systematic error on the yield of about 10% for the π^0 region, as deduced from comparisons to Monte Carlo simulations. It was checked that the missing mass distribution width only slightly depends on the invariant mass $M_{e^+e^-}$ (see Tab. 4.1, last column).

The same procedure was also applied for the pe^-e^- and the pe^+e^+ track combinations in order to estimate the combinatorial background (CB) originating mainly from a multi-pion production followed by a photon conversion in the detector material. The resulting e^+e^- invariant mass distributions of the signal and the CB are shown in Fig. 4.15 (left panel) together with the signal to background ratio (inset) for the identified pe^+e^- events. In the invariant mass region above the prominent π^0 Dalitz decay peak, the signal is measured with a small background. The number of the reconstructed signal e^+e^- pairs and the number of the CB pairs is quoted in Table 4.1. In Fig. 4.15 (right panel), the missing mass distribution of the pe^+e^- system with respect to the projectile-target is shown for the events with the invariant mass $M_{e^+e^-} > 0.14$ GeV/c^2.

$\mathbf{M}_{ee}^{inv}$ GeV/c^2	$\mathbf{N}_{SIG}$	$\mathbf{N}_{CB}$	$\sigma(M_{pe^+e^-}^{miss})$ GeV/c^2
$M_{ee} < 0.14$	7240	600	–
$M_{ee} > 0.14$	280	26	0.047
$0.14 < M_{ee} < 0.28$	184	19	0.051
$M_{ee} > 0.28$	96	7	0.042

Table 4.1: Number of e^+e^- (or e^+e^+ and e^-e^- for CB) pairs in a given invariant mass range: signal pairs (N_{SIG}) and combinatorial background (N_{CB}). The last column presents the width (σ) of the missing mass distribution $np \to pe^+e^-X$.

The data are compared to a Monte Carlo simulation - green solid curve (model A, see Sect. 4.3.1 for details). Its total yield has been normalized to the experimental yield to demonstrate the very good description of the shape of the distribution. One should note that a broadening of the missing mass distribution is caused by the momentum distribution of the neutron in a deuteron, which is accounted for in the simulation. The spectrometer resolution causes half of the measured width.

Contributions to the systematic error of the e^+e^- yield were studied carefully by means of Monte Carlo simulations. They are due to the absolute time reconstruction, particle identification, rejection of γ conversion, CB subtraction, missing mass window cut, and efficiency correction uncertainty. All errors, added quadratically, result in a total systematic error of 10%.

4.3.1 npe⁺e⁻ final state

The most recent calculations of Shyam and Mosel [Shy10b] and Bashkanov and Clement [Bas14] offer an explanation of inclusive dielectron data measured in np collisions at $T = 1.25$ GeV (see Sect. 4.1.2.5). A characteristic feature of both models is an enhancement in the dielectron invariant mass spectrum for $M_{e^+e^-} > 0.3$ GeV/c^2 due to the intermediate ρ–like state in the in-flight emission by the exchanged charged pions, which are present in the case of the $np \to npe^+e^-$ reaction, unlike in the $pp \to ppe^+e^-$ reaction. A major difference between the models is that the charged pions are exchanged between two Δs in Ref. [Bas14] (Fig. 4.7 in Sect. 4.1.2.5) and between two nucleons in Ref. [Shy10b] (Fig. 3.11 in Sect. 3.6.2). These models were selected as a basis for the simulation (described in details below).

The model [Bas14] assumes a sub-threshold ρ–meson production, via intermediate double $\Delta^+\Delta^0$ or $\Delta^{++}\Delta^-$ excitation, and its subsequent e^+e^- decay, according to a strict vector dominance model [Sak60]. The total cross section, for the $np \to \Delta\Delta$ channel, has been predicted to be $\sigma_{\Delta\Delta} = 170\ \mu b$. The dielectron decays of the γ^* have been modeled in the simulations following the VDM prescription for the ρ–meson differential decay rate and assuming the isotropic electron decay in the virtual photon rest frame.

The remaining dielectron sources (π^0, Δ and η Dalitz decays) were computed using the PLUTO event generator [Frö07]. The detailed description of the procedure was published in Refs. [HC10,Doh10], and in fact the calculations in Ref. [Bas14] use exactly the same method. For the Δ Dalitz decay, the QED model was used, with the constant electromagnetic Transition Form Factors (eTFF) fixed to their values at the real-photon point. As a consequence, the Coulomb form factor is neglected and the e^+ or e^- angular distribution with respect to the γ^* in the rest frame of the γ^*, is taken as $\propto 1 + \cos^2\theta$, in agreement with data [HC17b] (Sect. 4.2).

The following channels are included in the simulations: (i) $np \to \Delta^{+,0}(n,p) \to np\pi^0 \to npe^+e^-\gamma$ (ii) $np \to np\eta \to npe^+e^-\gamma$ and (iii) $np \to \Delta^{+,0}(n,p) \to (p,n)e^+e^-(n,p)$. One should note that the latter channel accounts for the part of the bremsstrahlung radiation related to the Δ excitation, since the pre-emission graphs associated with the Δ excitation have a small contribution (see Sect. 3.6.2). It is assumed that one-pion production is dominated by the Δ excitation which saturates the $I = 1$ component of the np reaction. The iso-scalar component of the np reaction at the HADES energy is much smaller, as shown in Refs. [Sar04, Bys87], and has been neglected. The cross section $\sigma_{\Delta^{+,0}}$ for the production of the Δ^+ and Δ^0 resonances in the np reactions has been deduced in Ref. [Tei97] within the framework of the resonance model by a fit to the available data on one-pion production in nucleon-nucleon reactions and amounts to $\sigma_{\Delta^+} = \sigma_{\Delta^0} = 5.7$ mb. Furthermore, the angular distributions for the production of the Δ excitation, deduced from the partial wave analysis of the one-pion production in the pp collisions at the same energy [HC15a] (Sect. 2.1.2), were included in the simulation. These distributions provide a small correction with respect to the one-pion exchange model [Tei97], which were originally included in the PLUTO event generator.

The contribution of the η (see Ref. [Frö07] for details of the implementation) to the exclusive npe^+e^- channel is negligible but was included for comparison with the calculations of the inclusive production [HC10], where it plays an important role. This model is later referred as the model A.

The model of Shyam and Mosel [Shy10b] (Sect. 3.6.2) is based on a coherent sum of NN bremsstrahlung and isobar contributions. It demonstrates a significant enhancement of the radiation in the high-mass region due to contributions from the charged internal pion line and the inclusion of the respective electromagnetic pion form factor. This mechanism modifies the contribution of the bremsstrahlung radiation from the nucleon charge-exchange graphs, which are absent in the case of the $pp \to ppe^+e^-$ reaction. The other part of the bremsstrahlung corresponds to the Δ excitation on one of the two nucleon lines and its subsequent Dalitz decay (Ne^+e^-). Although the latter dominates the total cross section at $M_{e^+e^-} < 0.3$ GeV/c^2, the modified nucleon-nucleon contribution makes a strong effect at higher masses. Unfortunately, the proposed model does not provide details about angular distributions of the final state particles. In the simulation the bremsstrahlung generator included in the PLUTO package [Frö07] was used, with a modification of the dielectron invariant mass distribution to account for the results of Ref. [Shy10b]. Since there is no guidance in the model on angular distributions of the protons and of the virtual photons, the distribution introduced in the model A for the Δ production was assumed, and denoted as the model B.

The modeling of the quasi-free np collisions has been implemented in both models based on a spectator model [Frö07]. This model assumes that only one of the nucleons (in HADES case, the neutron) takes part in the reaction while the other one, the proton, does not interact with the projectile and is on its mass shell. The momenta of the nucleons in the deuteron rest frame are anti-parallel and generated from the known distribution [Ben73].

4.3.2 Comparison to models

The exclusive final state $np\gamma^*$ can be characterized by five independent variables selected in an arbitrary way. Assuming azimuthal symmetry in the production mechanism, only four variables are needed. The decay of the γ^* into the e^+e^- pair can be characterized by two additional variables. The following observables have been chosen:

- the three invariant masses of the e^+e^- pair ($M_{e^+e^-}$, equivalent to the γ^* mass), the proton–e^+e^- system ($M_{pe^+e^-}$) and of the proton-neutron (M_{np}) system, respectively
- the two polar angles of the proton ($\cos^{c.m.}(\theta_p)$) and of the virtual photon ($\cos^{c.m.}(\theta^*_\gamma)$) defined in the center-of-mass system and the polar angle of the lepton (e^- or e^+) in the γ^* rest frame ($\cos(\theta^{e-\gamma^*}_{\gamma^*})$) with respect to the direction of the γ^* in the c.m.s. The center-of-mass system is defined by incident neutron at half deuteron energy (ignoring "Fermi motion") and target proton at rest.

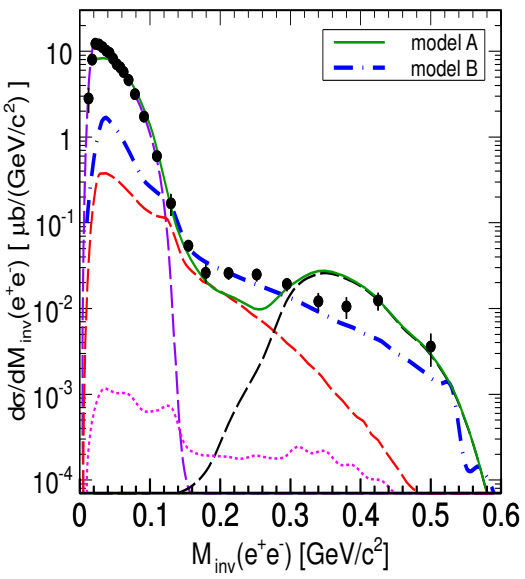

Figure 4.16: Dielectron differential cross section as a function of the invariant mass of e^+e^- within the HADES acceptance. The data (black dots) are corrected for the detection and reconstruction inefficiency and presented per GeV/c^2. The simulated cocktail (curves) of the π^0 (dashed violet), η (dotted magenta), Δ (dashed red) Dalitz decays, ρ from the double $\Delta-\Delta$ interaction process (dashed black) according to the model [Bas14] and the sum (contributions from π^0, η, Δ and ρ - solid green curve) - model A. The dot-dashed blue curve shows the bremsstrahlung contribution from Ref. [Shy10b] - model B.

4.3.2.1 Invariant masses

The dielectron invariant mass distributions is very sensitive to the coupling of the virtual photon to the ρ–meson. Figure 4.16 displays the dielectron invariant mass distribution and a comparison to the simulated spectra. As already observed in the case of the inclusive e^+e^- production [HC10] (Sect. 4.1), the e^+e^- yield in the π^0 region is found to be in a very good agreement with the π^0 production cross section of 7.6 mb used as an input to the simulation (see Sect. 4.3.1). One should note that the contribution from $np \to np\pi^0(\pi^0 \to e^+e^-\gamma)$ channel could not be completely eliminated by the selection on the pe^+e^- missing mass due to the finite detector mass resolution. This contribution is well described by the simulations, confirming the assumed cross section of the one-pion production. The good description obtained in the exclusive case demonstrates in addition that the acceptance on the detected proton and the resolution of the pe^+e^- missing mass are well under control.

The distribution for invariant masses larger than the π^0 mass ($M_{e^+e^-} > M_{\pi^0}$) is dominated by the exclusive $np \to npe^+e^-$ reaction (as also proven by the missing mass distribution in Fig. 4.15 - right panel), which is of main interest for this study. In this mass region the general features of the dielectron yield are reproduced by the model A. The Δ Dalitz decay dominates for the e^+e^- invariant mass between 0.14 GeV/c^2 and 0.28 GeV/c^2, while the ρ contribution prevails at higher invariant masses. The η Dalitz

decay gives a negligible contribution. A closer inspection reveals that the Δ Dalitz alone cannot describe the yield in the mass region $0.14 < M_{e^+e^-} < 0.28$ GeV/c^2. This is not surprising since the nucleon-nucleon bremsstrahlung is also expected to contribute in this region. On the other hand, the ρ contribution overshoots the measured yield at higher masses, even in a stronger way, than observed in the case of the inclusive data [Bas14] (Fig. 4.6 in Sect. 4.1.2.5). The low mass cut of the ρ contribution is due to the threshold at the double-pion mass, which should be absent in the case of the dielectron decay but is the feature of the applied decay model [Bas14].

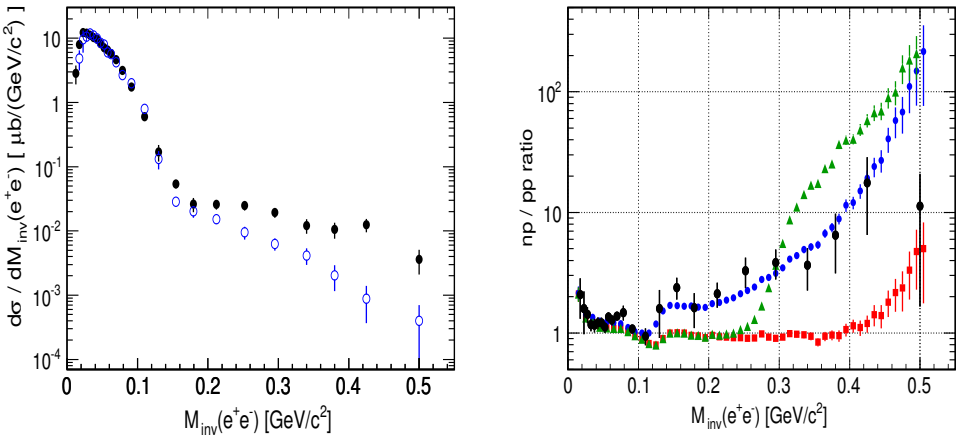

Figure 4.17: Left panel: dielectron invariant mass distribution for npe^+e^- (black dots) and ppe^+e^- (blue open circles) normalized to the same π^0 cross section within the HADES acceptance. Right panel: the ratio of the differential cross sections (in absolute scale, within the HADES acceptance) from $np \to npe^+e^-$ and $pp \to ppe^+e^-$ exclusive channels (black dots). The ratio of the model (A and B) and the pp Monte Carlo simulation is presented by green triangles (model A) and blue dots (model B). In addition a difference in phase volumes between np and pp collisions in the aforementioned channels is estimated (red squares). For details, see text.

The simulation based on the model B presents a rather different shape, with a smooth decrease of the yield as a function of the invariant mass. It was indeed shown in Ref. [Shy09] that the introduction of the pion electromagnetic form factor at the charged pion line (Fig. 3.11 right graph) enhances significantly the yield above the π^0 peak, but does not produce any structure. The yield for $M_{e^+e^-} < 0.14$ GeV/c^2 is strongly underestimated, which is expected, due to the absence of π^0 Dalitz process in the model, which aimed only at a description of the $np \to npe^+e^-$ (see Sect. 4.1.2.1). Above the π^0 peak, model B comes in overall closer to the data than model A, but it underestimates the yield at the very end of the spectrum ($M_{e^+e^-} > 0.35$ GeV/c^2). The exclusive yield calculated within the model B might slightly depend on the hypothesis we have made on the angular distributions (see Sect. 4.3.1). The expected effect is however rather small, since the proton angular distribution is well described by the simulation, as will be shown in Sect. 4.3.2.2. The comparison of the simulations based on both models with the experimental dilepton invariant mass distributions seem to favour the explanation of the dielectron excess due to the electromagnetic form factor on the charged pion line, as suggested in Ref. [Shy10b].

The exclusive invariant mass distribution can be also compared with the ppe^+e^- final state measured by the HADES at the same beam energy [HC17b] (Sect. 4.2). The latter one is well described by various independent calculations which all show the dominance of the Δ Dalitz decay process for invariant masses larger than 0.14 GeV/c^2. Thus, it can serve as a reference for the identification of some additional contributions appearing solely in the npe^+e^- final state. Figure 4.17 (left panel) shows the comparison of the e^+e^- invariant mass distributions normalized to the π^0 production measured in the reaction $np \to npe^+e^-$. It reveals a different shape above the pion mass.

The right panel of Fig. 4.17 shows the ratio of both differential cross sections, with their absolute normalization, as a function of the invariant mass in comparison to three different simulations. The error bars plotted for data and simulations are statistical only. The ratio of the two cross sections in the π^0 region within the HADES acceptance and inside the $M_{pe^+e^-}$ missing mass window amounts to $\sigma^{np}_{\pi^0}/\sigma^{pp}_{\pi^0} = 1.48 \pm 0.24$, which is well reproduced by the simulations for the π^0 Dalitz decay. The ratio of the cross sections in the full solid angle is 2, according to the measured data [HC15a] and as expected from the isospin coefficients for the dominant Δ contribution. However, the ratio measured inside the HADES acceptance is smaller because it is reduced by the larger probability to detect a proton in addition to the e^+e^- pair for the ppe^+e^- final state as compared to npe^+e^-. For the e^+e^- invariant masses larger than the pion mass, the ratio clearly demonstrates an excess of the dielectron yield in the exclusive np channel over the one measured in pp. It indicates an additional production process which is absent in the pp reactions, as proposed by the discussed models.

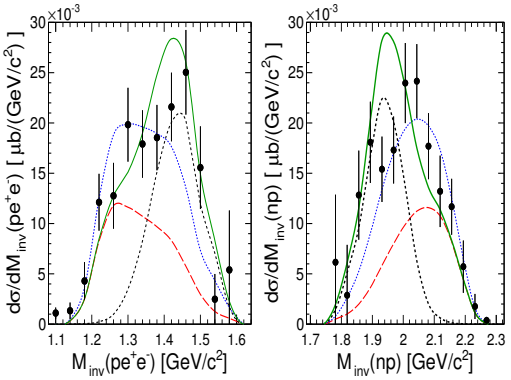

Figure 4.18: npe^+e^- final state within the HADES acceptance. Differential cross section as a function of the invariant mass of pe^+e^- (left panel) and of np (right panel) compared to model A (solid green), with the following components: Δ Dalitz (dashed red), ρ–meson decay from the double–Δ interaction (short-dashed black) and model B (blue dotted).

In order to exclude trivial effects, like the different phase space volumes available in the pp and quasi-free np collisions due to the neutron momentum spread in the deuteron, the ratio of the cross sections of Δ channels in both reactions is investigated (red squares on the right panel of Fig. 4.17). An enhancement is indeed present but only at the limits of the available phase space. It confirms that the phase space volume difference gives a very small contribution to the measured enhancement in the npe^+e^- channel.

The green triangles (model A) and blue dots (model B) in Fig. 4.17 (right panel) represent the ratio of the respective model simulation and the pp Monte Carlo simulation: the sum of π^0 and Δ Dalitz decays (Δ with a pointlike eTFF) [HC17b]. The ratios take into account the differences in the phase volume between np and pp, as mentioned above. Similar to the comparison of the dielectron invariant mass distribution in Fig. 4.16, the calculation of [Shy10b] (model B) gives a better description of the data for the invariant masses larger than the π^0 mass.

Figure 4.18 shows the two other invariant mass distributions of the pe^+e^- ($M_{pe^+e^-}$, left panel) and the np (M_{np}, right panel) systems. Both distributions are plotted for masses of the virtual photon $M_{e^+e^-} > 0.14$ GeV/c^2 and are compared to the models A and B. For the model A, the Δ and ρ contributions are shown separately. As expected, the distribution at low $M_{pe^+e^-}$ is dominated by low mass dielectrons, originating mainly from the Δ decays (the observed shape in the simulation is due to an interplay between $\Delta^+ \to pe^+e^-$ and $\Delta^0 \to ne^+e^-$ decays, both contributing with same cross sections) and at higher masses by the ρ–like channel. On the other hand, the invariant mass distribution of the np system is dominated at low masses by the ρ contribution, which in the model A overshoots slightly the data. In general, the high-mass enhancement visible in the e^+e^- mass spectrum is consistently reflected in the shapes of the two other invariant mass distributions.

4.3.2.2 Angular distributions

In the discussion of the angular distributions two bins of the dielectron invariant mass are considered separately: $0.14 < M_{e^+e^-} < 0.28$ GeV/c^2 and $M_{e^+e^-} > 0.28$ GeV/c^2. The selection of the two mass bins is dictated by the calculations which suggest two possible different production regimes, with a dominance of the ρ–like contribution in the second bin.

Figure 4.19 displays the differential angular distributions of the proton in the c.m.s., both within the HADES acceptance and after acceptance corrections. In the first case, the experimental distributions are compared to the predictions of the simulations on an absolute scale. In the second case, the simulated distributions are normalized to the experimental yield after acceptance corrections in order to compare the shapes.

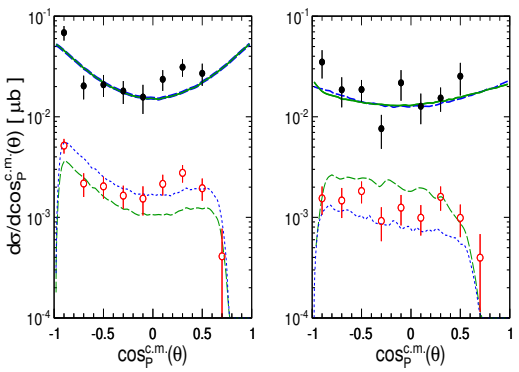

Figure 4.19: Differential cross sections for the dilepton production in npe^+e^- channel as a function of the proton emission angle in the c.m.s.: for $0.14 < M_{e^+e^-} < 0.28$ GeV/c^2 (left panel) and $M_{e^+e^-} > 0.28$ GeV/c^2 within the HADES acceptance (open red dots) and the full solid angle (full black dots). The solid curves display predictions from the simulations in the full solid angle normalized to the experimental yield: the green curve represents model A (in the low mass bin mostly Δ, in the high mass bin mostly ρ), dashed blue represents model B. The dotted/dashed curves are within the detector acceptance for model A (dashed green) and B (dotted blue) (see text for details), respectively.

As can be deduced from Fig. 4.16, according to model A, the low-mass bin is dominated in the simulation by the Δ Dalitz decay process, while the ρ–like contribution determines the dielectron production in the higher mass bin. In the first mass bin, the distribution exhibits a clear anisotropy, pointing to a peripheral mechanism. The simulated distributions for the models A (dashed green curve) and B (dotted blue curve) differ in magnitude but have similar shapes. This is due to the fact that the angular

distribution for the model B is the same as in the Δ contribution of model A, which dominates in this mass region (see Sec. 4.3.1) - both contributions have the same angular distribution in the full solid angle (solid green and superimposed dashed blue curves). The shape of the experimental angular distribution is rather well accounted for by both simulations, where the angular distributions for the Δ production from the partial wave analysis is used, leading to a symmetric forward/backward peaking. However, there is an indication for some enhancement above the simulation in the npe^+e^- channel for the forward emitted protons, unfortunately cut at small angles by the HADES acceptance. It might be due to the charge exchange graphs involving nucleons, which are not properly taken into account by the symmetric angular distribution used as an input for the simulation. Indeed, in the case of the Δ excitation, charge exchange and non-charge exchange graphs have the same weight, which yields a symmetric angular distribution for the proton in the center-of-mass system. This is different for nucleon graphs, where the contribution of the charge exchange graphs to the cross section are enhanced due to the isospin coefficients by a factor 4 and, therefore, forward emission of the proton is favored.

For the higher invariant e^+e^- masses, the angular distribution is more isotropic and is described rather well by both simulations which again exhibit similar characteristics. The flattening of the distributions reflects the different momentum transfers involved in the production of heavy virtual photons. However, as already mentioned, the angular distribution in model B follows the Δ production angular distribution, while in model A it is properly calculated for the ρ production via the double$-\Delta$ mechanism.

It is interesting to observe that the two angular distributions are very similar. In particular, the distribution with respect to $\cos_p^{c.m.}(\theta)$ from the model A is symmetric, although graphs with emission of the neutron from a Δ^- excited on the incident neutron (and corresponding emission of the proton from the excitation of a Δ^{++} on the proton at rest) are highly favoured by isospin factors and induce a strong asymmetry for the production of the Δs, as shown for example in Ref. [Hub94].

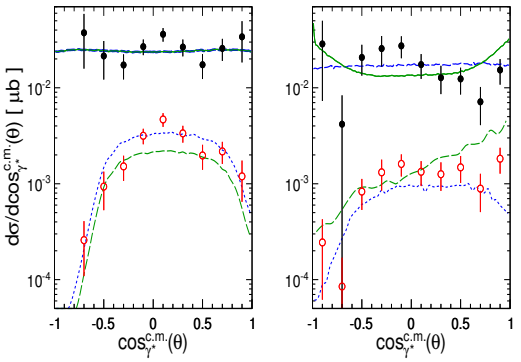

Figure 4.20: Differential cross sections for the dielectron production in the npe^+e^- channel as a function of the virtual photon emission angle in the c.m.s. for $0.14 < M_{e^+e^-} < 0.28$ GeV/c^2 (left panel) and $M_{e^+e^-} > 0.28$ GeV/c^2 (right panel). The red open dots present data within the HADES acceptance while the black full dots show the acceptance corrected data. See caption of Fig. 4.19 for the legend.

Figure 4.20 presents similar angular distributions as discussed above but for the virtual photon. The distributions are also strongly biased by the HADES acceptance, which suppresses virtual photon emission in the forward and even more strongly in the backward direction. In the lower mass bin, where the Δ contribution is dominant, a deviation from the isotropic distribution could be expected due to the polarization of the Δ resonance. However, the experimental distributions are compatible with an isotropic

emission, as assumed in the simulation. In the larger mass bin, it is interesting to see that the model A (solid green curve) predicts a significant anisotropy, related to the angular momentum in the double−Δ system for the ρ emission by the charged pion line between the two Δs, which is the dominant contribution in this mass bin. However, the HADES data present a different trend, which seems also to deviate from isotropy but with a smaller yield for the forward and the backward emission. Unfortunately, as already mentioned for the proton angular distributions, the verification of these distributions based on the hypothesis of an emission by the charged pion between two nucleons is not possible, since the calculations in Ref. [Shy10b] do not provide them and the distribution of the model B remains here rather flat (dashed blue curve in Fig. 4.20).

Finally, the distributions of leptons in the rest frame of the virtual photon are studied. These observables are predicted to be particularly sensitive to the timelike electromagnetic structure of the transitions [Bra95]. Indeed, for the Dalitz decay of the pseudoscalar particle, i.e. pion or η mesons, the angular distribution of the electron (or positron) with respect to the direction of the virtual photon in the meson rest frame is predicted to be proportional to $1 + \cos^2(\theta_e)$. These predictions were confirmed in our measurements of the exclusive pion and eta meson decays in proton-proton reactions [HC12b] (Sect. 4.6).

For the Δ Dalitz decay, the angular distribution has a stronger dependence on the electromagnetic form factors due to the wider range in e^+e^- invariant masses. Assuming the dominance of the magnetic transition in the $\Delta \to Ne^+e^-$ process, the authors of Ref. [Bra95] arrive at the same distribution as for the pseudo-scalar mesons. Concerning the elastic bremsstrahlung process, only predictions based on the soft photon approximation exist in the literature [Bra95]. According to this model, the corresponding angular distributions show at HADES energies a small anisotropy with some dependence on the dielectron invariant mass. On the other hand, the angular distribution of leptons from the ρ–meson decay from pion annihilation, measured with respect to the direction of the pion in the virtual photon rest frame, has a strong anisotropy, e.g. $\propto 1 - \cos^2(\theta_e)$.

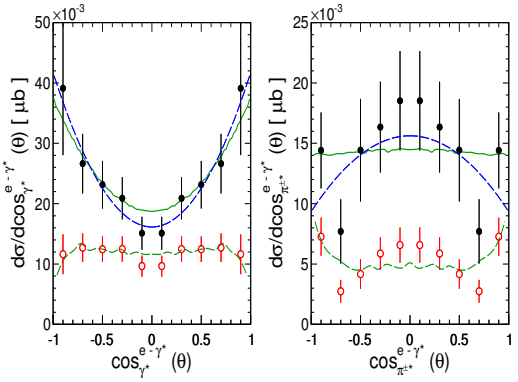

Figure 4.21: Angular distributions of the leptons in the rest frame of the virtual photon, calculated in the pe^+e^- rest frame and for the dielectron mass of $0.14 < M_{e^+e^-} < 0.28$ GeV/c^2 (left panel), and with respect to the direction of the charged pion exchange for dielectrons with $M_{e^+e^-} > 0.28$ GeV/c^2 (right panel). See caption of Fig. 4.19 for the legend except the dashed blue curve which shows a fit with a function $A(1 + B\cos^2(\theta_e))$.

Figure 4.21 presents e^+ and e^- angular distributions for the experimental data and the two bins of the dielectron invariant mass. The distributions are symmetric due to the fact that both angles, between electron and γ^* as well as positron and γ^*, in the rest frame of the virtual photon, have been plotted. For the left panel (bin with the smaller masses, $0.14 < M_{e^+e^-} < 0.28$ GeV/c^2) the distribution has been calculated

with respect to the γ^* direction, obtained in the pe^+e^- rest frame, while for the right panel (bin with the larger masses, $M_{e^+e^-} > 0.28$ GeV/c^2) it has been calculated with respect to the direction of the exchanged charged pion momentum. The latter one has been calculated as the direction of the vector constructed from the difference between the vectors of the incident proton and reconstructed emitted neutron and boosted to the rest frame of the virtual photon. The open red symbols present the data within the HADES acceptance (multiplied by a factor 5) while the full black symbols show the acceptance corrected data. The solid green curve displays a prediction from the simulation in the full solid angle while the dashed green curve, is normalized to the experimental distributions within the HADES acceptance for a better comparison of the shape. The dashed blue curve shows a fit with a function $A(1 + B\cos^2(\theta_e))$. In the lower mass bin the data follow the distribution expected for the Δ, $B = 1.58 \pm 0.52$ and the fit almost overlays with the simulated distribution. This seems to confirm the dominance of the Δ in this mass bin, in agreement with both models. However, it would be interesting to test the possible distortion that could arise due to contribution of nucleon graphs, following Ref. [Shy10b]. For these graphs, the distribution of the e^+ or e^- angle in the virtual photon rest frame should depend on the electric and magnetic nucleon form factors in a very similar way to the $e^+e^- \leftrightarrow \bar{p}p$ reactions, e.g. following $|G_M|^2(1+\cos^2\theta) + (4m_p^2/q^2)|G_E|^2\sin^2\theta$, where m_p is the proton mass. In the calculation of Ref. [Shy10b], the anisotropy of the e^+ (e^-) angular distribution should therefore derive from the VDM form factor model. A similar fit to the higher mass bin in the same reference frame (not shown) gives a significantly smaller anisotropy $B = 0.25 \pm 0.35$ which changes the sign, when the distribution of the lepton with respect to the exchanged charged pion is fitted ($B = -0.4 \pm 0.20$), as shown in Fig. 4.21 (right panel). The latter may indicate the dominance of the ρ decay, as suggested by both models [Shy10b, Bas14].

The systematic uncertainty of the data points presented in Figs. 4.19-4.21 includes the normalization error 7%, particle identification, track reconstruction and efficiency correction 10%, and the model dependent acceptance correction uncertainty. The latter one can be deduced in the following way. In the lower mass bin, $0.14 < M_{e^+e^-} < 0.28$ GeV/c^2, both models A and B have implemented the same angular distribution of the Δ resonance. Hence, the difference in the data points corrected either with the help of model A or model B, despite the differences in the invariant mass distribution (Fig. 4.16), is negligibly small (< 0.5%). However, one should notice that the most contributing Δ resonance is modelled with the pointlike eTFF here. The electromagnetic structure of Δ resonance has been investigated via the Dalitz decay in Ref. [HC17b], including a comparison with various eTFF models (Refs. [Ram16, Zét03a, Wan05]). The production of the Δ resonance was investigated in the partial wave analysis approach [HC15a]. Based on these results the systematic model uncertainty, related to the Δ resonance, is estimated on the level of 10%. In the higher mass bin, $M_{e^+e^-} > 0.28$ GeV/c^2, both models A and B were used for the one-dimensional and two-dimensional acceptance correction, resulting in the discrepancy of 6%. Finally, all uncertainties, added quadratically, give the systematic error 14 – 16%.

4.4 Summary for e^+e^- production at T = 1.25 GeV

The inclusive dielectron distributions measured in *pp* and quasi-free *np* collisions at $T = 1.25$ GeV unraveled a very strong isospin dependence of the dielectron production. The *pp* collisions are essentially described by two leading contributions, π^0 and Δ Dalitz decays. However, in the case of *np* collisions, a significant enhancement in the intermediate dilepton mass region was observed. Contributions previously predicted by various models from the electromagnetic decays of hadrons and long-lived mesons, mainly η, failed to describe the data.

The $ppe^+e^-\gamma$ channel identified by HADES allows study of the π^0 Dalitz decay and to verify the Δ production characteristics derived from the partial wave analysis of hadronic final states. All distributions are in a perfect agreement with expectations from simulations. In particular, the angle between e^+ or e^- and γ^* in the γ^* rest frame follows the $1 + \cos^2\theta$ distribution predicted for the decay of pseudoscalar mesons. Moreover, the yield is consistent with the measurements in the $pp \to pp\pi^0$ channel, where π^0 was identified by the missing mass technique (Sect. 2.1.1).

These results of Δ production are used for the interpretation of the $pp \to ppe^+e^-$ channel, and allows to extract, for the first time, the branching ratio of the Δ Dalitz decay $(4.19 \pm 0.62$ syst. incl. model $\pm$ 0.34 stat.$) \times 10^{-5}$. The value is found to be in agreement with estimates based on calculations, using either constant electromagnetic form factors [Zét03a, Doh10] or a quark constituent model [Ram16]. Comparisons to models suggest important role of intermediate ρ–meson in the dilepton decay and pion cloud contribution in the baryon wave function.

The measurements of npe^+e^- ($p_{spect.}$) channel confirm that the e^+e^- invariant-mass differential cross section in *np* collisions presents a similar excess with respect to the one measured in the $pp \to ppe^+e^-$ channel, as previously observed for the corresponding inclusive e^+e^- distributions, hence suggesting the baryonic origin of this effect. Two models were tested, providing an improved description of the inclusive e^+e^- production in the *np* reaction at large invariant masses. The first one consists of an incoherent cocktail of dielectron sources including (in addition to π^0, Δ and η Dalitz decay) a contribution from the ρ–like emission via the double–Δ excitation following the suggestion by Bashkanov and Clement [Bas14]. The second model is based on the Lagrangian approach by Shyam and Mosel [Shy10b] and provides a coherent calculation of the $np \to npe^+e^-$ reaction including nucleon and resonant graphs. In both models, the enhancement at large invariant masses is due to the VDM electromagnetic form factor which is introduced for the production of the e^+e^- pair from the exchanged pion. The evolution of the shape of the experimental e^+ and e^- angular distribution in the γ^* rest frame seems to confirm the emission via an intermediate virtual ρ at the largest invariant masses. Since this process is absent in the reaction $pp \to ppe^+e^-$, it provides a natural explanation for the observed excess.

The first observation of dielectron excess measured in the inclusive *np* reaction with respect to the *pp* reaction triggered a lot of theoretical activity and raised interesting suggestions of mechanisms specific to the *np* reaction. Understanding in detail the e^+e^- production in *np* collisions is a necessary step towards the description of e^+e^- production in heavy-ion collisions where medium effects are investigated. On the other hand, the description of the $np \to npe^+e^-$ process is challenging because it implies many diagrams with unknown elastic and transition electromagnetic form factors of baryons in the timelike region. The HADES exclusive measurement of the quasi-free $np \to npe^+e^-$ reaction at $T = 1.25$ GeV is sensitive to various underlying mechanisms and in particular sheds more light on contributions which are specific to the *np* reaction.

4.5 Inclusive e^+e^- production (pp at T = 2.2 GeV)

The HADES data measured in proton-proton collisions at kinetic beam energy 2.2 GeV were analyzed in Sect. 2.3 in the inclusive one-pion (π^0, π^+) and η production channels. The dominant resonance contributions were confirmed and cross sections of $\Delta(1232)$, $N(1440)$, $N(1520)$, and $N(1535)$ resonances were reported. Based on this production scheme, results with data obtained on inclusive e^+e^- identification in the $pp \to ppe^+e^-X$ reaction were studied. As a result, the inclusive production cross sections of π^0 and η mesons at 2.2 GeV were deduced. The differential $d\sigma/dM_{e^+e^-}$ cross section of e^+e^- signal pairs is shown in Fig. 4.22. The spectrum is corrected for inefficiencies and trigger bias, with cuts on a single electron/positron momentum $p_e > 0.1$ GeV/c, and pair opening angle $\alpha_{e^+e^-} > 9°$. The total number of reconstructed e^+e^- pairs amounts to 19.000, with 2.000 pairs for the masses above the π^0 mass ($M_{e^+e^-} > 0.15$ GeV/c^2), up to the kinematical cut-off limit for the e^+e^- mass at 0.89 GeV/c^2. The ratio of the signal (S) to combinatorial background (CB) (Fig. 4.22 inset) is essentially above 1.

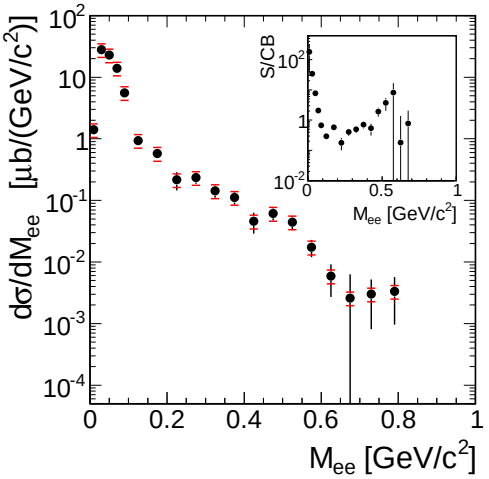

Figure 4.22: Dielectron invariant mass distributions in $pp \to ppe^+e^-X$ at energy of 2.2 GeV. The spectrum is presented within the HADES acceptance, after efficiency correction and CB subtraction. Cuts on minimum momentum $p_e > 0.1$ GeV/c and pair opening angle $\alpha_{e^+e^-} > 9°$ are applied. Black vertical bars indicate statistical errors while horizontal red bars indicate systematic errors. The inset: signal to combinatorial background (S/CB) ratio.

The HADES dielectron spectra from pp collisions at 2.2 GeV were also compared with the DLS experiment, which provided e^+e^- data for the pp reaction at 2.09 GeV [DC98]. Figure 4.23 presents the comparison for the pair mass distributions $d\sigma/dM_{e^+e^-}$ (left panel) and the pair transverse momentum spectrum $1/(2\pi P_\perp)\, d\sigma/dP_\perp$ (right panel), the latter one with the condition $M_{e^+e^-} > 0.15$ GeV/c^2. To compare the data, the DLS acceptance filter [DC97] was imposed on the HADES data, giving within statistical and systematic uncertainties, very good agreement between both data samples, thus confirming the previous DLS results.

4.5.1 e^+e^- production channels

The e^+e^- data were compared with the expected dielectron sources in Figs. 4.24 (pair invariant mass) and 4.25 (pair transverse momentum). They were implemented in the PLUTO event generator [Frö07, Doh10] and filtered within the HADES acceptance. The following channels were modeled with the cross sections as listed:

- $\pi^0 \to \gamma e^+e^-$ decay with π^0 production cross section σ = 14 mb. The π^0 channels listed in Ref. [Bal88] provide a lower limit of 12 mb.
- $\eta \to \gamma e^+e^-$ decay with η production in the range of 0.26 – 0.35 mb. The known exclusive η production cross section is at 0.14 mb (see Sect. 2.3.3).

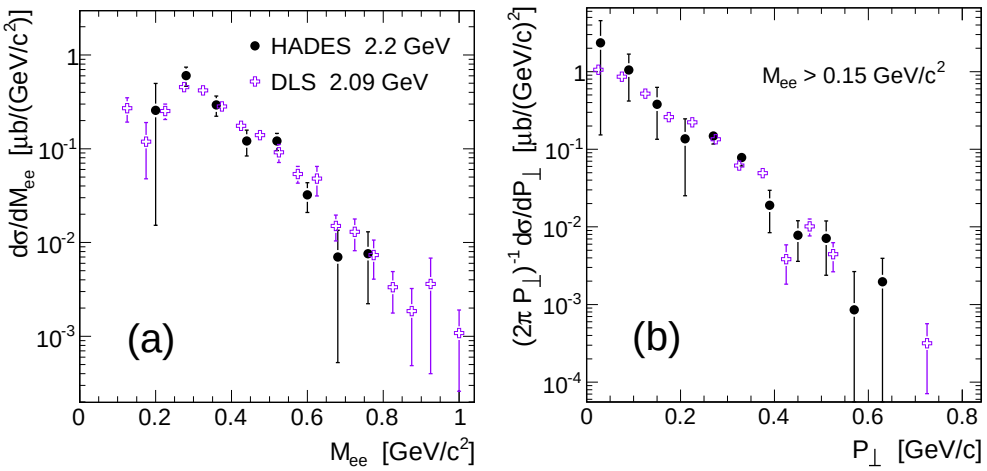

Figure 4.23: e^+e^- cross sections measured by HADES in *pp* collisions at 2.2 GeV (black dots) and by DLS at 2.09 GeV (open crosses, see Ref. [DC98]): invariant mass distributions (left panel), pair transverse-momentum distributions (right panel). Error bars are statistical only, systematic errors (not shown) are 23% for DLS and 29% for HADES.

- $\omega \to \pi^0 e^+e^-$, $\omega \to e^+e^-$, and $\rho \to e^+e^-$ decays, with exclusive vector meson (ω, ρ) production of 0.01 mb [CTC07].
- $\Delta^{0,+}(1232)$ excitation, followed by the nucleon-pion or Dalitz decays, with cross section in the range 10 – 21 mb.

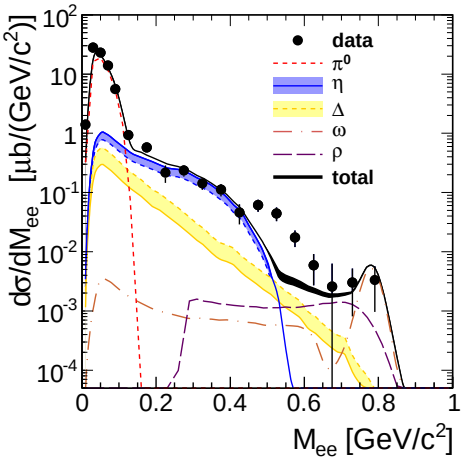

Figure 4.24: Dielectron invariant mass distribution measured in proton-proton reaction at 2.2 GeV, presented within the HADES acceptance (full circles, only statistical errors are shown). The comparison with simulated dielectron sources of π^0, η, ω, Δ Dalitz decays, and ω, ρ direct decays. The shaded bands delimit the range of modeled Δ (yellow band) and η (blue band) contributions as discussed in the text, with the dashed delimiters corresponding to high cross section limit, and the solid ones to low cross section limit.

The wide range of Δ cross sections depends on meson production description. One assumption, leading to the upper cross section of 21 mb (dashed curve of the yellow band in Figs. 4.24 and 4.25), is driven by a single pion production mediated by Δ excitation only, and the isospin relation, $\sigma_\Delta = 3/2\,\sigma_{\pi^0}$. Another assumption, resulting in the lower cross section of 10 mb (solid yellow curve in figure), is a sum of one-pion production of 3.6 mb from a resonance model in Ref. [Tei97], and two-pion production of 6.4 mb from the effective Lagrangian model in Ref. [Cao10]. Another dielectron

channel, marked with a blue band in Figs. 4.24 and 4.25, is related to η Dalitz decay. Both production channels saturate the e^+e^- invariant mass spectrum up to the $M_{e^+e^-} \approx 0.45$ GeV/c^2 (see also Fig. 4.25b). Based on the components of the e^+e^- cocktail it is possible to deduce the inclusive cross sections of scalar mesons. For $M_{e^+e^-} < 0.15$ GeV/c^2 the dominating π^0 Dalitz decay allows to fix the inclusive π^0 production cross section at $\sigma_{\pi^0} = 14 \pm 3.5$ mb. The quoted 25% error is determined mostly by systematic effects (normalization, trigger bias correction, acceptance correction).

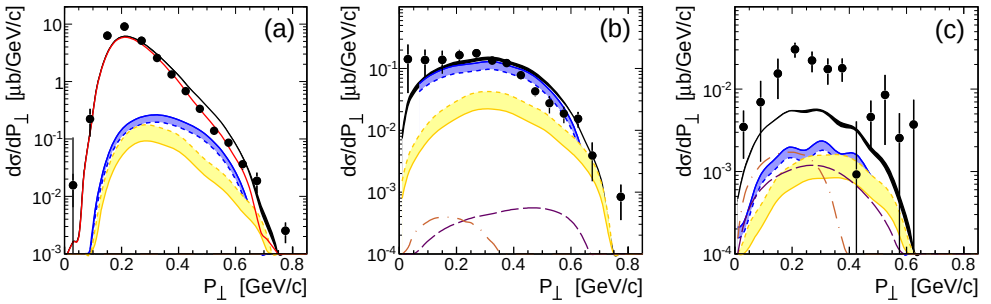

Figure 4.25: Pair transverse momentum distributions $d\sigma/dP_\perp$ measured in pp collisions at 2.2 GeV within the HADES acceptance. Three mass bins are shown: (a) $M_{ee} < 0.15$, (b) $0.15 < M_{ee} < 0.45$, and (c) $M_{ee} > 0.45$ GeV/c^2. For legend, see Fig. 4.24.

In the intermediate mass region, $0.15 < M_{e^+e^-} < 0.45$ GeV/c^2, the subtraction of Δ Dalitz decay contribution allows for estimation of η–meson cross section. The upper limit $\sigma_\Delta = 21$ mb corresponds to $\sigma_\eta = 0.26$ mb, while the lower limit $\sigma_\Delta = 10$ mb results in $\sigma_\eta = 0.35$ mb. The average value can be written, $\sigma_\eta = 0.31 \pm 0.08 \pm 0.05$ mb, with the systematic error, and model dependence error. The mass above η unravels strong excess of dielectron pairs in data as compared to simulation (see also Fig. 4.25c). The possible missing sources are N^* resonances, e.g. $N(1520)$ and $N(1720)$, coupling to the ρ–meson. An enhancement could be also possible due to vector meson dominance form factors of the nucleon resonances [Kri02].

4.5.2 Comparison to models

Similar to investigation presented in Sect. 4.1.2, attempts to describe the dilepton spectra from pp collisions at 2.2 GeV were made by a number of models. Brief overview is given below.

4.5.2.1 GiBUU model

In pp collisions at 2.2 GeV, the spectrum below mass $M < 0.15$ GeV/c^2 is still dominated by the π^0 Dalitz decay, but at higher mass the role of Δ Dalitz decay is less pronounced (Fig. 4.26). The beam energy is above η–meson production threshold and the respective Dalitz decay contributes (dash-dashed curve in figure). It also reaches the pole mass of ρ (green long dashed curve) and ω (direct decay: blue dashed, Dalitz decay: dot-dashed turquoise curve) mesons, which dominate the high-mass part of the dilepton spectrum. The Δ Dalitz decay is presented for two cases: a pointlike (lower limit) and the Iachello-Wan (see App. B.3) electromagnetic transition form factor (upper limit), plotted as a red hatched area. However, the Δ contribution plays a less important role here, since the η and ρ contributions are much larger.

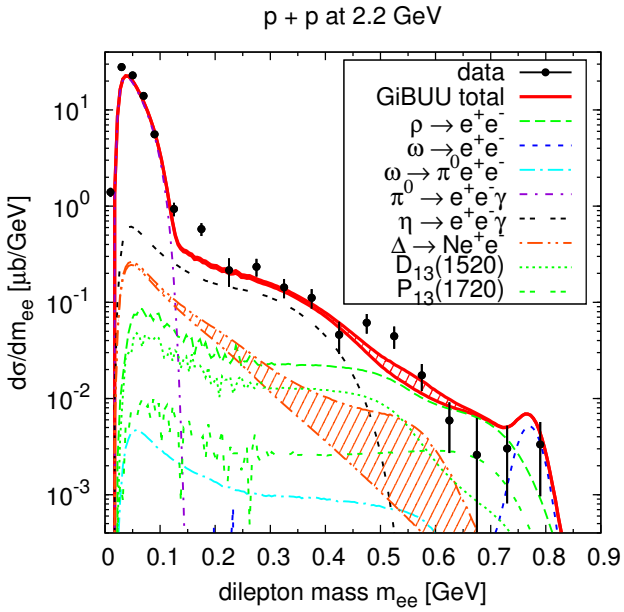

Figure 4.26: Dilepton mass spectrum within the HADES acceptance, compared with the GiBUU calculation [Wei12]. The $P_{33}(1232)$ resonance is presented without and with electromagnetic transition form factor (red hatched area), while the $D_{13}(1520)$ and $P_{13}(1720)$ are modeled with a pointlike eTFF. For color code, see legend. Figure adopted from Ref. [Wei12].

Unlike the ρ–meson channel modeled in Sect. 4.5.1 by the phase space production, in GiBUU two resonances contributing to the ρ, $D_{13}(1520)$ and $P_{13}(1720)$, result in a better description of the data, with some minor deviations. The $N(1520)$ resonance is underestimated and, on the other hand, $N(1720)$ overestimates the data.

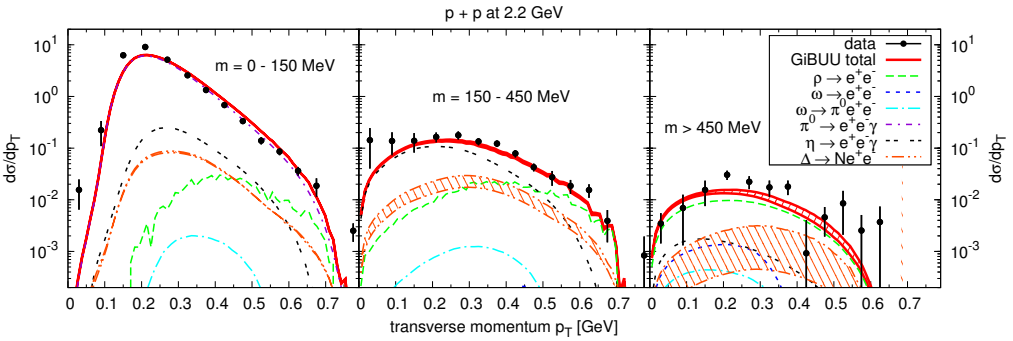

Figure 4.27: Pair transverse momentum distributions in three mass bins (as in Fig. 4.24). The red hatched area indicates the effect of the Δ form factor.

Figure 4.27 show the transverse momentum spectra in three mass bins as in Fig. 4.24. The GiBUU calculation gives a better description of the data, most notably, from the larger ρ contribution in the highest mass bin.

4.5.2.2 HSD model

The Hadron-String-Dynamics (HSD) transport approach presented in Ref. [Bra13] is compared with data in Fig. 4.28 (for details, see Sect. 4.1.2.4). Left panel shows the invariant mass spectrum, qualitatively described similarly as in the GiBUU model (see above). However, although Δ Dalitz contribution is treated here with the pointlike form factor, a higher production cross section, as compared to the GiBUU, is implemented. The difference is clearly seen in the low mass, where Δ Dalitz decay reaches the same level as η Dalitz decay. It results in the overall increase of the yield. Another difference is the pp bremsstrahlung (without resonance excitation, as in Ref. [Kap06]) implemented in the HSD. The contribution of the $N(1520)$ to the ρ cross section is included as suggested in Ref. [Pet98], but the branching ratio to a ρ has uncertainty between 15% and 25%. Such a resonance contribution presents an upper estimate for the ρ–meson production in NN and πN reactions at sub-threshold energies. The right panel of Fig. 4.28 shows the HSD results for the differential transverse momentum cross sections separated for different invariant mass bins, as in Figs. 4.25 (HADES analysis) and 4.27 (GiBUU model). The agreement between theory and experiment is very similar to the GiBUU model, despite the differences in the description of contributing sources.

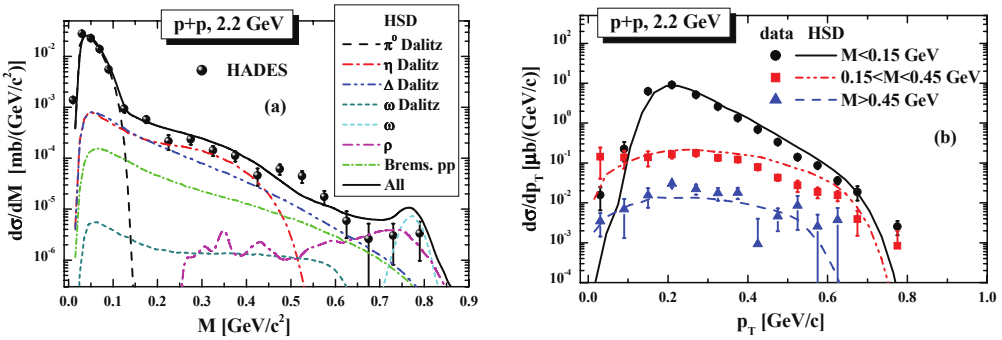

Figure 4.28: Left panel: The dilepton differential cross section $d\sigma/dM$ of the HSD model for pp reactions at 2.2 GeV in comparison to the experimental data. For the contributions, see legend. Right panel: HSD results for the differential dilepton transverse momentum cross section for different mass bins: $M < 0.15$ GeV/c^2 (black curve), $0.15 < M < 0.55$ GeV/c^2 (red dot-dot-dashed curve), and $M > 0.55$ GeV/c^2 (blue dashed curve). All spectra are presented within the HADES acceptance.

4.5.2.3 UrQMD model

The microscopic Ultra-relativistic Quantum Molecular Dynamics (UrQMD) model is a hadronic non-equilibrium transport approach including all baryons and mesons with masses up to 2.2 GeV/c^2 [Bas98, Ble99, Pet08]. The ρ–meson production is calculated either as a two-step process, with the resonance R excitation followed by the decay: $N+N \to N+R \to N+N+\rho$, or in the pion annihilation, $\pi^+\pi^- \to \rho$. The mass dependent branching ratios of resonance decays are taken from Ref. [PDG16]. The pseudoscalar (π^0, η, η') and vector (ω) meson Dalitz decays are also decomposed into a two-step

process, first decay into a virtual photon and then the subsequent decay of the photon via electromagnetic conversion. The form factors used in this description are obtained by the vector meson dominance model (see Refs. [Lan85,Li96]). The direct vector meson (ρ_0, ω, ϕ) decays are also included. The $\Delta(1232)$ Dalitz decay is described with the parametrization of Wolf *et al.* [Wol90] (see also Sect. 3.4) with a modified coupling to fit the radiative decay width [Bra99].

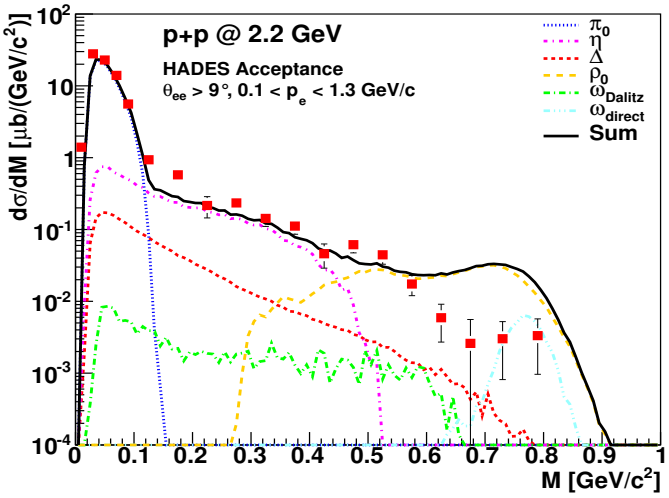

Figure 4.29: Dielectron invariant mass spectrum for *pp* at 2.2 GeV within the HADES acceptance, compared to the UrQMD transport model (for the color coding, see legend).

Figure 4.29 presents dilepton invariant mass spectrum for *pp* at 2.2 GeV (Ref. [End13]) within the HADES acceptance. The overall agreement of the UrQMD calculations and the HADES data is seen up to the ρ–meson pole mass, where the model significantly overestimates the yield. The further studies can be done with the data at higher energy 3.5 GeV where the full phase space is open for vector meson production.

4.6 Exclusive e^+e^- production (pp at T = 2.2 GeV)

To reconstruct the Dalitz decays of $\pi^0 \to \gamma e^+e^-$ and $\eta \to \gamma e^+e^-$ (see App. A.3.1), all events with two protons and one dielectron (ppe^+e^-) have been selected. The signal-to-background ratios are of the order of 3 in the π^0 region and of 4 in the η region. The missing masses of the two-proton system $M_{miss}(p,p)$ and of the four-particle system $M_{miss}(p,p,e^+,e^-)$ were reconstructed, in the same way as for the $pp\pi^+\pi^-$ events (Sect. 2.3.3). The correlation between the squares of both missing masses is shown in Fig. 4.30, left panel, after combinatorial background subtraction. The contributions from $pp \to pp\pi^0/\eta$ reactions, followed by Dalitz decays $\pi^0/\eta \to \gamma e^+e^-$, are pronounced for $M^2_{miss}(p,p)$ close to the π^0 and η mass squared, respectively. All events from the $pp \to ppe^+e^-\gamma$ reaction are centered around zero in the $M^2_{miss}(p,p,e^+,e^-)$ distribution.

Figure 4.30 (right panel) presents the $M^2_{miss}(p,p)$ distribution: signals from π^0 and η Dailtz decays are extracted with the rectangle cuts (see Fig. 4.30, left panel). The remaining background, of the order of 5%, is due to e^+e^- pairs from the Dalitz decay of a π^0 produced in multipion production processes (blue histogram). This contribution has been removed bin by bin, based on the simulation of the channels with two pions

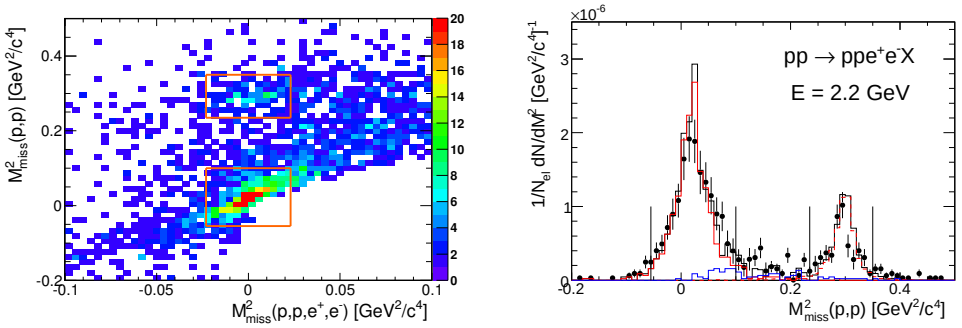

Figure 4.30: $pp \to ppe^+e^-$ reaction at 2.2 GeV. Left panel: The correlation between the two-proton missing mass squared ($M^2_{miss}(p,p)$) and the four-particle missing mass squared ($M^2_{miss}(p,p,e^+,e^-)$) is shown. The orange rectangles select the regions of the η peak, visible for $M^2_{miss}(p,p)$ around the η mass squared, and of the π^0 peak, visible for $M^2_{miss}(p,p)$ around the zero mass. Both selections are at $M^2_{miss}(p,p,e^+,e^-)$ close to the γ (zero) mass. Right panel: Distribution of the two-proton missing mass squared ($M^2_{miss}(p,p)$, black dots) for the ppe^+e^- events, after a cut on the missing mass to the four-particle system (left panel). The distribution is normalized to the pp elastic scattering yield. The histograms show the results of simulations: The red histograms peaking at the π^0 and η squared masses correspond to the exclusive π^0 and η production, respectively, followed by Dalitz decay. The blue histogram shows the contribution of multipion background, which is subtracted from the data (see text for details). The vertical lines depict the limits used to extract the experimental signals strength.

$\pi^0\pi^0$ (cross section 1.09 mb), and three pions, $\pi^0\pi^0\pi^0$, and $\pi^+\pi^-\pi^0$ (cross section 0.5 mb, see Ref. [Bal88]). The number of reconstructed π^0 Dalitz decays amounts to 6800 ± 200 (syst.) ± 82 (stat.), and the number of η Dalitz decays amounts to 235 ± 18 (syst.) ± 19 (stat.). The systematic error was evaluated by the variation of the missing-mass limits (vertical lines in Fig. 4.30, right panel) and the shape of the multipion background.

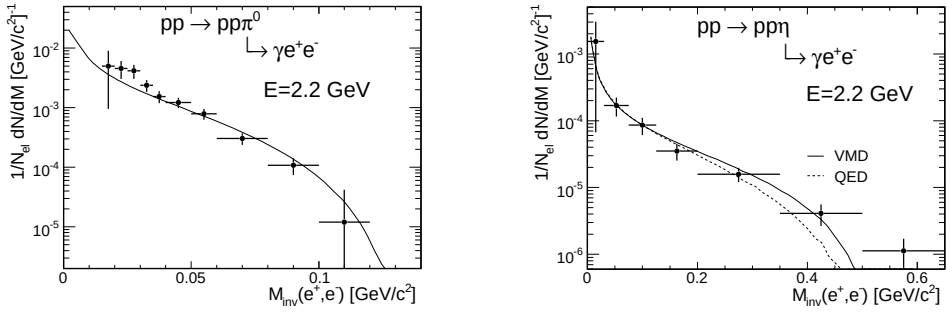

Figure 4.31: e^+e^- invariant mass distributions for the π^0 (left panel) and η (right panel) Dalitz decays, obtained after efficiency and acceptance corrections. The yields are normalized for the pp elastic scattering. The simulations (black solid curves) are based on resonance model (for details, see Sect. 2.3.2 and 2.3.3). In the case of η meson, the simulation with the VMD η form factor (solid curve) and without η form factor (labeled as QED, dashed curve) is shown.

4.6.1 π^0 and η form factors

The simulation of π^0 and η Dalitz decays is based on the resonance model [Tei97]. All contributions and the respective cross sections were taken as in Table 2.5 (Sect. 2.3.1), resulting in the red histogram in Fig. 4.30, right panel. The widths of the missing mass peaks, which do not depend on the details of the model and mainly reflect the momentum resolution of the particle tracks, are similar to the experimental ones. This justifies the procedure of the signal selection cuts from the simulation and allows for the model-driven acceptance correction. The acceptance and efficiency corrected e^+e^- invariant mass distributions are displayed in Fig. 4.31, with statistical errors and systematic errors added quadratically. In the case of the π^0 (left panel), the largest source of systematic error is the rejection of e^+e^- pairs from photon conversion, which is done by the cut on e^+e^- opening angle ($> 9°$), resulting in the loss of data at small e^+e^- invariant masses. The small excess around 0.03 GeV/c^2 is most likely due to a remaining contamination of conversion pairs. In the η region (right panel), the error is due to e^+e^- pairs from π^0 decay in multipion production processes. The yields are well reproduced by the simulation. In the case of the π^0, the production cross sections are constrained by independent data, thus the agreement in the $\pi^0 \to \gamma e^+e^-$ reconstructed yield provides a consistency check of the whole analysis chain for dileptons. In the case of the η production, the cross section was fixed by the HADES measurement in the hadronic channel (Sect. 2.3.3), thus the present analysis confirms the consistency of hadronic and leptonic reconstructions and the good control of the corresponding efficiencies.

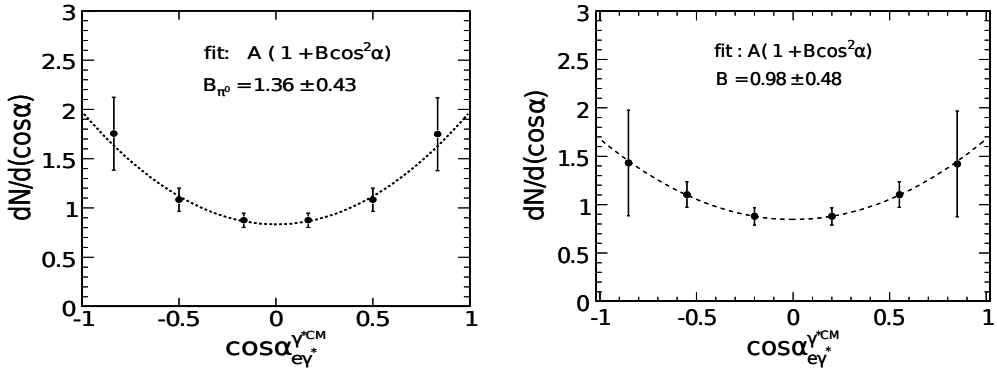

Figure 4.32: Angular distributions of electrons and positrons in the virtual photon rest frame, from π^0 (left panel) and η (right panel) Dalitz decay, after acceptance and efficiency correction. The dashed curves show a fit with a function $A(1 + B\cos^2\alpha^{\gamma^*}_{e\gamma^*})$ (see text for details). The normalization is arbitrary.

The possible contribution of Dalitz decays of baryon resonances, corresponding to a ppe^+e^- final state, is negligible (Fig. 4.31, right panel), except in the mass region close to the kinematical limit ($M_{inv}(e^+, e^-)$ = 0.547 GeV/c^2). This could explain the excess of measured yield above the simulation for the reaction $pp \to pp\eta$ for masses above 0.5 GeV/c^2. The shapes of e^+e^- invariant mass distributions are characteristic for their Dalitz decay. The description of the Dalitz decay processes in the simulation involves the modeling of the electromagnetic transition form factors (App. A.3.1). They were implemented in the simulation as pointlike (referred to as QED, dashed curves)

or VMD form factors (solid curves). The differences are negligible for the $\pi^0 \to \gamma e^+ e^-$ case, and show up for the $\eta \to \gamma e^+ e^-$ case only at larger values of the e^+e^- invariant mass. Unfortunately, the HADES data are not precise enough to provide any further quantitative constraint to these models.

4.6.2 π^0 and η angular distributions

An interesting feature of the Dalitz decay of pseudoscalar mesons is the transverse polarization of the virtual photon. The expected distribution of the angle $\alpha^{\gamma^*}_{e\gamma^*}$, that is, e^+ or e^- in the γ^* rest frame, is predicted to be proportional to $1 + B\cos^2\alpha^{\gamma^*}_{e\gamma^*}$ (Ref. [Bra95]). The calculation of this angle implies a boost of all particles in the π^0/η meson rest frame, followed by the boost of electron/positron in the virtual photon rest frame. Figure 4.32 shows the e^+ and e^- angular distributions in the π^0 (left panel) and η (right panel) Dalitz decay channels. The acceptance and efficiency corrections were calculated using the simulation of the dielectron production via Dalitz decays, as described above. The fit of a function (quoted above) results in the anisotropy coefficients, B = 1.36 ± 0.43 for the π^0, and B = 0.98 ± 0.48 for the η, in agreement with the QED prediction, B = 1 (Ref. [Bra95]).

4.7 Summary for e^+e^- production (pp at T = 2.2 GeV)

The presented data on inclusive e^+e^- production in the reaction pp at 2.2 GeV beam kinetic energy are in good agreement with the DLS result obtained earlier at 2.09 GeV. The employed cocktail of e^+e^- sources describes the π^0 region very well, but it does not saturate the data at invariant mass around 0.55 GeV/c^2. The transport models describe the data quite well, although they differ in details: HSD uses a pointlike form factor for Δ Dalitz decay, but the higher Δ production cross section as compared to the UrQMD. The ρ–meson distribution due to the coupling to baryon resonances is very different in the GiBUU and the HSD approach.

The identification of kinematically complete $ppe^+e^-\gamma$ channel allows for the reconstruction of π^0 and η Dalitz decay signals. They have been compared with Monte Carlo simulations of pseudoscalar meson production within the resonance model [Tei97] approach, followed by the subsequent Dalitz decays. In addition, the sensitivity to the pointlike and VDM-like electromagnetic transition form factors of baryon resonances has been investigated in the channel with the η–meson. Although the precision of the HADES data is not sufficient to provide constraints to the eTFF models but the analysis has confirmed that the e^+e^- invariant mass distributions presented above are fully consistent with the hadronic channels reconstructed in HADES. Yet other observables, the acceptance corrected e^+/e^- angular distributions in the γ^* rest frame, have shown the anisotropic behavior. The anisotropy coefficients from the fits to the data are in a good agreement with QED predictions for the pseudoscalar mesons.

4.8 Inclusive e^+e^- production (pp at T = 3.5 GeV)

At energy 3.5 GeV many hadron channels become available and various production scenarios are assumed in transport codes. In Hadron String Dynamics (see Sect. 4.1.2.4) and Giessen Boltzmann-Uehling-Uhlenbeck (Sect. 4.1.2.3) models, at this beam energy, hadrons are produced through string fragmentation [And83]. In the resonance Ultrarelativistic Quantum Molecular Dynamics transport model [Bas98] the decaying resonances are the sources of final state particles. First uncertainty in the dielectron production stems from the unknown inclusive cross sections of meson and baryon resonance productions, which can decay into e^+e^- pairs in two-body decays or Dalitz decays (see Sect. 3). Another uncertainty is related to the parametrization of the mass dependent resonance width. Various prescriptions are used in model calculations which differ at high resonance masses (see Eqs. 1.8 in Sect. 1.1). As a consequence, the resulting dielectron yield from the resonance Dalitz decays has a large uncertainty. Finally, the Dalitz decays of baryon resonances ($R \to Ne^+e^-$) depend on the electromagnetic structure of the $R \to N\gamma^*$ transition vertex (Sect. 3.4).

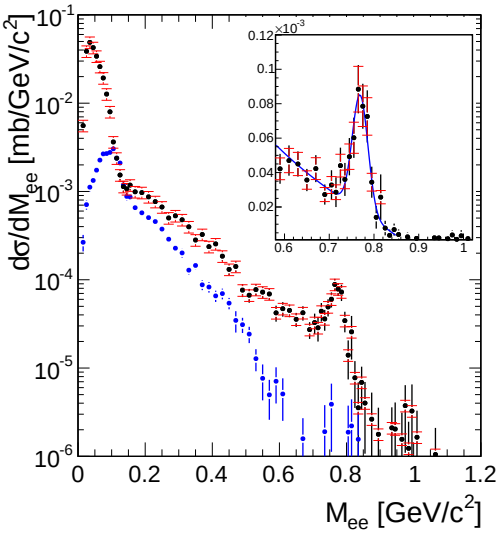

Figure 4.33: e^+e^- invariant mass distribution in $pp \to ppe^+e^-X$ reaction at energy of 3.5 GeV [HC12a]. The distribution (black dots) is after combinatorial background (blue) subtraction, efficiency corrected and within the HADES acceptance. The data are normalized to the pp elastic events. The inset: the ω−meson region shown on a linear scale.

The inclusive e^+e^- signal pair distribution, after a combinatorial background subtraction, is shown in Fig. 4.33. It is efficiency corrected and normalized to $N_{el}^{acc}/\sigma_{el}^{acc}$, where N_{el}^{acc} and σ_{el}^{acc} denote the measured yield of the pp elastic scattering and the differential elastic cross section from Ref. [Kam71] inside the acceptance of HADES, respectively. In total, $6.1{\times}10^4$ signal pairs were reconstructed, with $5.4{\times}10^4$ in the mass region below 0.15 GeV/c^2. The spectrum shows a clear peak around the pole mass of the ω−meson, corresponding to its direct decay into e^+e^- pairs. The peak is shown also on a linear scale in the inset, where it was fitted with a Gaussian distribution and a polynomial for the underlying continuum. The obtained mass resolution amounts to $\sigma/M_{pole}^{\omega} \approx 2\%$. The number of pairs in the mass range between 0.71 GeV/c^2 and 0.81 GeV/c^2, which corresponds to the $\pm 3\sigma$ interval around the reconstructed ω peak, amounts to 260.

4.8.1 Comparison to models

When neglecting the internal degrees of freedom of dielectron decay, e.g. helicity angles of virtual photons, the reaction $pp \to e^+e^-X$ can be described by three independent degrees of freedom, e.g. invariant mass, transverse momentum, and rapidity. An overview of inclusive dielectron channel from $pp \to ppe^+e^-X$ reaction at energy of 3.5 GeV, obtained in various models, is given below.

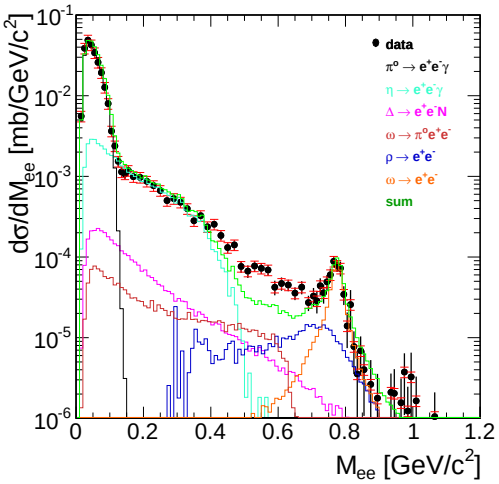

Figure 4.34: Left panel: e^+e^- invariant mass distribution compared to a simulated cocktail from the PYTHIA. Green curve represent the sum of all contributions (see legend for description).

Bottom panel: comparison of transverse momentum (p_t) - left group, and rapidity (y) - right group, presented in four invariant mass ($M_{e^+e^-}$) bins.

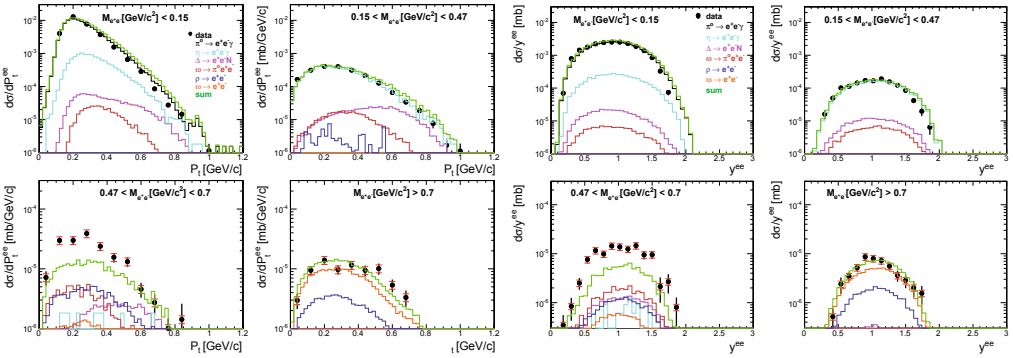

4.8.1.1 PYTHIA generator

The PYTHIA is a program developed at the Lund University [Sjö08] for the generation of high-energy collisions, comprising a coherent set of physics models for the evolution from a few-body hard process to a complex multihadronic final state. It is implemented in the transport models, e.g. HSD add GiBUU, to model hadron production. The inclusive cross sections for vector mesons, η, and $\Delta(1232)$ resonance, were adjusted in order to describe the measured dielectron yields in the invariant mass, transverse momentum and rapidity distributions (see below). The simulated dielectron sources, Dalitz decays of the pseudoscalar mesons π^0 and η, vector meson ω, and $\Delta(1232)$ resonance only, as well as direct vector meson decays $V \to e^+e^-$, where $V = \rho$, ω, were added incoherently. The decays were simulated outside the PYTHIA, in the PLUTO event generator (see App. C.3.1). The masses of ρ, ω and $\Delta(1232)$ were generated according

to relativistic Breit-Wigner distribution, replacing the implementation of the resonances with constant total widths around the resonance pole mass in the PYTHIA. In case of the $\Delta(1232)$ baryon resonance the mass dependence of the total width is calculated from its $N\pi$ decay channel with the cutoff parametrization as in Ref. [Man92], known as Blatt-Weisskopf or Manley Δ resonance parametrization (see Eq. 1.7). The mass dependence of the ρ and ω total width is parametrized as in Ref. [Bra08].

Figure 4.34, left panel, presents the comparison of invariant mass distribution for the data and the PYTHIA model. The simulated cocktail reproduces the data reasonably well except for the mass range around 0.55 GeV/c^2 where the yield is underestimated. The $\Delta(1232)$ is modeled with a pointlike electromagnetic transition form factor, fixed at the photon point, what is obviously not sufficient at high mass. However, one should note that contributions of higher Δ and N^* resonances are not included at all. The two sets of four figures (Fig. 4.34, bottom panel) present the comparison of the data to the PYTHIA simulations in the transverse momentum ($d\sigma/dp_t^{ee}$), and rapidity ($d\sigma/dy^{ee}$) distributions. They are split into four mass bins: (a) $M_{e^+e^-} < 0.15$ GeV/c^2 (upper left), (b) $0.15 < M_{e^+e^-} < 0.47$ GeV/c^2 (upper right), (c) $0.47 < M_{e^+e^-} < 0.7$ GeV/c^2 (lower left), and (d) $M_{e^+e^-} > 0.7$ GeV/c^2 (lower right). The low mass regions, (a) and (b), are dominated by the π^0 Dalitz decay and η Dalitz decays, respectively. Similar to the invariant mass distribution, in the p_t and y distributions, they are described by the PYTHIA cocktail very well. The high mass region (d), is saturated by the vector meson direct decays, again, well described in all representations. The mass region below the ω−meson pole mass (c), is not sufficiently described, pointing to the missing yield from baryon resonances, both in terms of their cross sections, transition form factors, and the coupling strength to $N\rho$ channel.

4.8.1.2 GiBUU model

Figure 4.35 shows a comparison of the GiBUU simulation to the HADES data. The η, ω and ρ production channels are fully accessible at energy of $\sqrt{s}$ = 3.18 GeV. In the GiBUU model, the η and ρ production is based on the cross sections obtained from PYTHIA.

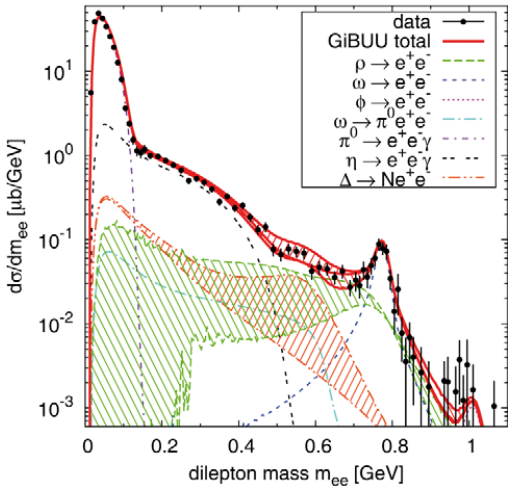

Figure 4.35: GiBUU description of the e^+e^- mass spectrum for pp at 3.5 GeV. $\Delta(1232)$ resonance is presented with both a pointlike (lower limit), and Iachello-Wan transition form factor (upper limit, red right-hatched area). The baryon resonance contributions to the ρ production are shown as green hatched area. The total contributions (from bottom to top) are plotted with Δ form factor (left hatched), ρ resonance contributions (right hatched). Figure adopted from Ref. [Wei12].

Above the mass of η–meson, two dielectron sources, described with the largest uncertainty, are investigated in details. The first source is related to the ρ contribution given by the resonance model and the PYTHIA. The PYTHIA result is given by the lower limit green dashed curve in Fig. 4.35. The green hatched area presents the ρ shape due to the production of ρ mesons via nucleon resonances, e.g. $NN \to NR(\to N\rho)$ and $NN \to \Delta R(\to N\rho)$. A major contribution to the low-mass part of the ρ spectral function comes from the $N(1520)$ resonance. Together with the $1/m_{ee}^3$ factor of the dilepton decay width (see Eq. A.30 in App. A.2.1), the ρ shape is strongly enhanced towards lower masses and dominates the dilepton spectrum in the intermediate mass region around $0.5 - 0.7$ GeV/c^2. This modification is solely caused by the production mechanism via baryon resonances. Therefore, the determination of the coupling constants of resonances to $N\rho$ channel plays an important role. However, the knowledge of the resonance contributions to the ρ channel is constrained only from the two-pion decay channels, which are known with large errors (see Ref. [PDG16]). Yet another uncertainty is related to the Δ (or in general, a baryon resonance) electromagnetic transition form factor. In Figure 4.35, similar to the description of pp data at 2.2 GeV (Sect. 4.5.2.1), the Δ Dalitz contribution is presented with two assumptions: using a pointlike form factor (lower limit, red dot-dot-dashed curve), and the Iachello-Wan (App. B.3) form factor, plotted as a red hatched area. The gap in the intermediate mass region, as shown in the PYTHIA model (Fig. 4.34, left panel), can now be filled either by the ρ production from baryon resonances, or by the Δ resonance with Iachello-Wan form factors. The sum of both modifications leads to the overestimation of dielectron yield, as compared to data.

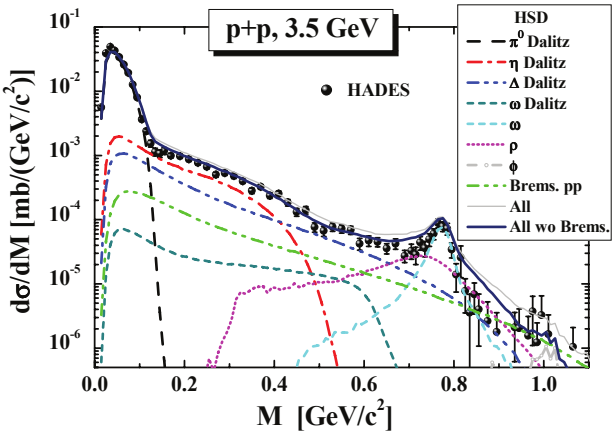

Figure 4.36: The differential cross section $d\sigma/dM$ from HSD calculations for e^+e^- production in pp reactions at energy of 3.5 GeV in comparison to the HADES data. The distribution is presented within the HADES acceptance.

4.8.1.3 HSD model

The Hadron-String-Dynamics (HSD) transport approach presented in Ref. [Bra13] (see Sect. 4.1.2.4) is compared with the HADES data in Fig. 4.36. The blue curve, labeled in the legend as "All wo Brems" shows the sum of all channels (labeled as "All") without pp bremsstrahlung, since at this energy no reliable bremsstrahlung calculations exist. The striking feature of the HSD is much higher yield of Δ Dalitz decay in comparison to the GiBUU or SMASH calculations. The HSD approach uses Wolf *et al.* [Wol90] parametrization of the Δ Dalitz decay, which predicts significantly larger contribution than Krivoruchenko formula [Kri02] (see Fig. 3.6 and Sect. 3.4). The Δ Dalitz yield compensates smaller ρ contribution, since the enhancement of the ρ–meson production by accounting for the $N(1520)$ channel is relatively small in the HSD model.

Although the overall description of the invariant mass spectrum is good, except the high mass region, the model should be also confronted with the data in different kinematical variables. Despite a number of adjustments (lowering of η, ω, and ρ dilepton decay contributions, as described in Ref. [Bra13]), the HSD predicts higher yield in the transverse momentum p_t representation, in all mass bins $M_{e^+e^-} > 0.15$ GeV/c^2 (see the PYTHIA model). It is a direct consequence of the large $\Delta(1232)$ contribution which seems not to be supported by the data.

4.8.1.4 UrQMD model

The dilepton invariant mass spectrum in the UrQMD model description ([End13], see Sect. 4.5.2.3) for pp at 3.5 GeV within the HADES acceptance is shown in Fig. 4.37. Although the UrQMD contains the excitation of many Δ and N^* resonances up to the mass of 2.25 GeV/c^2, only the Dalitz decay of the $\Delta(1232)$ isobar is explicitly included. The Δ Dalitz decay parametrization is the same as in the HSD, but the resonance total width uses Bass parametrization [Bas98] (see Eq. 1.8 and Fig. 1.1), leading to the lower dielectron yield. The e^+e^- contribution from decays of higher-lying resonances is included via their ρ decay branches what leads to an overestimation of the e^+e^- production from the ρ decays at high masses.

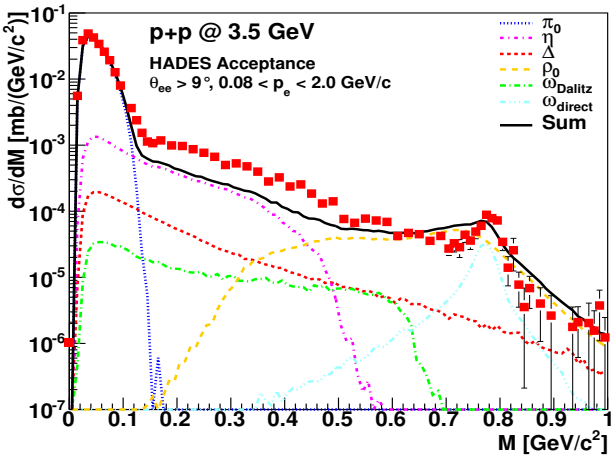

Figure 4.37: Dielectron invariant mass spectrum for pp at 3.5 GeV within the HADES acceptance, compared to the UrQMD transport model (for the color coding, see legend).

The UrQMD contribution is clearly underestimated in the intermediate mass bin, $0.15 < M_{e^+e^-} < 0.47$ GeV/c^2, which is populated mainly by the pairs originating from η Dalitz decays. This discrepancy can be also studied e.g. in transverse momentum representation, where UrQMD is low by a factor of 2 at low p_t and a factor of 5 too high at large p_t. This high–p_t part contains, in addition, a substantial contribution from the $\Delta(1232)$ Dalitz decay.

4.8.1.5 SMASH model

The recently developed hadronic transport model, SMASH (Simulating Many Accelerated Strongly-interacting Hadrons) [Wei16], is a microscopic approach based on the relativistic Boltzmann equation. It profits from the description of dielectron production developed in the UrQMD and the GiBUU models. It describes collisions at low and intermediate beam energies with the aim to provide a standard reference for hadronic systems with vacuum properties. The collision term is modeled by excitation and decay

of resonances and is restricted to binary collisions. Two particles collide, if the geometric collision criterion ($d_{trans} < \sqrt{\sigma_{tot}/\pi}$), employed also in the UrQMD [Bas98], is fulfilled. Only binary collisions and two body decays are performed in order to conserve detailed balance, therefore generic multi-particle decays are implemented with the intermediate resonance states (e.g., $\omega \to \rho\pi \to 3\pi$). The model includes well-established hadronic states listed in the PDG [PDG16] up to a mass of 2.35 GeV, with their corresponding decays and cross sections (for a tabulated list see Ref. [Wei16]). All spectral functions are described by relativistic Breit-Wigner functions and the hadronic partial widths are calculated following the framework of Manley and Saleski [Man92]. All resonances are either produced by inelastic scattering and absorption, or decays of other resonances. The dilepton emission in SMASH is calculated by direct or Dalitz decays of resonances. The directly decaying resonances, like e.g. the ρ meson, include Dalitz decay contributions in a factorization scheme $\Delta/N^* \to \rho X \to e^+e^-X$. The decay width of vector mesons is calculated under the assumptions of vector meson domiance [Li96]. Pseudoscalar meson Dalitz decays are described in Appendix A.3.1. Δ Dalitz decay is described by Krivoruchenko *et al.* formula [Kri02] (see Sect. 3.4), with the constant form factor fixed at the photon point, $F_\Delta(0) = 3.12$. The description of dilepton production in elementary collisions is used as a baseline for the binary reactions occurring in a nucleus-nucleus collision.

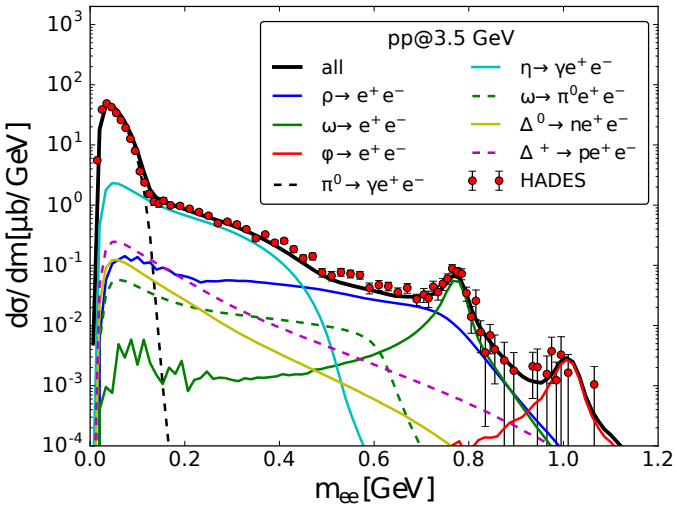

Figure 4.38: The SMASH model [Sta17] compared to the HADES data in *pp* collisions at 3.5 GeV. The most important role plays ρ–meson (blue curve) and its coupling to baryon resonances.

The HADES data in the kinetic energy range of 1 – 3.5 GeV/nucleon were systematically confronted with the SMASH model [Sta17]. Figure 4.38 shows the dielectron invariant mass spectrum produced in *pp* at 3.5 GeV. The good description of the experimental data results from the ρ–meson coupling to baryonic resonances. The significant contributions below two-pion threshold come from Dalitz decays of the light baryonic resonances, mainly $N(1520)$, $\Delta(1620)$, and $\Delta(1700)$.

4.8.2 π^0, η, ρ, and ω cross sections

Integration of the measured yield, followed by the efficiency correction and model-dependent extrapolation to the full phase space, allows for the determination of inclusive cross section of the produced mesons and Δ resonance. The π^0 yield was obtained by integrating the invariant mass between 0 and 0.15 GeV/c^2 (Fig. 4.33). In order

to minimize the model-dependent correction, the average factor was extracted from calculations based on URQMD and PYTHIA events. The measured data of π^0 Dalitz decay were corrected for the Dalitz decay branching ratio (see Table A.2 in App. A.3.1). Finally, the extracted cross section was corrected for the pions originating from the η and ω decays. The obtained inclusive cross section amounts to σ_{π^0} = 17±2.65±1 (model) mb, and is depicted as a red open circle in Fig. 4.39, left panel.

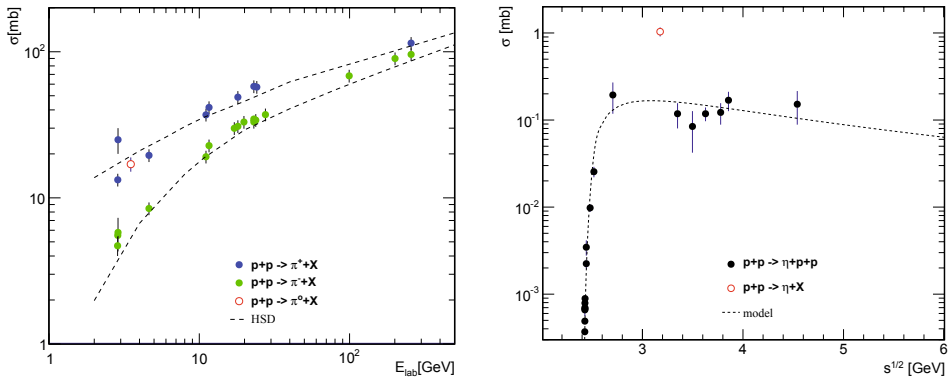

Figure 4.39: Left panel: pion inclusive production cross sections in pp collisions (π^+, blue dots, π^-, green dots, π^0, red open circle - extracted from the HADES data). The dashed curves refer to the parametrizations used in the HSD model. Right panel: η−meson exclusive production cross sections, with the inclusive production cross section obtained from the HADES data (red open circle). The dashed curve represents the exclusive $pp\eta$ production through the $N(1535)$ resonance predicted by the resonance model [Tei97] .

The yield integrated between 0.15 and 0.47 GeV/c^2 allows for the extraction of the η−meson inclusive cross section. The contributions of other sources were fixed based on the PYTHIA prediction for the Δ Dalitz decay (see Fig. 4.34, bottom panel) and based on the known ω cross section. These contributions were subtracted, introducing small systematic error of 3.7%. The model-dependent extrapolation was performed in the same way as in the π^0−meson case. The cross section amounts to $\sigma_\eta = 1.035 \pm 0.17 \pm 0.105$ (model) mb. Figure 4.39 shows the known exclusive η−meson cross sections, with a red open circle depicting the η inclusive cross section.

The inclusive production cross sections for the vector mesons were obtained from their multiplicities in full phase space generated by PYTHIA. The HADES spectrometer acceptance for e^+e^- pairs from vector meson decays is high, $\epsilon_{pair} \approx 40\%$ (see App. C), and does not introduce any bias. The obtained cross sections are $\sigma_\omega = 0.273 \pm 0.07$ mb, and $\sigma_\rho = 0.233 \pm 0.06$ mb, respectively. Figure 4.40 shows a compilation of measured production cross sections of vector mesons (ω, ρ) in pp collisions at different energies [Bal88]. Full dots represent the exclusive production channels, open dots (including a red open circle from the HADES data) represent the inclusive production channels.

The errors quoted for the extracted cross sections, besides the model error (for π^0 and η), are square roots of statistical and systematic errors, added quadratically. The systematic error includes both efficiency correction and the normalization error.

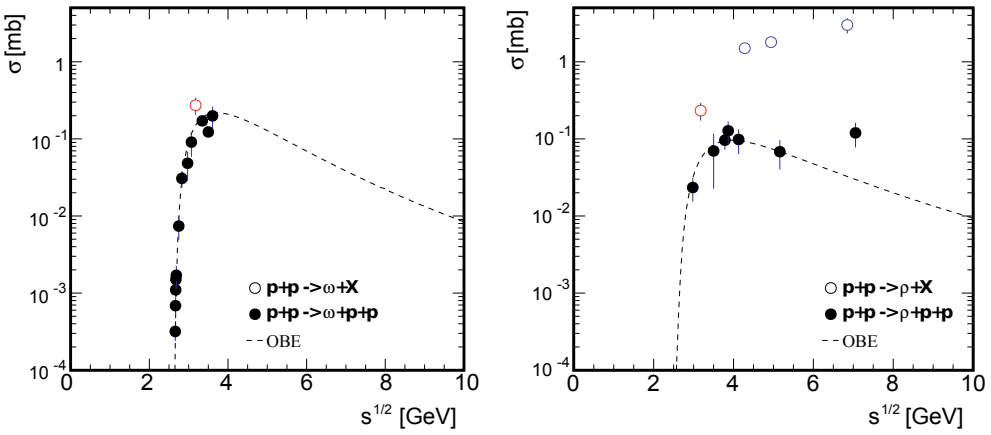

Figure 4.40: Cross-sections for the vector mesons ω (left panel) and ρ (right panel), in pp collisions as a function of $\sqrt{s}$. The data points represent the exclusive (full dots) and inclusive (open dots) production cross sections, respectively. The cross section values extracted from the HADES data are depicted in red. The dashed curves refer to the OBE calculations for the exclusive channels from Ref. [Sib97].

4.9 Exclusive e^+e^- production (pp at T = 3.5 GeV)

In Section 2.4 a detailed analysis of one-pion exclusive channels $pp\pi^0$, $np\pi^+$ in pp collisions at energy 3.5 GeV was presented. Δ and N^* resonance production cross sections were deduced by means of a resonance model [Tei97] and with the empirical angular distributions derivation. The obtained results can be used for the exclusive $pp \to ppe^+e^-$ final state. Such a channel selects, from all possible dielectron sources, only those related to the two-body vector meson decays and the resonance conversions, $R \to pe^+e^-$, which modeling, as demonstrated in Sect. 4.8 above, is the subject of the largest uncertainties. The other dielectron sources dominating the inclusive e^+e^- production (see Sect. 4.8), in particular the Dalitz decays of $\pi^0/\eta \to \gamma e^+e^-$ and $\omega \to \pi^0 e^+e^-$, can be effectively suppressed via kinematical constraints. In the calculations of the resonance Dalitz decay spectra, a pointlike $RN\gamma^*$ coupling (see Refs. [Zét03a, Zét03b] and App. B.1) will be used, constrained by experimental data on $R \to N\gamma$ transitions. The modifications of the respective electromagnetic transition form factors, due to the resonance-vector meson couplings, will be directly visible in the e^+e^- invariant mass distributions. Finally, the exclusive ppe^+e^- data are compared to the calculations assuming dominance of the ρ–meson.

4.9.1 ppe^+e^- final state

For the ppe^+e^- final state identification, events containing at least one proton track and one dielectron pair were selected. The electron tracks were identified by means of the RICH detector, providing also the electron emission angles for matching with tracks reconstructed in the MDC. In the next step, all pe^+e^- candidates were identified in a given event, and the same procedure was applied for the pe^+e^+ and the pe^-e^-

track combinations in order to estimate the combinatorial background (CB). The CB was calculated using the like-sign pair technique, given as a sum of like-sign pairs in events with one proton at least, as described in App. C.3.5.2. The main origin of the combinatorial background is from multi-pion (π^0) production followed by a photon conversion in the detector material.

Figure 4.41 (left panel) shows the missing mass distribution of the pe^+e^- system (black squares) together with the CB (a sum of the pe^+e^+ and pe^-e^- contributions depicted by red points). The blue histogram presents the signal after the CB subtraction. The CB contribution increases with the missing mass but it is small in the interesting region around the mass of a missing proton. The right panel of Fig. 4.41 displays the dielectron invariant mass distributions for events located inside the window centered around the proton mass ($0.8 < M_{miss}^{pe^+e^-} < 1.04$ GeV/c^2) for: (i) the unlike-sign pairs (black squares) and (ii) the CB (red dots) for the e^+e^- pairs with masses $M_{inv}^{e^+e^-} > 0.14$ GeV/c^2. The latter condition removes abundant pairs originating from the π^0 Dalitz decay and allows for better inspection of high-mass e^+e^- pairs stemming from the baryon resonance conversions ($R \to pe^+e^-$) and from vector mesons ($\rho/\omega \to e^+e^-$) decays.

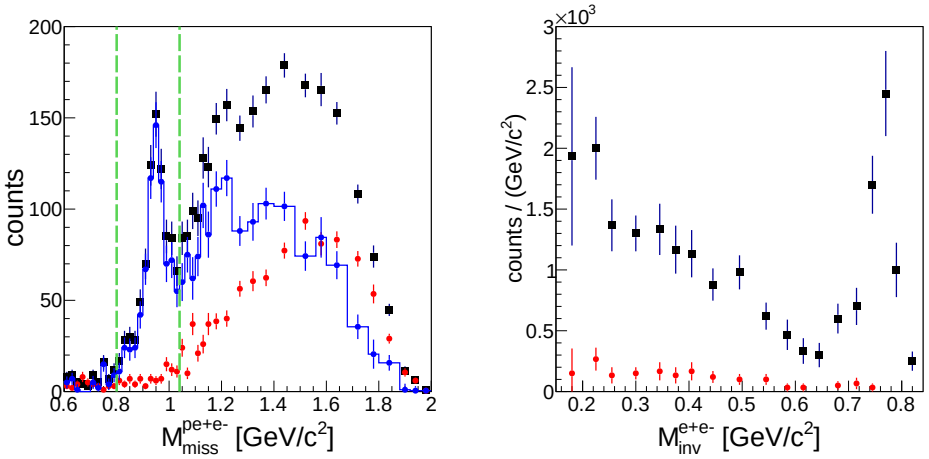

Figure 4.41: Left panel: missing mass distribution for the pe^+e^- system (black squares), sum of pe^+e^+ and pe^-e^- (red dots), accounting for the combinatorial background, and the signal pe^+e^- system (blue histogram) for $M_{e^+e^-} > 0.14$ GeV/c^2. Right panel: dielectron invariant mass for the signal pairs (black squares) and the CB (red dots) for the events inside the window around the mass of the missing proton (left panel: limited by the vertical dashed lines, $0.8 < M_{miss}^{pe^+e^-} < 1.04$ GeV/c^2). The total number of signal pairs amounts to 750. The number of counts is given per GeV/c^2 to account for the variable bin width used.

The missing mass $M_{miss}^{pe^+e^-}$ distribution, and the e^+e^- and the pe^+e^- invariant mass distributions are used below in comparison to various models. All experimental distributions are normalized to the measured elastic scattering yields (as explained in Sect. 2.4), and the simulation results are filtered through the acceptance and efficiency matrices followed by a smearing with the experimental resolution. The data are compared to simulations assuming the production cross sections σ_R of baryon resonances from Table 2.7 (Sect. 2.4.4) and the ω and ρ meson cross sections given in Sect. 2.4.1.

4.9.2 Pointlike RNγ* coupling

To begin with, the assumption of a pointlike $RN\gamma^*$ coupling, called QED model (App. B.1), was made. The missing mass distribution of the pe^+e^- system with respect to the beam-target system, after CB subtraction, is shown in Fig. 4.42 (left panel). The error bars represent statistical (vertical) and the normalization (red horizontal) errors. The distribution is compared with the result of the simulation (dashed curve) including the baryon resonances and ρ, ω and η meson sources. The baryon resonances included in the simulations are indicated by bold symbols in Table 2.7 and grouped into two contributions, appearing to be of similar size, originating from the $\Delta(1232)$ and the higher mass (Δ^+, N^*) states. The hatched area uncovers the model uncertainties related to the errors of resonance and meson production cross sections (see below for a more detailed discussion).

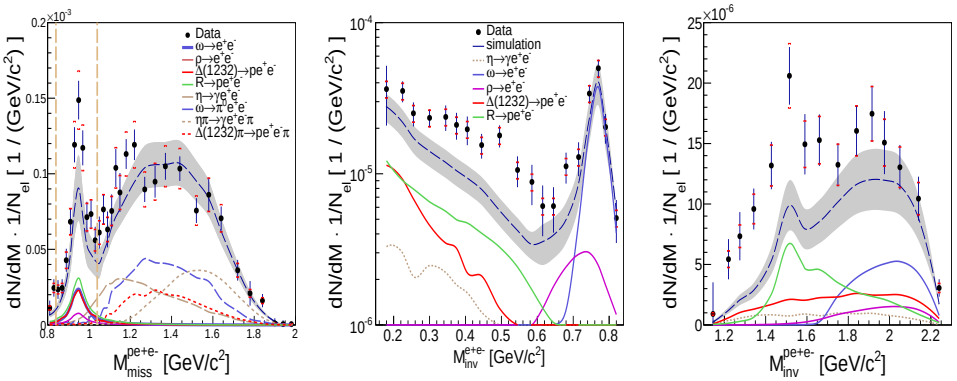

Figure 4.42: ppe^+e^- final state: pe^+e^- missing mass (left panel), dielectron (middle panel) and pe^+e^- (right panel) invariant mass distributions compared to the simulation result assuming a pointlike $RN\gamma^*$ coupling (QED-model). The invariant mass distributions have been obtained for events inside the indicated window (vertical dashed lines in the left panel) on the pe^+e^- missing mass. The hatched area indicates the model errors (for more details see text). Number of counts is per mass bin width.

In order to account for events with $M_{miss}^{pe^+e^-} > M_p$ the final states $p\Delta^{+,0}\pi^{0,+}$, $pp(n)\eta\pi^{0,+}$ were included in the simulations. Channels with two and more pions were omitted because of negligible contributions caused by smaller cross section and the small HADES acceptance for the very forward emitted protons. A very good description of the pe^+e^- missing mass distribution could be achieved with all the sources mentioned above, except for the yield in the proton missing-mass peak itself. It is important to note that the background under the proton peak, related to final states other than ppe^+e^-, is smaller than 6%. In particular, channels including the $\eta \to e^+e^-\gamma$ decay are strongly suppressed.

The middle part of Fig. 4.42 displays the e^+e^- invariant mass distribution for the events within the pe^+e^- missing mass window, shown by the vertical dashed lines in the left panel. It is compared to the simulation including dielectron sources originating from the baryon resonance decays and the two-body meson ρ, $\omega \to e^+e^-$ decays. A very good agreement in the vector mass pole is achieved. Since the exclusive production cross section of vector mesons at this energy are rather well known, the agreement confirms

that the normalization and the simulations of the HADES acceptance and reconstruction efficiencies are under control. On the other hand, an excess of the contributions from the baryon resonances is clearly visible below the vector meson pole. The effect is obviously related to the apparent excess in the proton missing-mass window. This is, however, not a surprise because one expects contributions from off-shell couplings of the resonances to the vector mesons. It is expected that such couplings modify the respective eTFF which were assumed to be constant in the simulations. Therefore, the observed enhancement below the vector mass pole can be interpreted as a fingerprint of the anticipated contribution.

The hatched area presents the model error on the dielectron conversion yields related to the discussed ambiguities of the resonance assignments. Apart from the resonance production cross sections, the overlapping states differ also in the branching ratios for the Dalitz decay (see Tables 2.6 in Sect. 2.4.1 and 2.7 in Sect. 2.4.4). However, the effect on the pair yield (hatched area) turns out to be rather moderate. This is because the relative variation of the pair yield due to changes in the resonance production cross sections is compensated by the respective changes in the branching ratios for the dielectron conversion. Consequently, one can conclude that the excess above the calculated yield cannot be explained by another choice of the resonances in the calculations. The substantially different shape of the experimental invariant mass distribution, as compared to the simulation, indicates also the importance of the off-shell vector couplings.

This conclusion seems to be corroborated by the comparison of the pe^+e^- invariant mass distribution with the simulation, displayed in Fig. 4.42 (right panel), which shows that the excess is indeed located around the $N(1520)$ resonance known to have a sizable decay branch to the ρ–meson.

4.9.3 Resonance–ρ coupling

The dielectron production through the resonance decay can be factorized as a two step process, proceeding through the intermediate ρ–meson production, $R \rightarrow p\rho \rightarrow pe^+e^-$. Such a scheme is used in transport models, the GiBUU [Bus12], the SMASH [Wei16], and the UrQMD [Bas98], as discussed in Sect. 4.8.1. The results of the two models were recently published in Ref. [Wei12] (GiBUU) and Refs. [Sch09, End13] (UrQMD), giving the prediction or comparison to HADES inclusive data [HC12a].

In order to compare the calculations of the contributions to the exclusive ppe^+e^- channel the final states including single resonance production are selected. The respective cross sections are given in Table 2.7 and the branching ratios to $p\rho$ are listed in Refs. [Bus12] and [Sch09]. Table 4.2 summarizes these branching ratios (columns "GiBUU" and "UrQMD") together with more recent results from a multichannel partial wave analysis which are discussed below.

First, the GiBUU events, provided by the authors of Ref. [Bus12], were filtered through the HADES acceptance and reconstruction efficiency matrices. For the resonance production a non isotropic production was assumed according to the measured t distributions (see Eq. 2.9) presented in Sect. 2.4.2. The ω meson production is generated assuming uniform phase space population. The two plots in Fig. 4.43 show a comparison of the dielectron and the pe^+e^- invariant mass distributions to the results of calculations normalized to the same elastic scattering yield. The total yield (solid

curves) is decomposed into the contributions originating from the $\Delta(1232)$ (red curves), the ω meson (blue curves) and the higher mass resonances (dashed green curve) which are mainly the decays of $N(1520)$ (38%), $N(1720)$ (22%), $\Delta(1620)$ (15%) and $\Delta(1905)$ (6.5%). The measured distributions are well described, except some lacking intensity at low dielectron and pe^+e^- invariant masses and some overshoot just below the vector meson pole. The missing yield might suggest an even stronger contribution of $N(1520)$, as also indicated by the comparison to pion spectra in Fig. 2.32 (Sect. 2.4.4), where the calculations based on cross sections used in the GiBUU do not describe the $n\pi^+$ invariant mass distributions around 1.5 GeV/c^2. On the other hand, the usage of the cross section for $N(1520)$ and $N(1440)$ obtained from the HADES analysis would overestimate the measured dielectron yield almost by a factor 2, if branching ratios from the GiBUU were used (see Table 4.2).

Resonances	GiBUU	UrQMD	KSU	BG	CLAS
$N(1520)$	21	15	20.9(7)	10(3)	13(4)
$\Delta(1620)$	29	5	26(2)	12(9)	16
$N(1720)$	87	73	1.4(5)	10(13)	-
$\Delta(1905)$	87	80	< 14	42(8)	-

Table 4.2: Branching ratios (in percent) for $R \to N\rho$ decays applied in GiBUU [Bus12] (second column) and UrQMD [Sch09] (third column) for the most important dielectron sources. KSU: $BR(N\rho)$ and its error (in brackets) from multichannel PWA [Shr12], BG: the difference between the total and the sum of all determined partial branching ratios (except $N\rho$) from the Bonn-Gatchina group [Ani12]. CLAS: results from the analysis [CC12a]. For details, see text.

Since the resonance sources contributing to the dielectron production in UrQMD [Bas98] are almost the same as in GiBUU [Bus12], one can estimate the corresponding yields. Indeed, according to Ref. [Sch09], the main contributions to the ρ production stem from $N(1720)$, $N(1520)$, $\Delta(1905)$ and $N(1680)$, respectively. The production cross sections are given in Table 2.7 and are by a factor $5-6$ larger than the corresponding cross sections used in the GiBUU code [Bus12]. Consequently, the calculated total dielectron yield below the vector meson pole, including the $\Delta(1232)$ contribution, is overestimated by a factor of about 3. The authors of Ref. [Sch09] came to similar conclusions comparing their calculations to the inclusive dielectron production measured by DLS [DC98].

The comparison in Fig. 4.43 shows, despite the fact that both models were well tuned to describe the total pion production cross sections, the predictions for dielectron production differ substantially. This is not a surprise since, in spite of the large branching ratios for the $N\rho$ decays assumed in the calculations, dielectrons are very sensitive to the resonance contributions. In particular, e^+e^- contributions from Dalitz decays of higher mass resonances are significant, larger than expected from $\Delta(1232)$ Dalitz decay, and require a good understanding of the $R \to pe^+e^-$ decay mechanism. In the factorization scheme, with off-shell ρ–resonance coupling, the dielectron yield depends on the $R \to p\rho$ branching ratios which are taken in both models within the limits given by the PDG [PDG16]. The extracted parameters are based on various multichannel analyses of pion induced reactions (mainly two-pion production), suffering from low statistics. A new comprehensive multichannel analysis of the pion and photon induced reactions,

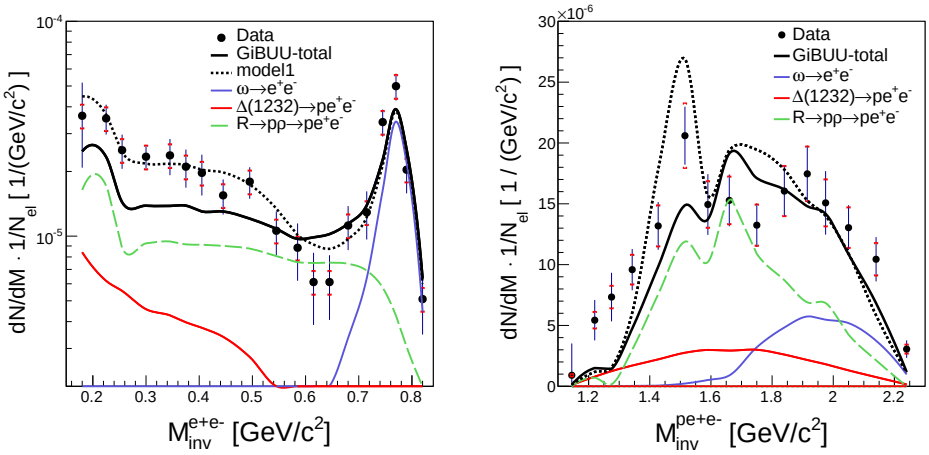

Figure 4.43: Experimental dielectron (left panel) and pe^+e^- (right panel) invariant-mass distributions compared to simulations based on the input from GiBUU (solid curve). Contributions from higher mass resonances, $\Delta(1232)$ and the ω meson are indicated separately. Dotted curves show results of calculations using modified cross sections and $R \to N\rho$ branching ratios from Ref. [Ani12]. Number of counts is per mass bin width. For details, see text.

performed by Shrestha and Manley (KSU) [Shr12] and by the Bonn-Gatchina (BG) group [Ani12], however, shows smaller branching ratios for the $N\rho$ decays (see Table 4.2). In the BG analysis the dominant channel for the two-pion production is the $\Delta\pi$ channel. The group does not provide any branching ratios for the $p\rho$ decay ($\pi^+\pi^-$ final state is not included in the analysis), however, from the provided branching ratios (mainly πN and $\Delta\pi$) one can estimate the contribution left for the $p\rho$ decay. Table 4.2 shows the respective estimates, which for the most important resonances $N(1520)$, $N(1720)$ $\Delta(1620)$ predict branching ratios of the order of 10% only. The recent results from CLAS [CC12a] suggest lower values of the branching ratios (see the rightmost column in Table 2.7, Sect. 2.4.4).

Using the BG branching ratio would lead to an underestimation of the dielectron yield if the cross sections applied in GiBUU [Bus12] are strictly used. However, if the higher cross sections for the $N(1520)$, and smaller for the $N(1440)$, $N(1535)$, as extracted from the HADES simulations, are taken, the calculation explains the measured ppe^+e^- yield slightly better, as seen in Fig. 4.43 (model1 - dashed dotted curve). Hence, it remains still a subject of future work, both on theoretical and experimental sides, to better constrain the properties of the $R \to pe^+e^-$ decay.

4.10 Summary for e^+e^- production (pp at T = 3.5 GeV)

In summary, the inclusive invariant mass, transverse momentum and rapidity distributions of dielectrons (e^+e^- pairs) in pp interactions at 3.5 GeV beam kinetic energy were reported. In the vector meson mass region, a peak corresponding to direct ω decays is reconstructed with 2% mass resolution. The experimental distributions were compared to the results from the PYTHIA, GiBUU, HSD, UrQMD, and SMASH event generators, which use different physics assumptions to generate the parent hadrons decaying subsequently into e^+e^- at this projectile energy. The discrepancies in the descriptions, mainly related to the role of the $\Delta(1232)$ and higher-lying resonance Dalitz decays, as well as the couplings to the ρN channel, cannot be fixed by the inclusive data.

The inclusive production cross sections for ω and ρ mesons were determined, for the first time, from dielectron experimental data, together with the cross sections for π^0 and η mesons. In addition, based on the inclusive e^+e^- data at 3.5 GeV, the upper bound for the direct $\eta \to e^+e^-$ decay was improved by a factor of 6 compared to the value quoted in Ref. [CWC08], as shown in Appendix A.2.3. Even lower estimate was obtained from $p + Nb$ data at 3.5 GeV measured with HADES, see Ref. [HC13].

The analysis of the exclusive ppe^+e^- channel was focused on the dielectron production from electromagnetic baryon-resonance Dalitz-decays and two-body $\omega-$meson decay ($\omega \to e^+e^-$). Clear signals of the $\omega-$meson and the resonance decays have been established. In particular, a significant yield below the vector meson pole has been measured and attributed to the Dalitz decays of baryon resonances. Using the resonance model approach, upper limits for the various resonance contributions to the dielectron spectrum have been obtained assuming pointlike baryon-virtual-photon couplings. The calculated dielectron yields cannot reproduce the measured yield and suggest strong off-shell vector meson couplings, which should influence the respective electromagnetic Transition Form Factors (eTFF). Upcoming theoretical studies of the eTFF in the timelike region are eagerly awaited for a more detailed comparison with our data.

An alternative approach for the Dalitz decay of resonances assuming a factorization scheme $R \to p\rho \to pe^+e^-$ was studied following the implementation used in the GiBUU/SMASH and UrQMD codes. The GiBUU calculations explain the dielectron and pe^+e^- invariant mass distributions, except the low-mass region which are due to a too small $N(1520)$ contribution visible also in the comparison of the model to the $n\pi^+$ invariant mass distribution. On the other hand simulations based on the resonance cross sections used in UrQMD overestimate dielectron yields by a factor 3. However, the calculated dielectron yields depend strongly on the $R \to p\rho$ branching ratios which, according to new results from multichannel analysis of pion and photon reactions off the proton, might be smaller than presently used in transport calculations. This conclusion is also corroborated by the calculations employing smaller branching ratios and the cross sections for resonance production derived from the HADES on the $pp\pi^0$ and $np\pi^+$ channels. Further theoretical studies, including our results on exclusive ppe^+e^-, are needed to better understand the electromagnetic decays of baryon resonances.

Chapter 5

Summary and outlook

The data collected by the HADES Collaboration in elementary collisions allowed for investigation of hadronic channels. One-pion production reactions in pp at 1.25 GeV were compared to predictions of a modified OPE resonance model [Tei97] and investigated with the Bonn-Gatchina [Ani06] partial wave analysis method (Sect. 2.1). Extended studies provided good description of the data and confirmed the dominant contribution of $\Delta(1232)$, yet with a sizable impact of $N(1440)$ and non-resonant partial waves. In quasi-free np collisions at 1.25 GeV, two-pion production was compared with the various model predictions (Sect. 2.2) with the aim of studying the excitation of baryonic resonances coupled to the ρ–meson in the isospin $I = 1$ channel. The model contributions from the double–Δ, $N(1400)$, and $\Delta(1600)$ excitation were compared with experimental data, demonstrating the significance of the double–Δ channel. The exclusive hadronic channels with one-pion and η–meson were identified with high statistics also in pp collisions at 2.2 GeV (Sect. 2.3) and compared to model predictions based on a resonance model [Tei97]. The π^0 and η exclusive production cross-section were extracted. Finally, a combined analysis of one-pion exclusive channels $pp\pi^0$, $pn\pi^+$ in pp collisions at 3.5 GeV (Sect. 2.4) allowed for the estimation of Δ and N^* resonance production cross sections for resonances with masses below 2 GeV/c^2. In addition, the angular distributions for the production of resonances were determined within the modified resonance model approach.

Dielectron pairs, reconstructed in inclusive and exclusive channels at various energies by HADES, delivered unique information on production and decays of meson and baryon resonances. First, the inclusive e^+e^- channel was reconstructed for pp and np collisions at $T = 1.25$ GeV (Sect. 4.1). In the pp case, the dielectron distribution was satisfactorily described by the OPE models, with the dominating contribution of π^0 and Δ Dalitz decays. There was, however, some uncertainty left related to the possible electromagnetic transition form factors of the Δ Dalitz decay which has been resolved by studies of the exclusive state (see below). The quasi-free np collisions were studied by means of a deuteron beam and a proton spectator measured at the forward angles. In such a reaction and at this energy, η–meson production was possible, and np bremsstrahlung played an important role, in contrary to pp channel, where it could be neglected due to destructive interferences. A significant enhancement in the intermediate dilepton mass region was observed. The contributions predicted by various models from the electromagnetic decays of hadrons failed to describe the data, as it was discussed in Sect. 4.1.2. Particularly interesting was comparison of a microscopic one-boson exchange models, by Kaptari and Kämpfer (Sect. 3.6.1), and Shyam and Mosel (Sect. 3.6.2). The total e^+e^- contribution was calculated there as a coherent sum of amplitudes including contributions of the Δ resonance and the nucleon-nucleon bremsstrahlung. Kaptari and Kämpfer prediction overshot both pp and np data above

the π^0 mass. Shyam and Mosel calculation introduced the pion electromagnetic form factor, which significantly enhanced the dielectron yield for $M_{ee} > 0.3$ GeV/c^2, and partially explained the enhancement. The pion form factor did not make any difference in the proton-proton case, because the $\Delta(1232)$ dominated over NN bremsstrahlung, and the model described the data very well.

The most advanced analysis of the exclusive dielectron channels in pp collisions at 1.25 GeV utilized the results of the partial wave analysis, as discussed above. The contributing channels, $\Delta(1232)$ and $N(1440)$, were extracted, as well as non-resonant parts. The NN bremsstrahlung contribution was modeled according to Shyam and Mosel calculation. The study of the π^0 Dalitz decay in the $ppe^+e^-\gamma$ channel allowed to verify the Δ production derived from hadronic channels. All observed spectra, in particular angular projections in the center-of-mass system, as well as in the helicity and Gottfried-Jackson reference frames, showed a perfect agreement with the data (Sect. 4.2.1), and with predictions for the decay of pseudoscalar mesons. The consistency of the yield measured in the $pp \to pp\pi^0$ channel proved that both the production description and the dielectron reconstruction are under control. The analysis of the $pp \to ppe^+e^-$ exclusive channel for the masses above the π^0 region allowed to identify, for the first time, Δ Dalitz decay (Sect. 4.2.2). This process gives the insight into the electromagnetic structure of baryonic transitions in the interval of squared momentum transfer $4m_e^2 < q^2 < (M_B - M_N)^2$, where m_e, M_B and M_N are the electron, resonance and nucleon masses, respectively. This kinematical region is complementary to the spacelike region of negative q^2 probed in electron scattering. The Δ Dalitz differential decay width was modeled using either constant electromagnetic transition form factors or a quark constituent model of Ramalho and Peña (App. B). The important role of the intermediate ρ–meson and the pion cloud contributions were discussed. Finally, the branching ratio of the Δ Dalitz decay was extracted, BR($\Delta \to pe^+e^-$) = (4.19 ± 0.62 syst. incl. model ± 0.34 stat.) × 10^{-5}. This unique result has been included in the 2018 Review of Particle Physics.

The analysis of the npe^+e^- ($p_{spect.}$) exclusive channel unraveled the dielectron excess over yield from the ppe^+e^- channel, similar to the one observed in the inclusive channels (Sect. 4.3). The data were confronted with the two models (Sect. 4.3.2). Shyam and Mosel calculation was based on the Lagrangian approach and provided a coherent sum of the nucleon and resonant graphs. Bashkanov and Clement calculation was an incoherent sum of dielectron sources, π^0, η, and Δ Dalitz decays, as well as the contribution from the ρ–like emission via the double–Δ excitation. In both models the enhancement at large invariant masses is due to off-shell ρ–meson. A better description of the experimental distributions was obtained with the model based on Shyam and Mosel calculations, where the effect is related to the nucleon charge-exchange graphs. However, this conclusion should be tempered by the fact that the angular distributions of the final products were not provided by the calculations but based on phenomenology. On the other hand, the double–Δ excitation process is expected to play a role in the e^+e^- production. The contribution of the double–Δ excitation to the e^+e^- production can be only supplied if the effect is included as a coherent contribution in a full model including the nucleon and $\Delta(1232)$ graphs.

The kinetic beam energy of 2.2 GeV (Sect. 4.5) allowed for the η–meson production, reaching also the pole masses of the ρ and ω. Already at this energy the comparison with various models unraveled big differences (Sect. 4.5.2). Their nature stems from the modeling of the $\Delta(1232)$ resonance, where different production cross sections were used (e.g. HSD used higher value than UrQMD). It was demonstrated that the electro-

magnetic transition form factors used (as shown in the GiBUU calculation) influence the dielectron yield. On the other hand, higher resonances also contribute via the resonance coupling to the ρN. Here, significant differences appeared between the models, the ρ–meson line shape was very different in the HSD and the GiBUU calculations. It is worth noticing that the inclusive e^+e^- channel was compared also with the former DLS dielectron spectrum measured at slightly lower energy of 2.09 GeV, both experimental results are in a good agreement. The analysis of the ppe^+e^- exclusive channel allowed for the reconstruction of π^0 and η Dalitz decays (Sect. 4.6). The e^+e^- invariant mass distribution was found in accordance with description of the meson electromagnetic transition form factors (eTFF) given by the Vector Dominance Model. The π^0 production cross section was found in agreement with independent measurements while the η production cross section was found in accordance with the HADES measurement in the hadronic channel (see discussion above). Further, the baryon resonance contribution was identified but its description was not unique due to unknown structure of electromagnetic transition form factors, which could not be fixed by the inclusive data. Although the precision of the HADES data was not sufficient to provide quantitative constraints to the eTFF models but the analysis confirmed the consistency of the hadronic and leptonic reconstructions and the good control of the corresponding efficiencies. Another important fingerprint of the dielectron sources are the angular distributions of e^+ or e^- in the γ^* rest frame, which are expected to be proportional to $1+B\cos^2\alpha$. The obtained anisotropy coefficients, B = 1.36 ± 0.43 for the π^0, and B = 0.98 ± 0.48 for the η, respectively, are in agreement with the QED prediction for pseudoscalar mesons.

The pp collisions measured at energy T = 3.5 GeV (Sect. 4.8) allowed for the reconstruction of a peak corresponding to direct ω decays, with 2% mass resolution. The inclusive production cross sections for ω and ρ mesons were determined from dielectron experimental data for the first time, together with the cross sections for π^0 and η mesons. The inclusive e^+e^- invariant mass, transverse momentum and rapidity distributions were confronted with various transport model calculations (PYTHIA, GiBUU, HSD, UrQMD, and SMASH). The comparison unraveled that the knowledge on Δ and N^* resonance production cross sections, and resonance–ρ couplings, are essential for the description of dielectron data. In addition, the upper bound for the direct $\eta \to e^+e^-$ decay was defined based on the inclusive e^+e^- data [PDG14]. The analysis of the exclusive ppe^+e^- channel (Sect. 4.9) was focused on the dielectron production from electromagnetic baryon resonance Dalitz decays and two-body ω–meson decay. A significant yield below the vector meson pole was measured and attributed to the Dalitz decays of baryon resonances. The data were compared to Monte Carlo simulations in the resonance model approach, with the production cross sections and angular production of baryon resonances deduced in the channels with one pion, as discussed above. The upper limits for the various resonance contributions to the dielectron spectrum were obtained assuming pointlike $R\gamma^*$ couplings. The calculated in this ansatz dielectron yields did not reproduce the measured yield, suggesting the strong off-shell vector meson couplings, influencing the respective electromagnetic transition form factors. Another approach for the Dalitz decay of resonances was studied within the GiBUU [Bus12, Wei12] and UrQMD [Bas98] transport models (Sect. 4.9.3), applying a two step factorization $R \to p\rho \to pe^+e^-$ in the dilepton production. It turned out that to describe the data the resonance cross sections and also the resonance–ρ couplings must be modified in accordance to the newest multichannel partial wave analyses [Shr12, Ani12], or the CLAS collaboration [CC12a] results. These results demonstrate high sensitivity of the HADES data and their importance for the progress in the description of dielectron decays.

5.0.1 Towards pion beam results

The analysis of NN collisions unraveled that the combined exclusive hadronic and leptonic channel results are the unique tool to characterize dielectron decays. However, full isolation of decays from overlaping baryonic resonances has not been yet achieved. In such a situation, the study of Dalitz decays of broad resonances can be performed more effectively with pion beams. First, the overlap between the different states is much reduced, since, in the dominant s channel processes, the resonance is produced with a given mass $M = \sqrt{s}$. The πN interaction is also better controlled, which makes the theoretical description of these reactions easier. In addition, results on baryon resonance excitation from known pion photo- or electroproduction amplitudes can be directly used. Finally, the detection of the e^+e^- pair is sufficient to extract the exclusive $\pi^- p \to n e^+ e^-$ channel using the missing neutron mass constraint, while in the case of the $pp \to pp e^+ e^-$ reaction, the detection of the pe^+e^- is needed for the exclusive channel reconstruction, which significantly reduces the count rate due to the reduced acceptance of the HADES spectrometer. The measurements of hadronic channels will also provide a strong impact on world database, considering the very poor existing statistics, which motivates projects of future meson beam facilities [Bri15].

Indeed, all information on the N^* and Δ resonances listed in the PDG [PDG16] originates from the partial wave analysis of πN total, elastic and charge exchange-scattering data performed by three major groups. Two of them (Karlsruhe-Helsinki [Höh83] and Carnegie-Mellon-Berkeley [Cut79]) were using only data from experiments conducted before 1980. The available statistics was 10 kevents for each of the $\pi^\pm p \to \pi^\pm p$ reaction, 1.5 kevents for $\pi^- p \to \pi^0 n$, with only 17% of polarized data. The George Washington University (SAID) is the only group providing the partial wave analysis for the πN elastic scattering data. They use also the updated database (13 kevents of each of $\pi^\pm p \to \pi^\pm p$, 3 kevents of $\pi^- p \to \pi^0 n$ and 250 events of $\pi^- p \to \eta n$; 25% of polarized data) [Arn06] and continuously include the new available data sets. For example, $\pi^\pm p$ elastic scattering by EPECUR [Ale15], added to the SAID database, demonstrates how big improvements in statistics are possible with the modern experiments and, in fact, demanded for the low energy data in order to construct the unbiased partial wave amplitudes. Another very important channel is $\pi\pi N$, since many well established resonances couple to it. The most extensive study in the resonance energy region 1.32 – 1.93 GeV was made by Manley *et al.* [Man84] (with an update [Man92]) within the isobar approximation. The analysis relied on 241 214 bubble chamber events, they were divided into 22 energy bins and the simultaneous fit to two-pion channels (no $\pi^- p \to \pi^0\pi^0 n$ channel) was performed. The single energy solution was extracted for each energy bin and every isobar channel, delivering results on N^* coupling to ρN, $\Delta\pi$ and σN channels. This complete work had great impact on resonance parametrizations used in various transport models (GiBUU [Bus12, Wei12] and UrQMD [Bas98]). Since then new experimental data became only available in the $\pi^- p \to \pi^0\pi^0 n$ channel from the Crystal Ball collaboration (349 611 events at the energy range $W = 1213 - 1527$ GeV [CBC04]) and in the $\pi^- p \to \pi^+\pi^- n$ channel from the CHAOS collaboration (20 kevents, low energies, $W = 1257 - 1302$ GeV, [Ker98]) and from ITEP (40 kevents, high energy $W = 2060$ GeV [Ale98]). The database for $\pi^+\pi^-$ in the energy range $W = 1.3 - 2.0$ GeV remains scarce and often lacks differential distributions. Therefore, there is a strong need for detailed new measurements in all charged channels.

Pion-induced measurements on proton and nuclei are the part of the HADES scientific program. The GSI pion beam covers the momentum range between 0.6 and 1.7 GeV/c, corresponding to baryon masses of 1.43–2.0 GeV/c^2 (see App. C.1.8 for details). The first experimental run was dedicated to strangeness production in pion-induced reactions on light (^{12}C) and heavy (^{74}W) nuclei at a beam momentum of 1.7 GeV/c. The goal of the second run was to measure the excitation function of two-pion production in the $\pi^- p$ reaction around the pole of the $N(1520)D_{13}$ resonance [HC16c]. Data at four different pion beam momenta (656, 690, 748 and 800 MeV/c) were collected with polyethylene target $(C_2H_4)_n$ and carbon target, respectively. Events from the reactions on proton are deduced after subtraction of the reactions on carbon, as described in App. C.3.6.2. The largest statistics were collected in the case of the momentum of 690 MeV/c, aimed for the first world measurements of e^+e^-. All spectra were normalized to the $\pi^- p$ elastic scattering, measured in the same experimental run (see App. C.3.6.2).

Identification of two charged pions ($\pi^+\pi^-$) or proton and pion ($p\pi^-$) in the final state allows for the reconstruction of the kinematically complete exclusive channels via cuts in the missing mass distributions around the value of the not detected neutron or neutral pion. The obtained resolution of the $\pi^+\pi^-$ missing mass peak amounts to 1.5% (σ) for a fixed beam momentum or even less, 0.8 – 1.0%, when using the beam momentum reconstructed in the pion tracker (see App. C.1.8) for each event. In both cases the peak position is at the expected value of the neutron mass with an accuracy of ±1 MeV/c^2. The resolution of the $p\pi^-$ missing mass squared is above 40% (σ) and above 30% for the pion tracker momentum used in the reconstruction. The peak position is slightly lower (3 – 4 MeV/c^2) than 135 MeV/c^2 (π^0 mass) and close (1 – 2 MeV/c^2 below) in the case of the pion tracker momentum [HC16b]. The number of reconstructed events in the $n\pi^+\pi^-$ exclusive channel amounts to more than 400 000 (beam momentum 656 MeV/c), 7 900 000 (690 MeV/c), 815 000 (748 MeV/c) and 526 000 (800 MeV/c). The number of reconstructed events in the $p\pi^-\pi^0$ exclusive channel amounts to more than 122 000 (beam momentum 656 MeV/c), 3 100 000 (690 MeV/c), 490 000 (748 MeV/c) and 368 000 (800 MeV/c). Those numbers dramatically improve the world data base of two-pion production in pion-induced experiments in the energy range around the $N(1520)$ resonance, and allow for investigation of the branching ratios of this resonance, with a special interest for the ρN decay. This decay channel has not been reported in the present edition of Particle Data Group [PDG16] at all. The former estimation, 15–25%, published in Ref. [PDG14], is obsolete, similar to other results obtained from the analysis of old experimental data. The HADES result would be a highly anticipated update on the missing $N(1520)$ branching ratio entry.

The two-pion data samples, measured at the four above mentioned pion beam momenta, have been included into the multichannel partial wave analysis developed by the Bonn-Gatchina group [Ani05, Sar16]. This analysis includes pion induced reactions (including Crystal Ball data [CBC04] with neutral two-pion channel) and a large number of pseudoscalar meson photoproduction data taken with polarized beam and target. The analysis also includes the information about photoproduction of vector mesons. The analysis is in progress and will define the channels giving the largest contribution to two-pion final state: $\sigma N(939)$, $\Delta(1232)\pi$, ρN, and in particular the $N(1520)$ production cross section and the $N(1520) \to \rho N$ decay, establishing the input to dielectron analysis.

In parallel to hadronic channels, the dielectron channel, $\pi^- p \to n e^+ e^-$, has been measured for the first time. The largest statistics has been collected for the pion beam momentum 690 MeV/c, resulting in 13100 dielectron pairs in the π^0 mass region and 3300 dielectron pairs for $M^{inv}_{e^+e^-} > 140$ MeV/c^2, after combinatorial background subtrac-

tion (see Ref. [HC16a]). The existing microscopic models of dielectron production in the pion-induced reacions differ by and order of magnitude in the e^+e^- yield prediction (see Refs. [Lut02, Lut06, Lut03, Tit01, Käm03, Ris01]), mainly due to strong negative or positive interferences below or above the ω–meson threshold, and lack of knowledge on the $RN\rho$ coupling. The e^+e^- exclusive channel will allow for the direct investigation of the $N(1520)$ Dalitz decay and coupling to the ρN channel. Additional information can be obtained from the angular distribution of dielectrons originating from the process $\pi N \to Ne^+e^-$. In Ref. [Spe17] the spin density formalism has been used to calculate the angular distribution of dileptons originating from the decay of a virtual photon. In particular, the anisotropy coefficients including the $N(1520)$ and $N(1440)$ resonances, have been computed. The results are essential for the description of the data obtained by the HADES Collaboration on this reaction. Recently, the partial wave analysis has been extended to fit directly the dielectron data within the spin density formalism. The work is in progress and will provide the precise description of the e^+e^- exclusive channel.

5.0.2 Spectrometer upgrade and future plans

The HADES detector is currently being upgraded. For experiments planned in 2018, a new Electromagnetic Calorimeter (ECAL, see Refs. [Czy11,Svo14,RR14,Svo15]) based on lead glass crystals will replace the PreShower detector (App. C.1.6). The ECAL will enable measurements of real photons emitted from nuclear matter and neutral meson production via their photonic decays (e.g. $\pi^0/\eta \to \gamma\gamma$). It will also improve the electron-hadron separation of the spectrometer for the purpose of future experiments of HADES at FAIR in elementary and heavy ion collisions in the energy range of 2 – 10 GeV/nucleon. The reconstruction of neutral mesons is essential also for the complete partial wave analysis of π^-N reactions. In addition, the CsI photocathodes of the RICH (App. C.1.2) has been replaced by a new photon detector, aiming at a significant increase of the electron efficiency. In 2019, the existing Forward Wall (App. C.1.7) will be renewed and complemented by two sets of straw tube modules, taking advantage of a technology developed for PANDA [Smy17]. Each station will consist in four double layers of straws with about 1500 channels readout. The first station will be placed 3.3 m behind the target, and the second one 1.6 m further. Thanks to the position resolution of 150 μm (σ), angles and vertices of the forward emitted particles will be reconstructed with a good precision. In addition, two Resistive Plate Counter (RPC) modules (see App. C.1.5) will be installed behind the second Straw Tube Station for time-of-flight measurements with a resolution of 70 ps (σ).

The HADES collaboration developed an important program in elementary reactions. By measuring e^+e^- emission in hadronic reactions, new information about the timelike structure of baryonic resonances can be accessed. The Dalitz decay branching ratio of the $\Delta(1232)$ has been measured for the first time using proton-proton reactions and, for heavier resonances, the role of far off-shell ρ–mesons as a mediator of the electromagnetic interaction was clearly revealed in the e^+e^- invariant mass spectra. Recently, a new step was taken with an exploratory experiment using the GSI pion beam in the $N(1520)$ region. It demonstrated the interest of pion beam experiments to perform direct studies of baryon Dalitz decays and to improve the determination of hadronic couplings. The experiments with the pion beam as well as the *pp* collisions at the highest available energy (T = 4.5 GeV) will be continued in 2018 – 2021, after the SIS18 upgrade as an injector for the FAIR facility. In addition, a program aiming at studying electromagnetic transitions between hyperons will be started at the present SIS18 facility and continued at higher energies at SIS100 (FAIR).

Appendix A

Mesons and dileptons

The dilepton sources in the 1 – 2 GeV/nucleon energy range have been listed in Section 3. In this chapter, the role and origin of vector mesons is discussed. A detailed overview of dilepton production in two- and three-body vector and pseudoscalar meson decays is given.

A.1 Vector mesons

Vector mesons play a special role in non-perturbative QCD, where they can be treated as field carriers in the electromagnetic hadron interactions. They are introduced as gauge bosons, in analogy to a photon in QED, since both carry the same spin and parity ($J^P = 1^-$). The coupling of hadrons to vector mesons is expressed by coupling constants, there is a constant for each meson decay into virtual photon, and a coupling constant describing ρN for each baryon. Vector mesons can be described as resonances in current-current correlation tensor [Shu93, Ste96, Ste97, Gal91, Kap94]:

$$\Pi_{\mu\nu}(q) = i \int e^{iq\cdot x} \langle\, 0 \,|\mathcal{T} j_\mu(x) j_\nu(0)|\, 0 \,\rangle \, d^4x, \tag{A.1}$$

where $\mathcal{T}$ is time-ordering operator and j_μ is the electromagnetic current. The latter one can be written in the $SU(3)$ flavor symmetry [Kli96]

$$j_\mu = Q\,\bar{\psi}\,\gamma_\mu\,\psi \;=\; \frac{1}{\sqrt{2}}\,J^\rho_\mu + \frac{1}{3\sqrt{2}}\,J^\omega_\mu - \frac{1}{3}\,J^\phi_\mu = \frac{1}{2} j^Y_\mu + V^3_\mu, \tag{A.2}$$

where $\psi = (u, d, s)$ is a vector in flavor space with the subsequent quark wave functions, γ_μ denote Dirac matrices, and Q is the quark charge matrix

$$Q = \begin{pmatrix} \frac{2}{3} & 0 & 0 \\ 0 & -\frac{1}{3} & 0 \\ 0 & 0 & -\frac{1}{3} \end{pmatrix}. \tag{A.3}$$

The isospin current ($I = 1$) is j^Y_μ and the hypercharge current ($I = 0$) is $V^3_\mu = \frac{1}{2}\,\bar{\psi}\gamma_\mu\lambda^3\psi$, where λ^3 is the Gell-Mann matrix. The vector currents J^ρ, J^ω, and J^ϕ, describe the respective quark components of vector mesons:

$$\begin{aligned} \frac{1}{\sqrt{2}} J^\rho_\mu &= \frac{1}{2}(\bar{u}\gamma_\mu u - \bar{d}\gamma_\mu d) \;=\; V^3_\mu, \\ J^\omega_\mu &= \frac{1}{\sqrt{2}}(\bar{u}\gamma_\mu u - \bar{d}\gamma_\mu d), \\ J^\phi_\mu &= \bar{s}\gamma_\mu s. \end{aligned} \tag{A.4}$$

The current conservation condition $\partial_\mu j^\mu = 0$ leads to $q_\mu \Pi^{\mu\nu} = q_\nu \Pi^{\mu\nu} = 0$ and hence the tensor (Eq. A.1) is purely transversal in vacuum:

$$\Pi_{\mu\nu}(q) = \Big(g_{\mu\nu} - \frac{q_\mu q_\nu}{q}\Big)\Pi(q). \tag{A.5}$$

The scalar dimensionless correlation function,

$$\Pi(q) = \frac{1}{3} g^{\mu\nu} \Pi_{\mu\nu}(q), \tag{A.6}$$

is proportional to the hadron production cross section in e^+e^- annihilation collisions [Kli97] at a given total center-of-mass energy $\sqrt{s}$:

$$R(s) = \frac{\sigma(e^+e^- \to hadrons)}{\sigma(e^+e^- \to \mu^+\mu^-)} = -\frac{12\pi}{s}\,\mathrm{Im}\,\Pi(s), \tag{A.7}$$

where $\sigma(e^+e^- \to \mu^+\mu^-) = 4\pi\alpha/3s$ and $\alpha = e^2/4\pi = 1/137$.

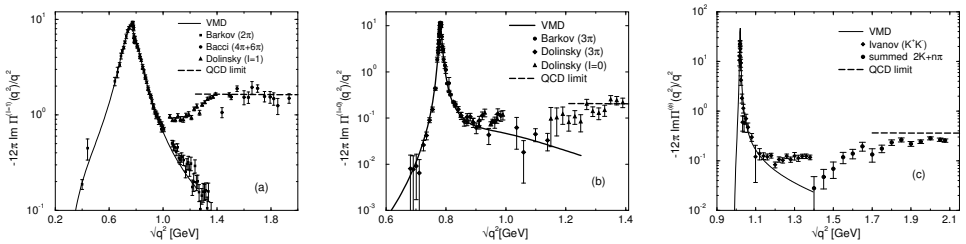

Figure A.1: The ratio $\sigma(e^+e^- \to hadrons)/\sigma(e^+e^- \to \mu^+\mu^-)$ as a function of the total center-of-mass energy: (a) the isovector channel with ρ–meson; (b) the isoscalar channel with ω–meson; (c) ϕ–meson channel. Solid black curve represents VDM. For energies $\sqrt{s} \geq 1$ GeV a continuum (perturbative QCD limit) for processes $e^+e^- \to 4\pi, 6\pi$, is also shown (dashed line). Experimental data are taken from Refs. [Bar85, Dol91, Bar87, Iva81, Man82, Cor82].

Resonance R in $e^+e^- \to hadrons$ channel appears as a sharp maximum in $\mathrm{Im}\,\Pi(s)$ around $s = m_R^2$. Indeed, the low mass region is dominated by the light vector mesons, ρ^0, ω and ϕ. They can be distinguished by looking at different hadronic channels, i.e. $e^+e^- \to \mathrm{n}\,\pi$ (n - number of pions produced), carrying the respective isospin quantum numbers. The G–parity conservation requires that the ρ–meson couples only to channels with even number of pions (n = 2, 4, 6...) and isospin $I = 1$ (Fig. A.1a). The annihilation of e^+e^- into odd numbers of pions determines the isoscalar current involving the ω–meson (Fig. A.1b). In the case of $\phi(1020)$–meson, the channel with three pions is strongly suppressed, $BR(\phi \to \rho\pi + \pi^+\pi^-\pi^0) = 15.32\%$, as compared to kaonic decays, $BR(\phi \to K^+K^-) = 48.9\%$ and $BR(\phi \to K_L^0 K_S^0) = 34.2\%$ [PDG16]. This is explained by the Okubo-Zweig-Iizuka (OZI) rule [Oku63, Zwe66, Iiz66, Oku77]. This rule says that processes with the disconnected quark lines, when Feynman diagram can be separated into two diagrams of incoming and outcoming states, are strongly suppressed as compared to processes with connected quark diagrams. The ϕ–meson decays then mainly into OZI-allowed channels such as K^+K^- and $K_L^0 K_S^0$ (Fig. A.1c).

Figure A.1 shows also QCD predictions for large momentum transfers $\sqrt{s} \geq 1$ GeV. In this case the observables do not include initial state hadrons and are inclusive

with respect to details of the final state. The ratio $R(s)$ can be written as a product of the electromagnetic currents carried by electrons and quarks, resulting in:

$$R(s) = R_{EW}\left(1 + \delta_{QCD}(s)\right), \tag{A.8}$$

where $R_{EW} = N_c \sum_q Q_q^2$ is purely electroweak prediction, which at low energies is dominated by photon exchange ($N_c = 3$ for light quarks, Q_q see Eq. A.3 for quark charge matrix). The δ_{QCD} is correction due to QCD effects:

$$\delta_{QCD}(s) = \sum_{n=1}^{\infty} c_n \left(\frac{\alpha_s(s)}{\pi}\right)^n + ..., \tag{A.9}$$

where $\alpha_s(s)$ is the QCD running coupling constant (for a review see Ref. [Deu16]), for the leading order expansion term $c_1 = 1$ and three lightest quarks, one gets:

$$R(s) = 3\left[(\tfrac{2}{3})^2 + (-\tfrac{1}{3})^2 + (-\tfrac{1}{3})^2\right]\left(1 + \frac{\alpha_s(s)}{\pi}\right). \tag{A.10}$$

More terms in the α_s series expansion can be found in Ref. [Bai12].

At low energies ($\sqrt{s} < 1$ GeV), the quark electromagnetic current (j_μ) is carried entirely by the vector meson fields (V^μ), as postulated in vector meson dominance [Sak60], in the identity

$$j_\mu = \sum_V \frac{m_V^2}{g_V} V^\mu, \tag{A.11}$$

where the m_V is the vector meson mass (m_ρ =775.26 MeV/c^2, m_ω = 782.65 MeV/c^2, m_ϕ = 1019.46 MeV/c^2, see Ref. [PDG16]). In the framework of the second quantization, j_μ is a creation operator which acts on the QCD vacuum and creates quark-antiquark pairs, overlapping with the mesonic states:

$$\langle\, 0 \,|\, j_\mu \,|\, V \,\rangle = -\frac{m_V^2}{g_V}\epsilon_\mu, \tag{A.12}$$

where ϵ_μ is a polarization vector. The coupling constants g_V can be obtained from the vector meson two-body dilepton decays as will be discussed in App. A.2.

A.2 Two-body decays

The two-body decay width of a particle with a mass M and a four-momentum $\boldsymbol{P}$ in the laboratory reference frame, decaying into particles of masses m_1, m_2, and four-momenta $\boldsymbol{p_1}$, and $\boldsymbol{p_2}$, respectively, is:

$$\frac{d\Gamma}{d\Omega} = \frac{1}{32\,\pi^2}\,|\mathcal{M}|^2\,\frac{\boldsymbol{p_1}}{M^2}, \tag{A.13}$$

where $\mathcal{M}$ is the transition matrix element, and $d\Omega = d\phi_1 d(\cos\theta_1)$ is the solid angle of particle 1. In the rest frame of the particle of mass M,

$$|\boldsymbol{p_1}| = |\boldsymbol{p_2}| = \frac{\lambda^{1/2}(M^2, m_1^2, m_2^2)}{2M}, \tag{A.14}$$

where

$$\lambda(x^2, y^2, z^2) = (x^2 - (y+z)^2)\,(x^2 - (y-z)^2) \tag{A.15}$$

denotes the Källén function, also known as triangle function [Käl64].

A.2.1 Two-body decays of vector mesons

The decay of vector mesons is an example of process where the square matrix element can be written, with the additional summation over possible photon polarizations, in the form:

$$\sum_{pol} |\mathcal{M}|^2 = \frac{e^2}{k^4}\, \mathcal{W}_{\mu\nu}\, \mathcal{L}^{\mu\nu}, \tag{A.16}$$

where $e^2 = 4\pi\alpha$, $1/k^2$ is the photon propagator, $\mathcal{W}_{\mu\nu}$ is the hadronic tensor with the $\mathcal{M}_{\mu}^{had}$ being the hadronic part of the matrix element

$$\mathcal{W}_{\mu\nu} = \sum_{pol} \mathcal{M}_{\mu}^{had}\, \mathcal{M}_{\nu}^{had\,*}, \tag{A.17}$$

and $\mathcal{L}^{\mu\nu}$ is the lepton tensor describing the coupling of the virtual photon to the dilepton pair

$$\mathcal{L}^{\mu\nu} = 4\left(k_1^{\mu}k_2^{\nu} + k_1^{\nu}k_2^{\mu} - (k_1 \cdot k_2 + m_l^2)\, g^{\mu\nu}\right), \tag{A.18}$$

where k_1 and k_2 are momenta of the subsequent leptons, each of a mass m_l. The hadronic tensor describes the internal structure of hadrons, and the coupling to virtual photon involved in the decay process. Hence, the decay of vector mesons can be factorized as a two-step process [Koc93, Ko96], meson to virtual photon transition followed by the virtual photon conversion into a dilepton pair:

$$|\mathcal{M}(V \to l^+l^-)|^2 = |\mathcal{M}(V \to \gamma^*)|^2\ \frac{1}{M^4}\ |\mathcal{M}(\gamma^* \to l^+l^-)|^2, \tag{A.19}$$

where $M = m_{\gamma^*} = m_{l^+l^-}$. The first matrix element can be evaluated with the VMD ansatz (Eq. A.11) of Sakurai [Sak60, Sak69]:

$$|\mathcal{M}(V \to \gamma^*)|^2 = \frac{e^2 m_V^4}{g_V^2}, \tag{A.20}$$

and the second matrix element describes the conversion of the virtual photon γ^* into a dilepton pair, calculated from the lepton tensor [Koc93]:

$$|\mathcal{M}(\gamma^* \to l^+l^-)|^2 = \frac{e^2}{3}\,(M^2 + 2m_l^2). \tag{A.21}$$

Finally,

$$|\mathcal{M}(V \to l^+l^-)|^2 = \frac{e^4\, m_V^4}{3\, g_V^2\, M^4}\,(M^2 + 2m_l^2), \tag{A.22}$$

and from Eq. A.13 one gets

$$\Gamma(M) = \frac{4\pi\alpha^2}{3\, g_V^2}\,\frac{m_V^4}{M^3}\left(1 - \frac{4m_l^2}{M^2}\right)^{1/2}\left(1 + \frac{2m_l^2}{M^2}\right). \tag{A.23}$$

When neglecting the lepton mass ($m_l \approx 0$), the meson decay width at the vector meson pole mass ($M = m_V$) is, as obtained by Sakurai [Sak60]:

$$\Gamma(V \to l^+l^-) = \frac{4\pi\alpha^2}{3}\,\frac{m_V}{g_V^2}. \tag{A.24}$$

vector meson	decay channel	branching ratio	g_V
ρ	e^+e^-	$(4.72 \pm 0.05) \times 10^{-5}$	5.03
ρ	$\mu^+\mu^-$	$(4.55 \pm 0.28) \times 10^{-5}$	4.96
ω	e^+e^-	$(7.36 \pm 0.15) \times 10^{-5}$	17.05
ω	$\mu^+\mu^-$	$(9.0 \pm 3.1) \times 10^{-5}$	> 10.7
ϕ	e^+e^-	$(2.955 \pm 0.029) \times 10^{-4}$	-12.89
ϕ	$\mu^+\mu^-$	$(2.87 \pm 0.19) \times 10^{-4}$	-14.37

Table A.1: Vector mesons branching ratios at meson poles, for the dielectron and dimuon decays [PDG16]. The coupling constant g_V is deduced from decay widths. Following the $SU(3)$ symmetry and the universal coupling constant g_γ = 5.66, the coupling constants are: g_ρ = 5.66, g_ω = 17.0, g_ϕ = -12.02.

The coupling constants g_V and branching ratios for the subsequent vector mesons ($V = \rho, \omega, \phi$) and decays ($l^+l^- = e^+e^-, \mu^+\mu^-$) are available from the measured dilepton experimental decay widths (Table A.1). Their values have similar relations than the ones deduced from $SU(3)$ flavor symmetry (see coefficients in Eq. A.4), that is, $g_\rho : g_\omega : g_\phi = 1 : 3 : -3/\sqrt{2}$. The decay widths $\Gamma(V \to e^+e^-)$ are proportional to m_V/g_V^2 (Eq. A.24). Therefore, in the context of $SU(3)$ symmetry, they can be expressed in terms of a single vector meson-photon coupling constant, which amounts to g_γ = 5.66:

$$\Gamma(\rho \to e^+e^-) : \Gamma(\omega \to e^+e^-) : \Gamma(\phi \to e^+e^-) = \frac{m_\rho}{2\,g_\gamma^2} : \frac{m_\omega}{18\,g_\gamma^2} : \frac{m_\phi}{9\,g_\gamma^2} \simeq 1 : 9 : 4.5. \tag{A.25}$$

The experimental decay width follows the $SU(3)$ pattern, with the exception of the observed g_ρ = 5.03, instead of the $SU(3)$ value of 5.66. The VDM assumption is that the same coupling constant describes the meson-hadron interactions linking strong and electromagnetic interactions by vector meson gauge fields. As an example the ρ–meson decay into two pions can be analysed, the $\Gamma(\rho \to \pi^+\pi^-)$ decay width is calculated in a similar way as for dielectron decay. The transition matrix element is (Ref. [Koc93]):

$$\mid M(\rho \to \pi^+\pi^-) \mid^2 = g_{\rho\pi\pi}^2\,(m_\rho^2 - 4m_\pi^2), \tag{A.26}$$

and the decay width is (Refs. [Li95, Kli96]):

$$\Gamma(\rho \to \pi^+\pi^-, M = m_\rho) = \frac{g_{\rho\pi\pi}^2}{48\pi}\,m_\rho \left(1 - \frac{4m_\pi^2}{m_\rho^2}\right)^{3/2}. \tag{A.27}$$

Taking into account values $\Gamma(\rho \to \pi^+\pi^-)$ = 147.8 MeV, m_ρ = 775.26 MeV/c^2, and $m_{\pi^\pm}$ = 139.57 MeV/c^2 [PDG16], the coupling constant is $g_{\rho\pi\pi}$ = 5.95, close to the universal coupling constant g_γ, which supports the VDM ansatz. It is important to notice, however, that the calculations of $\Gamma(V \to l^+l^-)$ (Eq. A.23) and $\Gamma(\rho \to \pi^+\pi^-)$ (Eq. A.27) have been made for the meson pole mass. For the broad ρ–meson the decay widths should be parametrized with the mass M, as given in Ref. [Bra99], for the dipion decay:

$$\Gamma(\rho \to \pi^+\pi^-, M) = \Gamma(\rho \to \pi^+\pi^-, m_\rho)\,\frac{m_\rho}{M}\left(\frac{M^2 - 4m_\pi^2}{m_\rho^2 - 4m_\pi^2}\right)^{3/2}, \tag{A.28}$$

or in a simpler form, which reduces to Eq. A.27 when $M = m_\rho$,

$$\Gamma(\rho \to \pi^+\pi^-, M) = \frac{g_{\rho\pi\pi}^2}{48\pi}\,\frac{M^2}{m_\rho}\left(1 - \frac{4m_\pi^2}{M^2}\right)^{3/2}. \tag{A.29}$$

On the other hand, the parametrization for the dielectron decay follows Eq. A.23, and with the lepton mass neglected ($m_l \approx 0$) is

$$\Gamma(\rho \to e^+e^-, M) = \Gamma(\rho \to e^+e^-, m_\rho) \left(\frac{m_\rho}{M}\right)^3 = \frac{4\pi\alpha^2}{3g_\rho^2} \frac{m_\rho^4}{M^3}. \tag{A.30}$$

In summary, the total decay width of the ρ–meson in vacuum, neglecting for simplicity pion mass, is given by $\Gamma_{tot} \approx \Gamma_{\rho\to\pi\pi} \sim M$ and decreases with the mass. On the other hand, the partial decay width into dilepton channel, $\Gamma_{\rho\to e^+e^-} \sim 1/M^3$, what leads to a considerable shift of strength in the dilepton spectrum towards lower masses. This low mass enhancement can be a signature of vector meson contribution.

A.2.2 Pion annihilation

In heavy-ion collisions, pion annihilation is an important production mechanism of the ρ–meson, what can be connected with the dilepton observables in a process $\pi^+ + \pi^- \to l^+ + l^-$. The matrix element $\mathcal{M}(\pi^+\pi^- \to l^+l^-)$ is usually calculated in the framework of the vector dominance model and the considered process can be understood as the formation of a vector meson by the annihilation of pions which subsequently, through the coupling to the photon, decays into a lepton pair (Fig. A.2, left panel). Hadrons are extended objects and do not couple pointlike to the photon, therefore pions acquire an electromagnetic form factor (Fig. A.2, right panel). The matrix element for this process can be written:

$$\mathcal{M} = \bar{u}\gamma^\mu v \frac{e^2}{q^2} \sum_V \frac{1}{g_V} \frac{m_V^2}{m_V^2 - q^2 - im_V\Gamma_V} g_{V\pi\pi}(p_1 - p_2)_\mu, \tag{A.31}$$

where $\bar{u}\gamma^\mu v$ is the leptonic current, q is the four-vector of the virtual photon and $1/q^2$ is the photon propagator, $q^2 = M^2$ is the invariant mass of the lepton pair, p_1 and p_2 are momenta of the incoming pions. The $g_{V\pi\pi}$ coupling strength in general is not a constant and can be parametrized as a function of M (for details, see Ref. [Koc93]). The formula describes the coupling of the photon to the two incoming pions via the electromagnetic pion form factor, including the vacuum propagator of the intermediate vector meson. The squared matrix element after the spin summation, for the dominant ρ–meson, can be decomposed:

$$|\mathcal{M}(\pi^+\pi^- \to l^+l^-)|^2 = \frac{|\mathcal{M}(\pi^+\pi^- \to \rho)|^2 \, |\mathcal{M}(\rho \to \gamma^*)|^2 \, |\mathcal{M}(\gamma^* \to l^+l^-)|^2}{\left[(m_\rho^2 - M^2)^2 + m_\rho^2\Gamma_\rho^2\right] M^4}, \tag{A.32}$$

where the subsequent matrix contributions were given in Eqs. A.26, A.22, A.21, and $\Gamma_\rho(M)$ in Eq. A.28. The cross section for a two-body scattering process in the center-of-mass frame (p_i is pion momentum, and p_f is lepton momentum, respectively)

$$\left.\frac{d\sigma}{d\Omega}\right|_{CM} = \frac{1}{64\pi^2 s} \frac{p_f}{p_i} |\mathcal{M}|^2, \tag{A.33}$$

allows to calculate the cross section for the process $\pi^+\pi^- \to e^+e^-$:

$$\sigma_{\pi^+\pi^-\to e^+e^-}(M) = \frac{4\pi}{3} \frac{\alpha^2}{M^2} \sqrt{1 - \frac{4m_\pi^2}{M^2}} \, |F_\pi(M)|^2. \tag{A.34}$$

The pion form factor is defined in the timelike region ($q^2 > 0$), by the following matrix element [Kli96]:

$$\langle\, \pi^{\pm}(p_1) \mid j_\mu \mid \pi^{\pm}(p_2) \,\rangle = \pm(p_1 - p_2)_\mu \, F_\pi(M), \tag{A.35}$$

and finally:

$$\mid F_\pi(M) \mid^2 \;=\; \frac{g^2_{\rho\pi\pi}}{g^2_\rho} \, \frac{m^4_\rho}{(M^2 - m^2_\rho)^2 + m^2_\rho \Gamma^2_\rho}. \tag{A.36}$$

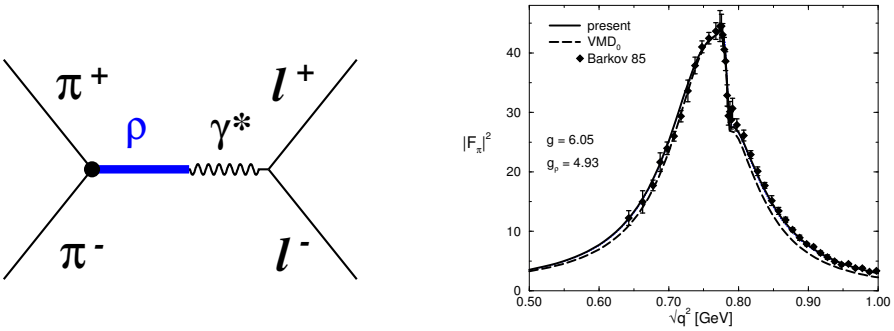

Figure A.2: Left panel: $\pi^+\pi^-$ annihilation in the vector dominance description. Right panel: pion form factor $|F_\pi(q)|^2$, in the timelike region, obtained via e^+e^- annihilation (Ref. [Kli96]).

One should note that the region accessible in the e^+e^- annihilation experiments (see Fig. 3.2) is limited to $q^2 > 4\pi^2_\pi$ and assuming the universal coupling constant value, $g_{\rho\pi\pi} = g_\rho$, there is $F_\pi(q^2 = 0) = 1$, restoring the electric charge of pion. The VMD approach gives quite good description of the electromagnetic pion form factor (Fig. A.2, right panel, dashed curve), however more precise calculations (Ref. [Kli96], solid curve in the figure) give the perfect desription of the data. They introduce the $g_{\rho\pi\pi}$ constant, renormalized with one-pion loop contribution, modifying the pion self-energy, and the $\rho - \omega$ mixing (Ref. [Hat94]), visible at $q^2 \approx 0.8$ GeV.

A.2.3 Two-body decays of pseudoscalar mesons

The pseudoscalar two-body dielectron decays are very rare processes, therefore they are not important contribution to the dilepton spectrum, but allow to study low-energy dynamics in the Standard Model and might be a filtering processes for light dark matter particles (see Ref. [Dor10]). First prediction for the $\pi^0 \to e^+e^-$ decay was given by Drell [Dre59], the mean branching ratio given in Ref. [PDG16] amounts to $BR = (6.46 \pm 0.33) \times 10^{-8}$. The decay proceeds in the lowest order of QED as a one-loop process via the two-photon intermediate state (Fig. A.3).

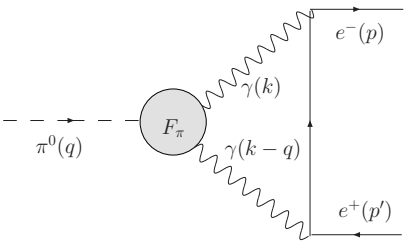

Figure A.3: The $\pi^0 \to e^+e^-$ process: triangle diagram with a pion $\pi^0 \to \gamma^*\gamma^*$ form factor in the vertex.

The normalized branching ratio R is:

$$R(\pi^0 \to e^+e^-) = \frac{BR(\pi^0 \to e^+e^-)}{BR(\pi^0 \to \gamma\gamma)} = 2\left(\frac{\alpha}{\pi}\frac{m_e}{m_\pi}\right)^2 \sqrt{1-4\frac{m_e^2}{m_\pi^2}}\,\left|\mathcal{A}(m_\pi^2)\right|^2, \qquad \text{(A.37)}$$

and relative to the $\pi^0 \to \gamma\gamma$ rate, $(98.823 \pm 0.034) \times 10^{-2}$, it is suppressed by a factor α^2, and further by $2(m_e/m_{\pi^0})^2$ due to the approximate helicity conservation of the interaction. The amplitude $\mathcal{A}$ includes the the form factor $F_{\pi\gamma^*\gamma^*}(k, k-q)$ (see Fig. A.3) of the transition $\pi^0 \to \gamma^*\gamma^*$ with off-shell photons. In the real photon limit, $F_{\pi\gamma^*\gamma^*}(0,0) = 1$, the amplitude is model independent and leads to the unitary bound for the branching ratio, $BR(\pi^0 \to e^+e^-) \geq 4.69 \times 10^{-8}$ [Ber60], neglecting radiative corrections. Various models provided the form factor [Ber83b], within the conventional vector-meson dominance scheme [Ame93], chiral perturbation theory [Sav92, Kne99], and including radiative corrections [Ber83a, Dor08] and higher-order QED corrections [Hus14]. The most precise experimental result [Abo07], from the KTeV E799-II experiment at Fermilab, is based on 794 $\pi^0 \to e^+e^-$ events using $K_L \to 3\pi^0$ as a neutral pion source. It established $BR(\pi^0 \to e^+e^-) = (6.44 \pm 0.25_{stat.} \pm 0.22_{syst.}) \times 10^{-8}$, above the unitary bound from $\pi^0 \to \gamma\gamma$, and within 2σ discrepancy with theoretical expectations from the standard model (see Refs. [Dor07, Wei17]).

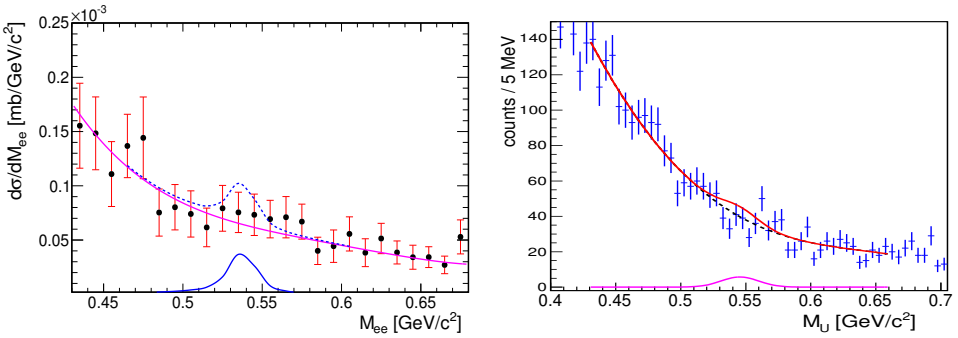

Figure A.4: Left panel: Invariant mass distribution of e^+e^- pairs in the η meson mass range [HC14a]. The experimental data is fitted with a polynomial distribution (magenta curve), excluding the area around the η–meson pole mass. The simulated yield of direct dielectron decays of the η–meson (blue curve) is presented on top of the background (dashed blue curve). Right panel: Invariant mass distribution of e^+e^- pairs in the η–meson mass region reconstructed in the $p(3.5\text{ GeV}) + Nb$ reaction [HC14b]. The data is fitted with a polynomial (dashed black curve) with a simulated signal from the η direct decay, corresponding to the upper limit of branching ratio 2.5×10^{-6} is superimposed (solid red and pink curves).

In the case of $\eta \to e^+e^-$ decay, no direct measurement is present. The calculations based on chiral perturbation theory and quark models etimate the branching ratio at $BR(\eta \to e^+e^-) = (5 \pm 1) \times 10^{-8}$ [Sav92, Dor07]. The most recent estimation of the branching ratio upper limit is derived from the HADES data [HC14a,HC14b]. In Figure A.4, left panel, the dielectron invariant mass spectrum from $p+p \to p+p+e^++e^-+X$ at 3.5 GeV (Sect. 4.8) was plotted in the η meson mass range. The polynomial background was fitted to data, excluding the area around the η meson mass. With the help of

method describing the treatment of upper confidence limits for null results, given by Feldman and Cousins (Ref. [Fel98]), an upper limit for the signal counts with a 90% confidence was estimated. Thus, an upper limit for the branching ratio is $5.6{\times}10^{-6}$. The inclusive η cross section, $\sigma_\eta = 1.035$ mb, was extracted from the dielectron analysis (see Sect. 4.8.2), and the hypothetical peak from $\eta \to e^+e^-$ decay was plotted in Fig. A.4, left panel. The obtained upper estimation was 6 times lower than the value of 2.7×10^{-5} from Ref. [CWC08].

Even better estimation was derived from the analysis of $p + Nb$ data at 3.5 GeV measured with HADES. Using the inclusive η cross section from Ref. [HC13], the upper limit for $BR(\eta \to e^+e^-)$ was derived to be $2.5{\times}10^{-6}$ (Fig. A.4, right panel), with a confidence level of 90%. A combined results of pp and $p + Nb$ data give the upper limit of $2.3{\times}10^{-6}$. It is the best available estimate (Ref. [PDG16]), however, still significantly larger than theoretical predictions.

A.3 Three-body decays

The decay of a particle with mass M into three particles with masses m_1, m_2 and m_3 is known as a Dalitz decay [Dal54]. It can be completely described using two variables and the standard Dalitz plot presents the correlation between invariant masses squared of two pairs of the decay products, m_{12}^2 versus m_{23}^2. The intermediate resonance can decay into two particles first, with one decay product being unstable and immediately decaying into two additional decay products. Similar to the two-body decays (see Eq. A.13), the differential decay width can be described with the matrix element:

$$\frac{d\Gamma}{dm_{12}\, d\Omega_1^*\, d\Omega_3} = \frac{1}{(2\pi)^5}\,\frac{1}{16M^2}\,|\mathcal{M}|^2\,|\mathbf{p_1^*}|\,|\mathbf{p_3}|. \tag{A.38}$$

Let $\mathbf{p}$, $\mathbf{p_1}$, $\mathbf{p_2}$ and $\mathbf{p_3}$, denote the four-momentum vectors of the mother-particle and the subsequent decay products. $m_{12}^2 = (P - p_3)^2$ and $\mathbf{p_1^*}$, Ω_1^* are the four-momentum and the angle of particle 1 in the reference frame of the two-body system $1-2$, Ω_3 is the angle of particle 3 in the rest frame of decaying mother-particle. The $|\mathbf{p_1^*}|$ and $|\mathbf{p_3}|$ are given (similar to Eq. A.14) by:

$$\begin{aligned} |\boldsymbol{p_1^*}| &= \frac{\lambda^{1/2}(m_{12}^2, m_1^2, m_2^2)}{2m_{12}}, \\ |\boldsymbol{p_3}| &= \frac{\lambda^{1/2}(M^2, m_{12}^2, m_3^2)}{2M}. \end{aligned} \tag{A.39}$$

If the decaying particle is scalar or averaging over all spin states, followed by the integration over the angles, leads to the standard form of the Dalitz plot:

$$\frac{d\Gamma}{dm_{12}^2\, dm_{23}^2} = \frac{1}{(2\pi)^3}\,\frac{1}{32M^3}\,\overline{|\mathcal{M}|^2}. \tag{A.40}$$

The Dalitz plot gives the information on $|\mathcal{M}|^2$. If there are no angular correlations between the decay products then the distribution of these variables is flat. However, if resonance processes are involved, the Dalitz plot unravels a non-uniform distribution with a peak around the mass of the resonant decay.

A.3.1 Dalitz decays of mesons

Dalitz decays $A \to Bl^+l^-$ are often reduced to two-body decays of B and a virtual photon (with an invariant mass M), decaying into a dilepton pair l^+l^- (see Fig. A.5a). The matrix element factorizes in a similar manner as in Eq. A.19:

$$|\mathcal{M}(A \to Bl^+l^-)|^2 = |\mathcal{M}(A \to B\gamma^*)|^2 \ \frac{1}{M^4} \ |\mathcal{M}(\gamma^* \to l^+l^-)|^2 . \tag{A.41}$$

The differential decay width can be written as the product of the conversion rate of the virtual gamma [Kro55] and the decay width $\Gamma(A \to B\gamma^*)$,

$$\frac{d\Gamma(A \to Bl^+l^-)}{dM} = \frac{2\alpha}{3\pi M} \sqrt{1 - \frac{4m_l^2}{M^2}} \left(1 + \frac{2m_l^2}{M^2}\right) \Gamma(A \to B\gamma^*). \tag{A.42}$$

In the case of the conversion to a dielectron pair, the electron mass is neglected ($m_e \approx 0$) and the formula reduces to:

$$\frac{d\Gamma(A \to Be^+e^-)}{dM} = \frac{2\alpha}{3\pi M} \Gamma(A \to B\gamma^*). \tag{A.43}$$

As shown in Fig. A.5b for π^0, η, η' and ω meson, the dielectron invariant mass for η' and ω shows a yield enhancement at larger invariant masses due to the ρ–meson dominance in the photon–e^+e^- conversion process. Assuming the isotropic decay $A \to B\gamma^*$ in the A rest frame, the width is given by:

$$\Gamma(A \to B\gamma^*) = \frac{\lambda^{1/2}(m_A^2, m_B^2, M^2)}{16\pi m_A^3} \ |\mathcal{M}(A \to B\gamma^*)|^2 . \tag{A.44}$$

The missing element which has to be provided is the matrix element $\mathcal{M}(A \to B\gamma^*)$. In Dalitz decays, the transitions from A to B plus γ^*, are either from a pseudoscalar meson (π^0, η, η') into a vector particle (photon, where spin-parity relation is $0^- \to 1^- + 1^-$), or from a vector meson (ω) into a pseudoscalar meson ($1^- \to 0^- + 1^-$). Therefore the transition form factor $f_{AB}(M^2)$ has the same structure and the matrix element can be written [Koc93]:

$$|\mathcal{M}(A \to B\gamma^*)|^2 = \tfrac{1}{2} \left|f_{AB}(M^2)\right|^2 \ \lambda(m_A^2, m_B^2, M^2). \tag{A.45}$$

Typically, the partial decay width $\Gamma(A \to B\gamma^*)$ is normalized to the decay width of the real photon ($M = q^2 = 0$):

$$\Gamma(A \to B\gamma) = \frac{(m_A^2 - m_B^2)^3}{32\pi m_A^3} \ |f_{AB}(0)|^2 , \tag{A.46}$$

and the normalized form factor is

$$F_{AB}(M^2) = \frac{f_{AB}(M^2)}{f_{AB}(0)}, \tag{A.47}$$

where $F_{AB}(0) = 1$. The decay width is then:

$$\Gamma(A \to B\gamma^*) = \Gamma(A \to B\gamma) \ \frac{\lambda^{3/2}(m_A^2, m_B^2, M^2)}{(m_A^2 - m_B^2)^3} \ \left|F_{AB}(M^2)\right|^2 , \tag{A.48}$$

or the differential decay width [Lan85] is:

$$\begin{aligned}\frac{d\Gamma(A\to Bl^+l^-)}{dM^2\,\Gamma(A\to B\gamma)} &= \frac{\alpha}{3\pi}\sqrt{1-\frac{4m_l^2}{M^2}}\left(1+\frac{2m_l^2}{M^2}\right)\frac{1}{M^2}\\ &\times\left[(1+\frac{M^2}{m_A^2-m_B^2})^2-\frac{4m_A^2M^2}{(m_A^2-m_B^2)^2}\right]^{3/2}\\ &\times\left|F_{AB}(M^2)\right|^2 = X_{QED}\times\left|F_{AB}(M^2)\right|^2,\end{aligned}\tag{A.49}$$

with X_{QED} denoting the single-differential decay width of pure QED. In the case of a pseudoscalar meson (A) conversion,

$$A\to B\,\gamma^*\to\gamma\,l^+l^-,\tag{A.50}$$

where B is a photon, the corresponding normalization reaction is $A\to 2\gamma$, and the differential decay width turns into:

$$\begin{aligned}\frac{d\Gamma(A\to\gamma l^+l^-)}{dM^2\,\Gamma(A\to\gamma\gamma)} &= \frac{2\alpha}{3\pi}\sqrt{1-\frac{4m_l^2}{M^2}}\left(1+\frac{2m_l^2}{M^2}\right)\frac{1}{M^2}\\ &\times\left[1-\frac{M^2}{m_A^2}\right]^3\times\left|F_A(M^2)\right|^2 = X_{QED}\times\left|F_A(M^2)\right|^2.\end{aligned}\tag{A.51}$$

It is easy to show that the substitution $m_B\to 0$ in Eq. A.49 leads to the half of Eq. A.51, due to the two possible choices of the virtual photon in reaction (A.50).

The form factor $F_{AB}(M^2)$ describes the hadron-virtual photon transitions, therefore it can be obtained from the vector dominance model:

$$F_{AB}(M^2)=\left\{\sum_V\frac{g_{ABV}}{g_V}\,\frac{m_V^2}{m_V^2-M^2-i\Gamma_V m_V}\right\}\Big/\left\{\sum_V\frac{g_{ABV}}{g_V}\right\}.\tag{A.52}$$

where g_{ABV} and g_V are the coupling constants, which can be fixed from the quark model or from the experimental data on $A\to BV$, $A\to B\gamma$ and $V\to l^+l^-$ decays. In the narrow width approximation (neglecting Γ_V) the form factor is:

$$F_{AB}(M^2)=\left\{\sum_V\frac{g_{ABV}}{g_V}\,\frac{1}{1-M^2/m_V^2}\right\}\Big/\left\{\sum_V\frac{g_{ABV}}{g_V}\right\}.\tag{A.53}$$

Additionally, in the small momentum transfers regime, it is convenient to write an expansion:

$$F_{AB}(M^2)\approx 1+M^2\left.\frac{dF_{AB}}{dM^2}\right|_{M^2=0}=1+M^2\,b_{AB}=1+\tfrac{1}{6}\,M^2\,\langle\,r_{AB}^2\,\rangle,\tag{A.54}$$

The mean radius

$$\langle\,r_{AB}^2\,\rangle^{1/2}\;=\;\left(\,6\,\left.\frac{dF_{AB}}{dM^2}\right|_{M^2=0}\,\right)^{1/2}\tag{A.55}$$

is the characteristic size of the transition which reflects the extended hadron structure. Another useful practice to describe the standard VMD form factor is the monopole approximation:

$$F_{AB}(M^2)\;=\;\frac{1}{1-\frac{M^2}{\Lambda^2}}\approx 1+\frac{M^2}{\Lambda^2}\tag{A.56}$$

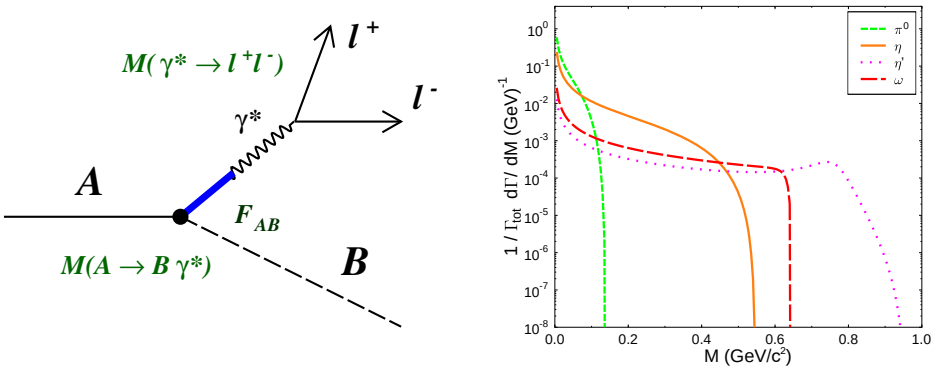

(a) (b)

Figure A.5: (a) Diagram of the meson dilepton Dalitz decay; (b) Dilepton invariant mass distribution for various (π^0, η, η', ω) meson Dalitz decays [Ern98].

where Λ is the effective virtual vector meson mass. In the limit of small q^2, the slope of the transition form factor $b_{AB} = \Lambda^{-2}$ (see Eq. A.54), is associated with the size of the pseudoscalar meson, $b_{AB} = \langle r_{AB}^2 \rangle/6$ (see Eq. A.55). At $M^2 = 0$ the slope definition is:

$$b_{AB} \;=\; \Lambda^{-2} \;=\; \left.\frac{dF_{AB}}{dM^2}\right|_{M^2=0} \;=\; \frac{\sum\limits_{V=\rho^0,\omega,\phi} \dfrac{g_{ABV}\; g_V}{m_V^2}}{\sum\limits_{V=\rho^0,\omega,\phi} g_{ABV}\; g_V}. \qquad \text{(A.57)}$$

In experiments, the one-pole approximation is used to extract the slope of the form factor. There are a few alternative parametrizations used in literature, i.e. for the π^0 (Ref. [Lan85]):

$$F_{\pi^0\gamma}(M^2) \;=\; 1 + b_{\pi^0}\; M^2, \qquad \text{(A.58)}$$

however, another popular form of the parametrization is also:

$$F(x^2) \;=\; 1 + a\; x^2, \qquad \text{(A.59)}$$

where $x = M/m_\pi$ and a is a dimensionless slope parameter, with $a = b_{\pi^0}\, m_\pi^2$. By assuming that the virtual photon (of mass M) is coupled to the π^0 through a vector meson, it is possible to relate the parameter a to the mass m_V of the vector meson involved, $a \simeq (m_\pi/m_V)^2$. Therefore, a should be positive with a value $a \simeq 0.031$, corresponding to the ρ mass. In the early 60's Gell-Mann *et al.* [GM61, GM62] showed that the π^0 form factor is dominated by the ρ and ω meson resonances and got a positive a equal to $m_\pi^2\,(m_\rho^{-2} + m_\omega^{-2})/2$. The early experiments with bubble chambers [Sam61, Kob61] reported a negative value of a, a counter experiment [Dev69] found a compatible with zero. First positive value of a was identified in the analysis of Fisher *et al.* [Fis78], where π^0 mesons were tagged from $K^+ \to \pi^+\pi^0$ decays. The slope $a = 0.10 \pm 0.03$, or equivalently, $b_{\pi^0} = 5.5 \pm 1.6$ GeV^{-2}, with statistical errors only, is very dependent on the radiative corrections [Mik72], which double the slope value.

One-pole approximation for η–meson ($\eta\gamma$ vertex) and ϕ–meson ($\phi\eta$ or $\phi\pi^0$ vertex) follows general Eq. A.56. The first experimental fit reported $b_\eta = \Lambda_\eta^{-2} = -0.7 \pm 1.5$ (stat. errors only) GeV^{-2} [Jan75], for $\eta \to \gamma e^+ e^-$. The Lepton-G Collaboration provided better constrained value $b_\eta = 1.9 \pm 0.4$ GeV^{-2} [Dzh80] (for $\eta \to \mu^+\mu^-\gamma$), what corresponds to

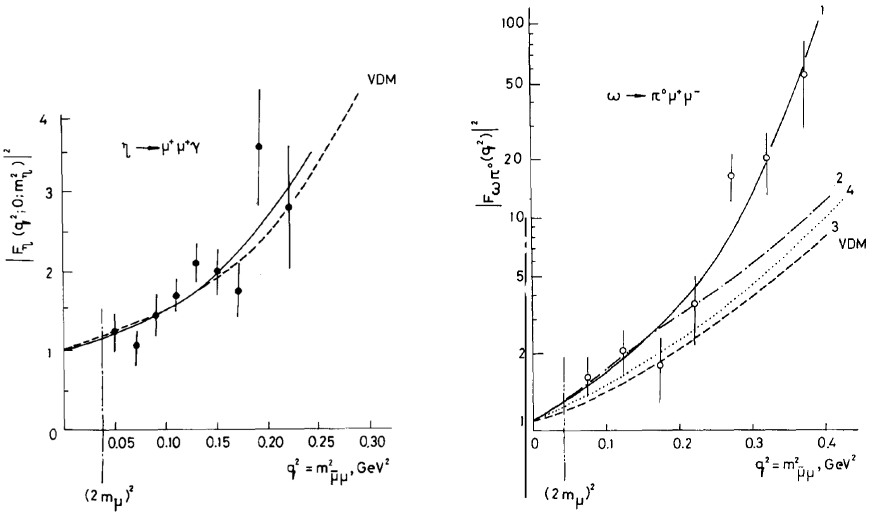

Figure A.6: $\eta\gamma$ (left panel) and $\omega\pi^0$ (right panel) vertex electromagnetic transition form factor, fitted with one-pole formula (solid curve) and the VDM prediction (dashed curve). Experimental data are provided by the Lepton-G Collaboration [Dzh80,Dzh81]. Figures adopted from Ref. [Lan85].

$\Lambda_\eta = 0.72 \pm 0.09$ GeV. In the case of the η' or ω, the square of the form factor is described by:

$$
\begin{aligned}
|\,F_{\eta'\gamma}(M^2)\,|^2 &= \frac{\Lambda^2_{\eta'}\,(\Lambda^2_{\eta'} + \gamma^2_{\eta'})}{(\Lambda^2_{\eta'} - M^2)^2 + \Lambda^2_{\eta'}\,\gamma^2_{\eta'}}, \\
|\,F_{\omega\pi^0}(M^2)\,|^2 &= \frac{\Lambda^2_{\omega}\,(\Lambda^2_{\omega} + \gamma^2_{\omega})}{(\Lambda^2_{\omega} - M^2)^2 + \Lambda^2_{\omega}\,\gamma^2_{\omega}},
\end{aligned}
\tag{A.60}
$$

where the parameters Λ and γ correspond to the mass and width of the Breit-Wigner shape for the effective contributing vector meson. The expected values are $\Lambda \approx M_\rho \approx 0.7$ GeV, and $\gamma \approx \Gamma_\rho \approx 0.12$ GeV. The experiments, performed by the Lepton-G Collaboration, provided fitted values $b_{\eta'} = \Lambda^{-2}_{\eta'} = 1.7 \pm 0.4$ GeV^{-2} [Dzh79] (for $\eta' \to \mu^+\mu^-\gamma$) and $b_{\omega\pi^0} = \Lambda^{-2}_{\omega} = 2.4 \pm 0.2$ GeV^{-2} [Dzh81] (for $\omega \to \pi^0\mu^+\mu^-$). Writing the mass and the width, they are $\Lambda_{\eta'} = 0.77$ GeV, $\gamma_{\eta'} = 0.1$ GeV, as well as $\Lambda_\omega = 0.65$ GeV, and $\gamma_\omega = 0.04$ GeV. The successful description within the VMD ansatz was prominent for π^0, η (Fig. A.6, left panel) and η', but in the case of ω–meson (Fig. A.6, right panel) the VMD model failed to describe the data. In addition, experimental data lacked the statistics and were not reliable in terms of systematic error handling.

In the 80's and 90's, various collaborations were analyzing data with the focus on meson form factors. They were investigated not only via meson Dalitz decays, but also in two-photon transitions, $\gamma\gamma^* \to \pi^0$, η, and η', that means with at least one spacelike photon with $q^2 < 0$. The TCP/2γ Collaboration [TC90] published $\Lambda_\eta = 0.70 \pm 0.08$ GeV, and $\Lambda_{\eta'} = 0.85 \pm 0.07$ GeV, in agreement with [Jan75]. The CELLO Collaboration [CC91] results were obtained by extrapolation from a measurement in the region of large spacelike momentum transfer assuming vector dominance. The following values are then model-dependent and with statistical errors only: $\Lambda_{\pi^0} = 0.75 \pm 0.03$ GeV (137 events), $\Lambda_\eta = 0.84 \pm 0.06$ GeV (68 events), $\Lambda_{\eta'} = 0.79 \pm 0.04$ GeV (41 events). Pion

beam experiment at Saclay [Fon89] delivered again negative value of the π^0 form factor slope, a = −0.11 ± 0.03 (stat.) ± 0.08 (syst.). Two more experiments, measured in the SINDRUM I magnetic spectrometer at the PSI [Dre92], and with pion beam at TRIUMF facility [Far92], reported a positive π^0 form factor slope, however with large total errors: a = 0.025 ± 0.014 (stat.) ± 0.026 (syst.), and a = 0.026 ± 0.054 (tot.), respectively. The measurements with the SND detector at VEPP-2M collider delivered information on conversion decays $\eta \to \gamma e^+e^-$, and $\phi \to \eta e^+e^-$ [Ach01]. The η−meson transition form factor slope was $b_{\eta\gamma}$ = 1.6 ± 2.0 GeV^{-2}, which presents no statistically significant difference with the negative value from Ref. [Jan75], due to a large error. The ϕ−meson transition form factor was measured for the first time, resulting in $b_{\phi\eta}$ = 3.8 ± 1.8 GeV^{-2}, based on 213 events. Further, the CMD-2 Collaboration published results on the same η and ϕ decays [Akh01], however, no form factor slopes were deduced, but only branching ratios. They estimated also an upper limit for the $\phi \to \eta\mu^+\mu^-$ decay.

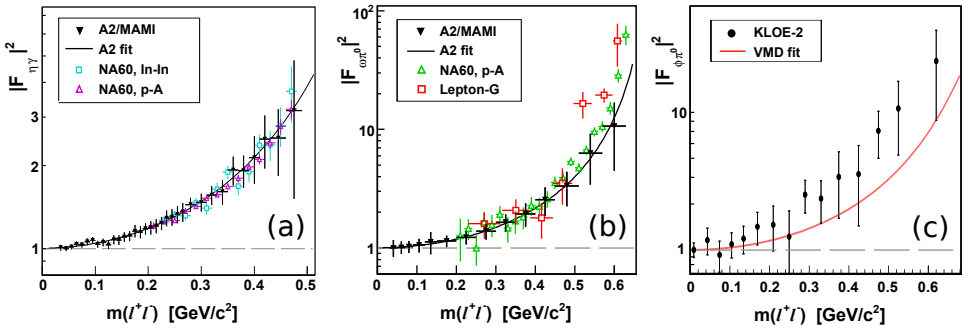

Figure A.7: Meson transition form factors: (a) $|F_{\eta\gamma}|^2$ fit compared with experimental data of NA60 $In-In$ [NC09] (open cyan squares), NA60 $p-A$ [NC16] (open magenta triangles) and A2/MAMI γp [MAM17a] (black triangles) reactions; (b) $|F_{\omega\pi^0}|^2$ fit compared with Lepton-G [Dzh81] (open red squares), NA60 $p-A$ [NC16] (open green triangles) and A2/MAMI γp [MAM17a] (black triangles) reactions; (c) $|F_{\phi\pi^0}|^2$ VMD fit compared with KLOE-2 e^+e^- [KC16] (black points) reactions.

The experimental results mentioned above, are confronted in Refs. [Lan85, Ame92] with the vector meson dominance predictions (see Eq. A.52), which are $\Lambda_{\pi^0} = M_{\rho,\omega}$ = 0.78 GeV, Λ_η = 0.75 GeV, and $\Lambda_{\eta'}$ = 0.83 GeV. Other calculations discussed in Ref. [Ame92], i.e. constituent-quark loops [Bra81, Ame83, Pic84] or chiral perturbation theory [Bij88, Bij90, Eck89], are not far from the VMD predictions. The anomalous case of ω−meson triggered theoretical efforts, via modified ρ propagator [Köp74], effective Lagrangian approach to vector mesons [Kli96], or an extended VMD model with more excited ρ states [Fae00]. They improved the ω form factor description, yet overestimating the form factor at low mass, and underestimating it at high mass, in the region of the kinematic cut-off. The conclusion was that accurate experiments, with precision of the order of a few percent, are required in order to decide on the correct scheme accounting for the $AB\gamma^*$ (A pseudoscalar meson, B photon) transition form factors.

In the last decade, the new experimental facilities allowed for a significant improvement on meson Dalitz decay studies. The reaction $\gamma p \to p\eta$ measured with the Crystal Ball and TAPS photon detector setup at the electron accelerator MAMI-C led to identification of 1345 events of the $\eta \to \gamma e^+e^-$ decay [Ber11], hence the slope value b_η = 0.192 ± 0.35 (stat.) ± 0.13 (syst.) GeV^{-2}, corresponding to Λ_η = 0.72 ± 0.06 (stat.) ± 0.025 (syst.) GeV. The NA60 experiment at the CERN SPS studied low-mass muon pairs

in 158 GeV/nucleon $In-In$ collisions, and in proton-nucleus ($p-A$) collisions using a 400 GeV proton beam and various targets (Be, Cu, In, W, Pb and U). The heavy-ion data analysis allowed to deduce high precision electromagnetic transition form factors of the Dalitz decays $\eta \to \mu^+\mu^-\gamma$ and $\omega \to \mu^+\mu^-\pi^0$ [NC09], that is $b_\eta = 1.95 \pm 0.17$ (stat.) $\pm$ 0.05 (syst.) GeV^{-2} and $b_\omega = 2.24 \pm 0.06$ (stat.) $\pm$ 0.02 (syst.) GeV^{-2}. The results have been improved even more in the recently published $p-A$ analysis [NC16], with $b_\eta = 1.934 \pm 0.067$ (stat.) $\pm$ 0.050 (syst.) GeV^{-2}, and $b_\omega = 2.223 \pm 0.026$ (stat.) $\pm$ 0.037 (syst.) GeV^{-2}. The low-mass electron pairs were studied in the $\gamma p \to \pi^0 p$, ηp and ωp reactions, followed by the subsequent meson Dalitz decays, with the A2 tagged-photon facility at the Mainz Microtron, MAMI. The improved value for the slope parameter of the π^0 electromagnetic transition form factor is $a = 0.030 \pm 0.010$ (tot.) [MAM17b]. Similarly, the fit to $5.4{\times}10^4$ events of the $\eta \to e^+e^-\gamma$ resulted in $\Lambda_\eta^{-2} = 1.97 \pm 0.11$ (tot.) GeV^{-2} (Fig. A.7a), and the fit to $1.1{\times}10^3$ events of the $\omega \to e^+e^-\gamma$ resulted in the value $\Lambda_{\omega\pi^0}^{-2} = 1.99 \pm 0.2$ (tot.) GeV^{-2} [MAM17a], which is lower than in the di-muon reconstruction, but closer to the theoretical value (Fig. A.7b). The last improvement on the π^0 electromagnetic transition form factor slope parameter, from $1.11{\times}10^6$ fully reconstructed $K^\pm \to \pi^\pm\pi^0$, $\pi^0 \to e^+e^-\gamma$ Dalitz decay events, was reported by the NA62 Collabration in Ref. [NC17]. The value of $a = 0.0368 \pm 0.0057$ represents the most precise experimental determination of the π^0 slope in the timelike momentum transfer region (Fig. A.8, left panel). The comparison of results determined experimentally for 40 years is shown in Fig. A.8, right panel.

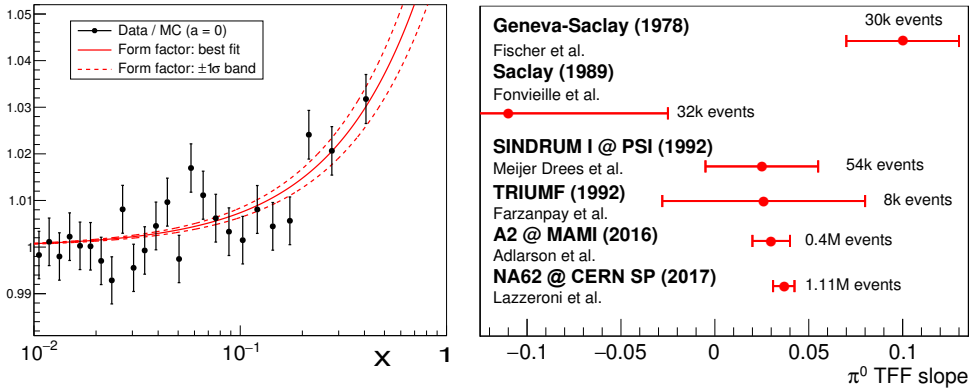

Figure A.8: Left panel: the ratio of the reconstructed x distributions (see Eq. A.59) for the π^0 Dalitz decay NA62 data and Monte Carlo simulation, where the MC sample corresponds to $a = 0$. The sold red curve represents the form factor $F_{\pi^0}(x^2)$ with the slope value $a = 3.68{\times}10^{-2}$, the dashed curve marks the $\pm1\sigma$ band. Right panel: historical comparison of the π^0 eTFF slope measurements in the timelike momentum transfer region in various experiments, see text for details. Figures adopted from Ref. [NC17].

The most recent η' form factor determination (Ref. [BC15]) was based on $1.3{\times}10^9$ J/ψ events collected with the BESIII detector. The η' are produced via the $J/\psi \to \gamma\eta'$ decay, followed by the $\eta' \to \gamma e^+e^-$ Dalitz decay. The fit, following the parametrization in Eq. A.60, gives $\Lambda_{\eta'} = 0.79 \pm 0.04$ (stat.) $\pm$ 0.02 (syst.) GeV, and $\gamma_{\eta'} = 0.13 \pm 0.06$ (stat.) $\pm$ 0.03 (syst.) GeV. This result improves the precision of the old fit in the timelike region, given by the Lepton-G Collaboration (Ref. [Dzh80]), and is in agreement with the VMD model preditions, as well as with the transition form factor slope determination in the spacelike region from the CELLO Collaboration (Ref. [CC91]).

meson	decay channel	branching ratio	$\mathbf{b = \Lambda^{-2}\ [GeV^{-2}]}$
π^0	γe^+e^-	$(1.174 \pm 0.035) \times 10^{-2}$	2.020 ± 0.313 (NA62)
η	γe^+e^-	$(6.9 \pm 0.4) \times 10^{-3}$	1.97 ± 0.11 (A2/MAMI)
η	$\gamma \mu^+\mu^-$	$(3.1 \pm 0.4) \times 10^{-4}$	1.934 ± 0.084 (NA60)
η'	γe^+e^-	$(4.73 \pm 0.30) \times 10^{-4}$	1.60 ± 0.19 (BESIII)
η'	$\gamma \mu^+\mu^-$	$(1.09 \pm 0.27) \times 10^{-4}$	1.7 ± 0.4 (Lepton-G)
ω	$\pi^0 e^+e^-$	$(7.7 \pm 0.6) \times 10^{-4}$	1.99 ± 0.2 (A2/MAMI)
ω	$\pi^0 \mu^+\mu^-$	$(1.34 \pm 0.18) \times 10^{-4}$	2.223 ± 0.045 (NA60)
ϕ	$\pi^0 e^+e^-$	$(1.33 \pm 0.1) \times 10^{-5}$	2.02 ± 0.11 (KLOE-2)
ϕ	ηe^+e^-	$(1.08 \pm 0.04) \times 10^{-4}$	1.28 ± 0.10 (KLOE-2)

Table A.2: Meson Dalitz decays with dilepton pairs in the final state: branching ratio (the mean values from Ref. [PDG16]), and transition form factor slope $b = dF/dM^2$ ($M^2 = 0$), in the one-pole approximation $b = \Lambda^{-2}$ [GeV^{-2}]. The best experimental value of the slope b (the source quoted in brackets).

The KLOE-2 Collaboration aimed at production of ϕ–meson based on e^+e^- collisions at $\sqrt{s} \sim m_\phi$ collected at the DAΦNE collider. Based on 29625 $\phi \to \eta e^+e^-$ events, with ϕ identified from the $\phi \to 3\pi^0$ decays, the form factor slope $b_{\phi\eta} = 1.28 \pm 0.1$ GeV^{-2} was determined [KC15]. This value is very different from the SND old result (Ref. [Ach01]), but close to the VMD prediction, which is $b_{\phi\eta} = 1$ GeV^{-2} [Fae00]. Further, the sample of 9500 $\phi \to \pi^0 e^+e^-$ events allowed to determine, for the first time, the $F_{\phi\pi^0}(M^2)$ transition form factor (Fig. A.7c), and the one-pole parametrization fit resulted in a slope $b_{\phi\pi^0} = 2.02 \pm 0.11$ GeV^{-2} [KC16].

The summary of the mean values of the $A \to B\, l^+l^-$ Dalitz decay branching ratios for mesons ($A = \pi^0$, η, η', ω, ϕ), together with transition form factors (the slope parameter b), is given in Table A.2. The VMD-inspired one-pole approximation fits to experimental data (Eqs. A.58–A.60) give good description for π^0, η, and η' mesons, but fail in the case of ω and ϕ mesons. High-precision data triggered also effort on theoretical side. They are VMD-inspired extensions [Lic11], leading-order chiral Lagrangian calculations, including light vector mesons and Goldstone bosons [Ter10a,Ter10b,Ter12], dispersion theory [Sch12,Dan15], extended vector meson dominance model [She03,Fuc05], or tri-mixing pattern in the light-cone constituent quark model [Qia10]. All theoretical predictions either improve the VMD description (for the π^0, η or η'), or just show good agreement with the data for the ω up to the mass 0.55 GeV/c^2, but still fail to describe the data points close to the upper kinematical limit, $m_\omega - m_{\pi^0}$. The situation with ϕ–meson is ambiguous. In the case of $\phi \to \eta e^+e^-$, the one-pole fit is not very far from the VMD estimation, but models i.e. chiral Lagrangian calculations, clearly overshoot the experimental transition form factor (see Ref. [KC15]). In the case of $\phi \to \pi^0 e^+e^-$, the dispersive analysis description starts to fail at masses above 0.3 GeV/c^2, the VMD description is lying far lower than the experimental data. However, the chiral effective field theory with resonances, with parameters extracted from a fit of the NA60 data [Iva12], follows the data points quite well (see Ref. [KC16]). Despite the tremendous experimental progress, many rare meson Dalitz decays are still not measured or poorly known, i.e. $\eta' \to \omega e^+e^-$, $\omega \to \eta l^+l^-$, $\phi \to \eta \mu^+\mu^-$, or $\phi \to \eta' e^+e^-$. On theoretical side, the ω form factor steep rise at the kinematical boundaries, remains unexplained.

Appendix B

Baryon resonance models

B.1 Zétényi and Wolf model

The model by Zétényi and Wolf [Zét03a, Zét03b] assumes a standard set of dilepton sources in pp collisions: two-body direct decays of ρ^0, ω, ϕ vector mesons and Dalitz decays of mesons $\pi^0 \to \gamma e^+ e^-$, $\eta \to \gamma e^+ e^-$, $\omega \to \pi^0 e^+ e^-$. In addition it includes the Dalitz decays of resonances with spins $J \leq 5/2$ and masses below 2.25 GeV/c^2. The resonance differential width of Dalitz decays is treated via the relation to the resonance virtual photon decay (Eq. 3.2), and further:

$$\Gamma_{R\to N\gamma^*}(M) = \frac{\sqrt{\lambda(m_R^2, m^2, M^2)}}{16\pi m_R^3} \frac{1}{N_{pol,R}} \sum_{pol} \langle N\gamma^*|T|R\rangle, \tag{B.1}$$

where m_R, m are masses of a resonance and a nucleon, $N_{pol,R}$ is a number of polarisation states of a resonance R and a summation runs over all physical polarisation states of the incoming and outgoing particles. The kinematical factor λ is defined in Eq. A.15. In the limit $m \to 0$, Eq. B.1 results in the radiative decay width. The virtual photon decay matrix element is related to the electromagnetic current matrix

$$\langle N\gamma^*|T|R\rangle = -\epsilon^\mu \langle N|J_\mu|R\rangle, \tag{B.2}$$

where ϵ^μ is the photon polarisation vector. Thus, in order to calculate the electromagnetic decays of resonances, the matrix elements of the electromagnetic current operator J_μ between the nucleon N and the resonance R has to be calculated. For the spins $J \geq 3/2$

$$\langle N|J_\mu|R\rangle = \bar{u}(p,\lambda)\Gamma_{\mu,\rho_1\ldots\rho_n} u^{\rho_1\cdots\rho_n}(p_R, \lambda_R), \tag{B.3}$$

where p_R, λ_R, p, λ are four-momentum and helicity of a resonance and nucleon, respectively. $u^{\rho_1\cdots\rho_n}(p_R, \lambda_R)$ are momentum-space wave functions, which are spinor-tensor amplitudes fulfilling the generalized Rarita-Schwinger relations [Lov97]. Taking into account the conservation of the electric charge

$$q^\mu \langle N|J_\mu|R\rangle = 0, \tag{B.4}$$

and Dirac equations

$$\begin{aligned} \bar{u}(p,\lambda)(\gamma^\mu p_\mu - m) &= 0, \\ (\gamma_R^\mu p_{R\mu} - m) u^{\rho_1\cdots\rho_n}(p_R, \lambda_R) &= 0, \end{aligned} \tag{B.5}$$

the number of parameters in $\Gamma_{\mu,\rho_1\ldots\rho_n}$ is limited to three independent terms. They include three form factors $f_i(q^2)(i = 1, 2, 3)$, to be determined from the experimental data, but their expression also depend on the resonance normality (see Sect. 3.4). In the case of spin $J = 1/2$, the matrix element (Eq. B.3) contains two independent terms of Γ_μ, hence two form factors. The Zétényi and Wolf model introduces the contribution of e^+e^- pairs from the direct two-body vector meson decays separately and the Vector Meson Dominance model (see Sect. 3.3) is not used in the resonance Dalitz decay description. As a consequence, form factors $f_i(q^2)$ are kept constant and reduce to coupling constants, g_1, g_2 for $J = 1/2$, and g_1, g_2, and g_3 for $J \geq 3/2$. However, the terms containing g_2 (for $J = 1/2$) and g_3 (for $J \geq 3/2$) have no singularities at $q^2 = 0$ and give zero contribution in Eq. B.1. Therefore, these coupling constants cannot be fixed by real photon amplitudes. The remaining terms with g_1 (for $J = 1/2$) and g_1, and g_2 (for $J \geq 3/2$) give similar virtual photon mass dependence except for the resonances of spin-parity $3/2^+$ and $5/2^-$, and for masses significantly larger than the Breit-Wigner mass. Zétényi and Wolf conclude, that in practical applications e.g. transport models, the masses are not far from the Breit-Wigner mass and thus the description with either g_1 or g_2, or a linear combination of both, does not generate a big difference in the dilepton yield. The largest uncertainty derives from the normalization of the coupling constants to the poorly known real photon amplitudes, in particular in the case of neutron excitations. The final conclusion is that only one coupling constant g_1 is used, to describe with a reasonable precision, the dilepton invariant mass distribution in the Dalitz decay width of baryon resonances. The value of this coupling constant is fixed to reproduce the radiative decay width.

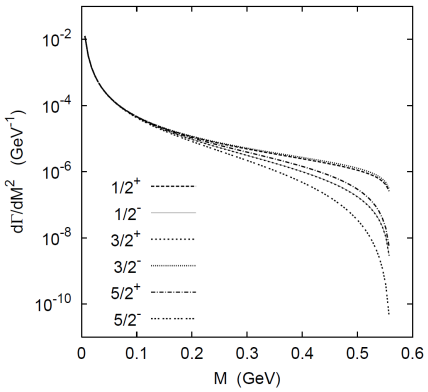

Figure B.1: Zétényi and Wolf model: differential width $d\Gamma/dM^2$ of the Dalitz decay of baryon resonances with different spins $\leq 5/2$ and parities. Calculation done for the selected resonance mass 1.5 GeV and photonic width 0.6 MeV [Zét03a].

The model prediction is demonstrated in Fig. B.1 for a hypothetical resonance with the mass $m_R = 1.5$ GeV/c^2, the real photon decay width $\Gamma_{R\to N\gamma} = 0.006$ GeV and for various spin-parities. There is a striking difference at the high invariant mass: the largest contributions are for spin-parity $1/2^+$ and $3/2^-$ resonances, the smallest contribution, lower by up to two orders of magnitude, is for $5/2^-$ resonance. The model provides the coupling constants $g_1^{p\gamma}$ or $g_1^{n\gamma}$ and thus the Dalitz decay widths for the following resonances: $N(1440)$, $N(1710)$, $\Delta(1910)$ ($J^P = 1/2^+$), $N(1535)$, $N(1650)$, $\Delta(1620)$ ($J^P = 1/2^-$), $\Delta(1232)$, $N(1720)$, $\Delta(1600)$ ($J^P = 3/2^+$), $N(1520)$, $N(1700)$, $\Delta(1700)$ ($J^P = 3/2^-$), $N(1680)$, $\Delta(1905)$ ($J^P = 5/2^+$), $N(1675)$, $\Delta(1930)$ ($J^P = 5/2^-$). The Dalitz decays of baryon resonances provide small contribution to e^+e^- invariant mass spectrum since they are decoupled from the vector meson contributions. The model can be referred as a model describing the baryon resonance with a pointlike constant form factor fixed consistently with the radiative decay width (QED model).

B.2 Krivoruchenko and Martemyanov model

The QED-based model by Krivoruchenko and Martemyanov [Kri01, Kri02] provides phenomenological, kinematically complete, relativistic expressions for the dilepton decay rates of nucleon resonances with arbitrary spin and parity with masses below 2 GeV/c^2. Similar to other models, in order to calculate the dilepton decays, one needs to know the electromagnetic transition form factors of nucleon resonances in the timelike region [Fae00]. The standard VDM [Sak60] with the ground-state $\rho-$, $\omega-$, and $\phi-$mesons predicts monopole form factors. The form factor pole corresponds to the masses of the $\rho-$ and $\omega-$mesons with the asymptotic behaviour $\sim 1/q^2$ at $q \to \infty$. It describes well the electromagnetic pion form factor which, according to the quark counting rules [Bro73, Bro75], decreases with the $F_\pi(q^2) \sim 1/q^2$. However, the quark counting rules for the Sachs form factors [Ros50, Hof58] predict $G_E(q^2) \sim G_M(q^2) \sim 1/q^4$ at $q \to \infty$. Moreover, the model should describe both radiative $RN\gamma$ and mesonic RNV decays but a normalization to the radiative branchings ($RN\gamma$) strongly underestimates the mesonic branchings (RNV) [Fri97, Fae03]. The problem is observed for almost all N^* and Δ resonances if compared to the existing $N\rho$ and $N\gamma$ data. The two independent couplings for the photons and vector mesons, as in the VDM model by Kroll *et. al.* [Kro67], can be used in order to resolve this discrepancy (see discussion in [Fri97]), however the form factor asymptotic behaviour is not in agreement with quark counting rules in such a case.

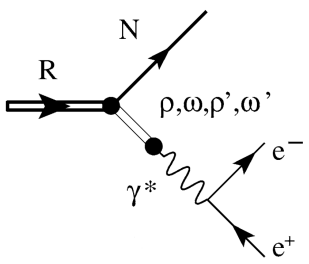

Figure B.2: Extended VMD model graph. The minimum number of the vector mesons required for each isotopic channel to obtain the correct asymptotic behaviour of radiative and mesonic decays is $3+l = 3+J-\frac{1}{2}$ (for $J-$spin resonance). The resonances considered in the model have spins $\frac{1}{2} \le J \le \frac{7}{2}$ therefore six intermediate mesons are required at maximum. The selected masses are: 0.769, 1.250, 1.450, 1.720, 2.150 and 2.350 GeV/c^2, where the mass 1.250 GeV/c^2 seemed to be a candidate for a vector meson on that time and the mass 2.350 GeV/c^2 is for an upper estimate.

The solution proposed by Krivoruchenko and Martemyanov includes the excited states in the electromagnetic current of the vector mesons (extended Vector Dominance Model, eVDM) and thus solves the problem of the vector meson to dilepton decay width ratios. The stronger suppression of the transition form factors at high q^2 is achieved by the destructive interference of the higher lying $\rho-$ and $\omega-$ vector mesons away from the ρ and ω poles (ϕ mesons are decoupled from the model due to the OZI rule) with the ground state vector mesons. The basic problem of the model is the lack of the data on resonance couplings and on form factors. For example, the couplings of the $\rho' = \rho(1450)$ and $\rho'' = \rho(1700)$ mesons to resonances or photon are not established. Therefore the unknown factors are fixed by fitting the radiative decay widths. The model uses also multi-channel πN partial wave analysis of Manley and Saleski [Man92], and Longacre *et al.* [Lon75, Lon77], as well as other model predictions [Kon82, Cap94] in order to constrain the total vector meson decay widths. Whenever it is possible, the parameters of the extended VMD model are determined from the fit to the photo- and electroproduction data measured in the spacelike region [Bar68, Bät72, Ste75] and the

vector-meson decay amplitudes of the nucleon resonances. On the time of the model fit, only the Δ resonance was well constrained and in many cases merely a single data point or no data were available at all. At present, the updated version of the eVMD model fit is expected, including a wealth of new electroexcitation data [CC09b, Azn12, Azn13] and *RNV* couplings based on the modern partial wave analysis [Ani12].

B.3 Iachello and Wan model

Semi-phenomenological two-component model, proposed by Iachello, Jackson and Lande in 1973 [Iac73] and developed further by Wan [Wan05, Wan06] is the first model of elastic and transition form factor which was analytically extended to the timelike region. The model provides a unitary description of the electromagnetic amplitudes on all possible transitions with final N or Δ resonance R up to 2 GeV. It parametrizes the electromagnetic transition of baryons with direct couplings to the photon and couplings to the photon mediated by vector mesons (Fig. B.3, left panel). The generic structure of the form factor can be written:

$$F(Q^2) = g(Q^2)\Big[\alpha_0 + \sum_i \alpha_i \frac{m_i^2}{m_i^2 + Q^2}\Big], \tag{B.6}$$

where $g(Q^2)$ is the intrinsic form factor and m_i's and α_i's are the masses and coupling constants of the vector mesons. The advantage of this model is that all form factors, expressed via helicity amplitudes $A_{1/2}(Q^2)$, $A_{3/2}(Q^2)$ and $S_{1/2}(Q^2)$), are obtained simultaneously in a unified algebraic model and very few parameters are needed to produce the results on a large set of resonances. In the case of proton and nucleon, the elastic form factors (magnetic G_{M_p}, G_{M_n} and electric G_{E_p}, G_{E_n}) perfectly describe the data both in spacelike and timelike calculations [Iac04] except neutron spacelike data above $Q^2 = 1$ (GeV/c)^2.

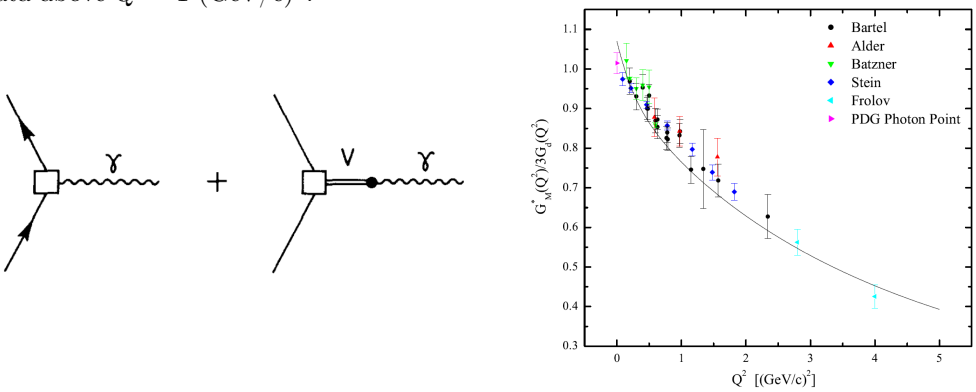

Figure B.3: Iachello-Wan two component model. Left panel: the direct coupling to the photon (left graph) and the coupling mediated by vector mesons (right graph). Right panel: G_M^* form factor fitted to the data (for the list see Ref. [Wan06]) and normalized to the dipole form factor $G_D(Q^2) = 1/(1 + Q^2/0.71)^2$.

In the case of $N - \Delta$ transition, the parameters are fixed from the elastic form factor parametrization and from fitting to the measured $N-\Delta$ transition magnetic form factor in the spacelike region (Fig. B.3, right panel). The analytical continuation of the $N-\Delta$ transition form factor into the timelike region is not trivial. It requires a complex

parametrization both in the intrinsic form factor $g(Q^2)$ and the vector meson propagator $m_\rho^2/(m_\rho^2+Q^2)$, the widths of the ω and ϕ mesons are small and can be neglected. The form factor $g(q^2)$ (where $q^2 = -Q^2$) introduces a phase θ in the spacelike region:

$$g(q^2) = \frac{1}{(1-\gamma e^{i\theta} q^2)^2}, \tag{B.7}$$

but uses the parametrization $\gamma = 0.25\ (\mathrm{GeV/c})^{-2}$ as in the timelike region. The vector meson propagator, in the limit $q^2 \gg 4m_\pi^2 \simeq 0.08\ \mathrm{GeV}^2$ is:

$$F_\rho(q^2) = \frac{m_\rho^2}{m_\rho^2 - q^2 - \frac{1}{\pi}\frac{\Gamma_\rho^0}{m_\pi} q^2\ \log\frac{q^2}{m_\pi^2} + i\frac{\Gamma_\rho^0}{m_\pi} q^2}, \tag{B.8}$$

where $\Gamma_\rho^0 = 0.149$ GeV in [Wan06] or $\Gamma_\rho^0 = 0.112$ GeV [Doh10] depends on the model.

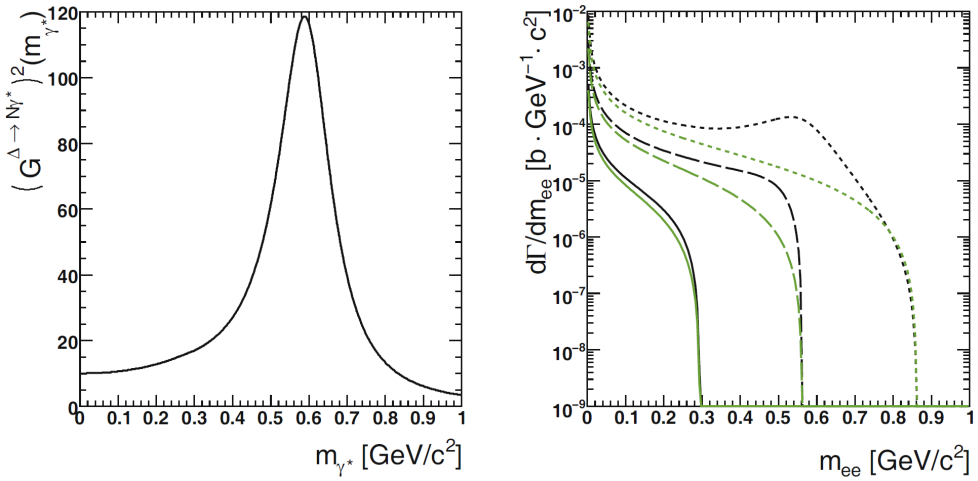

Figure B.4: Left panel: Magnetic $N-\Delta$ transition form factor in the Iachello and Wan two-component quark model. Right panel: The distribution $d\Gamma/dm_{ee}$ as a function of m_{ee} for three Δ masses: $m_\Delta = 1.232$ GeV (solid green curve), $m_\Delta = 1.5$ GeV (long-dashed green curve), $m_\Delta = 1.8$ GeV (short-dashed green curve) according to Eq. 3.9 with a constant G_M form factor, compared to the contribution calculated with the two-component quark model (upper set of black curves) [Doh10].

The resulting distribution of form factor values unravels a prominent peak centred around $m_{ee} \sim 0.77 \cdot m_\rho$ (Fig. B.4, left panel), hence the generated pole of the ρ–meson is at much lower value than expected (the mass $m_\rho = 0.765\ \mathrm{GeV/c^2}$ was used in the calculation). Finally, the distribution $d\Gamma/dm_{ee}$ for three selected Δ masses exhibits a rising enhancement of the decay width for larger Δ masses (Fig. B.4, right panel). The direct coupling to the quark core in the model is negligible up to $q^2 = 5\ (\mathrm{GeV/c})^2$ and the dominant contribution (99.7%) to the G_M form factor is estimated by the VDM in terms of the dressed ρ–meson propagator, being dominant for the range of q^2 involved in the Dalitz decays.

B.4 Ramalho and Peña model

The most recent and continuously developed covariant constituent quark model by Ramalho and Peña [Ram08a, Ram09b, Ram09a] is focused on the description of the form factors of nucleons and baryon resonances (in particular $\Delta(1232)$ [Ram12, Ram16], $N(1520)$ [Ram17], and $N(1440)$, $N(1535)$, $\Delta(1620)$, $N(1650)$ [Ram18]) both in the timelike and the spacelike region, hence it can be very useful for the experimental data interpretation. The model has two ingredients, the contribution from the quark core and the contribution of the pion cloud. The quark core component [Gro69, Gro08] describes the Δ resonance as a quark-diquark structure. The dominant $S-$wave orbital state is responsible for the magnetic dipole transition form factor G_M^*. The electric (G_E^*) and Coulomb (G_C^*) quadrupole form factors proceed through the transition to a D state of the Δ corresponding to a three-quark core spin of 3/2 ($D3$ state) and 1/2 ($D1$ state), respectively [Ram08b]. $D-$state contributions improve the description of the experimental electroproduction data for large four-momentum transfers $Q^2 \leq 6$ GeV^2 ($q^2 = -Q^2$ is the squared transferred momentum) collected at Jlab/CLAS [Fro99, CC06], MAMI [Bec00, Pos01a, Els06, Sta06, Spa07], LEGS [Bla97, Bla01], and MIT-Bates [Mer01, Spa05] but their contributions are in general small.

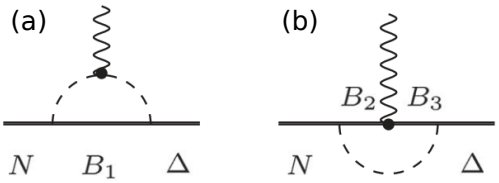

Figure B.5: Pion cloud contributions for the $\Delta \to \gamma^* N$ eTFFs.

Pure quark models can give a complete description only at higher Q^2 where contributions from the pion cloud are negligible. At small four-momentum transfers, the pion cloud needs to be introduced and parametrized. The model extrapolation to the timelike region needs the replacement of the physical Δ mass by an arbitrary W mass and introduction of a phase. The decomposition of the magnetic form factor can be written

$$G_M^*(Q^2, W) = G_M^B(Q^2, W) + G_M^\pi(Q^2, W), \tag{B.9}$$

where $G_M^B(Q^2, W)$ is the quark core bare form factor and $G_M^\pi(Q^2, W)$ is the contribution from any diagram involving a photon and pion loops (Fig. B.5). In order to understand the model features in the timelike region it is worth studying the subsequent components. The bare quark core

$$G_M^B(Q^2, W) = \frac{8}{3\sqrt{3}} \frac{M}{M+W} \left[f_{1\pm}(Q^2) + \frac{W+M}{2M} f_{2\pm}(Q^2) \right] \times \int \frac{d^3\mathbf{k}}{(2\pi)^2 \cdot 2\sqrt{m_D^2 + \mathbf{k}^2}} \Psi_\Delta(P_+, k) \Psi_N(P_-, k), \tag{B.10}$$

where M - nucleon mass, W - arbitrary resonance mass, Ψ_Δ and Ψ_N - Δ and nucleon radial wave functions depending on the Δ (P_+), nucleon (P_-) and intermediate diquark (k) momenta (their detailed form can be found in Ref. [Ram08a]), m_D - diquark mass. The electromagnetic photon-quark coupling is represented in terms of Dirac and Pauli quark form factors $f_{1\pm}$, $f_{2\pm}$. They are parametrized by means of a vector meson dominance (VMD) mechanism, therefore are composed of two components:

$m_{v\pm}^2/(m_{v\pm}^2 - q^2)$ and $M_h^2/(M_h^2 - q^2)$, where $m_{v+} = m_\omega$ (ω mass) is used for isoscalar functions and $m_{v-} = m_\rho$ (ρ mass) is used for isovector functions. The pole at $M_h = 2M$ simulates the meson resonance of a large mass (larger than ρ) in order to describe short range interactions. This kind of parametrisation is very useful for fitting the model to the lattice QCD, using the ρ and nucleon mass values in the lattice QCD regime (see Refs. [Ale08, Ale11, Ale13]). In particular, for pion masses $m_\pi > 400$ MeV/c^2, the pion cloud contributions are suppressed. The valence quark model is also in agreement with the estimation of the bare part of the dynamical model from the EBAC (Excited Baryon Analysis Center, [Sat96, Sat01, JD07]). For the extension to the timelike region, it has to be considered that two pole structures naturally appear, at q^2 equal to either m_ρ^2 or M_h^2. Since the kinematical upper limit is $q^2 \leq (W - M)^2$, only the case $q^2 = m_\rho^2$ has to be considered by introducing the finite Γ_ρ width in the ρ propagator:

$$\frac{m_v^2}{m_v^2 - q^2} \longrightarrow \frac{m_v^2}{m_v^2 - q^2 - i m_\rho \Gamma_\rho}, \tag{B.11}$$

and this way an imaginary part appears in the bare quark contribution. In the transition $\gamma^* N \to \Delta$ the isovector components contribute only (functions f_{i-} in Eq. B.10), therefore only the ρ meson pole is taken into account. The $\Gamma_\rho^0 = \Gamma_\rho(m_\rho^2) = 0.149$ GeV [PDG16] width is known for the physical decay of the $\rho \to \pi\pi$, and for the timelike region $q^2 \geq 0$, a parametrization is used in the form:

$$\Gamma_\rho(q^2) = \Gamma_\rho^0 \frac{m_\rho^2}{q^2} \left(\frac{q^2 - 4m_\pi^2}{m_\rho^2 - 4m_\pi^2} \right)^{3/2} \theta(q^2 - 4m_\pi^2), \tag{B.12}$$

where m_π is the pion mass and the cut below the 2π creation threshold $q^2 \leq 4m_\pi^2$ is enforced by the Heaviside step function $\theta(x)$. The imaginary contribution is present only for $q^2 > 4m_\pi^2 \approx 0.076$ GeV^2. Since the nucleon and resonance radial wave functions in Eq. B.10 are normalized, it can be obtained that $G_M^B(0, M_\Delta) \leq 2.07$ (see Ref. [Ram08a]), but the experimental value of the magnetic form factor $G_M^*(0, M_\Delta) \approx 3.0$. The covariant model without pion cloud explains only 55% of G_M^* at $q^2 = 0$.

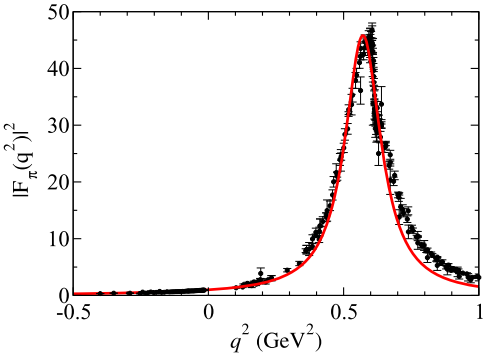

Figure B.6: Pion form factor $|F_\pi(q^2)|^2$ fit to the data, as listed in Ref. [Ram16]. The fit was restricted to $q^2 < 0.6$ GeV^2 and describes both the timelike and the spacelike data. The slight discrepancy for the q^2 values above the peak origins from the interference effects with the ω pole.

The comparison with data requires definition of the second term in Eq. B.9. The simplest parametrization of the pion cloud is double dipole approximation:

$$\frac{G_M^\pi}{3G_D} = \lambda_\pi \left(\frac{\Lambda_\pi^2}{\Lambda_\pi^2 + Q^2} \right)^2, \tag{B.13}$$

where the dipole factor is $G_D = 1/(1+Q^2/0.71)^2$ and λ_π (fraction of pion cloud at $Q^2 = 0$) and Λ_π^2 (falloff of the pion cloud) are adjustable parameters. The model dependence leads to unambiguities (e.g. due to nucleon wave functions) in G_M^B and G_M^π values.

In the most recent version [Ram16] the contribution of the pion cloud to G_M is parametrized with two terms: a photon directly coupling to a pion (Fig. B.5a) or coupling to intermediate baryon states (Fig. B.5b). Therefore, the pion cloud contribution is described with the more advanced formula:

$$G_M^\pi = 3\frac{\lambda_\pi}{2}\left[F_\pi(q^2)\Big(\frac{\Lambda_\pi^2}{\Lambda_\pi^2 - q^2}\Big)^2 + \tilde{G}_D^2(q^2)\right]. \tag{B.14}$$

Both terms (a) and (b) give a similar contribution [Ram13] and in the limit $q^2 = 0$ one has $G_M^\pi(0) = 3\lambda_\pi$, therefore since $G_M^*(0) \simeq 3$ it is clear that λ_π defines the fraction of the pion cloud contribution to $G_M^*(0)$. Λ_π is the cutoff of the pion cloud component (Fig. B.5a) form factor contribution.

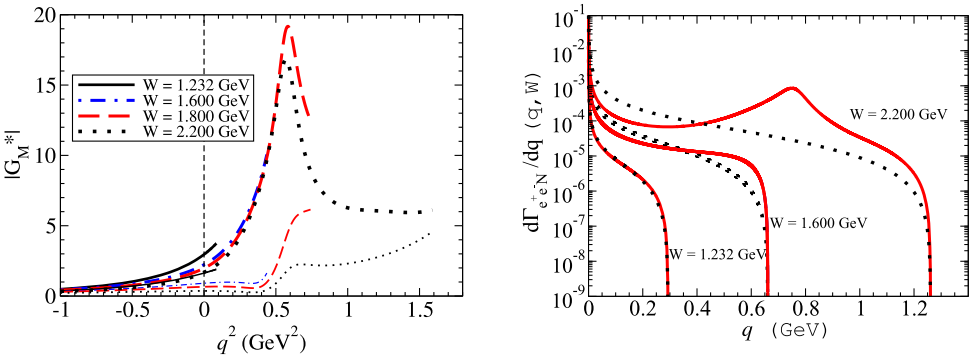

Figure B.7: Left panel: Magnetic form factor $|G_M^*(q^2)|$ for selected discrete resonance masses W = 1.232 GeV, W = 1.6 GeV, W = 1.8 GeV and W = 2.2 GeV. Thick curves represent total model contribution, thin curves indicate the quark core contribution. Right panel: The distribution $d\Gamma_{e^+e^-N}(q,W)/dq$ for three masses M_Δ: W = 1.232 GeV, W = 1.6 GeV, W = 2.2 GeV (red curves) compared to the results of Eq. 3.9 with a constant G_M form factor.

The parametrization of the pion form factor $F_\pi(q^2)$ is based on the Iachello-Wan expression for F_ρ (see Eq. B.8):

$$F_\pi(q^2) = \frac{\alpha}{\alpha - q^2 - \frac{1}{\pi}\beta q^2 \,\log\frac{q^2}{m_\pi^2} + i\beta q^2}. \tag{B.15}$$

By substitutions $\alpha \to m_\rho^2$ and $\beta \to \frac{\Gamma_\rho^0}{m_\pi}$ the Eq. B.8 is fully recovered. The parameters $\alpha = 0.696$ GeV^2 and $\beta = 0.178$ are obtained by the fit to the high precision data as in Fig. B.6. The obtained α value is larger than $m_\rho^2 \simeq 0.6$ GeV^2 but it is compensated by another logarithmic term in the denominator of Eq. B.15, which is dependent on the β parameter, and the pole correctly appears at the ρ mass. In the Iachello-Wan model $\beta \simeq 1.1$ therefore the resulting maximum was shifted to $q^2 \simeq 0.3$ GeV^2, not in agreement with the data.

The second term in Eq. B.14, the dipole form factor, is extended to the timelike region in the following way:

$$\tilde{G}_D^2(q^2) = \frac{\Lambda_D^4}{(\Lambda_D^2 - q^2)^2 + \Lambda_D^2 \Gamma_D^2}, \tag{B.16}$$

where $\Gamma_D(q^2)$ is defined:

$$\Gamma_D(q^2) = 4\Gamma_D^0 \Big(\frac{q^2}{q^2 + \Lambda_D^2} \Big)^2 \theta(q^2) \tag{B.17}$$

in order to avoid the pole at $q^2 = \Lambda_D^2$ and $\Gamma_D^0 = 4\Gamma_\rho^0 \simeq 0.6$ GeV. Again, due to $\theta(q^2)$ step function, $\Gamma_D = 0$ when $q^2 < 0$.

The magnetic dipole form factor contribution $|G_M^*(Q^2)|$ in the covariant spectator quark model is presented for selected $W = M_\Delta$ (1.232, 1.600, 1.800 and 2.200 GeV) in Fig. B.7, left panel. Thick curves represent the total contribution (sum of the pion cloud and the bare quark) while thin curves denote the bare quark contribution only. The pion cloud effect is dominating for $q^2 \leq 1.5$ GeV^2 reaching the maximum of the magnetic dipole form factor around the ρ–meson pole. The valence quark is dominant for larger q^2 values. The contributions in the timelike region are restricted by the kinematical limit $q^2 \leq (W - M)^2$. The dependence of the form factor on the resonance mass is due to the quark core part, which has an explicit resonance mass dependence, while the pion cloud part is independent on the resonant mass. The resulting differential Dalitz decay width $d\Gamma_{e^+e^-N}(q, W)/dq$ is presented in Fig. B.7 (right panel), where red curves represent the model contributions for selected resonance masses (W = 1.232, 1.6 and 2.2 GeV) compared to the description with the constant magnetic form factor G_M^* (as in Fig. B.4, right panel). For higher W and q values, the model naturally exceeds the QED (pointlike) approximation but for $q < 0.4$ GeV its contribution is below the QED prediction. The contribution at the resonance pole mass ($M_\Delta = 1.232$ GeV) is very similar for the valence quark model and the pointlike form factor model.

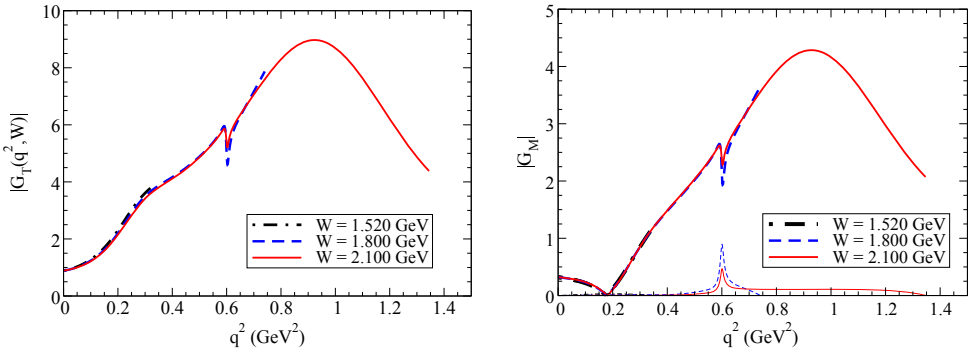

Figure B.8: $N(1520)$ eTFF for selected resonance masses W = 1.520, 1.8, 2.1 GeV. Left panel: Effective contribution of $N(1520)$ form factors $|G_T(q^2, W)|$. Right panel: Magnetic form factor $|G_M|$ (thick curve - total contribution, thin curves - bare quark contribution).

In the transition $\gamma^* N \to N(1520)$, the ω pole has to be included in the form:

$$\Gamma_\omega(q^2) = \Gamma_{2\pi}(q^2) + \Gamma_{3\pi}(q^2). \tag{B.18}$$

The first term corresponds to $\omega \to 2\pi$ decay and is described by the same formula as in Eq. B.12 but with m_ω (instead m_ρ) and $\Gamma_{2\pi}^0 = 1.428 \times 10^{-4}$ GeV, which is about 10^3 smaller than Γ_ρ^0. The second term is factorized as the process $\omega \to \rho\pi \to 3\pi$ and the $\Gamma_{3\pi}(q^2)$ function used in [Ram17] is taken from [Müh06, Müh07].

Further decomposition of the three form factors (G_M, G_E and G_C) is based on fitting to electroproduction data from the CLAS Collaboration [CC09b, CC12a] in the spacelike region. The model prediction for the combination of the electromagnetic transition form factors in the timelike region is presented in Fig. B.8 (left panel), for the three resonance masses W = 1.520 GeV, W = 1.8 GeV and W = 2.1 GeV. In addition, Fig. B.8 (right panel) shows the absolute value of magnetic form factor $|G_M|$, where thick curves denote total contributions and thin curves denote the bare quark contributions. It is clear that the dominant part comes from the pion cloud and the quark core part can be neglected, even at $q^2 = 0$, where it had a significant contribution in the case of the $\Delta(1232)$ resonance. This prediction is in agreement with the decay channels of the subsequent resonances. For example, $\Delta(1232)$ decays to $N\pi$ in 99.4% whereas $N(1520)$ decays to $N\pi$ in $55-65\%$, and to $N\pi\pi$ in $25-35\%$ [PDG16]. In the case of the $\Delta(1232)$ only magnetic form factor plays a role and both valence quark and pion cloud contributions are important at low q^2. The double-pion decay indicates the stronger contribution of the meson cloud in the case of the $N(1520)$ and for the $\gamma^* N \to N(1520)$ transition both magnetic and electric form factors have a significant contribution at low q^2. The evolution of $|G_T(q^2, W)|$ as a function of W shows that in the range $q^2 = 0-1$ GeV^2 the model predicts form factor contributions higher by one-two order of magnitudes as compared to the pointlike form factors [Doh10, Zét03a], where neither q^2 nor resonance mass dependence of the form factor is present.

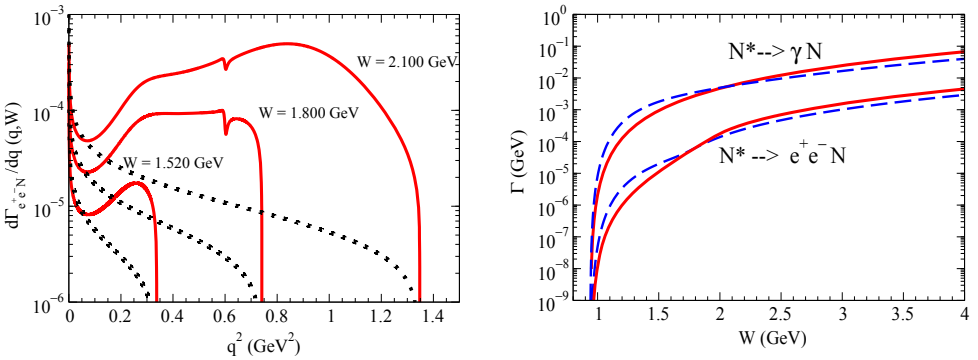

Figure B.9: Left panel: The distribution $d\Gamma_{e^+e^-N}(q, W)/dq$ for three $N(1520)$ masses, W = 1.520, 1.8 GeV, and 2.1 GeV (red curves), compared to the results of Eq. 3.9 with a constant G_M form factor (dotted curves). Right panel: $N(1520)$ (solid curves) and $\Delta(1232)$ (dashed curves) decay widths as a function of W for photon and Dalitz decays.

Finally, also $N(1520) \to e^+e^-N$ Dalitz decay width can be studied, as shown in Fig. B.9 (left panel) with the dilepton decay rate $d\Gamma(q, W)/dq$. The model prediction (red curves) exceeds significantly the pointlike form factor model (dotted curves) already for $q^2 > 0.1$ GeV^2 due to the pion cloud contribution. The integrated values of the decay widths Γ as a function of W are compared in Fig. B.9 (right panel) for the $N(1520)$ (solid red curves) and the $\Delta(1232)$ (dashed blue curves) in the photon and Dalitz decays, respectively. At the lower $W < 1.6$ GeV values the Δ has a dominant contribution, but at large W both resonances contribute in a similar way. The constituent valence quark model provides predictions of the baryon resonance electromagnetic form factors in the timelike region which can be tested in the experiments measuring the resonance Dalitz decays.

Appendix C

HADES Spectrometer

The **H**igh-**A**cceptance **D**i-**E**lectron **S**pectrometer (HADES) [HC09] is installed at GSI Darmstadt on SIS18. It allows to study both hadron and rare dilepton production in fixed target experiments, $\pi + N$, $\pi + A$, $N + N$, $p + A$, $A + A$ in the beam energy range of a few GeV per nucleon, reaching up to 4.5 GeV for a proton beam and 1.5 GeV/nucleon for a heavy-ion beam. The key parameters of the spectrometer are:

- a large geometrical acceptance for detecting dielectron pairs, $\epsilon_{pair} \approx 40\%$ for pairs with large opening angle (e.g. from $\omega \rightarrow e^+e^-$) and $\approx 10\%$ for close pairs with small opening angle (e.g. from $\pi^0 \rightarrow \gamma e^+e^-$)
- a high mass resolution, $\Delta M_{inv}/M_{inv} \approx 1 - 2\%$
- an excellent hadron discrimination allowing to obtain a clear e^+e^- sample (e.g. in $Au + Au$ collisions at 1.23 GeV/nucleon up to 200 charged particles in an event are passing the acceptance of the spectrometer and the dilepton signal is of the order of 10^{-4});
- a signal-to-background ratio greater than 1 for the mass region $M_{inv} \leq 1$ GeV/c^2
- a low material budget ($X/X_0 \sim 2{\times}10^{-3}$ for tracking chambers) to reduce background from secondary particles produced in detector material and multiple scattering of particles
- a high trigger rate of the order of $10 - 40$ kHz sufficient for collection of statistics necessary to study rare dielectron decays

The spectrometer (Fig. C.1) is divided azimuthally into 6 sectors and covers the polar angles within $18^\circ \leq \theta \leq 85^\circ$ and almost all azimuthal angles, excluding the edges of sectors and magnet coils. It consists of:

- a START detector: two Start and Veto modules, in front of and behind the target
- a RICH (Ring Imaging Cherenkov) hadron-blind threshold detector for the identification of electrons/positrons
- a set of four multiwire drift chambers (MDC) for reconstruction of the trajectory of the charged particles: two chambers (MDC I, II) in front of and two (MDC III, IV) behind the magnet

- a superconducting toroidal magnet: for the maximum field of 3.5 T (for a current of 3500 A) passing particles acquire transverse momentum ≤ 100 MeV/c
- a time-of-flight (TOF) detector, made of scintillator bars: in the area of polar angles $45° \leq \theta \leq 85°$ it is a high resolution detector (in terms of spacial and time measurement), while for $18° \leq \theta \leq 45°$ the TOFino, with smaller granularity and one-side readout was used; the TOFino detector was replaced by the Resistive Plate Chambers (RPC) during the spectrometer upgrade in 2010
- a PreShower electromagnetic cascade detector that improves the identification of dielectrons in the polar angles $18° \leq \theta \leq 45°$, where pions and electrons carry high momentum, and serves as a position sensitive reference detector for the TOFino
- a Forward Wall (FW) detector is a fine granularity matrix of plastic scintillators, which was positioned in most of experiments in a distance of 7 meters downstream the beam, in order to detect charged particles at low polar angles $0.33° \leq \theta \leq 7°$

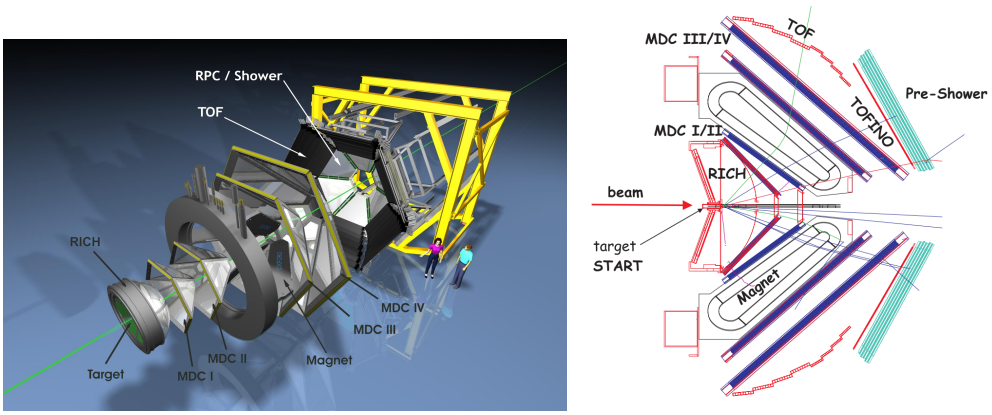

Figure C.1: Expanded view of the HADES detector with its main components (left picture), and schematic cross section view of HADES spectrometer (right panel) without the Forward Wall detector, which was placed 7 meters from the target behind the spectrometer.

C.1 HADES detectors

In the following sections, a brief description of the elements composing the HADES spectrometer are given: RICH, MDCs, TOF/TOFino, PreShower (detectors), and ILSE (magnet). Since 2007, for dp at 1.25 GeV/nucleon and pp at 3.5 GeV measurements, the Forward Wall (FW) detector has been added to the detector set-up. After the first decade of experiments, the spectrometer has been significantly upgraded: the TOFino was replaced by the Resistive Plate Chambers (RPC), the START/VETO diamond detectors were redesigned and installed before the measurements with pion beam and $Au + Au$ collisions (2010). In order to monitor the pion-beam momentum, the pion tracker (PT) has been built. It was operating during data taking in 2014, the details are presented in App. C.1.8.

C.1.1 START and VETO detector

The basic task of the START detector in the HADES spectrometer is to provide the starting point, which measures the time-of-flight of particles from the target to the TOF and TOFino detectors. Signals from particles that have not interacted with the target are eliminated. This selection is made by choosing the signal coincidence between the START module (positioned in front of the target) and the corresponding VETO module (positioned behind the target), so that the start signal is given for more than 10^7 particles per second. An additional task of the detector is to monitor the good positioning of the impinging beam. The first generation of the START and VETO detectors was made of poly-crystalline diamond material produced by Chemical Vapor Deposition (CVD) method [Spe94]. However, as noted in Ref. [Pie10], this technology resulted in significant losses of collected charge in this type of sensors and was not suitable for the detection of minimum-ionizing particles. The signal from the diamond detector in the case of lighter nuclei (e.g. carbon) was within the range of $70 - 80$ mV, therefore not much above the limit of electronic noise. The START detector was not operating during all measurements of the HADES until the spectrometer upgrade in 2010. In those cases the absolute time-of-flight had to be reconstructed based on the relative time between a pair of particles and proper particle identification hypothesis (see description in App. C.3.4).

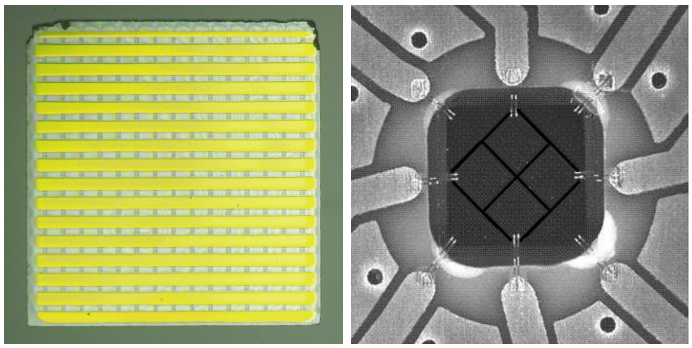

Figure C.2: START and VETO detectors used during Au+Au and pion-beam experiments.

The second generation of the detector was developed based on a mono-crystalline CVD diamond semiconductor (see Ref. [Pie10]) and successfully used during $Au + Au$ and $\pi + p/A$ experimental runs. The START detector (Fig. C.2, left panel) is a 4.7 mm broad and 70 µm thick module and consists of 16 stripes in a horizontal and a vertical direction. The segmentation allows for beam focusing and protects against the efficiency losses due to radiation damage (see Ref. [Pie14]). The diamond efficiency was found to be above 95% and the estimated time resolution amounts to about 50 ps. The VETO detector (Fig. C.2, right panel) is a 100 µm thick, poly-crystalline CVD diamond module, located behind the target. It is divided into 8 active pads and is used to exclude reactions, where no interaction with the target took place.

C.1.2 RICH detector

The RICH detector (Ring Imaging Cherenkov) plays a key role in the e^+/e^- identification in the HADES spectrometer [Zei99]. It is the innermost detector and covers the same polar and azimuthal angles as the spectrometer. The RICH consists of two separate chambers filled with gases (Fig. C.3). A chamber around the target is filled

with C_4F_{10} radiator gas at atmospheric pressure, in which passing e^+ or e^- produce photons in the Cherenkov effect. The photons are reflected from a spherical carbon mirror, pass the crystalline window CaF_2, and are focused to form a ring on a surface of a photon detector. Each sector of the photon detector is an independent wire chamber filled with CH_4, operating in a proportional mode. Photoelectrons, extracted out of the cathode coated with cesium iodide (CsI) by Cherenkov photons, create a charge on the anode wire under the voltage of 2500 V, which gives a gain of 10^5. The detector plane is divided into a matrix of 96×96 pads from which the signal is read. The response to a passing e^- or e^+ is a ring with a nearly constant diameter of about 5.5 cm (corresponding to 8 – 9 pads). The ring image is formed by the sequence of the cathode electrodes on which the charge above the electronic threshold was induced. Therefore, proper particle identification requires a non-trivial signal analysis based on image recognition.

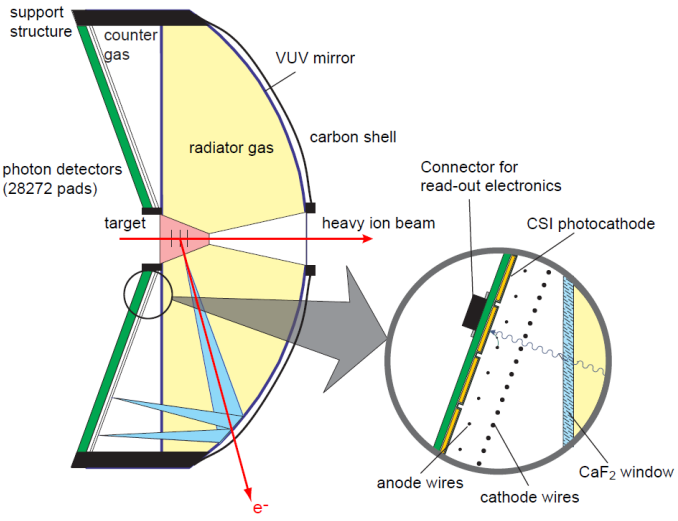

Figure C.3: Cross section view of the RICH detector. The trajectory of the electron emitted from the target (marked in red) passing through the radiator gas causes the emission of Cherenkov photons (blue cone), reflected further from the mirror and focused on the surface of the photon detector in the form of a ring. The magnified area on the right size shows the crystalline CaF_2 window and multiwire proportional chamber with photocatode pads coated with CsI.

The RICH is a threshold detector, sensitive in the wavelength region 145 nm $< \lambda <$ 220 nm. Figure C.4 presents the optical properties of the RICH media: transmittance of the C_4F_{10} and CH_4 gas at a distance of 400 mm, CaF_2 crystal of a thickness 5 mm, and the quantum efficiency of photoelectron extraction from the CsI coating the pad plane (see Ref. [Fab03]). The optical refractivity of radiator gas (C_4F_{10}) is n = 1.00151, hence $\gamma_{thr} = 1/\sqrt{1 - 1/n^2} = 18.3$. The Cherenkov photons appear for a charged particle with the velocity $\beta \geq 0.9985$. For energies available at the SIS accelerator in the HADES experiment, only electrons and positrons are the source of Cherenkov radiation, therefore the RICH detector remains completely insensitive to hadrons. For electrons ($m_0 = 0.511$ MeV/c^2) the momentum at the threshold is 9.3 MeV/c, for charged pions ($m_0 = 139.6$ MeV/c^2) 2.55 GeV/c, and for protons ($m_0 = 938.27$ MeV/c^2) 17.1 GeV/c.

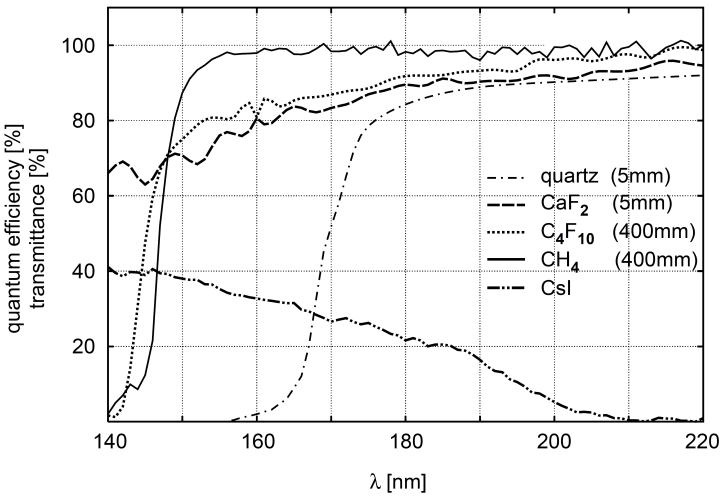

Figure C.4: Transmittance of radiator gas C_4F_{10}, multiwire proportional chamber gas CH_4, and crystal window CaF_2, as well as the CsI quantum efficiency. The quartz transmission is shown for comparison.

The average number of Cherenkov photons amounts to 110. It is proportional to the distance traveled by the charged particle in the radiator gas and varies, with the increasing polar angle, from 38 to 68 cm. The detection of conversion photons is limited on the one hand side by the radiator gas transmission coefficient, falling rapidly to zero for wavelengths smaller than 145 nm, on the other hand, the quantum efficiency of CsI, falling to zero for photons with wavelengths greater than 210 nm. The quantum efficiency of the CsI which decreased over years of operation due to the aging effect, led to an idea of replacing the MWPC by an array of Photo-Multiplier Tubes (PMTs), which will be operational in HADES from 2019 on.

C.1.3 MDC detectors

The system for the reconstruction of the trajectory of charged particles in the HADES spectrometer consists of four planes of Mini Drift Chambers (MDCs), two of which (MDC I, II) are in front of and two (MDC III, IV) are behind the area of the magnetic field produced by the superconducting magnet (Fig. C.5, left panel). The dimensions of the trapezoidal detectors in a given sector increase from 80×88 cm^2 for the smallest module (MDC I) to about 230×280 cm^2 for the largest chamber (MDC IV), to provide a constant coverage in the solid angle per sector. The single drift chamber (MDC detector) is assembled from the six layers of anode wires (with a potential of 0 V) and cathode wires (with a potential of −2 kV) separated by cathode wire planes. The sense and field wires are at different angles, ±0°, ±20°, and ±40° (Fig. C.5, right panel), in order to achieve the greatest possible precision in the particle trajectory reconstruction. Cathode wires in all planes are set at an angle of 90°. The distances between the wires, and thus also the size of a single drift cell (the area between the signal wire and adjacent field wires, with the top and bottom cathode wire) varies from 5×5 mm^2 for MDC I to 14×10 mm^2 for MDC IV. The HADES drift chambers are optimized towards the multiple scattering minimization, therefore each chamber is only 3 – 6 cm thick. The chambers are filled with a mixture of argon (70 – 84%) and quenching gases (CO_2 or isobutane) which absorb the photons from photoemission.

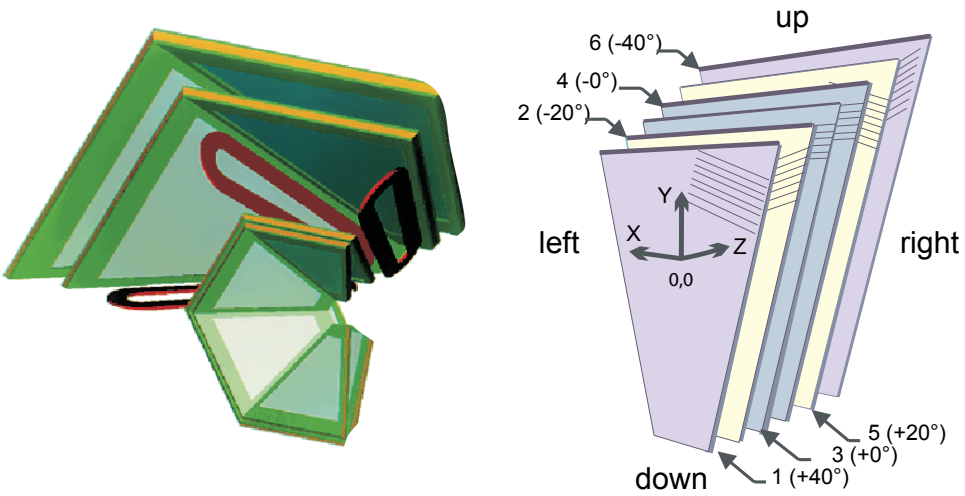

Figure C.5: Schematic layout of the HADES tracking system. Left panel: Two sets of Mini Drift Chambers (MDCs) with 24 wire planes per sector are placed in front and behind the magnetic field to measure particle momenta. Right panel: Schematic view of the six anode wire frames inside a HADES MDC.

The position of the chambers with a few hundred µm accuracy was obtained using the photo alignment method for MDC II (see Ref. [Sch08]). Further improvement in the description of the absolute position of chambers was obtained using minimization procedures based on the beam and cosmic tracks [Pec15]. The particle trajectory can be precisely determined with the good knowledge of the chamber position. The resolution in the polar angle direction is 60 – 100 µm and in azimuthal direction 120 – 200 µm [Mar05]. The single cell efficiency amounts to about 95%.

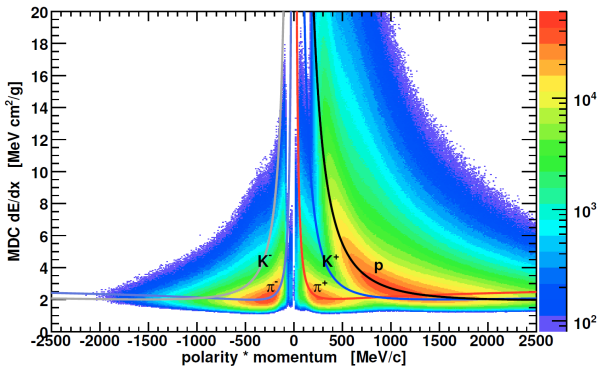

Figure C.6: The energy loss dE/dx as a function of momentum in Mini Drift Chambers. The curves indicate values expected for different particle species deduced from Bethe-Bloch formula.

The readout electronics of drift chambers is able to extract the width of measured signal defined as time-over-threshold, which can be translated by a non-linear transformation into energy loss dE/dx of a particle in MDC. Figure C.6 shows the energy loss versus particle momentum. Electrons and pions cannot be distinguished by this quantity but the energy loss can be used for rejection of protons and, in general, as additional particle signature in a multi-parameter analysis.

C.1.4 Magnet

The superconducting magnet ILSE (IronLess Superconduction Electromagnet) consists of six toroidal coils that form a hexagonal structure of the HADES spectrometer (Fig. C.7, left panel). The RICH, MDC I and II detectors are placed in the inner part of the magnet, whereas MDC III and IV, as well as TOF, TOFino and PreShower detectors are placed outside the magnet. The materials used to build the magnet were selected to minimize their contribution to the production of secondary particles. The cassettes are made of aluminum, the coils are made of niobium alloy and titanium in the form of twisted rods embedded in copper and then in the aluminum layer. The aluminum is necessary in the event of shutdown of the field, so that the energy of 1.41 MJ, stored in the field, does not damage the magnet. The discharged energy is converted into an external heat resistor. The coils can operate at maximum current $I = 3566$ A under the voltage of 200 V, which allows to produce a field 3.77 T in the coil and 0.8 T in the air between the coils. The coils of the magnet are cooled by a single phase liquid helium at $p = 2.8$ bar and $T = 4.7$ K. The magnet weighs 3.5 tons. In the HADES experiments the magnet current was set to either 3200 A (strong field) or 2500 A (medium field).

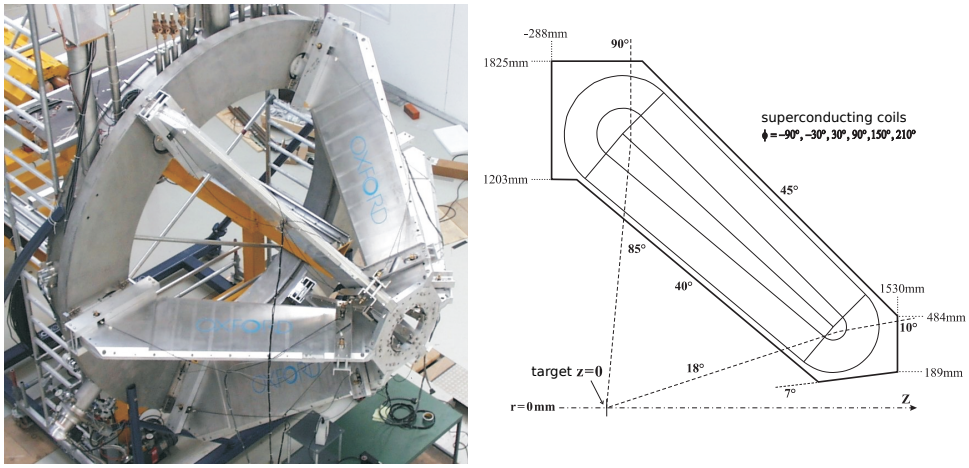

Figure C.7: Photography of a magnet during the assembly (left panel) and a cross section view of a superconducting coil (right panel).

The magnetic field is produced in a wide range of polar angles ($18° - 85°$) and in the full range of azimuthal angles (excluding coils). It vanishes in the region, where the detectors (RICH, MDC, TOF/TOFino and PreShower) are located. The geometry of the toroidal coils has been optimized in such a way that the the ratio of the transverse momentum (Δp_T) to the total momentum (p) of a particle is almost independent of the polar angle at which the charged particle enters the field area, and also independent of a particle momentum. The optimization of the field strength was performed for vector meson decays from $Au + Au$ collisions and beam energy of 1 GeV/nucleon. For electrons/positrons with momenta within $300 - 800$ MeV/c range, the relative change of the momentum, $\Delta p_T/p$, amounts to $14 \pm 1\%$. It means that the electron is deflected in the field always by an angle $\alpha \approx 8°$.

C.1.5 Time of Flight detectors

The time of flight detectors are mounted in six sectors, covering the full range of azimuthal angles. The TOF detector (Fig. C.8, left panel) covers the upper polar angles $45° < \theta < 88°$. It is composed of eight modules with eight scintillator rods each, with lengths from 147.5 cm to 236.5 cm. The four lower modules use rods with a cross-section of 2×2 cm^2, in four upper modules the rods have cross section 3×3 cm^2. The signal from each scintillator is read with photomultiplier tubes (PMT) attached on both sides. With its high granularity the TOF-detector allows to identify the polar angle with a resolution of $2-3$ cm and the azimuthal angle coordinate is constrained with a resolution of 2.5 cm. A time resolution amounts to $\sigma \approx 150$ ps [Ago98]. The efficiency of the TOF detector is about $95-97\%$. It is constrained by two factors, its own time resolution, and multiplicity of charged particles in a given reaction. For the $Au + Au$ collisions at 1.23 GeV/nucleon and for the 4% of most central collisions selected, the probability that more than one particle crosses the same TOF rod is about 4% [Har17]. The TOF signal amplitude allows for the specific energy loss dE/dx which can be used for a particle identification (Fig. C.9).

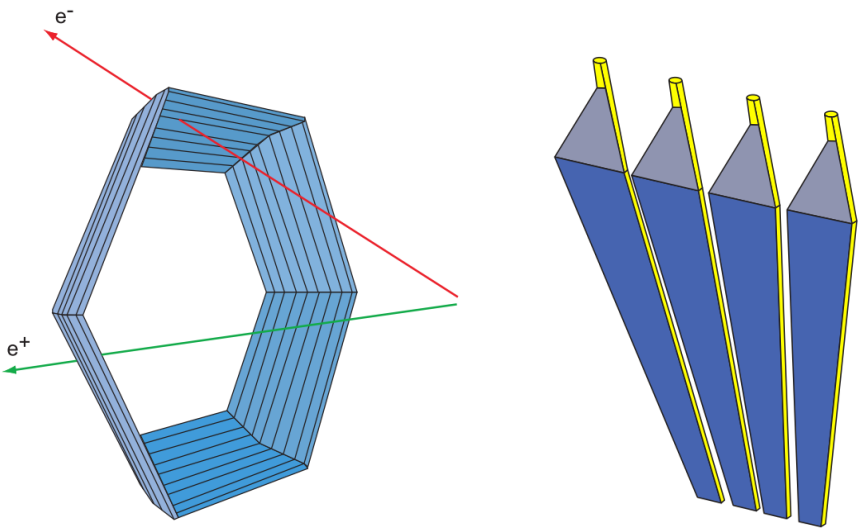

Figure C.8: The time-of-flight detector TOF (left panel) covers polar angles $45° < \theta < 88°$ and consists of six sectors with 8×8 scintillator modules, containing 8 strip each. The TOFino wall (right panel) covers the polar angles $18° < \theta < 45°$ and consists of four almost equal scintillator pads per sector.

In the area of low polar angles ($18° < \theta < 45°$), a simplified version of the time-of-flight detector, the TOFino (Fig. C.8, right panel), was used. In 2010 it was replaced by the Resistive Plate Chambers (see below). The TOFino detector was mounted directly on the PreShower detector frame and had a trapezoidal shape. In six sectors of the spectrometer there were 24 scintillator strips (4 per sector), which were read only at one side. The TOFino did not work as an independent detector, because the position of the flying particles could be determined only with the help of the PreShower detector. The large geometric surface of a single scintillator strip and its location close to mid-

rapidity region made the TOFino detector feasible for time-of-flight measurements with small charged particle multiplicities only. For example, in $C + C$ collisions at beam energy 1.9 GeV/nucleon, two or more hits per one plastic strip were in about 20% of events. In such a situation, there is no possibility to distinguish which particle a given signal could come from. The time resolution of the TOFino detector is about $\sigma \approx 450$ ps.

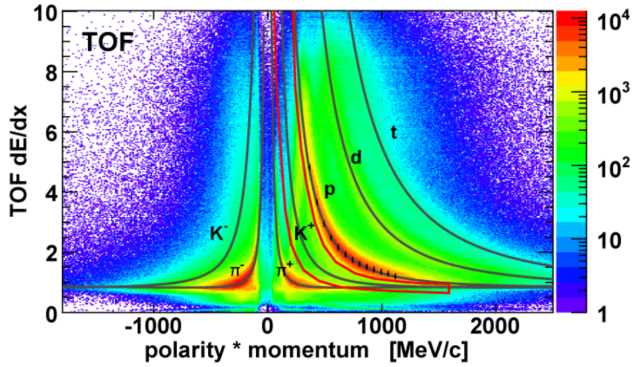

Figure C.9: The energy loss dE/dx as a function of momentum in the TOF detector. The curves indicate values expected for different particle species deduced from Bethe-Bloch formula.

In order to handle high particle multiplicities in $Au + Au$ collisions, the TOFino detector was replaced with the Resistive Plate Chambers (RPC) in 2010 (Fig. C.10), with a very high time resolution and a granularity sufficient for the high multiplicity regime of $Au + Au$ central collisions.

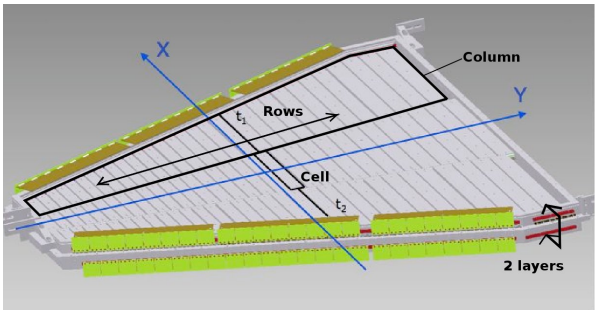

Figure C.10: Internal structure of a HADES RPC sector and the reference coordinate system. The detector is composed of strip counters with variable width, organized in two partially overlapping layers with 31 rows and 3 columns each.

The RPC wall consists of two layers [Bel09], each subdivided into three columns containing 31 strips (cells). The cell length ranges from 12 to 52 cm, and height ranges from 2.2 to 5 cm. The resistive material in cells are two glass electrodes and three aluminum electrodes (the middle at high voltage, the upper and lower are grounded) where the signal is read from. Cells are filled with the mixture of $C_2H_2F_4$ (90%) and SF_4 (10%) [Bla12]. Each single cell is shielded in order to prevent crosstalk effect and minimize the cluster size created by charged particles. During the Au+Au experiment at 1.23 GeV/nucleon [Kor14], the RPC efficiency was measured to be 95%. The time resolution was below $\sigma = 70$ ps, and the deduced time resolution for electrons, including contributions from the START detector and tracking, amounted to $\sigma = 81$ ps. For the most central collisions selected, the probability, that more than one particle crosses the same RPC cell, was about 5%.

C.1.6 PreShower detector

The PreShower electromagnetic cascade detector [Bal04] is the outermost HADES spectrometer detector. It covers the polar angles in the range $18° \leq \theta \leq 45°$ and full azimuthal angles. The PreShower consists of six identical sectors, arranged similarly to other detectors, in accordance with the hexagonal structure of the spectrometer. Each sector is an independent detection system and consists of three multiwire chambers, separated by lead-converter layers (Fig. C.11, right panel). A single chamber is limited by the cathode surfaces. One of the cathodes is a steel plate 0.5 mm thick, the other is the fiber glass plane with copper electrodes - pads, where the signal is read from (Fig. C.11, left panel). The pad shapes and the respective sizes were determined by Monte Carlo simulation in order to obtain a homogeneous average distribution of induced charge over the entire cathode surface in heavy-ion reactions. A layer of grounded field wires and signal wires, being the anodes in the chamber at the voltage of about 2500 V, is placed between cathode planes. The chambers are filled with a gas mixture of argon (30%) and isobutane (70%) with the admixture of heptane as a quenching gas. The selection of the gas mixture and voltage on the anode wires allows to choose the operation mode of the chamber. Primarily, the PreShower was designed to work in a self-quenching streamer mode, characterized by high amplitude of a signal, independent of the energy deposited by a passing particle. However, the detector was operating more stable and efficient enough at lower voltage, hence in a proportional mode.

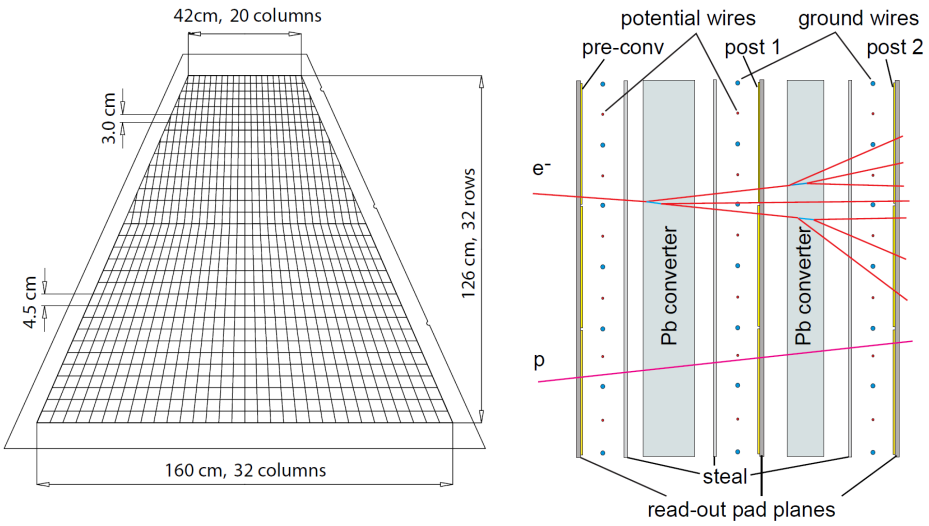

Figure C.11: The PreShower detector scheme of one-sector pad plane (left panel). The cathodes are arranged in 32 rows with 32 pads on a wider side and 20 pads on a narrower side. Schematic cross section view through the PreShower detector (right panel), composed of three gas chambers (pre-, post1-, and post2-chamber) separated with lead layers. Fast leptons create an electromagnetic cascade in lead converters.

A charged particle (e.g. electron, pion, or proton) passing through the chamber (see Fig. C.11, right panel), loses part of its energy in the gas, causing an avalanche of electrons developing towards the anode wire. The charge of a few pC is induced on the cathode electrodes, from where it is read by the electronics. The identification of electrons/positrons in the PreShower detector is based on the electromagnetic radiation

(bremsstrahlung) induced by passing electrons in the lead converters. Radiated photons may convert in the same material into e^+e^- pairs, which in turn may emit further bremsstrahlung photons. This leads to development of a cascade (or shower) of charged particles and thus the larger charge in the post1- and post2-chambers. The charge of the electromagnetic shower is integrated on the area of 3×3 pads surrounding the pad with the highest local charge value. The quantity

$$\sum_{post1} Q(p) + \sum_{post2} Q(p) - \sum_{pre} Q(p) \geq Q_{th}(p), \tag{C.1}$$

where $Q_{th}(p)$ in the momentum-dependent threshold, helps in discrimination between electrons (or positrons) and hadrons. The emission of bremsstrahlung in case of pions or protons is strongly suppressed due to their large masses. The fraction of fake candidates is about 10% for minimum ionizing protons or pions and increases for low momentum protons. However, this can be reduced without affecting the electron identification efficiency by applying a time-of-flight window obtained from the TOFino detector. Using the PreShower condition (Eq. C.1) and the time-of-flight window, more than 90% of the hadrons are rejected and the electron (positron) detection efficiency is at 80% and more for higher momenta.

The outer system of detectors, consisting of TOF, PreShower/TOFino (or RPC) detectors, is combined into **M**ultiplicity **E**lectron **T**rigger **A**rray (META) and used for the trigger condition.

C.1.7 Forward Wall detector

The Forward hodoscope Wall (FW) was installed in 2007 and first it was successfully used for tagging the spectator proton in the deuteron beam experiment (see Sect. 2.2.1). The FW is placed at 7 m behind the target and it covers polar angles $0.33° < \theta < 7.17°$. The mechanical set-up of the detector consists of 287 scintillator modules read out by photomultipliers. During the data taking from *dp* collisions at 1.25 GeV/nucleon not all modules were active (263 modules were operational).

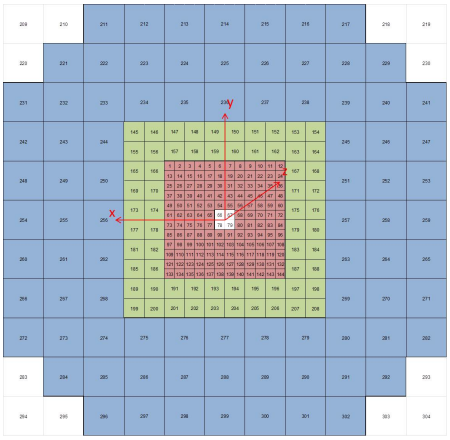

Figure C.12: Layout of the forward-wall with all scintillator blocks surrounding the beam line (red: 4×4 cm^2, green: 8×8 cm^2 and blue: 16×16 cm^2).

In order to achieve a reasonable angular and position resolution the size of the cells was selected in the following way: the innermost part was covered with cell sizes 4×4 cm^2 (see Fig. C.12, red squares), which increased to cell sizes of 8×8 cm^2 (green squares) and the outer region was covered with 16×16 cm^2 cells (blue squares). The thickness of the cells is 2.54 cm. The total transverse dimensions are 180×180 cm^2. Each cell is equipped with an individual PMT readout. The high voltage of each PMT is individually tuned in order to achieve overall high detection efficiency for protons. The estimated time resolution of the FW depends on the scintillator size and varies from 550 ps to 800 ps. Thus, the estimated momentum resolution of the detected particles (protons) is about 11 – 15%. The time resolution of the detector is rather poor and in the lack of magnetic field the detected hits are assigned to a given particle hypothesis. In $d+p \to n+p+(p_{spect})$ experiment, the signal from the fastest particle was considered as a spectator proton. The $d+p \to d+p$ channel could be separated by the time-of-flight (or momentum calculated), too. Its signal can be enhanced by the coplanarity condition between momentum vector of the incoming deuteron beam and scattered deuteron and spectator proton, as it has been demonstrated in Ref. [Kuc15]. Another possibility, utilized in the strangeness production analysis in pp at 3.5 GeV, is the kinematical refit (see Refs. [Sie10, Epp14]).

C.1.8 Pion Tracker

The idea of a pion beam facility at SIS18 dates back to the beginning of the HADES project (early 1990s). The first commissioning tests took place in 1999 [Sim99, Día02]. The secondary pion beam is generated by a primary ^{14}N beam provided by the SIS18 synchrotron with an intensity of $0.8-1.0\times10^{11}$ ions/spill close to the space-charge limit. Pions are then transported to the HADES target located 33 meters downstream from the production point. The beam line consists of 9 quadrupole and 2 dipole magnets (see Fig. C.13).

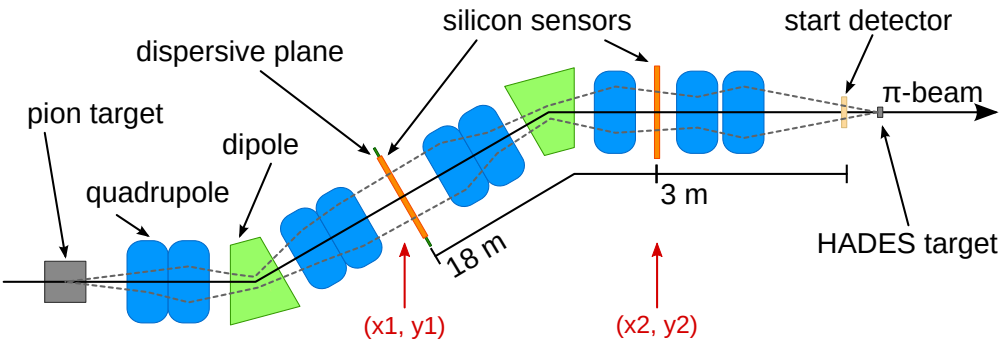

Figure C.13: Pion beam line from the production point (pion target) to the HADES target position. Quadrupole and dipole magnets guide the pions (the dashed line) through the in-beam tracking detectors (indicated by the arrows) [HC16c].

A transmission of 56% is achieved for a given central momentum with a distribution which can be described by a Gaussian with σ = 1.5%. The maximum pion intensity of 10^6 pions/spill was achieved at a momentum p = 1.0 GeV/c and decreased by half for the momenta p = 0.7 GeV/c or 1.3 GeV/c. The purity of the π^- beam is high and the small contamination of electrons and muons, lower than a few percent, does not influence the experimental results. A measurement of the momentum of each beam particle is

provided by a dedicated tracking system CERBEROS [Lal16, HC17a]. It is composed of two double-sided silicon detectors, 0.3 mm thick, covering the area of 10×10 cm^2 and segmented into 128 horizontal and vertical strips. The first silicon sensor (see Fig. C.13) is located close to the intermediate focal plane in order to minimize the multiple scattering effect and is sensitive mostly to the momentum offset. The second sensor is installed in the HADES cave and provides additional spatial information on the pion momentum vector at the target point. Combination of the measured hit position (X, Y) from both silicon planes allows to reconstruct the pion momentum with a resolution of about 0.3%. The focused pion beam spot exceeds the diameter of the target ($\phi = 12$ mm) what can result in severe contamination from interactions with the beam tube or target holder. In order to avoid this background and provide a start time information, a position sensitive diamond detector (see App. C.1.1) was placed 30 cm in front of the HADES target.

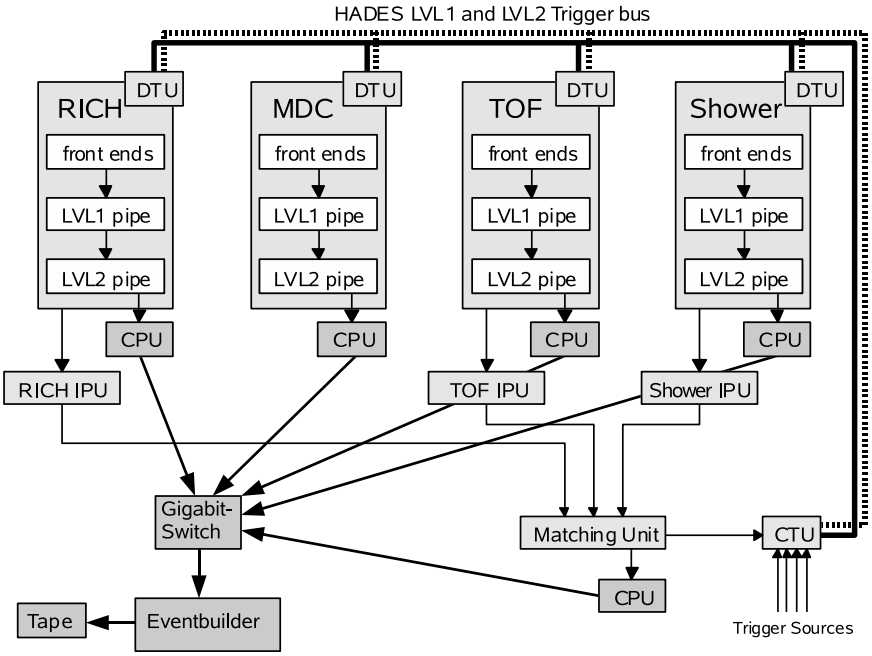

Figure C.14: The trigger distribution and data acquisition system diagram. Triggers are sampled by the central trigger unit (CTU) and transported via the trigger bus to the Detector Trigger Units (DTUs). The data is stored in the LVL1 pipe. At the same time pattern recognition algorithms are performed in Image Processing Units (IPUs) and if a Matching Unit (MU) forms a positive decision, the data is read out via the VME CPUs and sent to the Event Builder. Figure from [HC09].

C.2 Data acquisition and trigger

The trigger and data acquisition system of HADES is a distributed system (Fig. C.14). The Central Trigger Unit (CTU) manages and transmits the trigger signals to the individual subsystems, reacting on external trigger input sources such as multiplicity triggers, minimum bias or calibration triggers. The detector subsystems and the data readout boards are connected within a special network protocol, the TrbNet [Mic12].

The signals from the frontend electronics of the different detectors (RICH, MDC, TOF, PreShower) are collected by means of dedicated end-point boards linked to hubs and streamed via the Gigabit Ethernet to the event builders. The combined data are saved in HLD (**H**ades **L**ist **D**ata) files, stored on hard drives, and further on tapes. In order to reduce the amount of data stored and the dead time of the acquisition, a Central-Trigger-System (CTS) manages a two-level trigger system in the HADES experiments.

The first level trigger (noted as LVL1) consists of a fast hardware selection of central collisions, by measuring the hit multiplicity in the META system. It is possible to apply multiplicity condition in TOF, TOFino (RPC) and FW detectors independently, and sector-wise (e.g. two opposite sectors), in order to enhance the interesting decay channels. The decision time is around 100 ns, which is on average much faster than the time between two collisions.

The second level trigger (noted as LVL2) is devoted to selects events containing electron candidates. This is done by Image Processing Units (IPUs), using dedicated electron recognition algorithms in the different detector subsystems (for details, see Ref. [HC09]). The Matching Unit (MU) combines the IPU information into a single LVL2 trigger decision. It is then forwarded via the CTU to all subsystems with the latency corresponding to several events. Therefore, the detector readout boards need to buffer the data (LVL1 pipes) until the LVL2 trigger signal has been received. Depending on decision, the data are either copied into a separate memory (LVL2 pipe) or discarded.

The summary of trigger conditions used in the elementary collisions measured by HADES is given below.

Trigger configuration : pp at T = 1.25 GeV

The data readout in this experiment was started upon a first-level trigger (LVL1) decision with two different settings requiring: (LVL1A) a charged-particle multiplicity MULT ≥ 3 in HADES or (LVL1B) MULT ≥ 2 with hits in opposite sectors of the time-of-flight detectors, with at least one in the TOFino. The trigger conditions were chosen to enrich inclusive electron pair production ($pp \to e^+e^-X$) and elastic pp scattering for normalization purposes, respectively. The LVL1 condition was followed by a second level trigger (LVL2) requesting at least one lepton track candidate to record events of the type e^+e^-X. The LVL1A trigger efficiency amounts to 0.84 and it has been deduced in Monte Carlo simulations to be independent of the e^+e^- pair mass. All events with a positive LVL2 decision and every fifth LVL1 event, disregarding the LVL2 decision, were written to tape (in total 7.9×10^8 events).

Trigger configuration : dp at T = 1.25 GeV/nucleon

In the deuteron induced quasi-free np reactions, the running conditions were the same as the ones used for the pp run, except that LVL1A also required a coincidence with at least one charged particle hit in the Forward Wall. In total, 1.3×10^9 events were recorded for dp reactions.

Trigger configuration : pp at T = 2.2 GeV

The events were selected upon the following trigger conditions: a first-level trigger (LVL1) selected events with at least four charged hits in the time-of-flight (TOF) wall with additional conditions of two opposite sectors hit, two hits at polar angles $< 45°$. A second-level trigger (LVL2) required an electron or positron candidate. This trigger

scheme favored exclusive e^+e^- production in the $p+p \to p+p+\eta$ reaction with a subsequent η Dalitz decay. The inclusive e^+e^- emission still can be investigated with the trigger bias correction established in Monte Carlo simulations. The *pp* elastic scattering events were measured in the same experimental run, with an additional scaled-down (by a factor 32) LVL1 trigger condition, requiring only two charged hits in opposite HADES sectors. The total number of 2.7×10^8 LVL1 events were recorded, and 4.1×10^7 fulfilling the LVL2 condition.

Trigger configuration : pp at T = 3.5 GeV

The data readout was started upon a first-level trigger (LVL1) decision. Depending on the reaction channel of interest, two different settings of the LVL1 trigger were required: a charged-particle multiplicity MULT ≥ 3 to enhance inclusive dielectron production, and MULT ≥ 2 with hits in opposite sectors of the time-of-flight detectors to enrich elastic *pp* events used for the absolute normalization of the dielectron data. The LVL1 was followed by a second-level trigger (LVL2) requesting at least one electron candidate recognized in the Ring-Imaging Cherenkov Detector (RICH) and time-of-flight/preshower detectors. All events with positive LVL2 trigger decision and every third LVL1 event, irrespective of the LVL2 decision, were recorded (in total 1.17×10^9 events).

C.3 Analysis strategy

The ultimate goal of the data analysis of a given reaction channel is the association of the subsequent detector response to charged particles, combination of the space and time correlated signals into tracks, and finally, providing the description of a track candidate in terms of momentum and particle velocity. This allows for the particle identification hypothesis, which in the simplest case is a graphical two-dimensional selection on momentum *vs* β plane. Track candidates of a given particle species are then combined into a specific physical channel hypothesis. The cuts used are optimized in terms of the efficiency and purity of the signal maximization. The analysis strategy has been presented in detail in Ref. [HC09], and described in numerous PhD theses (e.g. see Refs. [Har17, Sch16, Sie13, Gal09]). The key aspects are summarized below.

C.3.1 Software package

The HADES software has been written in C++ and based on the ROOT framework [Bru97], which is object oriented framework for large scale data analysis. The main analysis code, called HYDRA [Gar03] (**H**ades s**Y**stem for **D**ata **R**eduction and **A**nalysis), is the scalable modular framework containing detector-specific and task-specific classes. The data can be retrieved from many sources, e.g. event servers, raw data files stored by the data acquisition system, and ROOT files created at the various stages of analysis. The data processing is realized via configurable task lists, which can define a sophisticated analysis work flow. The initialization of geometry, set-up and calibration parameters is handled from an Oracle database and/or from ROOT files, with full version management implemented. The analysis can be run in stand-alone batch mode or from interactive ROOT sessions. The important step of the analysis is the DST (**D**ata **S**ummary **T**apes) production which is a common basis of all analyses in the HADES collaboration. At this level, detector electronic signals are translated to physical information, e.g. hits on RICH, MDC, TOF, TOFino or RPC, and PreShower,

with the corresponding parameters (hit coordinates, time-of-flight values, energy loss) and higher level structures, e.g. reconstructed trajectories. Further data analysis depends on the reaction type. In elementary collisions, track combinations of particles expected in the final state of a given reaction channel are investigated within the PAT (**P**ostDST **A**nalysis **T**ool) framework, developed by the author. This framework allows for agile hypothesis definitions, correlation cuts, multi-variable selection cuts, and time recalibration, resulting in the identification of the final state. The ultimate analysis stage is based on user defined FAT (**F**inal **A**nalysis **T**ool) module, providing e.g. histograms, small ntuples or just figures. The Monte Carlo simulations of the spectrometer response are performed with the package GEANT3 [Gea94] from CERN. The detailed geometry and constructing materials, as well as the optical properties of detectors, are implemented. The realistic response of detectors hit with the passing particles is simulated within the HYDRA framework, and the corresponding detector parameters are verified for each experimental measurement separately. Event overlay, e.g. the embedding of simulated tracks into real events for efficiency and performance investigations, is supported as well. The reaction models are realized within the PLUTO event generator [Frö07, Doh10]. The PLUTO is a standalone simulation framework for heavy ion and hadronic physics reactions. Different models can be selected or defined, and the particles in the final state can be filtered with dedicated acceptance matrices for fast investigation. The input files for a full scale GEANT simulation, and further analysis, can be also produced. In this way, the realistic spectrometer response is obtained, allowing for the efficiency and acceptance corrections.

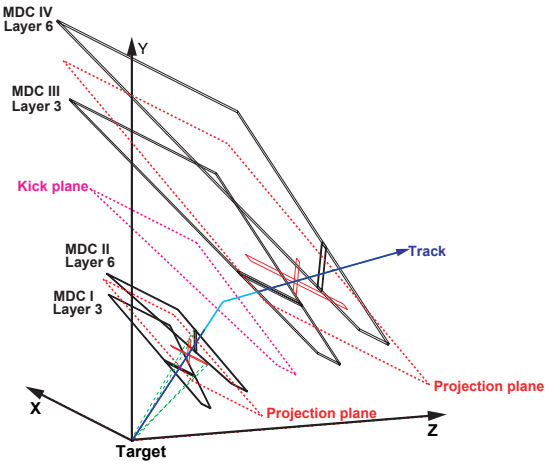

Figure C.15: Method of searching for track candidates in HADES. The drift chambers are approximated by only one layer (black lines). Red lines show the projection planes between the inner, respectively outer, drift chambers. Blue lines point to the vanishing point of the projection plane. The magenta line sketches the virtual kick plane, where the particle is deflected according to its momentum. Figure taken from Ref. [HC09].

C.3.2 Track reconstruction

The reconstruction of the particle trajectories in the tracking system of HADES is based on the correlated signal from the drift chambers (MDCs). In each chamber the crossing fired drift cells form wire clusters which are defined by the geometrical positions of wires. This is done by projection to a virtual plane, where a maximum representing a crossing point of fired wires corresponds to a point traversed by a particle (Fig. C.15). The target position and the location of the maximum in the projection plane define a straight (inner) track segment in space. The deflection of a charged particle by the toroidal magnetic field of the HADES magnet can be approximated by a momentum

kick on a nearly flat virtual kick plane in the field region (see Ref. [Gar03]). The track direction behind the field is defined then by the outer wire clusters and the intersection point of an inner segment with the virtual momentum kick plane. Finally, particle trajectory candidate is reconstructed from the matching of two points before (inner track segment) and two points behind (outer track segment) the magnetic field. The spatial resolution of the track candidate search is defined by the wire angles and spacing, which have been optimized for best resolution in the direction of particle deflection.

The standard method to determine the momentum of a particle traversing a known magnetic field is Runge-Kutta algorithm [Pre07]. Solving of the second-order differential equations of motion requires initial parameters, e.g. preliminary momentum, polarity and vertex. They are retrieved from the spline momentum reconstruction method, matching inner and outer track segments. The magnetic field is defined by a measured three-dimensional field map. The result of Runge-Kutta tracking is the charged particle trajectory reconstruction (with momentum and vector at the emission vertex), provided with the χ^2_{RK} value. It can be used either as a criterion for track quality selection or as a method for particle identification.

C.3.3 Particle identification

The HADES spectrometer is capable to identify all charged particles simultaneously in wide momentum range, particularly electrons which are rare signals. Two approaches of particle identification (PID) have been implemented, either using a set of cuts on various observables (the default approach), or applying a Bayesian method. The observables used for cuts are momentum, velocity, energy loss in MDC and TOF, and hit patterns in RICH and PreShower. For all tracks reconstructed in MDC chambers, the outer track segments are matched with hit points in the META detectors (TOF or PreShower/TOFino, RPC), providing another χ^2_{META} value of the matching quality. The main condition on electron/positron identification is the matching of the inner segment track with a ring in the RICH detector. If there is no ring correlated with a track, the particle is considered to be a hadron. Figure C.16 shows an example of particle species separation for reconstructed tracks matched with the TOF detector in the case of $Ar + KCl$ reaction. The graphical cut on correlated variables of β *vs* momentum allows for particle selection. Another cut can be applied on energy loss as a function of momentum (see Figs. C.6 and C.9).

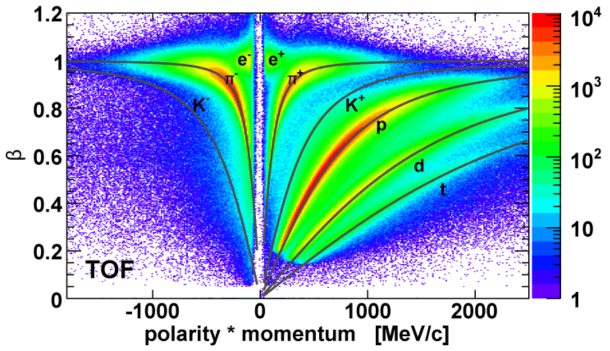

Figure C.16: The particle separation on two-dimensional plane of velocity (β) *vs* momentum in the TOF detector. Solid curves represent ideal values for a given particle species. Figure taken from $Ar + KCl$ at 1.756 GeV/nucleon measurement (see Ref. [Sch08]).

C.3.4 Time reconstruction

The correct particle velocity (β) can be deduced from the track length and absolute time-of-flight measured between the START detector and the TOF/TOFino detector signals. In experimental measurements of elementary collisions, performed before the spectrometer upgrade in 2010, the START detector was not operating. As a consequence, the start time was given for each event by the trigger signal, which was related to the earliest signal in either TOF, TOFino or FW detectors. Therefore, there was no common time reference for tracks in different events. The absolute time-of-flight can, however, be calculated for a defined hypothesis, where each reconstructed trajectory is assigned to be a given particle species. With the known trajectory length, momentum and ideal particle mass, the time-of-flight for each particle is calculated,

$$t_i^{calc} = \frac{l_i^{track}}{\beta \cdot c}, \tag{C.2}$$

where l_i^{track} is the i–th particle track length, β depends on the assigned ideal mass. In a general case of N particles, the reference particle (here, j–th) has to be chosen. The reference time for each (i, j) pair is defined as the mean time

$$\bar{t}_j = \frac{t_i^{calc} + t_j^{calc}}{2}. \tag{C.3}$$

If the measured (relative) time is t_i^{exp} and t_j^{exp}, with the help of half time difference

$$\Delta t_j = \frac{t_j^{exp} - t_i^{exp}}{2}, \tag{C.4}$$

the reconstructed time can be calculated as follows:

$$\begin{aligned} t_{ij}^{rec} &= \bar{t}_j - \Delta t_j \\ t_{ii}^{rec} &= \frac{\sum_{j,j\neq i}^{N} \bar{t}_j}{N-1}. \end{aligned} \tag{C.5}$$

Finally, the χ^2_{tot} for a given hypothesis is a measure which particle combination assignment is the best in terms of the reconstructed time-of-flights:

$$\chi^2_{tot} = \sqrt{\sum_i^N \chi_i^2},\ \chi_i^2 = \sqrt{\sum_j^N \frac{(t_{ij}^{rec} - t_j^{calc})^2}{\sigma_j^2(TOF, TOFino)}}. \tag{C.6}$$

The χ^2 calculation includes the TOF and TOFino detector resolution. In most cases there is no need to calculate all combinations in the event, as the reference particle is preferably measured in the TOF detector, and with a negative polarity (e.g. e^- or π^-), depending on a given hypothesis. The proper particle assignment results in the correct β *vs* momentum dependency.

C.3.5 Physical observables

C.3.5.1 Invariant mass

A common method to reconstruct a particle that decays into several charged secondary particles before it reaches the detector is to calculate the invariant mass. In a two-body decay, for the daughter particles identified with the masses m_1 and m_2, energy E_1 and E_2, momenta p_1, p_2 and their relative opening angle θ_{12}, the invariant mass reads:

$$m_{inv}c^2 = \sqrt{(E_1 + E_2)^2 - (\vec{p}_1 c + \vec{p}_2 c)^2}, \tag{C.7}$$

and further,

$$m_{inv} = \sqrt{(m_1^2 + m_2^2) + 2\left(\sqrt{m_1^2 + (\vec{p}_1 c)^2}\sqrt{m_2^2 + (\vec{p}_2 c)^2}\right) - 2\,|\vec{p}_1|\,|\vec{p}_2|\,c^2\cos\theta_{12}}. \tag{C.8}$$

Usually, after identification of the daughter particles, the ideal masses m_1 and m_2 are used. In this case, the errors from the time-of-flight measurement, as well as further systematic errors, are not propagated into the invariant mass spectrum. Accordingly, the width of the particles and resonances is composed only of their own decay widths, as well as the pulse resolution. In the case of dielectron pairs, the masses are neglected ($m_1 = m_2 \approx 0$), and the formula is simplified (here in units $c = 1$):

$$m_{inv} = 2\sqrt{|\vec{p}_1|\,|\vec{p}_2|}\,\sin\frac{\theta_{12}}{2}. \tag{C.9}$$

C.3.5.2 Signal and combinatorial background

In the low mass region $m_{e^+e^-} < 1$ GeV/c^2 the dominant sources of dileptons are π^0/η semi-leptonic or photon decays, followed by the photon conversions in the target and detector material. Moreover, several pions can be produced per event. Hence, a certain number of electron tracks (n_-) and positron tracks (n_+) can be identified within an event. In combination of all unlike sign pairs (n_{+-}^{tot}) it is not possible to decide which pairs derive from the same decay vertex and which are an accidental combination of individual tracks of separate decay processes. Therefore, two classes of unlike sign pairs can be distinguished: the signal of correlated dielectrons, n_{+-}^{sig} and the so-called combinatorial background (CB) pairs, n_{+-}^{cb}. Hence, the signal is calculated as follows:

$$n_{+-}^{sig} = n_{+-}^{tot} - n_{+-}^{cb}. \tag{C.10}$$

Both signal and combinatorial background are continuous spectra. The pairs of e^+ and e^- produced in different decays form an uncorrelated background. However, in $\pi^0/\eta \to \gamma e^+e^-$ Dalitz decays, or $\pi^0/\eta \to \gamma\gamma$ decays, followed by the $\gamma \to e^+e^-$ conversion in detector material, some e^+e^- pair combinations are correlated in the phase space since they originate from the same grandparent particle (e.g. pseudoscalar meson). Such a contribution to the background is referred to as correlated background (see Fig. C.17). The combinatorial unlike sign background can be estimated by the same-event like sign method or by the mixed event technique. The first method is based under the assumption that the same-event combinatorial like-sign background is identical to the combinatorial unlike-sign background and if acceptance and efficiency for electrons and positrons being the same. The like sign background can be described by the geometric mean of unlike sign combinatorial background (see Refs. [Gaz00, Abr00] for detailed derivation):

$$\langle n_{+-}^{cb}\rangle = 2\sqrt{\langle n_{++}\rangle\langle n_{--}\rangle}\,. \tag{C.11}$$

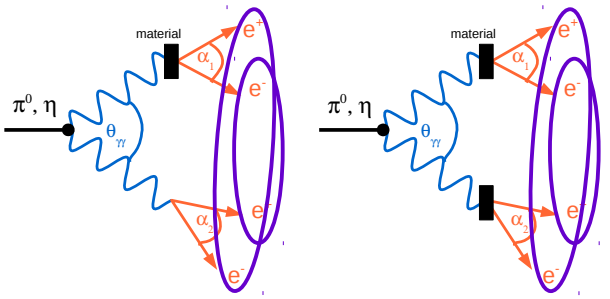

Figure C.17: The combinatorial background of correlated pairs (marked with ellipses) deriving from the π^0/η Dalitz decays (left figure) and decays to two photons, followed by the e^+e^- pair conversion in the target or detector material (right figure).

This result assumes that the reconstruction probability does not depend on the sign of the pair, which is true in most cases for large pair opening angles, but in general, a finite two-track resolution affects like-sign and unlike-sign pairs differently (for a correction factor calculation see Ref. [PC10]). Another disadvantage of the like-sign background estimation method are limitations in the available statistics. The respective error can be approximated as

$$\sigma\left(\sqrt{4\langle n_{++}\rangle\langle n_{--}\rangle}\right) \approx \sqrt{\langle n_{like-sign}\rangle}, \tag{C.12}$$

where

$$\sqrt{\langle n_{like-sign}\rangle} \approx 2\langle n_{++}\rangle \approx 2\langle n_{--}\rangle, \tag{C.13}$$

and Poissonian distribution for the statistical error and statistical independence of the positive and negative like-sign pair samples were assumed. It is worth noticing that the combinatorial background can be approximated by an arithmetic mean. Provided, that n_+ and n_- are larger than $|n_+ - n_-|$, one can write e.g. $n_{--} = n_{++} + \epsilon$, and

$$\sqrt{n_{++}n_{--}} = n_{++}\sqrt{1+\frac{\epsilon}{n_{++}}} \approx n_{++}\left(1+\frac{1}{2}\frac{\epsilon}{n_{++}}\right) = n_{++}+\frac{\epsilon}{2} = \frac{n_{++}+n_{--}}{2}. \tag{C.14}$$

The arithmetic mean always overestimates the geometrical mean. The CB has to be calculated for every distribution under investigation, e.g. the differential formula for the invariant mass:

$$\frac{dN_{CB}}{dM_{e^+e^-}} = 2\sqrt{\left(\frac{dN}{dM}\right)_{e^+e^+}\left(\frac{dN}{dM}\right)_{e^-e^-}}, \tag{C.15}$$

where e^+e^+ and e^-e^- stand for the same-event like-sign pairs.

In the mixed-event technique, tracks from different events are combined to yield the combinatorial unlike-sign background, thus they are inherently independent. In contrast to the same-event technique, requiring at least two tracks per event, the mixed-event approach utilizes also events with single tracks, what has to be taken into account during the data analysis. In order to obtain the mixed-event background, the mixed unlike-sign distribution has to be properly normalized with the number of same event pairs. The advantage of the mixed-event background distribution is that the statistical error can be easily reduced by increasing the number of mixed events (for details, see Ref. [Her02]).

C.3.5.3 Reference frames

The laboratory system is a natural reference frame for detectors, but there are other important reference systems allowing for the correct visualization of physical processes, including the production and decay mechanisms. Besides the rest mass, which is Lorentz invariant observable, the leading role play various angular projections in center-of-mass (c.m.s.) system, the Gottfried-Jackson (GJ) angle and the helicity angle.

The graph in Fig. C.18 is an example of the Δ^{++} resonance production in the one-pion exchange description, with three particles (n, p, π^+) in the final state. The two initial protons are indistinguishable, i.e. it is not known which is the projectile or the target. The graph will be used for an illustration of the aforementioned angular projections.

The center-of-mass system (c.m.s.) is the Lorentzian frame, where the total momentum is 0, and the projectile and target particles (in figure, p_{beam} and p_{target}) have identical momenta in opposite directions. Figure C.19 presents an example of one-pion production in the $p+p \to n+p+\pi^+$ channel, with three particles in the final state. The $\theta^n_{c.m.s.}$ distribution is the mirror reflection of the two-body $\theta^{p\pi^+}_{c.m.s.}$ distribution. An intermediate Δ^{++} resonance influences the angular distribution of the particles (as described by the one-pion exchange models, see Sect. 1.2) and the observed angular distribution should be very anisotropic.

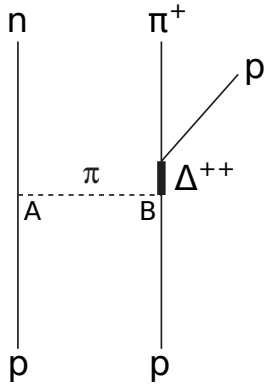

Figure C.18: An example of the Δ resonance production and decay in the one-pion exchange description. The Δ^{++} decays further into p and π^+, making three particles in the final state. Various angular distributions can be studied (see text for details).

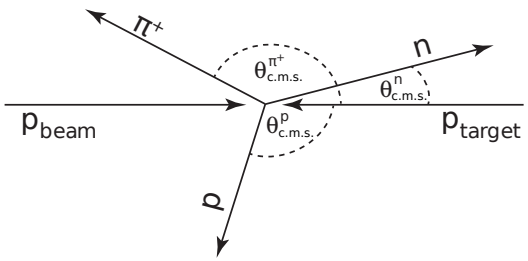

Figure C.19: Final state of three particles (n, p, π^+) and the subsequent angles ($\theta^n_{c.m.s.}$, $\theta^p_{c.m.s.}$, $\theta^{\pi^+}_{c.m.s.}$) in the center-of-mass system. The anisotropic angular distribution is sensitive to production and decay mechanisms but is also challenging from the experimental point of view, requiring large acceptance coverage.

The angular distributions in the center-of-mass are sensitive to the characteristics of the exchange meson. Light meson exchange (here π^+) results in very anisotropic distributions, whereas the exchange of heavy mesons are more isotropic. In elementary collisions discussed in the following chapters (pp or np), the center-of-mass system is calculated as a fixed value. However, in the case of the secondary beam which is the pion beam, the momentum is not fixed but has a certain beam momentum profile. If the fixed value is used for the center-of-mass frame determination, the obtained distributions are smeared additionally with the beam momentum resolution. In such a case a pion tracker can deliver information on the pion projectile momentum, which can be used for the c.m.s. calculation.

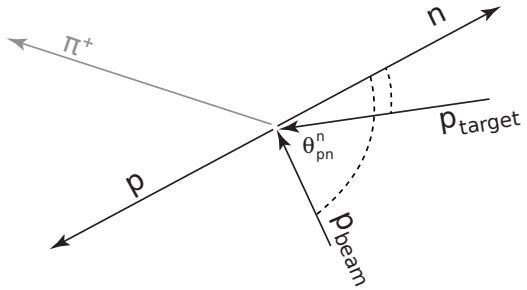

Figure C.20: The Gottfried-Jackson angle is defined as the angle between projectile and a particle in the final state, where both are observed in the same rest frame made e.g. out of two particles, and one of the rest frame components is a particle used for the GJ angle.

The Gottfried-Jackson (GJ) frame [Got64] (Fig. C.20) is the rest frame of two (e.g. $n\pi^+$) out of three (e.g. n, p, π^+) produced particles. In this frame, the GJ angle (e.g. $\theta^{\pi^+}_{n\pi^+}$) is defined as the angle between one of the rest frame particles (e.g. π^+) and the initial particle (e.g. p) boosted to the same rest frame. The superscript denotes the selected particle for the angle calculation, whereas the subscript indicates which rest frame is used. In the case of one-pion exchange (as in Fig. C.18), the $n\pi^+$ (or $p\pi^+$) rest frame is equivalent to the rest frame of the exchanged pion (π^{+*}) and the proton contributing to the vertex B. In such a case the reaction description is reduced from $2 \to 3$ to $2 \to 2$ of the form $\pi^{+*} + p \to p + \pi^+$, and only the kinematics at vertex B plays a role. The GJ angle distribution does not need to be symmetric. In addition, if two protons collide, the production may occur either at vertex A or vertex B, and the angular distribution has to be calculated by using the angle to both protons.

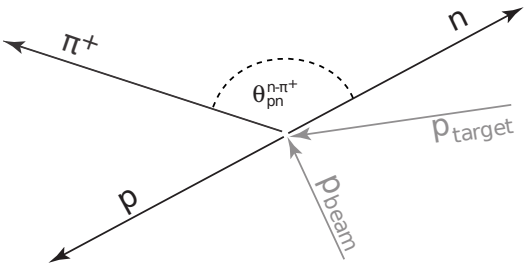

Figure C.21: The helicity angle is defined as the Lorentzian frame of two particles, i.e. it is the identical Lorentzian frame as the respective Jackson frame. Three helicity frames can be constructed by cyclic permutation for the three-body final state ($n\pi^+$, $p\pi^+$, and np in this example). E.g. the $\theta^{p-\pi^+}_{n\pi^+}$ angle is calculated between p and π^+ measured in the rest frame of $n\pi^+$.

The helicity frame (Fig. C.21) is also the rest frame of two particles (e.g. $n\pi^+$), but the helicity angle is defined between one of rest frame particles and the third particle (e.g. p) in the final state, observed in the same rest frame, e.g. $\theta^{p-\pi^+}_{n\pi^+}$ with a proton boosted to the $n\pi^+$ reference frame. Therefore the superscript contains both particles selected for the helicity angle calculation. If the Dalitz plot is distorted due to physical or kinematical effects, it must result in characteristic distributions in helicity frames. For example, the Δ^{++} resonance decaying into $p+\pi^+$ manifests its presence in the $m^2_{n\pi^+}$ (or m^2_{np}) axis in a Dalitz plot. The properties of mass and width of the resonance are seen in the $n\pi^+$ and np helicity frames. The decay pattern characteristic for the angular momentum of the resonance shows up in the $p\pi^+$ helicity frame. It is different from the isotropic if the resonance carries angular momentum $L > 0$ and if it is polarized, or if more resonances decay into the same channel and thus the interference effects can influence the distribution. The final-state interaction may also distort a Dalitz plot and, consequently, can be seen in helicity angle distributions.

In summary, three particles in the final state can be studied by plotting nine angular distributions (three center-of-mass angles, three GJ angles, and three helicity angles). Not all of these observables are kinematically independent from each other. The energy and momentum conservation reduces nine degrees of freedom to five, and with the azimuthal symmetry, only four independent degrees of freedom remain.

C.3.6 Normalization

In order to plot the differential cross section of a given physical channel, the reference reaction has to be identified. In all elementary NN reactions as well as $\pi^- p$ collisions, the elastic scattering has been measured in parallel to inelastic channels, allowing, with the use of the known cross sections from other experiments, for the deduction of the normalization for all channels.

C.3.6.1 Normalization in pp and np collisions

The normalization of the experimental yields is performed using the pp elastic scattering yield, recorded usually with the dedicated trigger condition, requiring only two particles in opposite sectors of the HADES spectrometer. The momentum conservation leads to the following relations between polar (ϕ) and azimuthal (θ) angles of both protons:

$$\begin{aligned} |\,\phi_1 - \phi_2\,| &= 180^\circ\,, \\ \tan\theta_1 \times \tan\theta_2 &= \frac{1}{\gamma^2_{c.m.s.}}, \end{aligned} \tag{C.16}$$

where $\gamma_{c.m.s.}$ is the Lorentz factor of the center-of-mass system. The elastic events are selected by a two-dimensional elliptic cut in the ($|\,\phi_1 - \phi_2\,|$, $\tan\theta_1 \times \tan\theta_2$) plane, with semi-axes corresponding to 3σ for each variable. These constraints account for the detector resolution and the momentum spread of the proton. Figure C.22 shows a proton polar angle in the laboratory system within the HADES acceptance. The data have been overlayed with the simulation of the pp elastic events at T = 1.25 GeV.

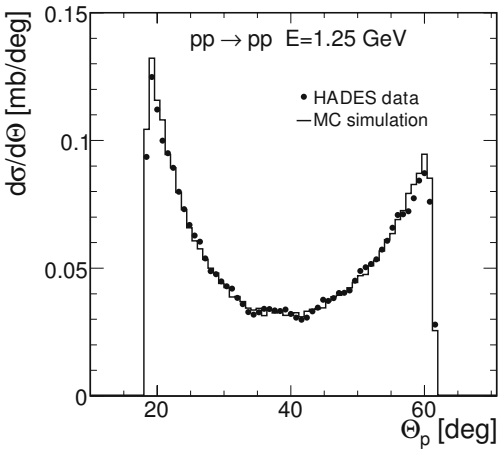

Figure C.22: pp elastic scattering at T = 1.25 GeV. Proton polar angle in the laboratory system: data (dots) corrected for efficiency are presented within the HADES acceptance. They are compared to the Monte Carlo simulation using the cross section parametrization published in Ref. [EC04] (black solid line histogram).

The reference *pp* elastic cross section for the polar angle range between 46° and 134° in the c.m.s. amounts to 3.99 ± 0.19 mb, as measured by the EDDA Collaboration (see Ref. [EC04]). The normalization error is estimated to be 8%, where 5% is derived from the error of the reference differential cross section and 6% is the systematic error of the reconstruction of events with elastic scattering. It the case of *dp* collisions at 1.25 GeV/nucleon, the quasi-elastic *pp* scattering yield was recorded with the trigger condition, requiring two particles in the opposite TOF/TOFino sectors and no particle registered in the FW. The proton momentum distribution in the deuteron and the dependence of the cross section on the *pp* center-of-mass energy were taken into account in the Monte Carlo simulation, using realistic momentum distributions implemented in the PLUTO event generator [Frö07]. The overall normalization error was estimated to be 7%, where 4% was derived from the error of the reference differential cross section from Ref. [EC04] and almost 6% was the systematic error of the reconstruction of events with elastic scattering in HADES [HC15b]. It the case of *pp* collisions at T = 3.5 GeV the *pp* elastic cross section has been obtained from Ref. [Kam71].

C.3.6.2 Normalization and carbon subtraction in π^-p collisions

$\pi^- p$ elastic scattering was measured in the pion beam experimental run to serve as the normalization for all other channels. First, events were pre-selected with the help of a cut on coplanar pion and proton reconstructed tracks (±5°) and $\tan\theta_{\pi^-} \times \tan\theta_p > 1$ selection. Events originating from scattering on polyethylene target (composed of both carbon and proton atoms in the ratio 1 : 2) and carbon target are depicted in Fig. C.23 (left panel) showing $\pi^- p$ missing mass squared. The proportion of carbon events (red curve) was scaled such that the left tail, far from the dominating elastic scattering peak on protons, should match the tail from polyethylene events (black curve). This scaling factor is in agreement with the number of all events recorded in the START detector (see App. C.1.1) during the measurement with the polyethylene target and the carbon target, respectively (after correction for the data acquisition dead time and taking into account different carbon densities of both targets). Scaling factor for the polyethylene and carbon target events, deduced in the elastic scattering channel, was used further to all inelastic channels.

The next step, performed for all investigated channels separately, was matching events of the same kinematic characteristics from polyethylene target and carbon target. Events were grouped into bins of similar missing mass values, then for all combinations among tracks measured with the polyethylene and the carbon target those with the lowest χ^2 were paired together. The calculation of the χ^2 correlation included: (a) the momentum, and (b) polar angle of the measured particles (π^+, π^-, proton), and (c) invariant mass of $\pi^+\pi^-$ and $p\pi^-$, respectively. This method delivers pure pion-proton reaction candidates. The event by event tagging and rejection of carbon events allows also for the further cut refinement, e.g. elastic scattering selection what is not possible when having also events with the pion scattering on carbon. A few approaches were investigated (e.g. two-dimensional graphical cuts on angle and momentum of p and π^- or condition on the same momentum of particles in the c.m.s.) in order to estimate the systematic error of the elastic scattering identification.

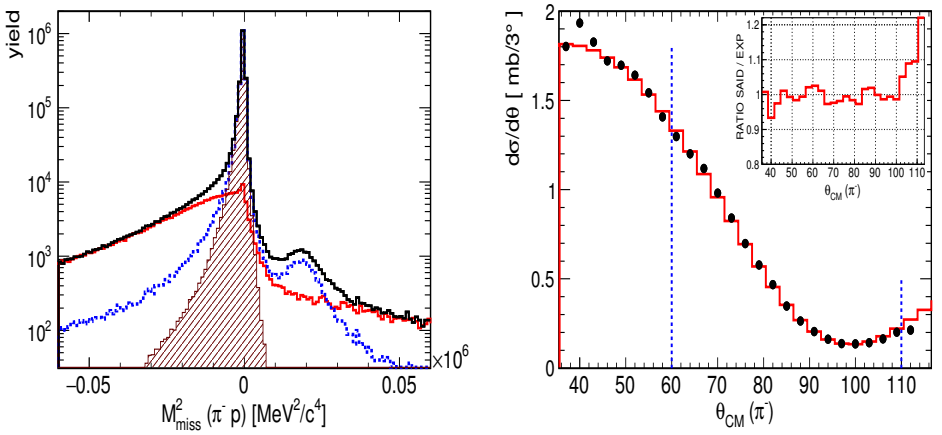

Figure C.23: Example of $\pi^- p \to \pi^- p$ elastic scattering at nominal beam momentum 800 MeV/c (791.1 MeV/c measured with the pion tracker). Left panel: uncorrected data, $\pi^- p$ missing mass squared with events from $(C_2H_4)_n$ (polyethylene) target (black histogram), C (carbon) target rescaled (red histogram) and their difference (blue dotted curve) - signal obtained by matching scattering on carbon in polyethylene target with scattering on carbon target on the event by event basis. Finally, elastic scattering selection (dark red dashed area). Right panel: angular projection of π^- in c.m.s. from $\pi^- p$ elastic scattering, corrected for the reconstruction inefficiencies and acceptance (black dots) compared with the distribution from the SAID database [Arn03] within the fiducial volume $60° < \theta_{\pi^-}^{c.m.s.} < 110°$ (limited by the vertical blue dashed lines). Inset: ratio of SAID data to reconstructed elastic events (red histogram).

To describe elastic scattering, events were generated in the framework of the PLUTO event generator [Frö07] with the angular parameterization taken from Ref. [Bro71]. Then, the full GEANT simulation of the detector response, followed by the same analysis strategy as used for the experimental data, were performed. Simulated elastic scattering events describe the measured data within the HADES acceptance very well and are used for the one-dimensional acceptance correction. The contribution from quasi-elastic scattering from C (red histogram) has been subtracted based on the missing mass distributions measured with polyethylene and carbon separately (as described above) and the difference agrees with the line shape expected for $\pi^- p$ events obtained from the full Monte Carlo simulations. The simulations took into account the momentum reconstructed with the help of the pion tracker (see App. C.1.8), with the most probable values of 654.1 MeV/c, 683.5 MeV/c, 738.9 MeV/c and 791.1 MeV/c. The corrected data are normalized to the distribution from the SAID database [Arn03] of the known differential $\pi^- p$ elastic scattering. It amounts to 3.01 mb, 3.10 mb, 3.08 mb and 2.59 mb for the subsequent pion beam momenta in the polar angle range between $60° - 110°$ in c.m.s. The corrected data for the pion beam momentum 791.1 MeV/c (nominal value 800 MeV/c) are presented in Fig. C.23, right panel. The deviation between SAID and experimental values is in the range $2 - 3\%$ (root-mean-square error).

C.3.7 Efficiency and acceptance corrections

To facilitate fast and easy comparison with the various reaction models, the detector acceptance and the reconstruction efficiencies were calculated and stored in the form of three-dimensional matrices (momentum, polar and azimuthal emission angles) for each particle species (p, π^+, π^-, e^+, e^-). The acceptance matrices describe the geometrical acceptance of the spectrometer, while the efficiency matrices account for the detection and reconstruction losses within the detector acceptance. The resolution effects were included by means of smearing functions acting on the generated momentum vectors.

Another approach is based on corrections calculated individually as one-dimensional functions. The correction function is constructed, for a given distribution, as ratio of the model yield in the full solid angle and the yield within the HADES acceptance, including all detection and reconstruction efficiencies obtained using the full analysis chain. It consists of three steps: (i) generation of events in the full space according to a specific reaction model, (ii) processing of the events through the realistic detector acceptance using the GEANT package, and (iii) applying specific detector efficiencies and the reconstruction steps as for the real data case. The respective correction functions are calculated as ratios of the distributions obtained after steps (ii) and (iii). In some cases the correction factors were calculated as two-dimensional functions of the dielectron invariant mass and the given angle using two reaction models.

The differences among models were used to estimate systematic errors related to model corrections. The models were verified to describe the measured distributions within the HADES acceptance reasonably well.

Acknowledgements

This monograph is essentially a culmination of my work over years, during which ideas had been forged, simulations were made, test measurements and experimental campaigns were carried out, and finally, analyzes were done, sometimes, iteratively repeated and improved over many years. Experimental physics today is a collective effort of many people. I have been fortunate in having some of the best physicists and friends to work with. I would like to honor them here and tell them big thanks!

Firstly, I would like to express my sincere gratitude to my advisor, present head of the Hadron Physics Department at the Jagiellonian University, a many-year spokesperson of the HADES Collaboration, Prof. Dr. hab. Piotr Salabura, for the continuous support of my work and related research, for his patience, motivation, and immense knowledge. His guidance helped me in all the time of research and writing of publications and this monograph.

My sincere thanks goes to Prof. Dr. Andrey Sarantsev, the leader of the Bonn-Gatchina partial wave analysis group. Andrey provided insight and expertise that greatly improved the research, and made a breakthrough in the quality of data interpretation. I want to thank him for the support he gave me, and great hospitality during my visits in Bonn and St. Petersburg.

I would like to thank Dr. Béatrice Ramstein for many years of collaboration and visits to Institut de Physique Nucléaire d'Orsay. Her insightful comments and detailed questions incented me to widen and improve my research from various perspectives.

I would also like to show gratitude to Prof. Dr. hab. Jerzy Smyrski who supported me during last year and introduced me into new exciting activities related to a forward tracker detector for the HADES and PANDA experiments.

I want to thank the HADES Collaboration spokesperson Prof. Dr. Joachim Stroth for the support, letting me represent the Collaboration at many international conferences and, last but not least, for the letter of support.

I thank my fellow mates for the stimulating discussions, long hours of work during experiments, various meetings, and for all the fun we have had in the last years. I want to name my old and new friends, who left the physics and who are still active participants (in alphabetical order): Adrian Dybczak, Izabela Ciepał, Małgorzata Gumberidze (Sudoł), Szymon Harabasz, Marcin Jaskuła, Marcin Kajetanowicz, Leszek Kidoń, Grzegorz Korcyl, Hubert Kuc, Rafał Lalik, Beata Michalska-Trębacz, Krzysztof Nowakowski, Jacek Otwinowski, Marek Pałka, Jerzy Pietraszko, Mateusz Płoskoń, Wawrzyniec Prokopowicz, Paweł Strzempek, Radosław Trębacz, Marcin Wiśniowski, and Tomasz Wójcik. It was great to have the opportunity to work with you.

Being an auxiliary supervisor of two Ph.D. theses I want to thank Anna Kożuch and Jacek Biernat, who were HADES Collaboration valuable members and good friends. I enjoyed the time with you and I am really happy you have done it.

I would also like to thank experts and scientists from many international institutes, in Frankfurt, München, Giessen, Dresden-Rossendorf, Řež, and Paris (in alphabetical order): Prof. Dr. Burkhard Kämpfer, Prof. Dr. Laura Fabbietti, Dr. Jürgen Friese, Dr. Ingo Fröhlich, Prof. Dr. Tetyana Galatyuk, Dr. Thierry Hennino, Dr. Romain Holzmann, Dr. Ilse Koenig, Dr. Wolfgang Koenig, Dr. Jochen Markert, Prof. Dr. Volker Metag, and Dr. Pavel Tlusty... and many more HADES Collaboration members. It is difficult to name them all.

I want to mention late Prof. Dr. hab. Andrzej Bałanda, my M.Sc. and Ph.D. supervisor, who encouraged me to join the HADES Collaboration and supported me over the years in many ways.

Most importantly, none of this could have happened without my family. This monograph stands as a testament to their unconditional love and encouragement. I want to thank them in Polish.

Podziękowania

Bardzo serdecznie dziękuję moim najbliższym za cierpliwość, wyrozumiałość, życzliwość i wsparcie, bez których nie napisałbym tej rozprawy. Biorąc udział w eksperymentach, wykonując symulacje i analizy, przygotowując prezentacje na konferencje, pisząc publikacje i tworząc tę monografię, zawsze byłem myślami przy Was.

W szczególny sposób dziękuję mojej żonie Agacie i dzieciom, Adasiowi i Zosi. Dzielnie znosiliście długie godziny, które poświęcałem pracy. W moim wysiłku jest też Wasz udział, a wasze wsparcie i obecność są najlepszą motywacją do efektywnej pracy. Serdeczne podziękowania ślę mojej Mamie, która bardzo wyczekiwała zakończenia tego dzieła, wspierając mnie i moją rodzinę na wiele sposobów. Moje myśli kieruję też do mojego śp. Taty, z wdzięcznością za wszystko co od niego otrzymałem. Dziękuję również mojej siostrze Dorocie wraz z rodziną, Andrzejem, Alicją i Ewą. Wszystkich Was kocham i o Was pamiętam!

Witold Przygoda

Bibliography

[Abo07] E. Abouzaid, M. Arenton, A.R. Barker, L. Bellantoni, A. Bellavance, E. Blucher, et al. Measurement of the rare decay $\pi^0 \to e^+e^-$. *Phys. Rev. D* **75**, 012004 (2007).

[Abr00] M.C. Abreu, B. Alessandro, C. Alexa, R. Arnaldi, J. Astruc, M. Atayan, et al. Dimuon and charm production in nucleus-nucleus collisions at the CERN-SPS. *Eur. Phys. J. C* **14**, 443 (2000).

[Ach01] M.N. Achasov, V.M. Aulchenko, K.I. Beloborodov, A.V. Berdyugin, A.G. Bogdanchikov, A.V. Bozhenok, et al. Study of conversion decays $\phi \to \eta e^+e^-$ and $\eta \to \gamma e^+e^-$ in the experiment with SND detector at VEPP-2M collider. *Phys. Lett. B* **504**, 275 (2001).

[Ago98] C. Agodi, A. Bassi, R. Bassini, G. Bellia, M. Benovic, C. Boiano, et al. The time-of-flight wall for the HADES spectrometer. *IEEE Trans. Nucl. Sci.* **45**, 665 (1998).

[Akh01] R.R. Akhmetshin, E.V. Anashkin, M. Arpagaus, V.M. Aulchenko, V.Sh. Banzarov, L.M. Barkov, et al. Study of conversion decays $\phi \to \eta e^+e^-$, $\eta \to e^+e^-\gamma$ and $\eta \to \pi^+\pi^-e^+e^-$ at CMD-2. *Phys. Lett. B* **501**, 191 (2001).

[Alb13] M. Albaladejo and E. Oset. Combined analysis of the $pn \to d\pi^+\pi^-$ and $pn \to pn\pi^+\pi^-$ cross sections and implications for the interpretation of the $pn \to d\pi^+\pi^-$ data. *Phys. Rev. C* **88**, 014006 (2013).

[Ale98] I.G. Alekseev, P.E. Budkovsky, V.P. Kanavets, L.I. Koroleva, I.I. Levintov, V.I. Martynov, et al. Study of the reaction $\pi^-p \to \pi^-\pi^+n$ on the polarized proton target at 1.78 GeV/c. Experiment and amplitude analysis. *Phys. Atom. Nucl.* **61**, 174 (1998).

[Ale08] C. Alexandrou, G. Koutsou, H. Neff, J.W. Negele, W. Schroers, and A. Tsapalis. Nucleon to delta electromagnetic transition form factors in lattice QCD. *Phys. Rev. D* **77**, 085012 (2008).

[Ale11] C. Alexandrou, G. Koutsou, J.W. Negele, Y. Proestos, and A. Tsapalis. Nucleon to Δ transition form factors with $N_F = 2 + 1$ domain wall fermions. *Phys. Rev. D* **83**, 014501 (2011).

[Ale13] C. Alexandrou, E.B. Gregory, T. Korzec, G. Koutsou, J.W. Negele, T. Sato, and A. Tsapalis. Determination of the $\Delta(1232)$ axial and pseudoscalar form factors from lattice QCD. *Phys. Rev. D* **87**, 114513 (2013).

[Ale15] I.G. Alekseev, V.A. Andreev, I.G. Bordyuzhin, W.J. Briscoe, Ye.A. Filimonov, V.V. Golubev, et al. High-precision measurements of πp elastic differential cross sections in the second resonance region. *Phys. Rev. C* **91**, 025205 (2015).

[Ame83] Ll. Ametller, L. Bergström, A. Bramon, and E. Massó. The quark triangle: Application to pion and eta decays. *Nucl. Phys. B* **228**, 301 (1983).

[Ame92] Ll. Ametller, J. Bijnens, A. Bramon, and F. Cornet. Transition form factors in π^0, η, and η' couplings to $\gamma\gamma^*$. *Phys. Rev. D* **45**, 986 (1992).

[Ame93] Ll. Ametller, A. Bramon, and E. Massó. $\pi^0 \to e^+e^-$ and $\eta \to \mu^+\mu^-$ decays reexamined. *Phys. Rev. D* **48**, 3388 (1993).

[And83] B. Andersson, G. Gustafson, G. Ingelman, and T. Sjöstrand. Parton fragmentation and string dynamics. *Phys. Rep.* **97**, 31 (1983).

[And93] B. Andersson, G. Gustafson, and H. Pi. The FRITIOF model for very high energy hadronic collisions. *Z. Phys. C* **57**, 485 (1993).

[And94] V.P. Andreev, A.V. Kravtsov, M.M. Makarov, V.I. Medvedev, V.I. Poromov, V.V. Sarantsev, et al. Experimental study of the reaction $pp \to pp\pi^0$ in the energy range 600-900 MeV. *Phys. Rev. C* **50**, 15 (1994).

[Ani05] A.V. Anisovich, E. Klempt, A.V. Sarantsev, and U. Thoma. Partial-wave decomposition of pion and photoproduction amplitudes. *Eur. Phys. J. A* **24**, 111 (2005).

[Ani06] A.V. Anisovich and A.V. Sarantsev. Partial decay widths of baryons in the spin-momentum operator expansion method. *Eur. Phys. J. A* **30**, 427 (2006).

[Ani12] A.V. Anisovich, R. Beck, E. Klempt, V.A. Nikonov, A.V. Sarantsev, and U. Thoma. Properties of baryon resonances from a multichannel partial wave analysis. *Eur. Phys. J. A* **48**, 15 (2012).

[Ape76] G.W. Van Apeldoorn, P.H.A. Van Dam, D. Harting, F.G. Hartjes, L.O. Hertzberger, D.L. Holthuizen, et al. Ionization measurements with an HPD in the analysis of $\bar{p}p$ interactions at 7.3 GeV/c. *Nucl. Instr. and Meth. A* **138**, 621 (1976).

[Ape79] G.W.Van Apeldoorn, D. Harting, D.J. Holthuizen, B.J. Pijlgroms, M.M.H.M. Rijssenbeek, and J.M. Warmerdam de Leeuw. Study of diffraction dissociation and double resonance production in the final state $\bar{p}p\pi^+\pi^-$ at 7.2 GeV/c. *Nucl. Phys. B* **156**, 111 (1979).

[AR98] L. Alvarez-Ruso, E. Oset, and E. Hernández. Theoretical study of the $NN \to NN\pi\pi$ reaction. *Nucl. Phys. A* **633**, 519 (1998).

[Arn03] R.A. Arndt, I.I. Strakovsky, and R.L. Workman. The SAID PWA program. *Int. J. Mod. Phys. A* **18**, 449 (2003).

[Arn06] R.A. Arndt, W.J. Briscoe, I.I. Strakovsky, and R.L. Workman. Extended partial-wave analysis of πN scattering data. *Phys. Rev. C* **74**, 045205 (2006).

[Azn12] I.G. Aznauryan and V.D. Burkert. Electroexcitation of nucleon resonances. *Progr. Part. Nucl. Phys.* **67**, 1 (2012).

[Azn13] I.G. Aznauryan, A. Bashir, V.M. Braun, S.J. Brodsky, V.D. Burkert, L. Chang, et al. Studies of nucleon resonance structure in exclusive meson electroproduction. *Int. J. Mod. Phys. E* **22**, 1330015 (2013).

[Bac67] T.C. Bacon, F.M. Bomse, T.B. Cochran, W.J. Fickinger, E.R. Goza, H.W.K. Hopkins, and E.O. Salant. Comparison of Isobar Production in pp and $\bar{p}n$ Interactions at 2.8 GeV/c. *Phys. Rev.* **162**, 1320 (1967).

[Bai12] P.A. Baikov, K.G. Chetyrkin, J.H. Kühn, and J. Rittinger. Adler function, sum rules and Crewther relation of order $\mathcal{O}(\alpha_s^4)$: The singlet case. *Phys. Lett. B* **714**, 62 (2012).

[Bal88] A. Baldini, V. Flaminio, W.G. Moorhead, and D.R.O. Morrison. *Total Cross-Sections for Reactions of High Energy Particles (Including Elastic, Topological, Inclusive and Exclusive Reactions).* Landolt-Börnstein. Springer, Berlin (1988).

[Bal04] A. Balanda, M. Jaskula, M. Kajetanowicz, L. Kidon, K. Korcyl, W. Kühn, et al. The HADES Pre-Shower detector. *Nucl. Instr. and Meth. A* **531**, 445 (2004).

[Bar68] W. Bartel, B. Dudelzak, H. Krehbiel, J. McElroy, U. Meyer-Berkhout, W. Schmidt, et al. Electroproduction of pions near the $\Delta(1236)$ isobar and the form factor $G_M^\star(q^2)$ of the $(\gamma N\Delta)$-vertex. *Phys. Lett. B* **28**, 148 (1968).

[Bar85] L.M. Barkov, A.G. Chilingarov, S.I. Eidelman, B.I. Khazin, M.Yu. Lelchuk, V.S. Okhapkin, et al. Electromagnetic pion form factor in the timelike region. *Nucl. Phys. B* **256**, 365 (1985).

[Bar87] L.M. Barkov, I.B. Vasserman, P.V. Vorob'ev, P.M. Ivanov, G.Ya. Kezerashvili, I.A. Koop, et al. Measurement of the properties of the ω meson with a cryogenic magnetic detector. *JETP Lett.* **46**, 164 (1987).

[Bas98] S.A. Bass, M. Belkacem, M. Bleicher, M. Brandstetter, L. Bravina, C. Ernst, et al. Microscopic models for ultrarelativistic heavy ion collisions. *Progr. Part. Nucl. Phys.* **41**, 255 (1998).

[Bas14] M. Bashkanov and H. Clement. On a possible explanation of the DLS puzzle. *Eur. Phys. J. A* **50**, 107 (2014).

[Bas17] M. Bashkanov, H. Clement, and T. Skorodko. Examination of the nature of the ABC effect. *Nucl. Phys. A* **958**, 129 (2017).

[Bät72] K. Bätzner, U. Beck, K.H. Becks, Ch. Berger, J. Drees, G. Knop, et al. Separation of σ_S and σ_T in the region of the $\Delta(1236)$ resonance and determination of the magnetic dipole transition form factor. *Phys. Lett. B* **39**, 575 (1972).

[BC15] M. Ablikim et al. (BESIII Collaboration). Observation of the Dalitz decay $\eta' \to \gamma e^+ e^-$. *Phys. Rev. D* **92**, 012001 (2015).

[Bec97] R. Beck, H.P. Krahn, J. Ahrens, H.J. Arends, G. Audit, A. Braghieri, et al. Measurement of the $E2/M1$ Ratio in the $N \to \Delta$ Transition using reaction $p(\vec{\gamma}, p)\pi^0$. *Phys. Rev. Lett.* **78**, 606 (1997).

[Bec00] R. Beck, H.P. Krahn, J. Ahrens, J.R.M. Annand, H.J. Arends, G. Audit, et al. Determination of the $E2/M1$ ratio in the $\gamma N \to \Delta(1232)$ transition from a simultaneous measurement of $p(\vec{\gamma}, p)\pi^0$ and $p(\vec{\gamma}, \pi^+)n$. *Phys. Rev. C* **61**, 035204 (2000).

[Bel09] D. Belver, A. Blanco, P. Cabanelas, N. Carolino, E. Castro, J. Diaz, et al. The HADES RPC inner TOF wall. *Nucl. Instr. and Meth. A* **602**, 687 (2009).

[Ben73] P. Benz, O. Braun, H. Butenschön, H. Finger, D. Gall, U. Idschok, et al. Measurement of the reaction $\gamma d \to \pi^- pp$, and determination of cross sections for the reaction $\gamma n \to \pi^- p$, at photon energies between 0.2 and 2.0 GeV. *Nucl. Phys. B* **65**, 158 (1973).

[Ber60] S.M. Berman and D.A. Geffen. The electromagnetic structure and alternative decay modes of the π^0. *Nuovo Cimento* **XVIII**, 1192 (1960).

[Ber81] M. Bernheim, A. Bussière, J. Mougey, D. Royer, D. Tarnowski, S. Turck-Chieze, et al. Momentum distribution of nucleons in the deuteron from the $d(e, e'p)n$ reaction. *Nucl. Phys. A* **365**, 349 (1981).

[Ber83a] L. Bergström. Radiative corrections to pseudoscalar meson decays. *Z. Phys. C* **20**, 135 (1983).

[Ber83b] L. Bergström, E. Massö, Ll. Ametller, and A. Bramon. Q^2 duality and rare pion decays. *Phys. Lett. B* **126**, 117 (1983).

[Ber11] H. Berghäuser, V. Metag, A. Starostinand P. Aguar Bartolomé, L.K. Akasoy, J.R.M. Annand, H.J. Arends, et al. Determination of the η–transition form factor in the $\gamma p \to p\eta \to p\gamma e^+ e^-$ reaction. *Phys. Lett. B* **701**, 562 (2011).

[Bes86] K. Beshliu, A.P. Ierusalimov, F. Kotorobaj, V.I. Moroz, A.V. Nikitin, and Yu.A. Troyan. Cross sections of reaction channels of np-interactions at p_n = 1-5 GeV/c. *Sov. J. Nucl. Phys.* **43**, 565 (1986).

[Bij88] J. Bijnens, A. Bramon, and F. Cornet. Pseudoscalar Decays into Two Photons in Chiral Perturbation Theory. *Phys. Rev. Lett.* **61**, 1453 (1988).

[Bij90] J. Bijnens, A. Bramon, and F. Cornet. Chiral perturbation theory for anomalous processes. *Z. Phys. C* **46**, 599 (1990).

[Bla97] G. Blanpied, M. Blecher, A. Caracappa, C. Djalali, G. Giordano, K. Hicks, et al. $N \to \Delta$ Transition from Simultaneous Measurements of $p(\vec{\gamma}, \pi)$ and $p(\vec{\gamma}, \gamma)$. *Phys. Rev. Lett.* **79**, 4337 (1997).

[Bla01] G. Blanpied, M. Blecher, A. Caracappa, R. Deininger, C. Djalali, G. Giordano, et al. $N \to \Delta$ transition and proton polarizabilities from measurements of $p(\vec{\gamma}, \gamma)$, $p(\vec{\gamma}, \pi^0)$, $p(\vec{\gamma}, \pi^+)$. *Phys. Rev. C* **64**, 025203 (2001).

[Bla12] A. Blanco, D. Belver, P. Cabanelas, J. Díaz, P. Fonte, J.A. Garzon, et al. RPC HADES-TOF wall cosmic ray test performance. *Nucl. Instr. and Meth. A* **661 Supp. 1**, S114 (2012).

[Ble99] M. Bleicher, E. Zabrodin, C. Spieles, S.A. Bass, C. Ernst, S. Soff, et al. Relativistic hadron-hadron collisions in the ultra-relativistic quantum molecular dynamics model. *J. Phys. G.* **25**, 1859 (1999).

[Bra81] A. Bramon and E. Massó. Q^2–duality for electromagnetic form factors of mesons. *Phys. Lett. B* **104**, 311 (1981).

[Bra95] E.L. Bratkovskaya, O.V. Teryaev, and V.D. Toneev. Anisotropy of dilepton emission from nuclear collisions. *Phys. Lett. B* **348**, 283 (1995).

[Bra97] E.L. Bratkovskaya and W. Cassing. Dilepton production from AGS to SPS energies within a relativistic transport approach. *Nucl. Phys. A* **619**, 413 (1997).

[Bra99] E.L. Bratkovskaya, W. Cassing, M. Effenberger, and U. Mosel. e^+e^- production from pp reactions at BEVALAC energies. *Nucl. Phys. A* **653**, 301 (1999).

[Bra01] E.L. Bratkovskaya, W. Cassing, and U. Mosel. Perspectives of e^+e^- production in pp, pd and pBe reactions at SIS energies. *Nucl. Phys. A* **686**, 568 (2001).

[Bra08] E.L. Bratkovskaya and W. Cassing. Dilepton production and off-shell transport dynamics at SIS energies. *Nucl. Phys. A* **807**, 214 (2008).

[Bra13] E.L. Bratkovskaya, J. Aichelin, M. Thomere, S. Vogel, and M. Bleicher. System size and energy dependence of dilepton production in heavy-ion collisions at 1-2 GeV/nucleon energies. *Phys. Rev. C* **87**, 064907 (2013).

[Bri15] W.J. Briscoe, M. Döring, H. Haberzettl, D.M. Manley, M. Naruki, I.I. Strakovsky, and E.S. Swanson. Physics opportunities with meson beams. *Eur. Phys. J. A* **51**, 129 (2015).

[Bro71] A.D. Brody, R.J. Cashmore, A. Kernan, D.W.G.S. Leith, B.S. Levi, B.C. Shen, et al. $\pi^- p$ Elastic Scattering in the c. m. Energy Range 1400-2000 MeV. *Phys. Rev. D* **3**, 2619 (1971).

[Bro73] S.J. Brodsky and G.R. Farrar. Scaling Laws at Large Transverse Momentum. *Phys. Rev. Lett.* **31**, 1153 (1973).

[Bro75] S.J. Brodsky and G.R. Farrar. Scaling laws for large-momentum-transfer processes. *Phys. Rev. D* **11**, 1309 (1975).

[Bro86] G.E. Brown, M. Rho, and W. Weise. Phenomenological delineation of the quark-gluon structure from nucleon electromagnetic form factors. *Nucl. Phys. A* **454**, 669 (1986).

[Bro91] G.E. Brown and M. Rho. Scaling effective Lagrangians in a dense medium. *Phys. Rev. Lett.* **66**, 2720 (1991).

[Bro02] W. Brodowski, R. Bilger, H. Calén, H. Clement, C. Ekström, K. Fransson, et al. Exclusive Measurement of the $pp \to pp\pi^+\pi^-$ Reaction Near Threshold. *Phys. Rev. Lett.* **88**, 192301 (2002).

[Bru69] D.C. Brunt, M.J. Clayton, and B.A. Westwood. Inelastic Reactions in Proton-Deuteron Scattering at 1.825 and 2.11 GeV/c. *Phys. Rev.* **187**, 1856 (1969).

[Bru97] R. Brun and F. Rademakers. ROOT: An object oriented data analysis framework. *Nucl. Instr. and Meth. A* **389**, 81 (1997).

[Bry72] R.A. Bryan and A. Gersten. Relativistic Treatment of Low-Energy Nucleon-Nucleon Scattering. *Phys. Rev. D* **6**, 341 (1972).

[Bry73] R.A. Bryan and A. Gersten. Relativistic Treatment of Low-Energy Nucleon-Nucleon Scattering. *Phys. Rev. D* **7**, 2802 (1973).

[Bug64] D.V. Bugg, A.J. Oxley, J.A. Zoll, J.G. Rushbrooke, V.E. Barnes, J.B. Kinson, et al. Proton-Proton Scattering at 970 MeV. *Phys. Rev.* **133**, B1017 (1964).

[Bus08] Oliver Buss. *Photon- and Pion-induced Nuclear Reactions in a Transport Approach.* PhD thesis, Justus-Liebig-Universität Gießen, Germany (2008).

[Bus12] O. Buss, T. Gaitanos, K. Gallmeister, H. van Hees, M. Kaskulov, O. Lalakulich, et al. Transport-theoretical description of nuclear reactions. *Phys. Rep.* **512**, 1 (2012).

[Byc73] E. Byckling and K. Kajante. *Particle Kinematics.* Wiley, New York (1973).

[Bys87] J. Bystricky, P. La France, F. Lehar, F. Perrot, T. Siemiarczuk, and P. Winternitz. Energy dependence of nucleon-nucleon inelastic total cross-sections. *J. Phys. France* **48**, 1901 (1987).

[Cal98] H. Calén, J. Dyring, K. Fransson, L. Gustafsson, S. Häggström, B. Höistad, et al. Measurement of the quasifree $p\vec{n}pn\eta$ reaction. *Phys. Rev. C* **58**, 2667 (1998).

[Cal99] H. Calén, J. Dyring, G. Fäldt, K. Fransson, L. Gustafsson, S. Häggström, et al. Higher partial waves in $pp \to pp\eta$ near threshold. *Phys. Lett. B* **458**, 190 (1999).

[Cao10] Xu Cao, Bing-Song Zou, and Hu-Shan Xu. Phenomenological analysis of the double-pion production in nucleon-nucleon collisions up to 2.2 GeV. *Phys. Rev. C* **81**, 065201 (2010).

[Cap94] S. Capstick and W. Roberts. Quasi-two-body decays of nonstrange baryons. *Phys. Rev. D* **49**, 4570 (1994).

[Cas99] W. Cassing and E.L. Bratkovskaya. Hadronic and electromagnetic probes of hot and dense nuclear matter. *Phys. Rep.* **308**, 65 (1999).

[CBC04] S. Prakhov et al. (Crystal Ball Collaboration). Measurement of $\pi^- p \to \pi^0\pi^0 n$ from threshold to p_{π^-} = 750 MeV/c. *Phys. Rev. C* **69**, 045202 (2004).

[CC91] H.-J. Behrend et al. (CELLO Collaboration). A measurement of the π^0, η and η' electromagnetic form factors. *Z. Phys. C* **49**, 401 (1991).

[CC06] M. Ungaro et al. (CLAS Collaboration). Measurement of the $N \to \Delta^+(1232)$ Transition at High-Momentum Transfer by π^0 Electroproduction. *Phys. Rev. Lett.* **97**, 112003 (2006).

[CC07] A. Lopez et al. (CLEO Collaboration). Measurement of Prominent eta Decay Branching Fractions. *Phys. Rev. Lett.* **99**, 122001 (2007).

[CC08] D. Adamová et al. (CERES Collaboration). Modification of the ρ meson detected by low-mass electron-positron pairs in central Pb-Au collisions at 158 AGeV/c. *Phys. Lett. B* **666**, 425 (2008).

[CC09a] M. Bashkanov et al. (CELSIUS/WASA Collaboration). Double-Pionic Fusion of Nuclear Systems and the "ABC" Effect: Approaching a Puzzle by Exclusive and Kinematically Complete Measurements. *Phys. Rev. Lett.* **102**, 052301 (2009).

[CC09b] I.G. Aznauryan et al. (CLAS Collaboration). Electroexcitation of nucleon resonances from CLAS data on single pion electroproduction. *Phys. Rev. C* **80**, 055203 (2009).

[CC11] P. Adlarson et al. (WASA – at – COSY Collaboration). Abashian-Booth-Crowe Effect in Basic Double-Pionic Fusion: A New Resonance? *Phys. Rev. Lett.* **106**, 242302 (2011).

[CC12a] V.I. Mokeev et al. (CLAS Collaboration). Experimental study of the $P_{11}(1440)$ and $D_{13}(1520)$ resonances from the CLAS data on $ep \to e'\pi^+\pi^- p'$. *Phys. Rev. C* **86**, 035203 (2012).

[CC12b] P. Adlarson et al. (WASA – at – COSY Collaboration). $\pi^0\pi^0$ Production in proton-proton collisions at $T_p = 1.4$ GeV. *Phys. Lett. B* **706**, 256 (2012).

[CC13a] P. Adlarson et al. (WASA – at – COSY Collaboration). Isospin decomposition of the basic double-pionic fusion in the region of the ABC effect. *Phys. Lett. B* **721**, 229 (2013).

[CC13b] P. Adlarson et al. (WASA – at – COSY Collaboration). Measurement of the $pn \to pp\pi^0\pi^-$ reaction in search for the recently observed resonance structure in $d\pi^0\pi^0$ and $d\pi^+\pi^-$ systems. *Phys. Rev. C* **88**, 055208 (2013).

[CC14a] P. Adlarson et al. (WASA – at – COSY Collaboration and SAID Data Analysis Center). Evidence for a New Resonance from Polarized Neutron-Proton Scattering. *Phys. Rev. Lett.* **112**, 202301 (2014).

[CC14b] P. Adlarson et al. (WASA – at – COSY Collaboration and SAID Data Analysis Center). Neutron-proton scattering in the context of the $d^*(2380)$ resonance. *Phys. Rev. C* **90**, 035204 (2014).

[CC15] P. Adlarson et al. (WASA – at – COSY Collaboration). Measurement of the $np \to np\pi^0\pi^0$ reaction in search for the recently observed $d^*(2380)$ resonance. *Phys. Lett. B* **743**, 325 (2015).

[CC16] P. Adlarson et al. (WASA – at – COSY Collaboration). Measurement of the $\vec{n}p \to d\pi^0\pi^0$ reaction with polarized beam in the region of the $d^*(2380)$ resonance. *Eur. Phys. J. A* **52**, 147 (2016).

[CEC08] U. Thoma et al. (CB-ELSA Collaboration). N^* and Δ^* decays into $N\pi^0\pi^0$. *Phys. Lett. B* **659**, 87 (2008).

[Cle15] H. Clement, M. Bashkanov, and T. Skorodko. From CELSIUS to COSY: on the observation of a dibaryon resonance. *Phys. Scr.* **T166**, 014016 (2015).

[Cle17] H. Clement. On the history of dibaryons and their final observation. *Progr. Part. Nucl. Phys.* **93**, 195 (2017).

[Coc72] D.R.F. Cochran, P.N. Dean, P.A.M. Gram, E.A. Knapp, E.R. Martin, D.E. Nagle, et al. Production of Charged Pions by 730-MeV Protons from Hydrogen and Selected Nuclei. *Phys. Rev. D* **6**, 3085 (1972).

[Col67] S. Coletti, J. Kidd, L. Mandelli, V. Pelosi, S. Ratti, V. Russo, et al. A bubble chamber study of proton-proton interactions at 4 GeV/c Part I - Elastic scattering, single-pion and deuteron production. *Nuovo Cimento A* **49**, 479 (1967).

[Col71] E. Colton, P.E. Schlein, E. Gellert, and G.A. Smith. Reaction $pp \to pp\pi^+\pi^-$ at 6.6 GeV/c. *Phys. Rev. D* **3**, 1063 (1971).

[Col09] W. Przygoda (HADES Collaboration). Dielectron production at 1-2 AGeV with HADES. *Nucl. Phys. A* **827**, 347 (2009).

[Col13] X. Dong (STAR Collaboration). Highlights from STAR. *Nucl. Phys. A* **904**, 19c (2013).

[Cor82] A. Cordier, D. Bisello, J.-C.Bizot, J. Buon, B. Delcourt, L. Fayard, and F. Mané. Study of the $e^+e^- \to \pi^+\pi^- K^+K^-$ reaction from 1.4 to 2.18 GeV. *Phys. Lett. B* **110**, 335 (1982).

[Cre13] V. Crede and W. Roberts. Progress towards understanding baryon resonances. *Rep. Prog. Phys.* **76**, 076301 (2013).

[CTC06] M. Abdel-Bary et al. (COSY-TOF Collaboration). Study of spectator tagging in the reaction $np \to pp\pi$ with a deuteron beam. *Eur. Phys. J. A* **29**, 353 (2006).

[CTC07] M. Abdel-Bary et al. (COSY-TOF Collaboration). Comparison of isoscalar vector meson production cross sections in proton-proton collisions. *Phys. Lett. B* **647**, 351 (2007).

[CTC08] S. Abd El-Bary et al. (COSY-TOF Collaboration). Two-pion production in proton-proton collisions with a polarized beam. *Eur. Phys. J. A* **37**, 267 (2008).

[CTC09] S. Abd El-Samad et al. (COSY-TOF Collaboration). On the production of $\pi^+\pi^+$ pairs in pp collisions at 0.8 GeV. *Eur. Phys. J. A* **42**, 159 (2009).

[Cut79] R.E. Cutkosky, C.P. Forsyth, R.E. Hendrick, and R.L. Kelly. Pion-nucleon partial-wave amplitudes. *Phys. Rev. D* **20**, 2839 (1979).

[Cve81] F.H. Cverna, P.R. Bevington, M.W. McNaughton, H.B. Willard, N.S.P. King, and D.R. Giebink. Single and double pion production from 800 MeV proton-proton collisions. *Phys. Rev. C* **23**, 1698 (1981).

[CWC08] M. Berłowski et al. (CELSIUS-WASA Collaboration). Measurement of η meson decays into lepton-antilepton pairs. *Phys. Rev. D* **77**, 032004 (2008).

[Czy11] W. Czyżycki, E. Epple, L. Fabbietti, M. Golubeva, F. Guber, A. Ivashkin, et al. Electromagnetic Calorimeter for HADES (2011), arXiv:nucl-ex/1109.5550v2.

[Dak82] L.G. Dakhno, A.V. Kravtsov, E.A. Lobachev, M.M. Makarov, V.I. Medvedev, G.Z. Obrant, et al. Measurement of the total cross sections for the reaction $pn \to pp\pi^-$ in the dibaryon-resonance energy region (500-1000 MeV). *Sov. J. Nucl. Phys.* **36**, 83 (1982).

[Dak83] L.G. Dakhno, A.V. Kravtsov, E.A. Lobachev, M.M. Makarov, V.I. Medvedev, G.Z. Obrant, et al. Measurement of the cross sections for production of pion pairs in nucleon-nucleon collisions at energies below 1 GeV. Isospin analysis. *Sov. J. Nucl. Phys.* **37**, 540 (1983).

[Dal54] R.H. Dalitz. Decay of τ Mesons of Known Charge. *Phys. Rev.* **94**, 1046 (1954).

[Dan15] I.V. Danilkin, C. Fernández-Ramírez, P. Guo, V. Mathieu, D. Schott, M. Shi, and A.P. Szczepaniak. Dispersive analysis of $\omega/\phi \to 3\pi$, $\pi\gamma^*$. *Phys. Rev. D* **91**, 094029 (2015).

[DC97] R.J. Porter et al. (DLS Collaboration). Dielectron Cross Section Measurements in Nucleus-Nucleus Reactions at 1.0 AGeV. *Phys. Rev. Lett.* **79**, 1229 (1997).

[DC98] W.K. Wilson et al. (DLS Collaboration). Inclusive dielectron cross sections in $p+p$ and $p+d$ interactions at beam energies from 1.04 to 4.88 GeV. *Phys. Rev. C* **57**, 1865 (1998).

[DC04] F. Balestra et al. (DISTO Collaboration). Exclusive η production in proton-proton reactions. *Phys. Rev. C* **69**, 064003 (2004).

[Deu16] A. Deur, S.J. Brodsky, and G.F. de Teramond. The QCD Running Coupling. *Progr. Part. Nucl. Phys.* **90**, 1 (2016).

[Dev69] S. Devons, P. Némethy, C. Nissim-Sabat, E. Di Capua, and A. Lanzara. Measurement of Neutral- and Charged-Pion Form-Factor Slopes. *Phys. Rev.* **184**, 1356 (1969).

[Dev76] R.C.E. Devenish, T.S. Eisenschitz, and J.G. Körner. Electromagnetic $N - N^*$ transition form factors. *Phys. Rev. D* **14**, 3063 (1976).

[Día02] J. Díaz, N. Yahlali, M. Ardid, M. Álvarez, V. Avdeichikov, H. Bokemeyer, et al. Design and commissioning of the GSI pion beam. *Nucl. Instr. and Meth. A* **478**, 511 (2002).

[Dmi86] V. Dmitriev, O. Sushkov, and C. Gaarde. Δ-formation in the $^1H(^3He,^3H)\Delta^{++}$ reaction at intermediate energies. *Nucl. Phys. A* **459**, 445 (1986).

[Doh10] F. Dohrmann, I. Fröhlich, T. Galatyuk, R. Holzmann, P.K. Kählitz, B. Kämpfer, et al. A versatile method for simulating $pp \to ppe^+e^-$ and $dp \to pne^+e^-p_{spec}$ reactions. *Eur. Phys. J. A* **45**, 401 (2010).

[Dol91] S.I. Dolinsky, V.P. Druzhinin, M.S. Dubrovin, V.B. Golubev, V.N. Ivanchenko, E.V. Pakhtusova, et al. Summary of experiments with the neutral detector at the e^+e^- storage ring VEPP-2M. *Phys. Rep.* **202**, 99 (1991).

[Dor03] E. Doroshkevich, M. Bashkanov, W. Brodowski, R. Bilger, H. Calén, H. Clement, et al. Study of baryon and search for dibaryon resonances by the $pp \to pp\pi^+\pi^-$ reaction . *Eur. Phys. J. A* **18**, 171 (2003).

[Dor07] A.E. Dorokhov and M.A. Ivanov. Rare decay $\pi^0 \to e^+e^-$: Theory confronts KTeV data. *Phys. Rev. D* **75**, 114007 (2007).

[Dor08] A.E. Dorokhov, E.A. Kuraev, Yu.M. Bystritskiy, and M. Sečanský. QED radiative corrections to the decay $\pi^0 \to e^+e^-$. *Eur. Phys. J. C* **55**, 193 (2008).

[Dor10] A.E. Dorokhov. Rare decay $\pi^0 \to e^+e^-$ as a test of standard model. *Phys. Part. Nucl. Lett.* **7**, 229 (2010).

[Dou76] P. Dougan, T. Kivikas, K. Lugnér, V. Ramsay, and W. Stiefler. Cross-sections for deuteron photo-disintegration from 139 to 832 MeV. *Z. Phys. A* **276**, 55 (1976).

[Dre59] S.D. Drell. Direct Decay $\pi^0 \to e^+ + e^-$. *Nuovo Cimento* **XI**, 693 (1959).

[Dre92] R.M. Drees, C. Waltham, T. Bernasconi, S. Egli, E. Hermes, F. Muheim, et al. Measurement of the π^0 electromagnetic transition form factor. *Phys. Rev. D* **45**, 1439 (1992).

[Dum83] O. Dumbrajs, R. Koch, H. Pilkuhn, G.C. Oades, H. Behrens, J.J. de Swart, and P. Kroll. Compilation of coupling constants and low-energy parameters. *Nucl. Phys. B* **216**, 277 (1983).

[Dym09] S. Dymov, M. Hartmann, A. Kacharava, A. Khoukaz, V. Komarov, P. Kulessa, et al. Observation of an "ABC" Effect in Proton-Proton Collisions. *Phys. Rev. Lett.* **102**, 192301 (2009).

[Dzh79] R.I. Dzhelyadin, S.V. Golovkin, M.V. Gritzuk, V.A. Kachonov, D.B. Kakauridse, A.S. Konstantinov, et al. Observation of $\eta' \to \mu^+\mu^-\gamma$ decay. *Phys. Lett. B* **88**, 379 (1979).

[Dzh80] R.I. Dzhelyadin, S.V. Golovkin, V.A. Kachanov, A.S. Konstantinov, V.F. Konstantinov, V.P. Kubarovski, et al. Investigation of the electromagnetic structure of the η meson in the decay $\eta \to \mu^+\mu^-\gamma$. *Phys. Lett. B* **94**, 548 (1980).

[Dzh81] R.I. Dzhelyadin, S.V. Golovkin, A.S. Konstantinov, V.F. Konstantinov, V.P. Kubarovski, L.G. Landsberg, et al. Study of the electromagnetic transition formfactor in $\omega \to \pi^0\mu^+\mu^-$ decay. *Phys. Lett. B* **102**, 296 (1981).

[EC04] D. Albers et al. (EDDA Collaboration). A precision measurement of pp elastic scattering cross-sections at intermediate energies. *Eur. Phys. J. A* **22**, 125 (2004).

[Eck89] G. Ecker, J. Gasser, A. Pich, and E. De Rafael. The role of resonances in chiral perturbation theory. *Nucl. Phys. B* **321**, 311 (1989).

[Edw11] R.G. Edwards, J.J. Dudek, D.G. Richards, and S.J. Wallace. Excited state baryon spectroscopy from lattice QCD. *Phys. Rev. D* **84**, 074508 (2011).

[Ehe96] W. Ehehalt and W. Cassing. Relativistic transport approach for nucleus-nucleus collisions from SIS to SPS energies. *Nucl. Phys. A* **602**, 449 (1996).

[Eis65] A.M. Eisner, E.L. Hart, R.I. Louttit, and T.W. Morris. Proton-Proton Scattering at 1.48 BeV. *Phys. Rev.* **138**, B670 (1965).

[Els06] D. Elsner, A. Süle, P. Barneo, P. Bartsch, D. Baumann, J. Bermuth, et al. Measurement of the LT-asymmetry in π^0 electroproduction at the energy of the $\Delta(1232)$-resonance. *Eur. Phys. J. A* **27**, 91 (2006).

[End13] S. Endres and M. Bleicher. Dilepton production at SIS energies with the UrQMD model. *J. Phys. Conf. Ser.* **426**, 012033 (2013).

[Eng96] A. Engel, R. Shyam, U. Mosel, and A.K. Dutt-Mazumder. Pion production in proton-proton collisions in a covariant one boson exchange model. *Nucl. Phys. A* **603**, 387 (1996).

[Epp14] Eliane Melanie Franziska Epple. *Measurable Consequences of an Attractive $\bar{K}N$ Interaction.* PhD thesis, Technische Universität München, Germany (2014).

[Eri88] T. Ericson and W. Weise. *Pions and Nuclei.* The International Series of Monographs on Physics (Book 74). Oxford University Press (1988).

[Erk74] K. Erkelenz. Current status of the relativistic two-nucleon one boson exchange potential. *Phys. Rep.* **13C**, 191 (1974).

[Erm11] K.N. Ermakov, V.I. Medvedev, V.A. Nikonov, O.V. Rogachevsky, A.V. Sarantsev, V.V. Sarantsev, and S.G. Sherman. The study of the proton-proton collisions at the beam momentum 1628 MeV/c. *Eur. Phys. J. A* **47**, 159 (2011).

[Erm14] K.N. Ermakov, V.I. Medvedev, V.A. Nikonov, O.V. Rogachevsky, A.V. Sarantsev, V.V. Sarantsev, and S.G. Sherman. The study of the proton-proton collisions at the beam momentum 1581 MeV/c. *Eur. Phys. J. A* **50**, 98 (2014).

[Erm17] K.N. Ermakov, V.A. Nikonov, O.V. Rogachevsky, A.V. Sarantsev, V.V. Sarantsev, and S.G. Sherman. Study of the proton-proton collisions at 1683 MeV/c. *Eur. Phys. J. A* **53**, 122 (2017).

[Ern98] C. Ernst, S.A. Bass, M. Belkacem, H. Stöcker, and W. Greiner. Intermediate mass excess of dilepton production in heavy ion collisions at relativistic energies. *Phys. Rev. C* **58**, 447 (1998).

[ES06] S.A. El-Samad, R. Bilger, K.-Th. Brinkmann, H. Clement, M. Dietrich, E. Doroshkevichand S. Dshemuchadse, et al. Single-pion production in pp collisions at 0.95 GeV/c (I). *Eur. Phys. J. A* **30**, 443 (2006).

[Fab03] L. Fabbietti, T. Eberl, J. Friese, R. Gernhäuser, J. Homolka, H.-J. Körner, et al. Photon detection efficiency in the CsI based HADES RICH. *Nucl. Instr. and Meth. A* **502**, 256 (2003).

[Fae00] A. Faessler, C. Fuchs, and M.I. Krivoruchenko. Dilepton spectra from decays of light unflavored mesons. *Phys. Rev. C* **61**, 035206 (2000).

[Fae03] A. Faessler, C. Fuchs, M.I. Krivoruchenko, and B. Martemyanov. Dilepton production in proton-proton collisions at BEVALAC energies. *J. Phys. G.* **29**, 603 (2003).

[Fäl11] G. Fäldt and C. Wilkin. Estimation of the ratio of the $pn \to pn\pi^0\pi^0/pn \to d\pi^0\pi^0$ cross sections. *Phys. Lett. B* **701**, 619 (2011).

[Far92] F. Farzanpay, P. Gumplinger, A. Stetz, J.-M. Poutissou, I. Blevis, M. Hasinoff, et al. Measurement of the slope of the π^0 electromagnetic form factor. *Phys. Lett. B* **278**, 413 (1992).

[Fel98] G.J. Feldman and R.D. Cousins. Unified approach to the classical statistical analysis of small signals. *Phys. Rev. D* **57**, 3873 (1998).

[Fer61] E. Ferrari and F. Selleri. Off-shell pion-nucleon scattering and dispersion relations. *Nuovo Cimento* **21**, 1028 (1961).

[Fer63] E. Ferrari and F. Selleri. An approach to the theory of single pion production in nucleon-nucleon collisions. *Nuovo Cimento* **27**, 1450 (1963).

[Feu97] T. Feuster and U. Mosel. Electromagnetic Couplings of Nucleon Resonances. *Nucl. Phys. A* **612**, 375 (1997).

[Fic62] W.J. Fickinger, E. Pickup, D.K. Robinson, and E.O. Salant. $p-p$ Interactions at 2 Bev. I. Single-Pion Production. *Phys. Rev.* **125**, 2082 (1962).

[Fis78] J. Fischer, P. Extermann, O. Guisan, R. Mermod, L. Rosselet, R. Sachot, et al. Measurement of the slope of the π^0–electromagnetic form factor. *Phys. Lett. B* **73**, 359 (1978).

[Fla83] V. Flaminio, W.G. Moorhead, D.R.O. Morrison, and N. Rivoire. *Compilation of cross sections I: π^+ and π^- induced reactions.* CERN-HERA 83-01. CERN (1983).

[Fon89] H. Fonvieille, N. Bensayah, J. Berthot, P. Bertin, B. Bihoreau, M. Crouau, et al. Dalitz decay. $\pi^0 \to \gamma e^+ e^-$ and the π^0 electromagnetic transition form factor. *Phys. Lett. B* **233**, 65 (1989).

[Fri97] B. Friman and H.J. Pirner. P-wave polarization of the ρ–meson and the dilepton spectrum in dense matter. *Nucl. Phys. A* **617**, 496 (1997).

[Fro99] V.V. Frolov, G.S. Adams, A. Ahmidouch, C.S. Armstrong, K. Assamagan, S. Avery, et al. Electroproduction of the $\Delta(1232)$ Resonance at High Momentum Transfer. *Phys. Rev. Lett.* **82**, 45 (1999).

[Frö07] I. Fröhlich, L. Cazon Boado, T. Galatyuk, V. Hejny, R. Holzmann, M. Kagarlis, et al. Pluto: A Monte Carlo Simulation Tool for Hadronic Physics. *PoS ACAT* **076** (2007).

[Fuc05] C. Fuchs, A. Faessler, D. Cozma, B.V. Martemyanov, and M. Krivoruchenko. Dilepton and vector meson production in elementary and in heavy ion reactions. *Nucl. Phys. A* **755**, 499 (2005).

[Gal87] C. Gale and B. Kapusta. Dilepton radiation from high temperature nuclear matter. *Phys. Rev. C* **35**, 1207 (1987).

[Gal89] C. Gale and J. Kapusta. Dilepton radiation from nucleon-nucleon collisions. *Phys. Rev. C* **40**, 2397 (1989).

[Gal91] C. Gale. Vector dominance model at finite temperature. *Nucl. Phys. B* **357**, 65 (1991).

[Gal09] Tetyana Galatyuk. *Di-electron spectroscopy in HADES and CBM: from p+p and n+p collisions at GSI to Au+Au collisions at FAIR.* PhD thesis, Johann Wolfgang Goethe-Universität, Frankfurt, Germany (2009).

[Gar03] Manuel Sánchez García. *Momentum Reconstruction and Pion Production Analysis in the HADES Spectrometer at GSI.* PhD thesis, University of Santiago de Compostela, Spain (2003).

[Gaz00] M. Gazdzicki and M.I. Gorenstein. Charm Estimate from the Dilepton Spectra (2000), arXiv:hep-ex/0003319v2.

[Gea94] *GEANT - Detector Description and Simulation Tool.* CERN Program Library Long Writeup W5013. CERN, Geneva, Switzerland (1994).

[Ger71] A. Gersten, R.H. Thompson, and A.E.S. Green. Relativistic Calculation of Nucleon-Nucleon Phase Parameters. *Phys. Rev. D* **3**, 2076 (1971).

[GM61] M. Gell-Mann and F. Zachariasen. Form Factors and Vector Mesons. *Phys. Rev.* **124**, 953 (1961).

[GM62] M. Gell-Mann, D. Sharp, and W. G. Wagner. Decay rates of Neutral Mesons. *Phys. Rev. Lett.* **8**, 261 (1962).

[Got64] K. Gottfried and J.D. Jackson. On the connection between production mechanism and decay of resonances at high energies. *Nuovo Cimento* **33**, 309 (1964).

[Gro69] F. Gross. Three-Dimensional Covariant Integral Equations for Low-Energy Systems. *Phys. Rev.* **186**, 1448 (1969).

[Gro08] F. Gross, G. Ramalho, and M.T. Peña. Pure S-wave covariant model for the nucleon. *Phys. Rev. C* **77**, 015202 (2008).

[Har62] E.L. Hart, R.I. Louttit, D. Luers, T.W. Morris, W.J. Willis, and S.S. Yamamoto. Multiple Meson Production in Proton-Proton Collisions at 2.85 BeV. *Phys. Rev.* **126**, 747 (1962).

[Har98] Ch. Hartnack, Rajeev K. Puri, J. Aichelin, J. Konopka, S.A. Bass, H. Stöcker, and W. Greiner. Modelling the many-body dynamics of heavy ion collisions: Present status and future perspective. *Eur. Phys. J. A* **1**, 151 (1998).

[Har12] Ch. Hartnack, H. Oeschler, Y. Leifels, E.L. Bratkovskaya, and J. Aichelin. Strangeness production close to the threshold in proton-nucleus and heavy-ion collisions. *Phys. Rep.* **510**, 119 (2012).

[Har17] Szymon Harabasz. *Reconstruction of virtual photons from Au+Au collisions at 1.23 GeV/u.* PhD thesis, Technische Universität, Darmstadt, Germany; Uniwersytet Jagielloński, Kraków (2017).

[Hat92] T. Hatsuda and S.H. Lee. QCD sum rules for vector mesons in the nuclear medium. *Phys. Rev. C* **46**, 34 (1992).

[Hat94] T. Hatsuda, E.M. Henley, Th. Meissner, and G. Krein. Off-shell $\rho - \omega$ mixing in QCD sum rules. *Phys. Rev. C* **49**, 452 (1994).

[HC09] G. Agakichiev et al. (HADES Collaboration). The high-acceptance dielectron spectrometer HADES. *Eur. Phys. J. A* **41**, 243 (2009).

[HC10] G. Agakichiev et al. (HADES Collaboration). Origin of the low-mass electron pair excess in light nucleus-nucleus collisions. *Phys. Lett. B* **690**, 118 (2010).

[HC12a] G. Agakichiev et al. (HADES Collaboration). Inclusive dielectron spectra in p+p collisions at 3.5 GeV kinetic beam energy. *Eur. Phys. J. A* **48**, 64 (2012).

[HC12b] G. Agakichiev et al. (HADES Collaboration). Study of exclusive one-pion and one-eta production using hadron and dielectron channels in *pp* reactions at kinetic beam energies of 1.25 GeV and 2.2 GeV with HADES. *Eur. Phys. J. A* **48**, 74 (2012).

[HC13] G. Agakichiev et al. (HADES Collaboration). Inclusive pion and η production in p+Nb collisions at 3.5 GeV beam energy. *Phys. Rev. C* **88**, 024904 (2013).

[HC14a] G. Agakichiev et al. (HADES Collaboration). Baryon resonance production and dielectron decays in proton-proton collisions at 3.5 GeV. *Eur. Phys. J. A* **50**, 82 (2014).

[HC14b] G. Agakichiev et al. (HADES Collaboration). Searching a dark photon with HADES. *Phys. Lett. B* **731**, 265 (2014).

[HC15a] G. Agakichiev et al. (HADES Collaboration). Analysis of pion production data measured by HADES in proton-proton collisions at 1.25 GeV. *Eur. Phys. J. A* **51**, 137 (2015).

[HC15b] G. Agakichiev et al. (HADES Collaboration). Study of the quasi-free $np \to np\pi^+\pi^-$ reaction with a deuterium beam at 1.25 GeV/nucleon. *Phys. Lett. B* **750**, 184 (2015).

[HC15c] G. Agakishiev et al. (HADES Collaboration). Analysis of pion production data measured by HADES in proton-proton collisions at 1.25 GeV. *Eur. Phys. J. A* **51**, 137 (2015).

[HC16a] F. Scozzi (for the HADES Collaboration). Studying $\rho - N$ couplings with HADES in pion-induced reactions. *EPJ Web of Conf.* **130**, 07021 (2016).

[HC16b] W. Przygoda (for the HADES Collaboration). Production and decay of baryonic resonances in pion induced reactions. *EPJ Web of Conf.* **130**, 01021 (2016).

[HC16c] W. Przygoda (for the HADES Collaboration). Resonance Production and Decay in Proton and Pion Induced Collisions with HADES. *JPS Conf. Proc.* **10**, 010013 (2016).

[HC17a] J. Adamczewski-Musch et al. (HADES Collaboration). A facility for pion-induced nuclear reaction studies with HADES. *Eur. Phys. J. A* **53**, 188 (2017).

[HC17b] J. Adamczewski-Musch et al. (HADES Collaboration). $\Delta(1232)$ Dalitz decay in proton-proton collisions at T = 1.25 GeV measured with HADES at GSI. *Phys. Rev. C* **95**, 065205 (2017).

[Hee08] H. Hees and R. Rapp. Dilepton radiation at the CERN super-proton synchrotron. *Nucl. Phys. A* **806**, 339 (2008).

[Her02] Gunar Hering. *Dielectron production in heavy ion collisions at 158 GeV/c per nucleon*. PhD thesis, Technische Universität, Darmstadt, Germany (2002).

[Hof58] G. Hofstadter, F. Bumiller, and M.R. Yearian. Electromagnetic Structure of the Proton and Neutron. *Rev. Mod. Phys.* **30**, 482 (1958).

[Höh83] G. Höhler. *Pion Nucleon Scattering. Part 1: Tables of Data. Part 2: Methods and Results of Phenomenological Analyses*. Landolt-Börnstein, Volume 9B2. Springer, Berlin (1983).

[Hol75] K. Holinde and R. Machleidt. Momentum-space OBEP, two-nucleon and nuclear matter data. *Nucl. Phys. A* **247**, 495 (1975).

[Hol76] K. Holinde and R. Machleidt. OBEP and eikonal form factor: I. Results for two-nucleon data. *Nucl. Phys. A* **256**, 479 (1976).

[Hub94] S. Huber and J. Aichelin. Production of Δ- and N^*-resonances in the one-boson exchange model. *Nucl. Phys. A* **573**, 587 (1994).

[Hul57] L. Hulthén and M. Sugawara. *Structure of Atomic Nuclei. Edited by S. Flügge. (The two-nucleon problem, p. 14)*. Handbuch der Physik, Vol. 39. Springer, Berlin (1957).

[Hus14] T. Husek, K. Kampf, and J. Novotný. Rare decay $\pi^0 \to e^+e^-$: on corrections beyond the leading order. *Eur. Phys. J. C* **74**, 3010 (2014).

[Iac73] F. Iachello, A.D. Jackson, and A. Lande. Semi-phenomenological fits to nucleon electromagnetic form factors. *Phys. Lett. B* **43**, 191 (1973).

[Iac04] F. Iachello and Q. Wan. Structure of the nucleon from electromagnetic timelike form factors. *Phys. Rev. C* **69**, 055204 (2004).

[Iiz66] J. Iizuka. A Systematics and Phenomenology of Meson Family. *Prog. Theor. Phys. Suppl.* **21**, 37 (1966).

[Iva81] P.M. Ivanov, L.M. Kurdadze, M.Yu. Lelchuk, V.A. Sidorov, A.N. Skrinsky, A.G. Chilingarov, et al. Measurement of the charged kaon form factor in the energy range 1.0 to 1.4 GeV. *Phys. Lett. B* **107**, 297 (1981).

[Iva12] S.A. Ivashyn. Vector to pseudoscalar meson radiative transitions in chiral theory with resonances. *Probl. At. Sci. Tech.* **2012, Issue 1**, 179 (2012).

[Jan75] M.R. Jane, P. Grannis, B.D. Jones, N.H. Lipman, D.P. Owen, V.Z. Peterson, et al. A measurement of the electromagnetic form factor of the eta meson and of the branching ratio for the eta Dalitz decay. *Phys. Lett. B* **59**, 103 (1975).

[JD07] B. Juliá-Díaz, T.-S.H. Lee, T. Sato, and L.C. Smith. Extraction and interpretation of $\gamma N \to \Delta$ form factors within a dynamical model. *Phys. Rev. C* **75**, 015205 (2007).

[Jer11] A.P. Jerusalimov, Yu.A. Troyan, A.Yu. Troyan, A.V. Belyaev, and E.B. Plekhanov. Study of the Reaction $np \to np\pi^+\pi^-$ at Intermediate Energies (2011), arXiv:hep-ex/1102.1574v1.

[Jer12a] A.P. Jerusalimov. Analysis of the Reaction: $np \to np\pi^+\pi^-$ from the Point of View of Oper-Model (2012), arXiv:nucl-th/1203.3330v1.

[Jer12b] A.P. Jerusalimov. Contribution of the "hanged" diagrams into the reaction $np \to np\pi^+\pi^-$ (2012), arXiv:nucl-th/1208.3982v1.

[Jer15] A.P. Jerusalimov, A.V. Belyaev, V.P. Ladygin, A.K. Kurilkin, A.Yu. Troyan, and Yu.A. Troyan. Study of the reaction $np \to np\pi^+\pi^-$ at 1.0 and 1.5 GeV. *Eur. Phys. J. A* **51**, 83 (2015).

[Joh02] J. Johanson, R. Bilger, W. Brodowski, H. Calén, H. Clement, C. Ekström, et al. Two-pion production in proton-proton collisions near threshold. *Nucl. Phys. A* **712**, 75 (2002).

[Jon73] H.F. Jones and M.D. Scadron. Multipole $\gamma N - \Delta$ Form Factors and Resonant Photo- and Electroproduction. *Ann. Phys.* **81**, 1 (1973).

[Käl64] G. Källén. *Elementary Particle Physics.* Addison-Wesley Publishing Company, London (1964).

[Kam71] R.C. Kammerud, B.B. Brabson, R.R. Crittenden, R.M. Heinz, H.A. Neal, H.W. Paik, and R.A. Sidwell. Large-Angle Proton-Proton Elastic Scattering at Intermediate Momenta. *Phys. Rev. D* **4**, 1309 (1971).

[Käm03] B. Kämpfer, A.I. Titov, and B.L. Reznik. Baryon Resonance Dynamics in $\pi N \to NV$ Reactions Near Threshold. *Nucl. Phys. A* **721**, 583c (2003).

[Kap94] J.I. Kapusta and E.V. Shuryak. Weinberg-type sum rules at zero and finite temperature. *Phys. Rev. D* **49**, 4694 (1994).

[Kap06] L.P. Kaptari and B. Kämpfer. Di-electron bremsstrahlung in intermediate-energy pn and Dp collisions. *Nucl. Phys. A* **764**, 338 (2006).

[Kap09] L.P. Kaptari and B. Kämpfer. Di-electrons from resonances in nucleon-nucleon collisions. *Phys. Rev. C* **80**, 064003 (2009).

[KC15] D. Babusci et al. (KLOE-2 Collaboration). Study of the Dalitz decay $\phi \to \eta e^+ e^-$ with the KLOE detector. *Phys. Lett. B* **742**, 1 (2015).

[KC16] A. Anastasi et al. (KLOE-2 Collaboration). Measurement of the $\phi \to \pi^0 e^+ e^-$ transition form factor with the KLOE detector. *Phys. Lett. B* **757**, 362 (2016).

[Ker98] M. Kermani, O. Patarakin, G.R. Smith, P.A. Amaudruz, F. Bonutti, J.T. Brack, et al. $\pi\vec{\pi}\pi\pi$ cross sections near threshold. *Phys. Rev. C* **58**, 3431 (1998).

[Kle10] E. Klempt and J.M. Richard. Baryon spectroscopy. *Rev. Mod. Phys.* **82**, 1095 (2010).

[Kli90] S. Klimt, M. Lutz, and W. Weise. Chiral phase transition in the SU(3) Nambu and Jona-Lasinio model. *Phys. Lett. B* **249**, 386 (1990).

[Kli96] F. Klingl, N. Kaiser, and W. Weise. Effective Lagrangian approach to vector mesons, their structure and decays. *Z. Phys. A* **356**, 193 (1996).

[Kli97] F. Klingl, N. Kaiser, and W. Weise. Current correlation functions, QCD sum rules and vector mesons in baryonic matter. *Nucl. Phys. A* **624**, 527 (1997).

[Kne99] M. Knecht, S. Peris, M. Perrottet, and E. de Rafael. Decay of Pseudoscalars into Lepton Pairs and Large-N_C QCD. *Phys. Rev. Lett.* **83**, 5230 (1999).

[Ko96] C.M. Ko, G.Q. Li, G.E. Brown, and H. Sorge. Enhancement of low-mass dileptons in SPS heavy-ion collisions: possible evidence for dropping rho meson mass in medium. *Nucl. Phys. A* **610**, 342 (1996).

[Kob61] H. Kobrak. Internal pairs from π^-–proton interactions at rest. *Nuovo Cimento* **20**, 1115 (1961).

[Koc84] J. Koch, E. Moniz, and N. Ohtsuka. Nuclear photoabsorption and Compton scattering at intermediate energy. *Ann. Phys.* **154**, 99 (1984).

[Koc93] P. Koch. Low mass lepton pair production and pion dynamics in ultrarelativistic heavy ion collisions. *Z. Phys. C* **57**, 283 (1993).

[Kon80] R. Koniuk and N. Isgur. Where Have All the Resonances Gone? An Analysis of Baryon Couplings in a Quark Model with Chromodynamics. *Phys. Rev. Lett.* **44**, 2720 (1980).

[Kon82] R. Koniuk. Baryon-vector-meson couplings in a quark model with chromodynamics. *Nucl. Phys. B* **195**, 452 (1982).

[Köp74] G. Köpp. Dispersion calculation of the transition form factor $F_{\pi\omega\gamma}(t)$ with cut contributions. *Phys. Rev. D* **10**, 932 (1974).

[Kor14] G. Kornakov, O. Arnold, E.T. Atomssa, C. Behnke, A. Belyaev, J.C. Berger-Chen, et al. Time of flight measurement in heavy-ion collisions with the HADES RPC TOF wall. *Journal of Instrumentation* **9**, C11015 (2014).

[Kri01] M.I. Krivoruchenko and A. Faessler. Remarks on Δ radiative and Dalitz decays. *Phys. Rev. D* **65**, 017502 (2001).

[Kri02] M.I. Krivoruchenko, B.V. Martemyanov, A. Faessler, and C. Fuchs. Electromagnetic Transition Form Factors and Dilepton Decay Rates of Nucleon Resonances. *Ann. Phys.* **296**, 299 (2002).

[Kro55] N.M. Kroll and W. Wada. Internal Pair Production Associated with the Emission of High-Energy Gamma Rays. *Phys. Rev.* **98**, 1355 (1955).

[Kro67] N.M. Kroll, T.D. Lee, and B. Zumino. Neutral Vector Mesons and the Hadronic Electromagnetic Current. *Phys. Rev.* **157**, 1376 (1967).

[Kru95] B. Krusche, J. Ahrens, G. Anton, R. Beck, M. Fuchs, A.R. Gabler, et al. Near Threshold Photoproduction of η Mesons off the Proton. *Phys. Rev. Lett.* **74**, 3736 (1995).

[Kuc15] Hubert Kuc. *Di-pion and di-electron production in quasi-free np reactions with HADES*. PhD thesis, Université Paris Sud, France (2015).

[Lac81] M. Lacombe, B. Loiseau, R. Vinh Mau, J. Côté, P. Pirés, and R. de Tourreil. Parametrization of the deuteron wave function of the Paris N-N potential. *Phys. Lett. B* **101**, 139 (1981).

[Lal16] Rafał Tomasz Lalik. *A beam detector for pion experiments and analysis of the inclusive Λ production in proton-proton reactions with HADES*. PhD thesis, Technische Universität München, Germany (2016).

[Lan85] L.G. Landsberg. Electromagnetic decays of light mesons. *Phys. Rep.* **128**, 301 (1985).

[Lap09] K. Lapidus. Dielectron production in pp and dp collisions at 1.25 GeV/u with HADES (2009), arXiv:nucl-ex/0904.1128v1.

[Leu10] S. Leupold, V. Metag, and U. Mosel. Hadrons in strongly interacting matter. *Int. J. Mod. Phys. E* **19**, 147 (2010).

[Li95] G.Q. Li and C.M. Ko. Can dileptons reveal the in-medium properties of vector mesons? *Nucl. Phys. A* **582**, 731 (1995).

[Li96] G.Q. Li, C.M. Ko, G.E. Brown, and H. Sorge. Dilepton production in proton-nucleus and nucleus-nucleus collisions at SPS energies. *Nucl. Phys. A* **611**, 539 (1996).

[Lic95] P. Lichard. Formalism for dilepton production via virtual photon bremsstrahlung in hadronic reactions. *Phys. Rev. D* **51**, 6017 (1995).

[Lic11] P. Lichard. Vector meson dominance and the π^0 transition form factor. *Phys. Rev. D* **83**, 037503 (2011).

[Liu13] B.C. Liu. ChPT Calculation for Two Pion Production in NN Collision Reaction at Threshold. *Few-Body Syst.* **54**, 353 (2013).

[Lon75] R.S. Longacre, A.H. Rosenfeld, T. Lasinski, and G. Smadja. N^* resonance parameters and K-matrix fits to the reactions $\pi N \to \Delta\pi + \rho N + \epsilon N$. *Phys. Lett. B* **55**, 415 (1975).

[Lon77] R.S. Longacre and J. Dolbeau. K-matrix fits to $N\pi \to N\pi$ and $N\pi\pi$ in the resonance region $\sqrt{s} = 1380$ to 1740 MeV. *Nucl. Phys. B* **122**, 493 (1977).

[Lov97] I. Lovas, K. Sailer, and W. Greiner. Generalized Rarita-Schwinger Equations for Non-Strange Baryons. *Heavy Ion Phys.* **5**, 85 (1997).

[Lut02] M.F.M. Lutz, Gy. Wolf, and B. Friman. Scattering of vector mesons off nucleons. *Nucl. Phys. A* **706**, 431 (2002).

[Lut03] M.F.M. Lutz, B. Friman, and M. Soyeur. Quantum interference of ρ^0- and $\omega-$mesons in the $\pi N \to e^+e^-N$ reaction. *Nucl. Phys. A* **713**, 97 (2003).

[Lut06] M.F.M. Lutz, Gy. Wolf, and B. Friman. Erratum to: "Scattering of vector mesons off nucleons". *Nucl. Phys. A* **765**, 495 (2006).

[Mac87] R. Machleidt. The Bonn meson-exchange model for the nucleon-nucleon interaction. *Phys. Rep.* **149**, 1 (1987).

[Mac01] R. Machleidt. High-precision, charge-dependent Bonn nucleon-nucleon potential. *Phys. Rev. C* **63**, 024001 (2001).

[MAM17a] P. Adlarson et al. (A2 Collaboration at MAMI). Measurement of the $\omega \to \pi^0 e^+ e^-$ and $\eta \to e^+e^-\gamma$ Dalitz decays with the A2 setup at the Mainz Microtron. *Phys. Rev. C* **95**, 035208 (2017).

[MAM17b] P. Adlarson et al. (A2 Collaboration at MAMI). Measurement of the $\pi^0 \to e^+e^-\gamma$ Dalitz decay at the Mainz Microtron. *Phys. Rev. C* **95**, 025202 (2017).

[Man58] S. Mandelstam. A Resonance Model for Pion Production in Nucleon-Nucleon Collisions at Fairly Low Energies. *Proc. R. Soc. Lond. A* **244**, 491 (1958).

[Man82] F. Mane, D. Bisello, J.-C. Bizot, J. Buon, A. Cordier, and B. Delcourt. Study of $e^+e^- \to K^0_S K^\pm \pi^\mp$ in the 1.4-2.18 GeV energy range: A new observation of an isoscalar vector meson: ϕ' (1.65 GeV). *Phys. Lett. B* **112**, 178 (1982).

[Man84] D.M. Manley, R.A. Arndt, Y. Goradia, and V.L. Teplitz. Isobar-model partial-wave analysis of $\pi N \to \pi\pi N$ in the c.m. energy range 1320 – 1930 MeV. *Phys. Rev. D* **30**, 904 (1984).

[Man92] D.M. Manley and E.M. Saleski. Multichannel resonance parametrization of πN scattering amplitudes. *Phys. Rev. D* **45**, 4002 (1992).

[Mar05] Jochen Markert. *Untersuchung Ansprechverhalten der Vieldraht-Driftkammern niedriger Massenbelegung des HADES-Experimentes.* PhD thesis, Johann Wolfgang Goethe-Universität, Frankfurt, Germany (2005).

[Mar11] B.V. Martemyanov, M.I. Krivoruchenko, and A. Faessler. Dilepton production in *pp* and *np* collisions at 1.25 GeV. *Phys. Rev. C* **84**, 047601 (2011).

[Mer01] C. Mertz, C.E. Vellidis, R. Alarcon, D.H. Barkhuff, A.M. Bernstein, W. Bertozzi, et al. Search for Quadrupole Strength in the Electroexcitation of the $\Delta^+(1232)$. *Phys. Rev. Lett.* **86**, 2963 (2001).

[Mic12] Jan Michel. *Development and Implementation of a New Trigger and Data Acquisition System for the HADES Detector.* PhD thesis, Johann Wolfgang Goethe-Universität, Frankfurt, Germany (2012).

[Mig55] A.B. Migdal. The Theory of Nuclear Reactions with Production of Slow Particles. *Sov. Phys. JETP* **1**, 2 (1955).

[Mik72] K.O. Mikaelian and J. Smith. Radiative Corrections to the Decay $\pi^0 \to \gamma e^+ e^-$. *Phys. Rev. D* **5**, 1763 (1972).

[Mos91] U. Mosel. Subthreshold particle production in heavy-ion collisions. *Ann. Rev. Nucl. Part. Sci.* **41**, 29 (1991).

[Mos02] P. Moskal, M. Wolke, A. Khoukaz, and W. Oelert. Close-to-threshold meson production in hadronic interactions. *Progr. Part. Nucl. Phys.* **49**, 1 (2002).

[Mos09] P. Moskal, R. Czyżykiewicz, H.-H. Adam, S.D. Bass, A. Budzanowski, E. Czerwiński, et al. Near-threshold production of the η meson via the quasifree $pn \to pn\eta$ reaction. *Phys. Rev. C* **79**, 015208 (2009).

[Müh06] P. Mühlich and U. Mosel. ω attenuation in nuclei. *Nucl. Phys. A* **773**, 156 (2006).

[Müh07] Pascal Mühlich. *Mesons in Nuclei and Nuclear Reactions with Elementary Probes.* PhD thesis, Justus-Liebig-Universität Gießen, Germany (2007).

[NC06] R. Arnaldi et al. (NA60 Collaboration). First Measurement of the ρ Spectral Function in High-Energy Nuclear Collisions. *Phys. Rev. Lett.* **96**, 162302 (2006).

[NC09] R. Arnaldi et al. (NA60 Collaboration). Study of the electromagnetic transition form-factors in $\eta \to \mu^+\mu^-\gamma$ and $\omega \to \mu^+\mu^-\pi^0$ decays with NA60. *Phys. Lett. B* **677**, 260 (2009).

[NC10] H.J. Specht et al. (NA60 Collaboration). Thermal Dileptons from Hot and Dense Strongly Interacting Matter. *AIP Conf. Proc.* **1322**, 1 (2010).

[NC16] R. Arnaldi et al. (NA60 Collaboration). Precision study of the $\eta \to \mu^+\mu^-\gamma$ and $\omega \to \mu^+\mu^-\pi^0$ electromagnetic transition form-factors and of the $\rho \to \mu^+\mu^-$ line shape in NA60. *Phys. Lett. B* **757**, 437 (2016).

[NC17] C. Lazzeroni et al. (NA62 Collaboration). Measurement of the π^0 electromagnetic transition form factor slope. *Phys. Lett. B* **768**, 38 (2017).

[Oku63] S. Okubo. ϕ-meson and unitary symmetry model. *Phys. Lett.* **5**, 165 (1963).

[Oku77] S. Okubo. Consequences of quark-line (Okubo-Zweig-Iizuka) rule. *Phys. Rev. D* **16**, 2336 (1977).

[Ose82] E. Oset, H. Toki, and W. Weise. Pionic modes of excitation in nuclei. *Phys. Rep.* **83**, 281 (1982).

[Pas07] V. Pascalutsa, M. Vanderhaeghen, and S.N. Yangd. Electromagnetic excitation of the $\Delta(1232)$-resonance. *Phys. Rep.* **437**, 125 (2007).

[Pät03] J. Pätzold, M. Bashkanov, R. Bilger, W. Brodowski, H. Calén, H. Clement, et al. The $p\vec{p} \to pp\pi^+\pi^-$ reaction studied in the low-energy tail of the Roper resonance. *Phys. Rev. C* **67**, 052202 (2003).

[PC10] A. Adare et al. (PHENIX Collaboration). Detailed measurement of the e^+e^- pair continuum in $p+p$ and $Au+Au$ collisions at $\sqrt{(}s_{NN}) = 200$ GeV and implications for direct photon production. *Phys. Rev. C* **81**, 034911 (2010).

[PDG94] L. Montanet et al. (Particle Data Group). Review of Particle Physics. *Phys. Rev. D* **50**, 1173 (1994).

[PDG10] K. Nakamura et al. (Particle Data Group). Review of Particle Physics. *J. Phys. G.* **37**, 075021 (2010).

[PDG12] J. Beringer et al. (Particle Data Group). Review of Particle Physics. *Phys. Rev. D* **86**, 010001 (2012).

[PDG14] K.A. Olive et al. (Particle Data Group). Review of Particle Physics. *Chin. Phys. C* **38**, 090001 (2014).

[PDG16] C. Patrignani et al. (Particle Data Group). Review of Particle Physics. *Chin. Phys. C* **40**, 100001 (2016).

[Pec15] O. Pechenova, V. Pechenov, T. Galatyuk, T. Hennino, R. Holzmann, G. Kornakov, et al. The alignment strategy of HADES. *Nucl. Instr. and Meth. A* **785**, 40 (2015).

[Pen02] G. Penner and U. Mosel. Vector meson production and nucleon resonance analysis in a coupled-channel approach for energies $m_N < \sqrt{s} < 2$ GeV. I. Pion-induced results and hadronic parameters. *Phys. Rev. C* **66**, 055211 (2002).

[Pet98] W. Peters, M. Post, H. Lenske, S. Leupold, and U. Mosel. The spectral function of the rho meson in nuclear matter. *Nucl. Phys. A* **632**, 109 (1998).

[Pet08] H. Petersen, M. Bleicher, S.A. Bass, and H. Stöcker. UrQMD-2.3 - Changes and Comparisons (2008), arXiv:hep-ph/0805.0567v1.

[Pic62a] E. Pickup, D.K. Robinson, and E.O. Salant. p–p Interactions at 2 Bev. II. Multiple-Pion Production. *Phys. Rev.* **125**, 2091 (1962).

[Pic62b] E. Pickup, D.K. Robinson, and E.O. Salant. Three-Pion Mass Distributions and the η Meson. *Phys. Rev. Lett.* **8**, 329 (1962).

[Pic84] A. Pich and J. Bernabéu. Rare decay modes of the neutral pion. *Z. Phys. C* **22**, 197 (1984).

[Pie10] J. Pietraszko, L. Fabbietti, W. Koenig, and M. Weber. Diamonds as timing detectors for minimum-ionizing particles: The HADES proton-beam monitor and START signal detectors for time of flight measurements. *Nucl. Instr. and Meth. A* **618**, 121 (2010).

[Pie14] J. Pietraszko, T. Galatyuk, V. Grilj, W. Koenig, S. Spataro, and M. Träger. Radiation damage in single crystal CVD diamond material investigated with a high current relativistic ^{197}Au beam. *Nucl. Instr. and Meth. A* **763**, 1 (2014).

[Pla16] M.N. Platonova and V.I. Kukulin. Hidden dibaryons in one- and two-pion production in NN collisions. *Nucl. Phys. A* **946**, 117 (2016).

[Pos01a] Th. Pospischil, P. Bartsch, D. Baumann, J. Bermuth, R. Böhm, K. Bohinc, et al. Measurement of the Recoil Polarization in the $p(\vec{e}, e'\vec{p})\pi^0$ Reaction at the $\Delta(1232)$ Resonance. *Phys. Rev. Lett.* **86**, 2959 (2001).

[Pos01b] M. Post and U. Mosel. Coupling of Baryon Resonances to the $N\omega$ channel. *Nucl. Phys. A* **688**, 808 (2001).

[Pre07] W.H. Press, S.A. Teukolsky, and W.T. Vetterling. *Numerical Recipes: The Art of Scientific Computing.* 3rd Edition. Cambridge University Press (2007).

[Qia10] W. Qian and B.-Q. Ma. Tri-meson mixing of π–η–η' and ρ–ω–ϕ in the light-cone quark model. *Eur. Phys. J. C* **65**, 457 (2010).

[Ram08a] G. Ramalho, M.T. Peña, and F. Gross. A covariant model for the nucleon and the Δ. *Eur. Phys. J. A* **36**, 329 (2008).

[Ram08b] G. Ramalho, M.T. Peña, and F. Gross. D-state effects in the electromagnetic $N\Delta$ transition. *Phys. Rev. D* **78**, 114017 (2008).

[Ram09a] G. Ramalho and M.T. Peña. Nucleon and $\gamma N \to \Delta$ lattice form factors in a constituent quark model. *J. Phys. G.* **36**, 115011 (2009).

[Ram09b] G. Ramalho and M.T. Peña. Valence quark contribution for the $\gamma N \to \Delta$ quadrupole transition extracted fromlattice QCD. *Phys. Rev. D* **80**, 113008 (2009).

[Ram12] G. Ramalho and M.T. Peña. Timelike $\gamma^* N \to \Delta(1232)$ form factors and Δ Dalitz decay. *Phys. Rev. D* **85**, 113014 (2012).

[Ram13] G. Ramalho and K. Tsushima. What is the role of the meson cloud in the $\Sigma^{*0} \to \gamma\Lambda$ and $\Sigma^* \to \gamma\Sigma$ decays? *Phys. Rev. D* **88**, 053002 (2013).

[Ram16] G. Ramalho, M.T. Peña, J. Weil, H. van Hees, and U. Mosel. Role of the pion electromagnetic form factor in the $\Delta(1232) \to \gamma^* N$ timelike transition. *Phys. Rev. D* **93**, 033004 (2016).

[Ram17] G. Ramalho and M.T. Peña. $\gamma^* N \to N^*(1520)$ form factors in the timelike regime. *Phys. Rev. D* **95**, 014003 (2017).

[Ram18] G. Ramalho. N^* Form Factors based on a Covariant Quark Model (2018), arXiv:hep-ph/1801.01476v1.

[Rap97] R. Rapp, G. Chanfray, and J. Wambach. Rho meson propagation and dilepton enhancement in hot hadronic matter. *Nucl. Phys. A* **617**, 472 (1997).

[Rap99] R. Rapp and J. Wambach. Low-mass dileptons at the CERN-SpS: evidence for chiral restoration? *Eur. Phys. J. A* **6**, 415 (1999).

[Rap00] R. Rapp and J. Wambach. Chiral symmetry restoration and dileptons in relativistic heavy ion collisions. *Adv. Nucl. Phys.* **25**, 1 (2000).

[Ris73] T. Risser and M.D. Shuster. Anomalous enhancements in multiple-pion production with deuterons. *Phys. Lett. B* **43**, 68 (1973).

[Ris01] D.O. Riska and G.E. Brown. Nucleon resonance transition couplings to vector mesons. *Nucl. Phys. A* **679**, 577 (2001).

[Rob94] C.D. Roberts and A.G. Williams. Dyson-Schwinger equations and their application to hadronic physics. *Progr. Part. Nucl. Phys.* **33**, 477 (1994).

[Ros50] M.N. Rosenbluth. High Energy Elastic Scattering of Electrons on Protons. *Phys. Rev.* **79**, 615 (1950).

[RR14] P. Rodríguez-Ramos, L. Chlad, E. Epple, L. Fabbietti, T. Galatyuk, M. Golubeva, et al. Electromagnetic Calorimeter for HADES Experiment. *EPJ Web of Conf.* **81**, 06009 (2014).

[Rüc76] R. Rückl. Direct lepton production by soft virtual bremsstrahlung. *Phys. Lett. B* **64**, 39 (1976).

[Sak60] J.J. Sakurai. Theory of Strong Interactions. *Ann. Phys.* **11**, 1 (1960).

[Sak69] J.J. Sakurai. *Currents and Mesons.* Chicago Lectures in Physics. University of Chicago Press (1969).

[Sam61] N.P. Samios. Dynamics of Internally Converted Electron-Positron Pairs. *Phys. Rev.* **121**, 275 (1961).

[Sar04] V.V. Sarantsev, K.N. Ermakov, V.I. Medvedev, T.S. Oposhnyan, O.V. Rogachevsky, and S.G. Sherman. The study of the neutral pion production in proton-proton collisions at beam momenta 1581 and 1683 MeV/c. *Eur. Phys. J. A* **21**, 303 (2004).

[Sar07] V.V. Sarantsev, K.N. Ermakov, V.I. Medvedev, O.V. Rogachevsky, and S.G. Sherman. Measurement of the cross sections for $\pi^+\pi^-$ production in pp collisions at energies below 1 GeV. *Phys. Atom. Nucl.* **70**, 1885 (2007).

[Sar08] A.V. Sarantsev, M. Fuchs, M. Kotulla, U. Thoma, J. Ahrens, J.R.M. Annand, et al. New results on the Roper resonance and the P_{11} partial wave. *Phys. Lett. B* **659**, 94 (2008).

[Sar10] V.V. Sarantsev, K.N. Ermakov, L.M. Kochenda, V.I. Medvedev, V.A. Nikonov, O.V. Rogachevsky, et al. The study of the negative pion production in neutron-proton collisions at beam momenta below 1.8 GeV/c. *Eur. Phys. J. A* **43**, 11 (2010).

[Sar16] A.V. Sarantsev. Properties of Baryons from Bonn-Gatchina partial Wave Analysis. *JPS Conf. Proc.* **10**, 010005 (2016).

[Sat96] T. Sato and T.-S.H. Lee. Meson-exchange model for πN scattering and $\gamma N \to \pi N$ reaction. *Phys. Rev. C* **54**, 2660 (1996).

[Sat01] T. Sato and T.-S.H. Lee. Dynamical study of the Δ excitation in $N(e, e'\pi)$ reactions. *Phys. Rev. C* **63**, 055201 (2001).

[Sav92] M.J. Savage, M. Luke, and M.B. Wise. The rare decays $\pi^0 \to e^+e^-$, $\eta \to e^+e^-$, and $\eta \to \mu^+\mu^-$ in chiral perturbation theory. *Phys. Lett. B* **291**, 481 (1992).

[Sch72] G. Schierholz. A relativistic one-boson-exchange model of nucleon-nucleon interaction. *Nucl. Phys. B* **40**, 335 (1972).

[Sch94] M. Schäfer, H.C. Dönges, A. Engel, and U. Mosel. Dilepton Production in Nucleon-Nucleon Interactions. *Nucl. Phys. A* **575**, 429 (1994).

[Sch08] Alexander Marc Schmah. *Produktion von Seltsamkeit in Ar+KCl Reaktionen bei 1.756 AGeV mit HADES.* PhD thesis, Technische Universität, Darmstadt, Germany (2008).

[Sch09] K. Schmidt, E. Santini, S. Vogel, C. Sturm, M. Bleicher, and H. Stöcker. Production and evolution path of dileptons at energies accessible to the HADES detector. *Phys. Rev. C* **79**, 064908 (2009).

[Sch12] S.P. Schneider, B. Kubis, and F. Niecknig. $\omega \to \pi^0\gamma^*$ and $\phi \to \pi^0\gamma^*$ transition form factors in dispersion theory. *Phys. Rev. D* **86**, 054013 (2012).

[Sch16] Heidi Schuldes. *Charged Kaon and ϕ Reconstruction in Au+Au Collisions at 1.23 AGeV.* PhD thesis, Johann Wolfgang Goethe-Universität, Frankfurt, Germany (2016).

[Sel65] F. Selleri. Virtual pion-nucleon scattering. *Nuovo Cimento A* **40**, 236 (1965).

[She03] K. Shekhter, C. Fuchs, A. Faessler, M. Krivoruchenko, and B. Martemyanov. Dilepton production in heavy-ion collisions at intermediate energies. *Phys. Rev. C* **68**, 014904 (2003).

[Shi82] F. Shimizu, H. Koiso, Y. Kubota, F. Sai, S. Sakamoto, and S.S. Yamamoto. Study of pp interactions in the momentum range 0.9 to 2.0 GeV/c. *Nucl. Phys. A* **389**, 445 (1982).

[Shr12] M. Shrestha and D.M. Manley. Multichannel parametrization of πN scattering amplitudes and extraction of resonance parameters. *Phys. Rev. C* **86**, 055203 (2012).

[Shu93] E.V. Shuryak. Correlation functions in the QCD vacuum. *Rev. Mod. Phys.* **65**, 1 (1993).

[Shy99] R. Shyam. $pp \to pK^+\Lambda$ reaction in an effective Lagrangian model. *Phys. Rev. C* **60**, 055213 (1999).

[Shy01] R. Shyam, G. Penner, and U. Mosel. Role of $N^*(1650)$ in the near threshold $p\vec{p}p\Lambda K^+$ and $p\vec{p}p\Sigma^0K^+$ reactions. *Phys. Rev. C* **63**, 022202(R) (2001).

[Shy03] R. Shyam and U. Mosel. Role of baryonic resonances in the dilepton emission in nucleon-nucleon collisions. *Phys. Rev. C* **67**, 065202 (2003).

[Shy07] R. Shyam. η-meson production in nucleon-nucleon collisions within an effective Lagrangian model. *Phys. Rev. C* **75**, 055201 (2007).

[Shy09] R. Shyam and U. Mosel. Dilepton production in nucleon-nucleon collisions reexamined. *Phys. Rev. C* **79**, 035203 (2009).

[Shy10a] R. Shyam and U. Mosel. Dilepton production in nucleon-nucleon collisions around 1 GeV/nucleon: A theoretical update. *Pramana - J. Phys.* **75**, 185 (2010).

[Shy10b] R. Shyam and U. Mosel. Dilepton production in proton-proton and quasifree proton-neutron reactions at 1.25 GeV. *Phys. Rev. C* **82**, 062201 (2010).

[Sib97] A. Sibirtsev, W. Cassing, and U. Mosel. Heavy meson production in proton-nucleus reactions with empirical spectral functions. *Z. Phys. A* **358**, 357 (1997).

[Sie10] Johannes Stephan Siebenson. *Exclusive analysis of the Λ(1405) resonance in the charged Σπ decay channels in proton proton reactions with HADES.* Master thesis, Technische Universität München, Germany (2010).

[Sie13] Johannes Stephan Siebenson. *Results from p+p reactions at the HADES experiment.* PhD thesis, Technische Universität München, Germany (2013).

[Sim99] R.S. Simon. Secondary pion beams at GSI. *Progr. Part. Nucl. Phys.* **42**, 247 (1999).

[Sjö08] T. Sjöstrand, S. Mrenna, and P. Skands. A brief introduction to PYTHIA 8.1. *Comput. Phys. Comm.* **178**, 852 (2008).

[Sko08] T. Skorodko, M. Bashkanov, D. Bogoslawsky, H. Calen, F. Cappellaro, H. Clement, et al. Excitation of the Roper resonance in single- and double-pion production in nucleon-nucleon collisions. *Eur. Phys. J. A* **35**, 317 (2008).

[Sko09] T. Skorodko, M. Bashkanov, D. Bogoslawsky, H. Calén, H. Clement, E. Doroshkevich, et al. Two-pion production in proton-proton collisions - experimental total cross sections and their isospin decomposition. *Phys. Lett. B* **679**, 30 (2009).

[Sko11a] T. Skorodko, M. Bashkanov, D. Bogoslawsky, H. Calén, H. Clement, E. Doroshkevich, et al. Exclusive measurement of the $pp \to nn\pi^+\pi^+$ reaction at 1.1 GeV. *Eur. Phys. J. A* **47**, 108 (2011).

[Sko11b] T. Skorodko, M. Bashkanov, D. Bogoslawsky, H. Calén, H. Clement, E. Doroshkevich, et al. ΔΔ excitation in proton-proton induced $\pi^0\pi^0$ production. *Phys. Lett. B* **695**, 115 (2011).

[Smy17] J. Smyrski, A. Apostolou, J. Biernat, W. Czyżycki, G. Filo, E. Fioravanti, et al. Design of the forward straw tube tracker for the PANDA experiment. *Journal of Instrumentation* **12**, C06032 (2017).

[Spa05] N.F. Sparveris, R. Alarcon, A.M. Bernstein, W. Bertozzi, T. Botto, P. Bourgeois, et al. Investigation of the Conjectured Nucleon Deformation at Low Momentum Transfer. *Phys. Rev. Lett.* **94**, 022003 (2005).

[Spa07] N.F. Sparveris, P. Achenbach, C. Ayerbe Gayoso, D. Baumann, J. Bernauer, A.M. Bernstein, et al. Determination of quadrupole strengths in the $\gamma^* p \to \Delta(1232)$ transition at $Q^2 = 0.20$ $(\mathrm{GeV/c})^2$. *Phys. Lett. B* **651**, 102 (2007).

[Spe94] K.E. Spear and J.P. Dismukes. *Synthetic Diamond: Emerging CVD Science and Technology.* Electrochemical Society. Wiley, New York (1994).

[Spe17] E. Speranza, M. Zétényi, and B. Friman. Polarization and dilepton anisotropy in pion-nucleon collisions. *Phys. Lett. B* **764**, 282 (2017).

[Sta06] S. Stave, M.O. Distler, I. Nakagawa, N. Sparveris, P. Achenbach, C. Ayerbe Gayoso, et al. Lowest-Q^2 measurement of the $\gamma^* p \to \Delta$ reaction: Probing the pionic contribution. *Eur. Phys. J. A* **30**, 471 (2006).

[Sta17] J. Staudenmaier, J. Weil, V. Steinberg, S. Endres, and H. Petersen. Dilepton production and resonance properties within a new hadronic transport approach in the context of the GSI-HADES experimental data (2017), arXiv:nucl-th/1711.10297v1.

[Ste75] S. Stein, W.B. Atwood, E.D. Bloom, R.L.A. Cottrell, H. DeStaebler, C.L. Jordan, et al. Electron scattering at 4° with energies of 4.5 – 20 GeV. *Phys. Rev. D* **12**, 1884 (1975).

[Ste96] J.V. Steele, H. Yamagishi, and I. Zahed. Dilepton and photon emission rates from a hadronic gas. *Phys. Lett. B* **384**, 255 (1996).

[Ste97] J.V. Steele, H. Yamagishi, and I. Zahed. Dilepton and photon emission rates from a hadronic gas. II. *Phys. Rev. D* **56**, 5605 (1997).

[Sus86] V.K. Suslenko and I.I. Gaisak. One Pion Exchange Model For The Reaction $pp \to np\pi^+$ And Its Verification On A Scale Of Differential Pion Spectra At Energy Of 0.66-GeV To 1.0-GeV. *Yad. Fiz.* **43**, 392 (1986).

[Svo14] O. Svoboda, C. Blume, W. Czyżycki, E. Epple, L. Fabbietti, T. Galatyuk, et al. Electromagnetic calorimeter for the HADES@FAIR experiment. *Journal of Instrumentation* **9**, C05002 (2014).

[Svo15] O. Svoboda, C. Blume, W. Czyżycki, E. Epple, L. Fabbietti, T. Galatyuk, et al. Verification of Electromagnetic Calorimeter Concept for the HADES spectrometer. *J. Phys. Conf. Ser.* **599**, 012026 (2015).

[TC90] H. Aihara et al. (TPC/2γ Collaboration). Investigation of the electromagnetic structure of η and η' mesons by two-photon interactions. *Phys. Rev. Lett.* **64**, 172 (1990).

[Tei96] Stefan Teis. *Transporttheoretische Beschreibung von relativistischen Schwerionenkollisionen bei SIS-Energien.* PhD thesis, Justus-Liebig-Universität Gießen, Germany (1996).

[Tei97] S. Teis, W. Cassing, M. Effenberger, A. Hombach, U. Mosel, and Gy. Wolf. Pion-production in heavy-ion collisions at SIS energies. *Z. Phys. A* **356**, 421 (1997).

[Ter10a] C. Terschlüsen and S. Leupold. Electromagnetic transition form factors of light vector mesons. *Phys. Lett. B* **691**, 191 (2010).

[Ter10b] Carla Terschlüsen. *Electromagnetic Transition Form Factors of Pseudoscalar and Vector Mesons.* PhD thesis, Justus-Liebig-Universität Gießen, Germany (2010).

[Ter12] C. Terschlüsen, S. Leupold, and M.F.M. Lutz. Electromagnetic transitions in an effective chiral Lagrangian with the η' and light vector mesons. *Eur. Phys. J. A* **48**, 190 (2012).

[Tho07] M. Thomère, C. Hartnack, G.Wolf, and J. Aichelin. Analysis of the dilepton invariantmass spectrum in C+C collisions at 2A and 1A GeV. *Phys. Rev. C* **75**, 064902 (2007).

[Tit00] A.I. Titov, B. Kämpfer, and B.L. Reznik. Production of ϕ mesons in near-threshold πN and NN reactions. *Eur. Phys. J. A* **7**, 543 (2000).

[Tit01] A.I. Titov and B. Kämpfer. Isoscalar-isovector interferences in $\pi N \to N e^+ e^-$ reactions as a probe of baryon resonance dynamics. *Eur. Phys. J. A* **12**, 217 (2001).

[Tsu00] T. Tsuboyama, F. Sai, N. Katayama, T. Kishida, and S.S. Yamamoto. Double-pion production induced by deuteron-proton collisions in the incident deuteron momentum range 2.1-3.8 GeV/c. *Phys. Rev. C* **62**, 034001 (2000).

[Ver79] B.J. Verwest. Field theoretical calculation of NN pion production. *Phys. Lett. B* **83**, 161 (1979).

[Wan05] Q. Wan and F. Iachello. A unified description of baryon electromagnetic form factors. *Int. J. Mod. Phys. A* **20**, 1846 (2005).

[Wan06] Qian Wan. *A Unified Approach to Hadron Electromagnetic Form Factors.* PhD thesis, Yale University, USA (2006).

[Wat52] K.M. Watson. The Effect of Final State Interactions on Reaction Cross Sections. *Phys. Rev.* **88**, 1163 (1952).

[Wei12] J. Weil, H. van Hees, and U. Mosel. Dilepton production in proton-induced reactions at SIS energies with the GiBUU transport model. *Eur. Phys. J. A* **48**, 111 (2012).

[Wei13] Janus Weil. *Vector Mesons in Medium in a Transport Approach.* PhD thesis, Justus-Liebig-Universität Gießen, Germany (2013).

[Wei16] J. Weil, V. Steinberg, J. Staudenmaier, L.G. Pang, D. Oliinychenko, J. Mohs, et al. Particle production and equilibrium properties within a new hadron transport approach for heavy-ion collisions. *Phys. Rev. C* **94**, 054905 (2016).

[Wei17] E. Weil, G. Eichmann, C.S. Fischer, and R. Williams. Electromagnetic decays of the neutral pion. *Phys. Rev. D* **96**, 014021 (2017).

[Wic86] A.B. Wicklund, M.W. Arenton, D.S. Ayres, R. Diebold, S.L. Kramer, E.N. May, et al. Study of the reaction $p_\uparrow p \to p\pi^+ n$ with polarized beam from 3 to 12 GeV/c. *Phys. Rev. D* **34**, 19 (1986).

[Wic87] A.B. Wicklund, M.W. Arenton, D.S. Ayres, R. Diebold, E.N. May, L.J. Nodulman, et al. Study of the reaction $p_\uparrow p \to p\pi^+ n$ with polarized beam from 1.18 to 1.98 GeV/c. *Phys. Rev. D* **35**, 2670 (1987).

[Wir95] R.B. Wiringa, V.G.J. Stoks, and R. Schiavilla. Accurate nucleon-nucleon potential with charge-independence breaking. *Phys. Rev. C* **51**, 38 (1995).

[Wol90] Gy. Wolf, G. Batko, W. Cassing, U. Mosel, K. Niita, and M. Schäfer. Dilepton production in heavy-ion collisions. *Nucl. Phys. A* **517**, 615 (1990).

[Wor12] R.L. Workman, M.W. Paris, W.J. Briscoe, and I.I. Strakovsky (CLAS Collaboration). Unified Chew-Mandelstam SAID analysis of pion photoproduction data. *Phys. Rev. C* **86**, 015202 (2012).

[Zei99] K. Zeitelhack, A. Elhardt, J. Friese, R. Gernhäuser, J. Homolka, A. Kastenmüller, et al. The HADES RICH detector. *Nucl. Instr. and Meth. A* **433**, 201 (1999).

[Zét03a] M. Zétényi and Gy. Wolf. Baryonic contributions to the dilepton spectrum of nucleon-nucleon collisions. *Phys. Rev. C* **67**, 044002 (2003).

[Zét03b] M. Zétényi and Gy. Wolf. Dilepton Decays of Baryon Resonances. *Heavy Ion Phys.* **17**, 27 (2003).

[Zha97] J. Zhang, R. Tabti, C. Gale, and K. Haglin. Another look at "soft" lepton pair production in nucleon-nucleon bremsstrahlung. *Int. J. Mod. Phys. E* **6**, 475 (1997).

[Zwe66] G. Zweig. *An SU_3 model for strong interaction symmetry and its breaking.* CERN-TH-412. CERN Report No. 8419 (1966).